Abstract

Uncovering Novel Biological Regulators of Ribosome Biogenesis

Carson Jerome Bryant

2023

Ribosomes are the complex macromolecular machines which assemble proteins in all forms of life, and their production process is known as ribosome biogenesis (RB). In eukaryotes, RB begins in the nucleolus with the transcription of the pre-ribosomal (pre-r)RNA, which undergoes modification, processing, and assembly into mature ribosomes. Malfunctioning RB can cause severe human diseases including rare developmental disorders called ribosomopathies, as well as cancer. Therefore, better understanding of the human RB machinery and its regulation is imperative for pursuing more effective clinical diagnoses and therapies. In this dissertation, I present work which simultaneously advances the field of RB in the areas of methodology, basic science, and clinical molecular pathology.

A key cell-based assay pioneered by the Baserga laboratory identifies novel candidate regulators of RB by monitoring for changes in nucleolar number. While robust, the nucleolar number assay does not directly quantify nucleolar production of pre-rRNA. To measure RB more directly, I adapted this pipeline into a high-throughput assay for nucleolar rRNA biogenesis, which simultaneously reports on synthesis and stability of the pre-rRNA. This new method uses 5-ethynyl uridine (5-EU) incorporation to

establish direct quantification of nucleolar function in high-throughput, facilitating closer study of RB in health and disease.

Although screening campaigns have broadly revealed novel protein regulators of human RB, I argue that non-coding (nc)RNAs comprise the next frontier in understanding RB regulation. Small ncRNAs called microRNAs are particularly exciting potential regulators of the RB pathway because they control other complex processes like development and cellular metabolism. Furthermore, a handful of microRNAs are already known to regulate RB. To investigate which other microRNAs may serve as novel nodes of RB control, I conducted a systematic screen of 2,603 human mature microRNA mimics in human MCF10A breast epithelial cells using the nucleolar number assay developed by the Baserga laboratory. I discovered 72 novel microRNA negative regulators of RB, 64 of which decrease nucleolar number in MCF10A cells. Bioinformatic analyses support the conclusion that the novel microRNA hits preferentially target transcripts encoding cell cycle factors or nucleolar proteins. Strikingly, 51/72 microRNA mimics strongly inhibited nucleolar rRNA biogenesis as measured by nucleolar 5-EU incorporation. Rigorous selection and validation of a subset of 15 microRNA mimic hits revealed that these hits starkly impair global protein synthesis and, unexpectedly, pre-rRNA processing. Consistent with my bioinformatic studies, most of these hits cause upregulation of the cell cycle inhibitor *CDKN1A* (*p21*). I also demonstrated that two microRNAs in the MIR-28 family, hsa-miR-28-5p and hsa-miR-708-5p, caused a severe defect in pre-18S rRNA processing by directly targeting the ribosomal protein transcript, *RPS28*. Additionally, I defined a role for the small oncogenic protein SPRR3

in promoting pre-rRNA transcription. Ultimately, my work illuminates novel microRNA attenuators of RB, forging a promising new path for microRNA mimic chemotherapeutics.

Together with an international team of medical researchers, I defined a new molecular basis for the ribosomopathy, alopecia, neurologic defects, and endocrinopathy (ANE) syndrome, which is caused by defects in the conserved ribosome assembly factor *RBM28*. Our team investigated a female pediatric ANE syndrome patient who presented with alopecia, craniofacial malformations, hypoplastic pituitary, and hair and skin abnormalities. Unlike previous cases, this patient possessed biallelic splicing variants at the 5′ splice sites of exon 5 (∆E5) and exon 8 (∆E8) in *RBM28*. My *in silico* analyses and minigene splicing experiments in cells indicated that each splice variant specifically causes skipping of its respective mutant exon. Using a yeast model, I demonstrated that the ∆E5 variant impairs overall growth and large subunit rRNA. In contrast, the ∆E8 variant is completely null, implying that the partially functional ∆E5 RBM28 protein enables survival but precludes correct development. My results define a new underlying pathology of ANE syndrome, further delineating an emerging class of assembly factor ribosomopathies and underscoring the importance of nucleolar processes in human health.

Looking forward, work outlined in this dissertation sets the stage for further inquiry into ncRNA regulators of RB, particularly by using more advanced genetic techniques, as well as into changes in nucleolar number, and into the importance of acquiring additional structural information about maturing human pre-ribosomes.

Uncovering Novel Biological Regulators of Ribosome Biogenesis

A Dissertation

Presented to the Faculty of the Graduate School

of

Yale University

In Candidacy for the Degree of

Doctor of Philosophy

by

Carson Jerome Bryant

Dissertation Director: Susan J Baserga, MD, PhD

May 2023

Acknowledgements

I am extremely grateful to many colleagues, friends, and family members for their professional and personal support during my PhD journey. I will thank as many of my supporters here as possible, and although I surely cannot name everyone: if we interacted during my time at Yale, please know I am a better scientist and person because of you – so I thank you.

To my advisor, Susan J Baserga, MD, PhD: Thank you, Susan, for accepting me into your lab, believing in my scientific potential, and trusting my judgment to try new experiments (and buy new equipment!) never-before-imagined in SHM C-114. Before I visited your office to inquire about rotating in your lab, I was caught at the nadir of my graduate school career in a toxic environment with little hope to continue on into my second year. The stress and dread of this period was excruciating. To meet you and Webster, on his beloved couch, and begin working in your lab was a welcome and vital relief. I am a much-improved scientist, communicator (on page and on stage), and philosopher because of your mentorship. Thank you for all your guidance, support, and trust over the years.

To my Committee, Joan A Steitz, PhD and Anthony J Koleske, PhD: Thank you, Joan and Tony, for always positively encouraging my progress while pushing me to think expansively and creatively about my work. The amount of brainpower that convened once every six months to hear about my newest scientific exploits is still inconceivable to me, and probably always will be. Thank you for modeling humility and resilience, both as

professional scientists of the highest caliber, and as marvelous people. I can only hope to pass forward the generosity that you have showed to me here at Yale.

To my outside thesis reader, Jennifer Gerton, PhD: Jen, thank you for all your time and critical thought in helping me improve my work. It was so lovely to chat with you at conferences in Kansas City and in Engelberg, and I'm very grateful for your support. And thanks for solving so many mysteries in the cell, including being part of the Telomere-to-Telomere team that finally illuminated that "dark matter of the genome," the ribosomal DNA arrays!

To my Baserga labmates, past and present: I thank the entire lab for its extraordinarily supportive culture, wherein each person wholly supported every other member and truly wanted nothing but success for one another. Thank you, Katie and Lisa, for being incredible mentors and colleagues to me during our overlapping time in the lab. I learned so much from you about how to survive and thrive as a graduate student. Your resilience and love for your families inspired me every day to be a better scientist while maintaining sight of what matters most in life. Thank you to my diligent baymate, Mason, for your unfaltering companionship and steady nature, which made sure I knew I always had a friend right by my side. I am so proud of all you've achieved, and I only hope to have provided you one-tenth the assurance you have given me. Thank you to Cecelia and Amber, for your kind friendship and your strength in the face of great adversity. Thank you to Ty and Courtney, for the fearlessness, joy, and style with which you imbued my life. Thank you to Emily Sutton, PhD and Emily McFadden, PhD, for your mentorship and encouragement that was essential for the final pushes to earn my

degree. Thank you to Yan, for sharing many of your life stories with me and for modeling immense courage and adventurousness.

To my collaborators at the Yale Center for Molecular Discovery (YCMD), Yulia Surovtseva, PhD and Laura Abriola, MS: Yulia and Laura, thank you so much for teaching me how to conduct high-throughput experiments, from both the bench science and data science perspectives. The trust you placed in me, epitomized by handing me the keys-to-the-high-content-kingdom (*i.e.*, permission to operate the IN Cell 2200 automated microscope without supervision) and by your faith to work alongside me in the lab, allowed me to build my confidence as an independent scientist. Given the tendency of Science to often make one feel as if they truly know nothing, this confidence was critical to my ability to persevere through my PhD. Thank you for your kindness and your support.

To my collaborators at Yale and in Brazil: Thank you to the laboratory of Sarah Slavoff, PhD, including Xiongwen Cao, PhD, Alex Khitun, PhD, Zhenkun Na, PhD, and Yang Vicki Luo, PhD. It was very exciting to follow the progress of your discoveries, and I am lucky to have made contributions to your work, minor though they were.

Thank you also to Filippo Pinto e Vairo, MD, Cláudia Lorea, MD, Hiram Larangeira de Almeida Jr, MD, Letícia Weinert, MD, and Leonardo Vedolin, MD. It was a pleasure to work alongside you and a privilege to help co-lead our international collaboration across hemispheres and scientific disciplines. Thank you also to the patient and the patient's family for allowing us to share their story about the rare ribosomopathy, ANE syndrome, with the scientific community.

To my other scientific mentors at Vanderbilt and beyond: Thank you to Chase Spurlock, PhD, for affording me the incredible privilege to "take a hand in the game" by working in Tom Aune's lab alongside you, when I was a rising high school senior and you were working towards your PhD. This first research experience ignited my passion for science and has been crucial to my career in ways I am only beginning to appreciate.

Thank you to David Cliffel, PhD and Evan Gizzie, PhD, for enabling and supporting me during my college research journey. Thank you also to Jens Meiler, PhD and Alissa Hare, PhD, as well as my many other mentors at Vanderbilt who taught me much about science and life, and made it possible for me to attend graduate school.

Thank you to Don Atha, PhD and Vytas Reipa, PhD at the National Institute of Standards and Technology (NIST) in Gaithersburg, MD. It was so exciting to work with and be co-mentored by both of you during my summer fellowship at NIST. I had an incredible experience in your labs where I truly felt, for the first time, that I could really make it as a professional scientist. Thank you also to the NIST SURF program and the other wonderful people I met at the Institute.

To my Yale cohort, my fellow graduate student colleagues, and my MB&B/YSM community: Thank you to each and every member of my BQBS cohort for your vision, tenacity, and collective support of one another, through all of grad school's peaks and troughs. Thanks to all the talented grad students and postdocs I met across the University during my PhD, for creating an uplifting and vibrant community throughout town. Thank you to the extended C-Wing community including the Neugebauer, Gilbert, Koleske, Koelle, Simon, Steitz, and Kabeche labs, for your abundant collegiality and

endless curiosity. Thank you to Stephen Chin-Bow, for always including me in your scientific and personal exploits, for making sure I knew how to safely close the autoclave all the way, and for designating me and Sallie as beneficiaries of your pizza-making skills. Thank you to Lindsay and our other fantastic custodial and maintenance staff. For always taking care of me and my co-workers at Yale and enabling our science, thank you to my friends in the Yale Medical Stockroom including Josh, John, Maria, Ms. Cynthia, Ms. Rosalind, Tyron, Chris, and George. Thanks in particular to Georgie, for always saving a seat for me in the Brannigan's Corner musical family.

To my New Haven community: Thank you for your remarkable fearlessness to envision a better tomorrow for workers at Yale, in the City, and beyond. Thank you for always believing in me and giving me the power to stand up and work alongside you as part of an incredible team. While I can only speculate about the enduring impact of my scientific contributions, I am proud to say I will always know that I helped permanently make Yale a better place.

To my "adopted" family in Pennsylvania: Thank you to the extended Thompson family for taking in me and Sallie as your own kin. Dan, thank you for noticing my Newport Jazz Festival shirt with the quote "Jazz means 'I dare you.' – Wayne Shorter" and asking if it was a literal definition. (Rest in Peace, Wayne!) I couldn't have asked for or ever expected to find a friend as true and honest as you. Thank you to Chris and Joel for all the memes and colorful humor. Thank you to Greg and Wendy for always opening your home and your hearts to us. Thanks to Uncle Steve for the PhD encouragement and Bigfoot sightings. Thanks to Uncle Eric for always being yourself. Thank you to Aunt Joy

and Uncle Richie, as well as Justin, Jason, and Jiffy for inspiring us with your blazing alacrity and ambition. Thanks to Dan, Chris, Joel, Steve, Garry, Mercy, Grace, and all the other band members in our merry crew for the great tunes and Soft Knees™.

To the Carter-Brown family: Thank you to Edward, Reba, and Katie for all the fun times and surprises in Murfreesboro or on vacation. Thanks for always making me feel right at home, for letting me watch TCM with you late into the evening, and for helping evolve my fashion sense. Thanks to Uncle Jeffy, Aunt Kristy, Reid, Aunt Debbie, Uncle Raymond, Uncle Henry, Aunt Diane, Granny Strode, and the rest of the Murfreesboro-Greenbrier axis, for your unwavering support of me and Sallie.

To my blood family in the US and abroad: Thank you to my parents for your love, faith, and sacrifice, which always ensured I had the best opportunities in my life. Thank you to my mother Patty for always fighting for me and our family, and for teaching me from a young age about the discrimination and sexism that you and other people without my privilege face on a daily basis. And thank you for teaching me how and why to fight against it. Thank you to my father Peter for your kind and charismatic spirit, and incessant curiosity. Thanks for showing me that any day you can help someone is a great day. Thank you to Aunt Beebe for always making sure I had a warm hug and some hot grub and cornbread waiting for me in Nashville, and for your unending patience (especially when you took me in to live with you one summer). Thanks to Uncle Tab for being the self-proclaimed Funcle (Fun-Uncle), and to Tab, Alex, Agnes, and Arman for inspiring me to be bold and leave my comfort zone as much as possible.

Thanks to Aunt Mary, Cousin Liam, and Uncle Bill (AKA “MLB”) for your thoughtfulness and liveliness, whether from across the country or just the room.

Lastly, but not leastly, to my Beautiful and Talented Wife: Thank you Sallie, for your unconditional love and support. Your vivacity and drive inspire me every day to be a better and stronger person. Thank you for being an incredible equestrian, small business owner, and caretaker for our cuddlesome kittens, Tipper and Flora. No one could ever understand me (or tolerate me) like you do, and I am so lucky to be your husband.

Table of Contents

List of Figures

List of Tables

Chapter 1

Eukaryotic ribosome biogenesis, its regulation, and the consequences of its dysregulation

McCool MA*, Bryant CJ*, Baserga SJ. MicroRNAs and long non-coding RNAs as novel regulators of ribosome biogenesis. Biochem Soc Trans. 2020;48(2):595-612. doi: 10.1042/BST20190854. PubMed PMID: 32267487; PMCID: 7200637.

* *These authors contributed equally as co-first-authors.*

1.1. Ribosomes, the machines that synthesize proteins, perpetuate biology

Ribosomes are complex macromolecular machines composed of ribosomal RNA (rRNA) and ribosomal proteins (RPs), which must be properly transcribed or translated, modified, folded, assembled, and, in eukaryotes, exported from the nucleus to the cytoplasm to begin producing proteins necessary for life (1-3). Ribosome biogenesis (RB) is the process by which new ribosomes are manufactured in the cell, and is facilitated by hundreds of *trans*-acting ribosome assembly factors (AFs). The two mature eukaryotic ribosomal subunits, the small 40S and large 60S, are aided by a slew of translation factors including aminoacyl-charged transfer (t)RNAs to engage protein-coding messenger (m)RNAs during cellular translation and accomplish polypeptide synthesis (4). Remarkably, the key peptidyl transferase reaction powering peptide bond synthesis is catalyzed only by ribosomal RNA (5, 6). It is therefore RNA, rather than DNA, protein, or lipid, which is the biomolecule beating at the heart of the ribosome, rendering the ribosome a ribozyme, and driving the pulse of biological existence.

Transcription of the rRNA is the critical first step in eukaryotic RB. In humans, a polycistronic 47S pre-rRNA transcript containing the small and large ribosomal subunit RNAs (18S or 28S and 5.8S rRNAs, respectively) is synthesized by RNA Polymerase 1 (RNAP1, or Pol I). The pre-rRNA then undergoes co- or post-transcriptional processing to remove externally- and internally-transcribed spacer sequences (5' ETS and 3' ETS; ITS1 and ITS2) (**Figure 1-1**) (1, 7-9). Separate from the primary transcript, the 5S rRNA is synthesized and processed in the nucleus, eventually being assembled into the 60S subunit core (10). The human 5S rRNA is encoded by multiple genes outside the

nucleolus that are transcribed by RNA Polymerase 3 (RNAP3, or Pol III), which also transcribes tRNAs critical for translation (11).

While rRNA is one key to the ribosome's catalytic activity, RPs provide structural ribosome stability, chaperone rRNA folding, and recruit proteins involved in subunit maturation or translation (1, 12, 13). Often, RPs possess domains for binding RNA or other proteins; globular domains localize RPs to sites in the rRNA, allowing unstructured loops to engage in charge shielding and rRNA folding (14). Near-identical RP paralogs exist as AFs or alternate forms of a given RP, although the paralogs generally do not functionally substitute for each other in humans (12, 15). Failure of paralogs to complement has given credence to the specialized ribosome hypothesis, which proposes that RP paralogs have tissue- or transcript-specific functions that can post-transcriptionally tune translation (15, 16).

AF proteins transiently interact with pre-ribosomal particles to advance subunit maturation. Over 200 AFs assist in eukaryotic RB, including enzymes, kinases, and snoRNP complexes containing small nucleolar (sno)RNAs (17, 18). In addition to performing rRNA modifications, snoRNPs are essential for cleavage of pre-40S pre-rRNA and likely of the primary transcript, probably by promoting correct folding of the pre-rRNA substrates and recruiting endonucleases (17, 19). More broadly, snoRNPs are intricately involved in pre-rRNA folding and processing, and potentially also function in splicing, gene expression, and other central processes (20).

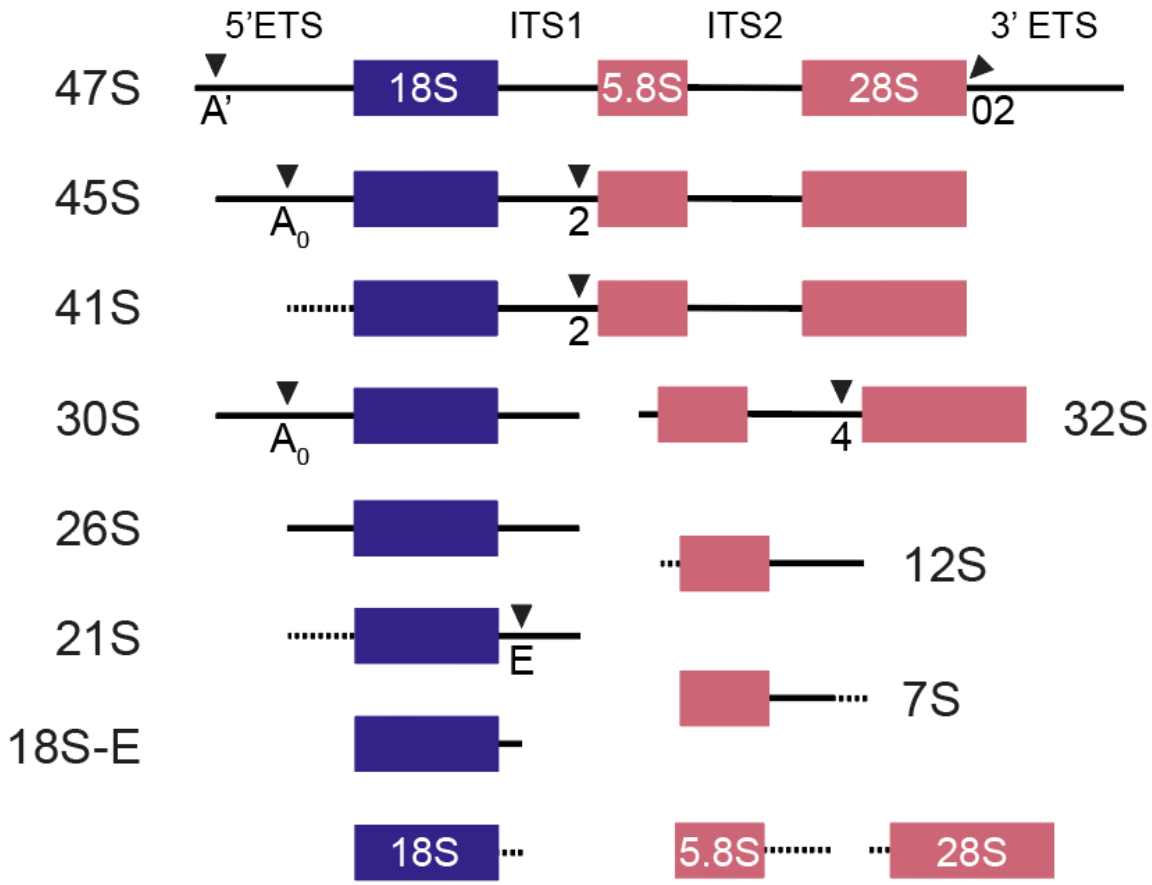

Figure 1-1. Simplified diagram of human pre-rRNA processing intermediates.

Mature 18S, 5.8S, and 28S rRNA regions are shown as blue (pre-40S) or red (pre-60S) rectangles. Intermediate names are indicated next to the relevant species, and transcribed spacers (solid black lines) are labeled at the top. Endonucleolytic cleavage sites are labeled with their names and represented with triangles. Dotted lines signify regions digested by exonucleases. ETS, external transcribed spacer; ITS, internal transcribed spacer. Figure adapted from **Chapter 3**. The reader may review Henras, *et al.* (8) for detailed processing pathway schematics.

Given the importance of protein synthesis to life, all living organisms possess ribosomes and a way to independently produce more. Both ribosomes and RB itself are essential, as evidenced by their strong conservation throughout the evolutionary tree of life. Indeed, nearly half of the genes in three different proposed universal gene sets of life (UGSLs) are direct components of the ribosome (21-24). The ribosomal component perhaps most conserved of all is the symmetric, "fossilized" rRNA cradle containing the peptidyl transferase center (PTC) (25, 26), though other regions of the rRNA exhibit considerable variability between even closely-related species (27-29). Conservation of the rRNA's PTC is so striking it has inspired synthetic reconstruction of a functional catalytic RNA-only proto-ribosome (30), whose spontaneous generation is a central tenet of the pre-biotic RNA World hypothesis (31-34). Moreover, phylogenetic studies have revealed the strong conservation of RB factors through *Archaea* and *Eukarya*, with complexity of RB increasing in more recently evolved organisms (35, 36). For example, additional eukaryote-specific rRNA elements called expansion segments are critical for expedient RB, perhaps due to their ability to recruit eukaryote-specific RPs or AFs that facilitate assembly of the larger eukaryotic ribosome (37, 38). Accreted complexity of the ribosome and its production process have been studied exhaustively in the baker's yeast, *Saccharomyces cerevisiae* (1, 2), and persist as the subject of contemporary studies in higher mammals and humans.

The magnitude of ribosome production is also a critical factor in cellular metabolism and energy management throughout biology. In *S. cerevisiae*, RNAP1 accounts for at least 60% of all transcription, and 60% of RNA Polymerase 2 (RNAP2,

or Pol II) activity is devoted to transcribing RPs and AFs (1, 39). Yeast produce over 2000 ribosomes per minute, yielding approximately 300,000 ribosomes per cell, and these figures balloon to 3500 ribosomes per minute totaling 3-10 million mature ribosomes in human HeLa cells (39-43). Together, these data clearly illustrate how RB is energetically and functionally biology's primary objective.

1.2. The nucleolus, a eukaryotic foundry for ribosomes

In eukaryotes, RB begins in the nucleolus, a dynamic phase-separated membraneless nuclear organelle formed at transcription sites of tandemly-repeated ribosomal DNA (rDNA) loci known as NORs, or nucleolar organizer regions (44-47). Each rDNA repeat is approximately 45 kb in length, with a 15 kb highly-transcribed region containing functional rDNA genes and a 30 kb intergenic spacer (IGS) region (7, 48). The rDNA genes are preceded by a promoter to which key transcription factors bind, including RRN3, UBTF, and the SL1 complex, to form the pre-initiation complex (PIC) and recruit RNAP1 for rDNA transcription (7, 49). rDNA promoter activity is a central node of control for RB (7), and may be modulated by elaborate upstream signaling pathways including the pro-growth PI3K/AKT/mTOR or MAPK/ERK pathways (7, 50, 51). Changes in rDNA topology (7, 48, 52) and the transcription of long non-coding (lnc)RNAs from the functional rDNA region or the IGS (7, 53, 54) also influence rDNA transcriptional activity.

Although the core rDNA unit is straightforward to describe, the rDNA repeats comprising NORs may vary in copy number and activity. Normal diploid human cells harbor approximately 300-400 rDNA repeats across 10 sites in the short p-arms of the five acrocentric chromosome pairs (chr 13-15, 21, 22), with syntenic (colinear) organization found in mice (8, 48, 55). Evolutionarily, having so many rDNA copies may shield the essential RB function from genetic disruption (56). Curiously, only a subset of the NORs in a given nucleus actively produces rRNA, and thereby create a true, functional nucleolus (55, 57-59). The activity of NORs may be regulated at the level of individual repeats or across the entire region (55, 60). Epigenetic chemical modifications (methylation), chromosomal architecture (nucleosome positioning and chromatin accessibility), or inhibition by ncRNAs may impact NOR activity status (55, 58, 61, 62). However, human NORs completely devoid of rDNA tandem repeats can still associate with other active NORs in nucleoli, suggesting genetic elements in the distal junctions beyond the rDNA genes and IGS may be critical facilitators of nucleolar formation (63, 64). While technical limitations have long relegated the NORs to being impenetrable genetic "dark matter" (65), cutting-edge results from the Telomere-to-Telomere (T2T) Consortium have finally unmasked the full sequence of the human genome, revealing the complexity and variability present in NORs and their ensconcing chromosomal milieu (66).

Structurally, the nucleolus is organized into three liquid-liquid phase separated (LLPS) partitions: the fibrillar center (FC), the dense fibrillar component (DFC), and the granular component (GC) (44, 45, 48). At the interface of the FC and DFC in the

nucleolar core, the RNAP1 machinery binds and transcribes active rDNA repeats (44, 45, 48). Many of these FC-DFC modules populate each human nucleolus (44). The primary 47S pre-rRNA precursor quickly moves to the surrounding DFC, which contains RPs and AFs critical for early pre-rRNA processing and modification including the snoRNP component enzymes fibrillarin (FBL) and dyskerin (DKC1) (44, 48). As their maturation continues, pre-ribosomal particles then enter the GC, where additional late processing and assembly factors are brought to bear (44, 45, 48). Important events in pre-60S maturation transpire in the GC including 5S RNP installation into the ribosome's central protuberance; conversely, pre-40S assembly is already largely complete here (44, 48, 67). Tartakoff, *et al.* envision the single yeast nucleolus as a coaxial cable whose energetic transcriptional core is shielded by double sheaths; this model is likely to hold in organisms with multiple nucleoli (67). Vectorial progression of maturing pre-ribosomes from the center of the nucleolus out to the nucleoplasm may be driven by subunit compaction, as the number of *trans* rRNA interaction sites once occupied by AFs decreases upon rRNA folding and permanent RP binding (44, 68). Heightened viscosity within the three nucleolar compartments concentrates pre-rRNA, RPs, and AFs, supercharging ribosome production to ensure that cellular translational demands are met (45). While experts agree on the existence of three distinct nucleolar subcompartments, the causal effect of LLPS on nucleolar function remains a question hotly investigated and debated in the field today (44, 69, 70).

Malfunctioning ribosome assembly can raise an alert in the cell, inducing a state called nucleolar stress. Canonically, free RPL5 or RPL11 proteins will sequester MDM2,

an E3 ligase which normally marks TP53 for degradation via ubiquitinylation; loss of this negative control leads to TP53 stabilization that causes cell cycle arrest and apoptosis (71-73). Depletion of other RPs or RB factors initiates this TP53 response dependent on RPL5 and RPL11 (74), and new work led by the Hannan laboratory implicates the nucleolar stress response as a key integrator of diverse genetic, pharmacological, and physiological cellular injuries (75).

Aberrant nucleolar morphology may occur depending on the severity of the activated nucleolar stress response. Segregated nucleolar caps may form upon rDNA damage, in which the NORs, FC, and DFC coalesce and invert orientation to the outer perimeter of the nucleolus; this reorganization likely enables recruitment of DNA repair factors and facilitates homologous repair of newly-clustered rDNA repeats (55, 76). Recently, Potapova and colleagues observed a striking, "bare" rDNA scaffold following inhibition of transcriptional cyclin-dependent kinases (CDKs) which co-regulate RNAP2, and also noted formation of nucleolar protein aggregates after HSP/proteasome inhibition (77).

1.3. Discovery of novel protein regulators of nucleolar structure and function

The higher-order regulatory potential of proteins on RB control has been rapidly surveyed by several recent high-content screening campaigns, particularly in human cells. This work builds on decades of RB investigations in the simpler unicellular eukaryote, *S. cerevisiae* (1, 2, 78, 79). Though its explorations are still incomplete, the field's

understanding of protein-mediated human RB regulation has been greatly expanded by the following screening endeavors.

The advent and accessibility of phenotypic cell-based assays have been critical in identifying novel regulators of human RB, although biochemical endpoints have also been useful. One successful strategy employed by the Kutay laboratory harnessed two HeLa lines harboring either fluorescently-tagged RPS2 or RPL29 to identify 40S- or 60S-specific defects using siRNA-mediated mRNA depletion (80-82). While normally the fluorescent RPs localize in both the nucleoli and the cytoplasm, knockdown of proteins involved in RB may result in aberrant accumulation of the fluorescent RPs in the nucleoplasm or in nucleoli. An initial candidate screen identified 153/464 RB factors, featuring good overlap with known factors. Follow-up studies for 40S or 60S defects probed the entire coding genome for novel protein regulators of RB, finding 612 total high-confidence hits in total (81, 82); unexpectedly, factors involved in biosynthetic pathways for glutamine (81) or polyamines (82) were identified as novel RB regulators from these studies.

Another cell-based assay for novel RB factors, pioneered by the Baserga laboratory, monitors changes in nucleolar number (83, 84). Human MCF10A breast epithelial cells, which have a nearly-normal karyotype and 2-4 nucleoli per nucleus in a normal state, were used to discover novel protein RB factors at a genome-wide scale (83, 84). The assay is predicated on the earlier observation that nucleolar number decreases upon depletion of NOL11, an assembly factor promoting RNAP1 transcription and early pre-rRNA processing (85). A similar phenomenon was observed by Hamdane, *et al.*,

who recorded a decrease in nucleolar number 72 h following *Ubtf* conditional elimination in mouse embryonic fibroblast (MEF) cells (86). However, it was also found that either a decrease or an increase in nucleolar number was a strong predictor of aberrant RB function (83, 84). A genome-wide siRNA knockdown campaign using this nucleolar number assay identified 252 high-confidence hits across both these phenotypes, unexpectedly revealing hits with roles in RNAP2 transcriptional control (PAX9, SUPT5H), cell signaling pathways (GRB2, CCN4), mitosis (CDCA8, CIAO2B, DYNC1H1, INCENP, RACGAP1, TPX2), and DNA repair and replication (RFC1, ATAD5, XRCC5), among many others (83, 84). I harnessed this nucleolar number screening platform in my campaign to uncover novel microRNA regulators of RB in **Chapter 3**.

While cell-based high-content screens have been especially fruitful, another screen using biochemical techniques also revealed novel protein regulators of human RB. Due to feasibility constraints, this screen interrogated a smaller subset of candidate coding genes rather than the entire proteome. The Lafontaine laboratory tested 625 nucleolar proteins for roles in pre-rRNA processing by conducting northern blots on total RNA from target-depleted HeLa cells (87). Ultimately this work identified 286 indispensable human pre-rRNA processing factors, 74 of which lacked orthologs in the yeast *S. cerevisiae* (87).

Surprisingly, comparing hits from screens conducted by the Baserga, Kutay, and Lafontaine labs reveals marginal overlap between datasets. While several dozen hits (~85) overlap between the Kutay and Lafontaine screens, which were conducted in HeLa cells, only about 30 hits were found in the Baserga screens in MCF10A cells and at least

one screen from another lab. Even more strikingly, only one hit, RPS11, was found in screens from all groups. This may be due to a combination of factors including using a different cell line and a different technique, especially given the unclear nature of what the nucleolar number assay reports (see **Chapter 5**). Altogether, both cell-based and biochemical probes of the human proteome have illuminated hundreds of novel protein regulators of RB.

1.4. Investigating non-coding RNAs on the next frontier of RB regulation

While additional protein RB factors likely remain to be discovered, I view non-coding (nc)RNAs as the next frontier of RB regulation to be explored. In particular, several handfuls of microRNAs and lncRNAs are already known to govern RB, substantiating the potential of ncRNAs to act as higher-order regulators of RB. Together with my colleagues McCool and Baserga, I cataloged a handful of known microRNA regulators of RB in our 2020 review (53), excerpts of which are presented below. Beginning in this review, my hypothesis that microRNAs may systematically regulate RB began to take shape, and became the impetus for my microRNA screen project detailed in **Chapter 3**.

MicroRNAs (miRNAs or miRs) are a class of short (~21 nucleotide, nt) non-coding RNAs that post-transcriptionally regulate mRNA stability and translatability. Canonical miRNA biogenesis is well-studied; typically, a primary miRNA transcript is synthesized by RNAP2 from a miRNA gene and then undergoes two processing steps

before being loaded into the Argonaute protein (AGO) to form an active RNA-induced silencing complex (RISC) (**Figure 1-2A**). The active silencing complex binds mRNA transcripts at a site usually within the 3'UTR of the targets. Based on the degree of miRNA:mRNA complementarity, RISC can induce translational repression (low complementarity) or transcript cleavage (high complementarity) (**Figure 1-2B**), thereby downregulating target expression post-transcriptionally (88, 89).

While most miRNAs originate from independently-transcribed miRNA genes, a number of non-canonical miRNA sources have been discovered. Mature miRNAs can be processed out of endogenously-transcribed intron lariats (mirtrons), short hairpin RNAs (shRNAs), tRNAs, and small nuclear and nucleolar RNAs (sn- and snoRNAs) (88). Notably, miRNA-like molecules interchangeably called small rDNA-derived RNAs or rRNA-hosted miRNA analogs (srRNAs or rmiRNAs) derive from precursor and mature rRNAs through poorly understood mechanisms (**Figure 1-2C**) (90, 91).

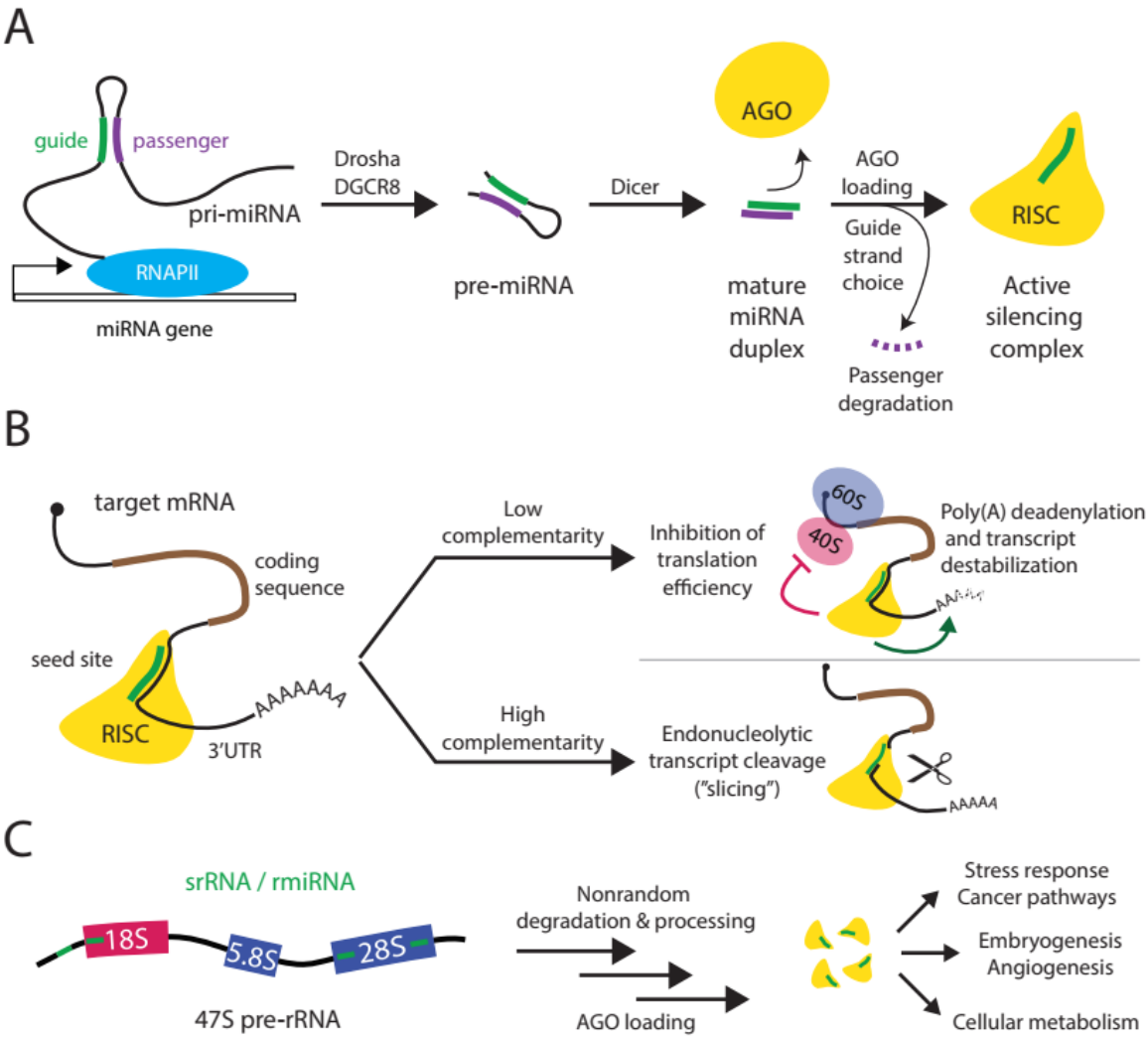

Figure 1-2. Biogenesis and function of miRNAs.

(A) Canonical generation and activation of cellular miRNAs. In most cases, a primary miRNA transcript (pri-miRNA) containing the mature miRNA sequence is synthesized by RNAPII from a miRNA gene. Nuclear processing of the pri-miRNA by a microprocessor complex containing Drosha and DGCR8 results in a trimmed intermediate precursor hairpin (pre-miRNA), which is exported to the cytoplasm for secondary processing by Dicer endonuclease to generate the mature miRNA duplex. Argonaute (AGO) protein binds the miRNA duplex to form an active RNA-induced silencing complex (RISC), retaining the "guide" strand and expelling the "passenger" strand (miRNA*) for degradation. Guide strand choice depends on conformational energetics of loading the mature duplex into Argonaute.

(B) miRNA-mediated post-transcriptional mRNA regulation depends on target complementarity. The active silencing complex is targeted to mRNA transcripts via complementary hybridization with the 6-base seed region of the loaded miRNA guide,

usually at a site within the 3'UTR of the targets downstream of the coding sequence (brown). Based on the degree of miRNA:mRNA complementarity, RISC can induce translational repression or transcript cleavage, thereby downregulating target expression post-transcriptionally. Low complementarity causes mRNA poly(A) deadenylation and reduces translation efficiency, while high complementarity can trigger endonucleolytic target degradation (slicing).

(C) rRNA-hosted miRNAs are stably generated and control diverse cellular processes and outcomes. Small rDNA-derived RNAs or rRNA-hosted miRNA analogs (srRNAs or rmiRNAs) are produced from functional (18S and 28S) and nonfunctional (5' ETS) regions of the 47S pre-rRNA transcript. The mechanisms for rmiRNA production are poorly-understood, but are not likely to be due to random degradation. Mature rmiRNAs have been observed to control diverse developmental, metabolic, and stress pathways.

Figure reproduced from (53).

srRNA/rmiRNA generation is likely not due to random degradation but rather controlled processing that creates stable srRNA products, and may be Drosha-dependent or independent (91-93). Functionally, rmiRNAs have been shown to bind AGO proteins and are implicated in regulation of various metabolic and developmental pathways. srRNAs in fly and human cells associate with AGO complexes (92). Differential hepatic srRNA expression was observed in diabetic mice, and specific srRNAs were found to modulate transcription of regulators of gluconeogenesis in mouse hepatoma cells (92). Several human rmiRNAs were predicted to target stress- and cancer-related pathways (91), and differential rmiRNA expression has been observed upon heat stress in rice (94) and wheat (95). In zebrafish, rmiRNAs mapping to the 18S and 28S rRNAs were found to be critical for early embryogenesis (93) and blood vessel formation (96), respectively. Additionally, differential spatiotemporal transcription of rDNA sequence variants may also alter rmiRNA expression (93, 97). Novel rRNA-derived miRNAs exemplify the emerging connection between miRNAs and ribosome biogenesis, underscoring how diverse cellular processes can be modulated by miRNAs that interact with ribosome production.

Dozens of miRNAs are stably enriched in the nucleolus in a variety of human and mammalian cell lines, and their localization is resistant to RNAP1 transcription inhibition or other cellular and nucleolar stresses (98-101). These nucleolar miRNAs may have diverse noncanonical biological roles including direct regulation of rRNA synthesis (102) or ribosomal subunit formation (103), protected formation of pre-silenced miRNA:mRNA pairs away from the crowded and competitive cytoplasm (101),

mediation of a defensive response to exogenous genetic material (99), or even targeting for deactivation by nucleolar deaminase editing (98). These initial observations warrant additional follow-up to better define the identities and roles of nucleolar miRNAs. For a more extensive discussion of miRNAs localized to the nucleolus, we refer the reader to a brief review by Catalanotto and coworkers (104).

A growing cadre of disease-associated miRNAs have been shown to control components, subprocesses, or regulators of ribosome biogenesis (**Figure 1-3**, **Table 1-1**). Dysregulation of miRNA expression correlates with the progression of many types of cancer (105, 106), and the link between cancer and ribosome biogenesis is well-established (107). We review recent publications that consider (i) direct interplay among cancer, ribosome biogenesis and miRNAs holistically and (ii) microRNA regulators of ribosome biogenesis in ribosomopathies and in Chronic Obstructive Pulmonary Disease (COPD).

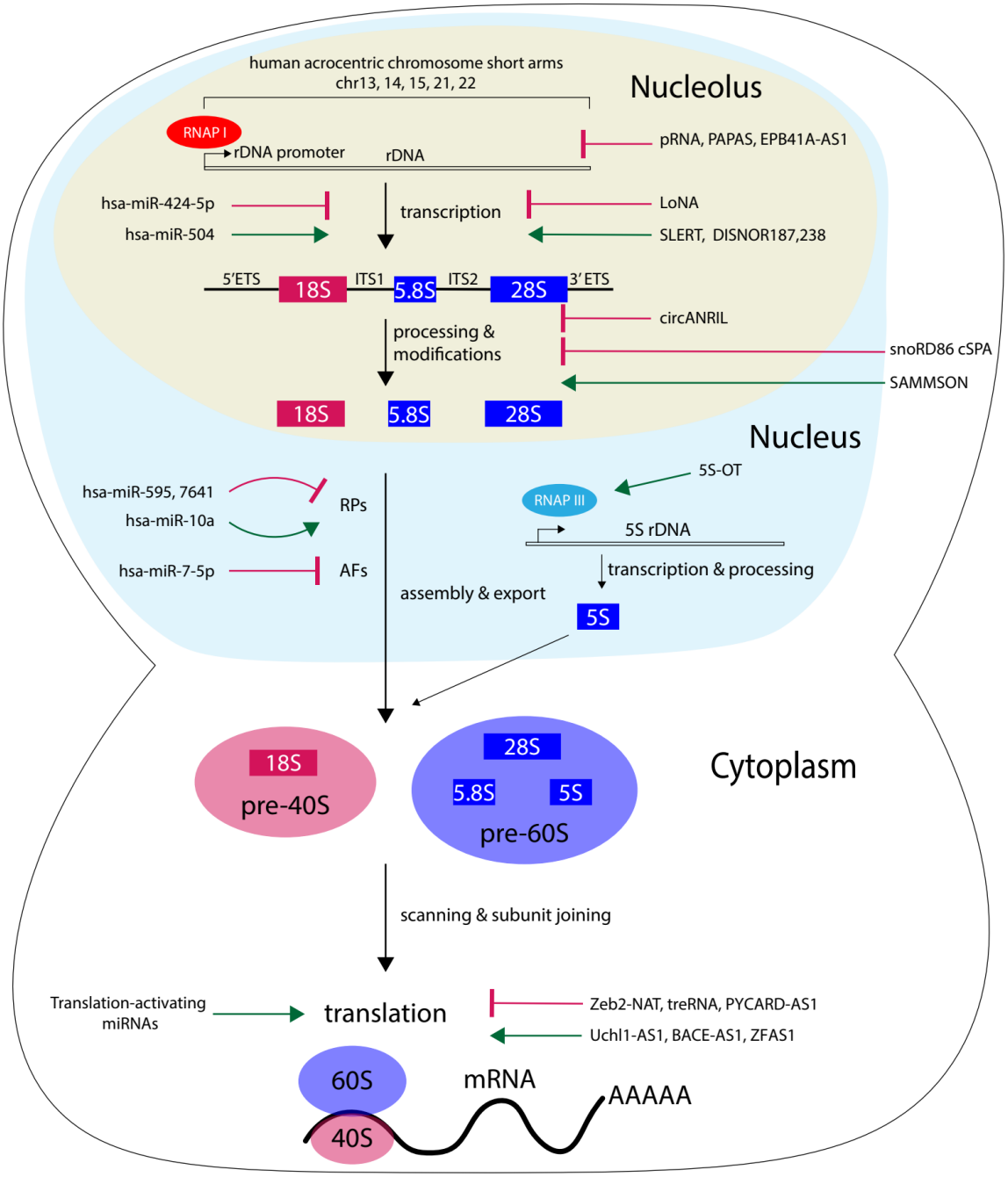

Figure 1-3. Ribosome biogenesis is regulated at multiple steps by miRNAs and lncRNAs.

The pre-rRNA is transcribed by RNAPI (red) and the 5S rRNA is transcribed by RNAPIII (blue). Pre-rRNA is processed in a series of steps to remove the external and internal transcribed spacer sequences (5' ETS and 3' ETS; ITS1 and ITS2). The rRNAs are assembled with ribosomal proteins (RPs) to make the mature 40S ribosomal subunit (in red; 18S rRNA) and 60S ribosomal subunit (in blue; 28S, 5.8S and 5S rRNAs) to translate mRNAs in the cytoplasm. Control by the indicated miRNAs (left) and lncRNAs

(right) can activate (green pointed arrow) or inhibit (red bar-headed arrow) specific steps in ribosome biogenesis.

Figure reproduced from (53).

Table 1-1. MicroRNAs and microRNA machineries involved in ribosome biogenesis.

Table reproduced from (53).

MicroRNA	Ribosome biogenesis steps controlled	Regulation of ribosome biogenesis	mRNA targets	Molecular function	Associated phenotypes or diseases	Ref.
miR-504	pre-rRNA transcription	Negative	*TP53*	miR-504 is a mirtron of FGF13 that targets *TP53*, derepressing transcription of *FGF13* and dampening pre-rRNA synthesis. TP53 protein represses transcription of miR-504 and *FGF13*. FGF13 represses pre-rRNA transcription in the nucleolus, which may mitigate oncogene-associated proteotoxic stress.	Cancer	(**Figure 1-3**, **Figure 1-4A**) (108)
miR-24, miR-130a, miR-145	pre-rRNA transcription, RP gene transcription (indirectly via *MYC* downregulation)	Negative	*MYC*	RPL5, RPL11, and RPS14 facilitate miRNA-mediated translational repression of *MYC* mRNA.	Cancer	(**Figure 1-4B**) (109-112)
Let-7 family	pre-rRNA transcription, RP gene transcription (indirectly via *MYC* downregulation)	Negative	*MYC, HRAS*	RPL22 knockdown upregulates *LIN28B* and decreases mature levels of Let-7 miRNA paralogs, unsilencing *MYC* and *HRAS* oncogenes.	Cancer, Diamond-Blackfan anemia	(113)
miR-7641	RP gene transcription	Negative	*RPS16*, *TNFS10*; other RPs indirectly	Inhibition of miR-7641 sensitizes cancer cells, improving doxorubicin apoptotic response. miR-7641 mimic reduces levels of RPS16 directly and 8 other RPs indirectly.	Cancer	(**Figure 1-3**) (114)
miR-7 (Chinese hamster ovary cells)	pre-rRNA transcription and processing (indirectly via Akt pathway)	Negative	Possible direct targets: *STRN3*, *CALU*, *CNN3*, *BMS1*, among others	miR-7 depletion in Chinese hamster ovary (CHO) cells unleashes cell proliferation and antibody production via derepression of the Akt pathway and ribosome biogenesis.	miR-7 depletion increases proliferation and antibody production	(**Figure 1-3**) (115)

MicroRNA	Ribosome biogenesis steps controlled	Regulation of ribosome biogenesis	mRNA targets	Molecular function	Associated phenotypes or diseases	Ref.
miR-424-5p	pre-rRNA transcription	Negative	*POLR1A*, *UBTF*, *RRN3*, *SMAD7*, *CDC25A*	Ribosome-related miR-424-5p targets including *POLR1A* and *UBTF* were found by Ago2 pulldown. miR-424-5p overexpression reduces muscle size in mice.	COPD, sarcopenia, muscle loss in ICU and aortic surgery patients	(**Figure 1-3**) (116)
miR-595	60S assembly; induces nucleolar stress response	Negative	*RPL27A*	miR-595 reduces RPL27A levels, inducing TP53 activation, nucleolar structural disruption, and blockade of erythroid proliferation and differentiation. Conversely, RPL27A overexpression leads to enhanced proliferation.	Myelodysplasia	(**Figure 1-3**) (117)
miR-145, miR-146a	Effects on ribosome biogenesis unclear; miRNAs associated with ribosomopathy	Unclear	*TIRAP*, *TRAF6*	Codepletion of miR-145 and miR-146a activates the innate immune response via IL-6 and phenocopies 5q- syndrome at the cellular level, leading to thrombocytosis and megakaryopoesis.	5q- syndrome ribosomopathy (myelodysplasia)	(118)
Zebrafish miRs (dre-miR-125c, dre-miR-140*, dre-miR-2191, dre-miR-30b, dre-miR-459*)	Effects on ribosome biogenesis unclear; miRNAs associated with ribosomopathy	Unclear	Unidentified	miRs associated with a RPL5-deficient zebrafish model of Diamond-Blackfan anemia were identified bioinformatically.	Zebrafish model of Diamond-Blackfan anemia	(119)
miR-369-3p, Let-7, miRcxcr-4 (synthetic)	Translational efficiency	Positive	*TNF*, *HMGA2*, CX synthetic transcript	MicroRNAs can induce translation of targets by binding 3' UTR AU-rich elements (AREs). Requisite FXR1 interacts with AGO2 to mediate increased translation efficiency. The translation-activating FXR1a-associated miRNP binds the 3'UTR of targets with shortened poly(A) tails.	Activation of translation of ARE-containing mRNAs	(**Figure 1-3**, translation-activating miRNAs) (120, 121)

MicroRNA	Ribosome biogenesis steps controlled	Regulation of ribosome biogenesis	mRNA targets	Molecular function	Associated phenotypes or diseases	Ref.
miR-10a	Translational efficiency	Positive	RPS: 2, 6, 16, 18, 20 RPL: 9, 13A, 15, 23	miR-10a directly binds RP mRNA downstream of 5'TOP motif in 5' UTR. Overexpressing miR-10a increases mature rRNA levels, protein synthesis, and 3T3 cell proliferation, while inhibiting miR-10a has an opposite effect.	Increased RP levels and global translation	(**Figure 1-3**, **Figure 1-4C**) (122)
Dicer and Drosha	Translational efficiency	Positive		Senescent cells have lower translation, though mRNA levels do not change significantly. Dicer and Drosha expression is lower in senescent cells, and Dicer/Drosha knockdown recapitulates translation downregulation and mRNA changes observed in senescent cells.	Cellular senescence	(123)

The well-studied cancer switches *TP53* and *MYC* are regulated by several miRNAs (124) and are intimately connected with ribosome biogenesis (107, 125). A genetic circuit encompassing hsa-miR-504, the nucleolar protein isoform FGF13 1A, and genome guardian TP53 attenuates ribosome biogenesis in a manner promoting cell survival in models of oncogenic escape (**Figure 1-3**, **Figure 1-4A**) (108). miR-504 is an *FGF13* mirtron that targets *TP53*, although constitutive transcription of the *FGF13/MIR504* locus itself is negatively regulated by *TP53* via understudied mechanisms. Concerted upregulation of FGF13 1A and miR-504 represses pre-rRNA transcription and TP53 translation, in turn attenuating global protein synthesis, oncogenic proteotoxic and oxidative stress, and tumor cell apoptosis.

Several ribosomal proteins are necessary for miRNA-mediated regulation of the *MYC* oncogene, which itself controls transcription of rDNA, RPs, AFs, and translation initiation factors (125). uL5 (RPL11), uL18 (RPL5), and uS11 (RPS14), which stabilize TP53 in the nucleolar stress response (74, 126, 127), have been shown to escort the armed RISC complex to *MYC* transcripts for silencing by hsa-miR-24 (109, 110) or hsa-miR-145 (**Figure 1-4B**) (112). UV irradiation also induces uL5-guided *MYC* repression by hsa-miR-130a (111). Via LIN28B, eL22 (RPL22) indirectly controls the maturation of hsa-miR-let-7 family paralogs (113) that repress *MYC*, *KRAS*, *HMGA1* and *HMGA2*, and other oncogenes (128, 129).

Additionally, miRNAs affecting cancer treatment outcomes or oncogene expression have links with ribosome biogenesis. hsa-miR-7641 has been shown to repress uS9 (RPS16) directly and 8 other ribosomal proteins indirectly, and miR-7641

depletion sensitized breast and colon cancer cells to doxorubicin-induced apoptosis (**Figure 1-3**) (114). The tumor suppressor hsa-miR-7-5p, which has been reported to target oncogenic *EGFR*, *BCL2* (130), *RELA* (p65) (131), among others (132-134), may also play a role in downregulating ribosome biogenesis. Depletion of the miR-7 homolog in Chinese hamster ovary (CHO) cells unleashed cell proliferation and antibody production, correlating with derepression of ribosomal assembly factor BMS1 and Akt pathway activators STRN3 and Ezrin (**Figure 1-3**) (115). Overall, miRNAs can fine-tune the balance between proliferation and oncogenesis by modulating upstream regulators of ribosome biogenesis such as *TP53* and *MYC*, as well as other oncogenes, RPs, and AFs downstream of pre-rRNA transcription.

Although miRNAs generally downregulate expression of their target genes, select cases have unveiled miRNA-mediated enhancement of transcript-specific or global translation (**Table 1-1**). Both endogenous and synthetic miRNAs can increase translation efficiency of target transcripts by a specialized microRNA ribonucleoprotein (miRNP) complex that lacks the normally-present repressor protein GW182/TNRC6 but contains the RNA binder FXR1a (120, 121, 135). hsa-miR-10a binds the 5' UTR of RP transcripts harboring a 5'TOP motif, upregulating their translation, augmenting ribosome biogenesis, and enhancing proliferation (**Figure 1-3**, **Figure 1-4C**) (122). The 5'TOP motif is a *cis*-regulatory RNA element found in all RPs and several translation factors in higher eukaryotes; its presence enables coordinated upregulation of global protein synthesis and ribosome production by La family proteins (LARP1 in humans) (136). Such noncanonical translational activation is also implicated in cellular quiescence

and senescence, two paused growth states instigated by mTOR deactivation that feature diminished ribosome biogenesis (137, 138). Translation-activating miRNAs were originally discovered in quiescent human cells (120, 135), and downregulation of miRNA processing machinery initiates global translation reduction and induction of senescence (**Figure 1-3**) (122). In summary, miRNAs can also enhance ribosome biogenesis and global protein synthesis via targeted RP upregulation or mechanisms implicated in cellular aging.

Studies continue to emerge and implicate novel nucleolar miRNAs and lncRNAs in ribosome biogenesis regulation. Although canonical miRNA-mediated translational repression occurs in the cytoplasm, new roles have been revealed for miRNAs localized to the nucleolus including regulation of RNAP1 and subunit assembly (102, 103), defense against exogenous nucleic acids (99), and precise control of miRNA stability and target recognition (98, 101). Further study of nucleolar miRNAs and lncRNAs will illuminate how non-coding RNAs other than rRNA shape the dynamic landscape of the nucleolus.

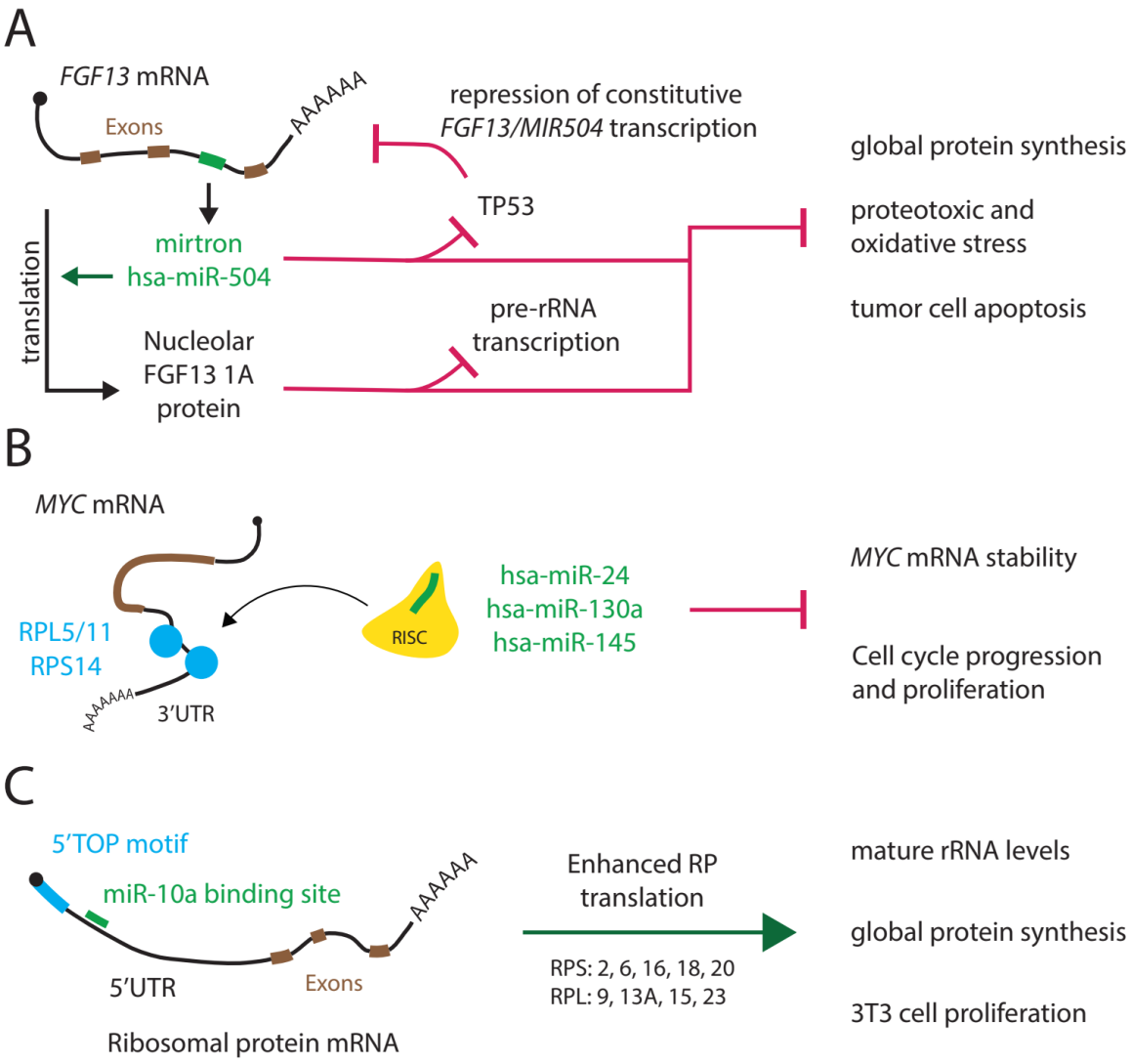

Figure 1-4. Examples of miRNA-mediated control of ribosome biogenesis.

(A) hsa-miR-504 regulates *TP53* levels and pre-rRNA transcription. miR-504 is generated from an *FGF13* intron (exons in brown, miR-504 mirtron in green) and targets *TP53* transcripts. Through an uninvestigated mechanism, TP53 protein dampens constitutive transcription of the *FGF13/MIR504* locus. *FGF13* upregulation increases levels of miR-504 and the nucleolar protein isoform FGF13 1A, repressing TP53 translation and pre-rRNA transcription. This results in attenuation of global translation, reduction of oncogenic proteotoxic and oxidative stress, and decreased tumor cell apoptosis.

(B) RPL5, RPL11, and RPS14 enable miRNA silencing of *MYC*. RPL5, RPL11, and RPS14 (blue) can bind the 3'UTR of *MYC* transcripts, and can guide active RISC complexes (yellow) loaded with miRNAs targeting *MYC* (green) to the mRNA. This RP-guided, miRNA-mediated *MYC* repression modulates cell cycle progression and

proliferation, and attenuates ribosome biogenesis indirectly.

(C) hsa-miR-10a enhances RP translation efficiency by binding 5'TOP mRNAs. miR-10a (green) was found to bind the 5'UTR of at least five small and four large RP mRNAs containing a 5'TOP motif (blue), increasing their translation efficiency. Augmented RP production enhances cellular capacity for ribosome biogenesis and proliferation.

1.5. Ribosomopathies: a wrench in the works sabotages life itself

Proper RB is necessary for normal, healthy development and life in humans. A slew of RB diseases known as ribosomopathies have been uncovered in the last two decades (139-143). The first ribosomopathy identified was Diamond-Blackfan anemia (DBA), which results in insufficient red blood cell production caused by mutations in one or more of at least ten RPs in the small and large subunits (143, 144). In that disease, mutations in RPL5 and RPL11 are associated with specific developmental defects including cleft palate and abnormal thumbs (145). More hematologic ribosomopathies exist, including 5q- syndrome (acquired anemia, RPS14) (143), Shwachman-Bodian-Diamond syndrome (neutropenia, SBDS) (146), and Fanconi anemia (leukemia and bone marrow failure, FANC proteins) (147, 148).

Other disparate diseases have been linked to RPs or AFs. Treacher Collins syndrome patients present with craniofacial developmental defects (143, 149) caused by mutations in RNAP1 and RNAP3 components (150) and in *TCOF1*, which is necessary for proper pre-rRNA transcription and methylation (151, 152). An impaired protein-protein interaction between two AFs, UTP4 and NOL11, is implicated in the pathogenesis of North American Indian Childhood Cirrhosis (85, 153), which presents as liver failure before adulthood (149, 154).

Relevant to this thesis, I highlight the rare ribosomopathy called alopecia, neurologic defects, and endocrinopathy (ANE) syndrome (155-160). Patients present early in life with the syndrome's titular clinical features, including hair loss, developmental delay, and aberrant hormonal balance (155-158). Recessive variants that

impair the function of the pre-60S AF and hub protein, RBM28, are causative of ANE syndrome. While RBM28 has eluded reconstructive placement in structural models of pre-60S particles (161-164), likely due to the transient nature of its interaction (165), biochemical studies have defined a role for RBM28 in pre-60S processing and assembly (160, 166, 167). My work investigating a novel biallelic molecular basis for ANE syndrome, rooted in improper splicing of the *RBM28* gene, is presented in **Chapter 4**.

MicroRNAs are involved in two classical hematologic ribosomopathies, myelodysplastic syndrome (MDS) and Diamond-Blackfan anemia (DBA). As part of the 5q- MDS deletion, hsa-miR-145 and hsa-miR-146a (118) are lost, while deletion of hsa-miR-595 occurs in –7/7q- MDS (117). In murine hematopoietic progenitor cells, codepletion of miR-145 and miR-146a homologs relieved repression of TIRAP and TRAF6, activating the innate immune response via IL-6 and leading to 5q- syndrome-like thrombocytosis and megakaryopoiesis (118); these features were mirrored in similar experiments on patient bone marrow. miR-595 silences *RPL27A* resulting in TP53 activation, disruption of nucleolar architecture independent of TP53, reduction of mature 60S subunits, and blockade of erythroid proliferation and differentiation (**Figure 1-3**) (117). *RPL27A* derepression enhanced proliferation in cell lines and was observed in –7/7q- MDS patients, though the authors cite the need for further translational studies (117). Finally, tens of miRNAs were found to be differentially expressed in RP-depleted zebrafish models of the ribosomopathy Diamond-Blackfan anemia (DBA) (119). Potential targets of the upregulated miRNAs were enriched for functions in

transcriptional regulation and neuronal and cellular development. It will be of interest to reexamine other ribosomopathies for miRNAs important for pathogenesis.

Other disease-associated miRNAs have been connected to ribosome biogenesis. Chronic Obstructive Pulmonary Disease (COPD) and intensive care unit patients with muscle wasting exhibit elevated expression of hsa-miR-424-5p, which targets the RNAP1 pre-initiation complex factors *POLR1A* and *UBTF* (**Figure 1-3**) (116). miR-424-5p was found to downregulate mature rRNA levels in myoblasts and to cause muscle atrophy in mice (116). We hypothesize that yet-undiscovered miRNA regulators of ribosome biogenesis may also play central roles in diseases arising from defects in growth-sensitive biological processes, such as development and angiogenesis, that are already known to be partially controlled by miRNAs (168, 169). In cancer and various ribosomopathies, microRNAs comprise another conduit by which biochemical defects become the basis of medical pathogenesis. Continued work will help elucidate new miRNAs that play a role in ribosomopathy pathogenesis and disease-related nucleolar stress responses.

How such pathologically-diverse diseases can result from impaired ribosome function or biogenesis remains a central question in the field. Two hypotheses are prominent. Green argues that certain tissues may be more sensitive to particular ribosomal defects (*i.e.*, decreased functional ribosome concentration) due to differences in transcript-specific initiation rate, and in ribosome rescue and recycling between tissues (140). Alternatively, Barna has championed specialized ribosomes as the pathological culprit, proposing that ribosomal heterogeneity causes tissue-specific defects (15, 140).

While these hypotheses are not mutually-exclusive, further studies are needed to determine their relative contributions to ribosomopathy diversity.

Chapter 2

A high-throughput assay for directly monitoring nucleolar rRNA biogenesis

Bryant CJ*, McCool MA*, Abriola L, Surovtseva YV, Baserga SJ. A high-throughput assay for directly monitoring nucleolar rRNA biogenesis. Open Biol. 2022;12(1):210305. doi: 10.1098/rsob.210305. PubMed PMID: 35078352; PMCID: 8790372.

* *These authors contributed equally as co-first-authors.*

2.1. Work Contributed

This manuscript was published in 2022. I and my dedicated colleague and labmate Mason McCool share co-first authorship. Along with SJ Baserga, L Abriola, and YV Surovtseva, I conceptualized the project. I conducted the assay development and optimization, including CellProfiler pipeline augmentation as well as image and data analysis with consultation from L Abriola and YV Surovtseva. I performed the BMH-21 dose response analysis. I wrote the protocol for performing the optimized assay. Mason McCool performed the RT-qPCR and the ribosome biogenesis factor screen, and I analyzed the images he collected. I also assembled all the figures, with input from my co-authors.

2.2. Introduction

Cells of all organisms manufacture mature ribosomes, the core machinery of protein translation, through a process known as ribosome biogenesis (RB) (reviewed in 1, 170). In eukaryotic cells, the first steps of RB occur in the nucleolus, a membraneless nuclear organelle discovered in the 1830's (reviewed in 44, 45, 171), where RNA Polymerase 1 (RNAP1) transcribes the primary pre-ribosomal RNA (pre-rRNA) precursor (reviewed in 7, 172, 173). Subsequently, a series of RNA processing and modification steps transpire, largely within the nucleolus, to create the mature cytoplasmic 18S, 5.8S, and 28S rRNA molecules in human cells (8, 174). Ribosomal proteins (RPs) bind (pre-)rRNA substrates in a hierarchical progression throughout this

maturation process, bolstering the stability of the nascent transcript by chaperoning its folding away from incorrect, energetically-minimized conformations (12, 175). Dysregulation of RB, and particularly of RNAP1 transcription, is a causative factor in a myriad of human disease states, including cancer (107, 176-180), ageing (137, 173), and rare diseases called ribosomopathies (139, 141, 181).

Given the importance of nucleolar function in human health and disease, the creation of more robust tools for measuring rRNA biogenesis within the nucleolus is essential for understanding the basic biological mechanisms through which RB can be regulated, as well as for developing next-generation small molecule or biologic therapeutics. In the past decade, a cadre of studies using high-throughput screening (HTS) have elucidated novel mechanisms through which human RB is regulated (81, 83, 84, 87); several candidate therapeutics targeting the nucleolus have also been discovered with HTS chemical library or natural product campaigns (182-186). While several HTS modalities for monitoring nucleolar form and morphology have been described (83, 187, 188), none of these platforms directly measure nucleolar rRNA biogenesis, or the synthesis and accumulation of nascent pre-rRNA within the nucleolus. To date, the lack of a direct high-throughput assay for nucleolar rRNA biogenesis constrains researchers' ability to select for and validate the most promising candidate regulators of RB.

To monitor nucleolar function in a high-throughput manner, we sought to adapt a 5-ethynyl uridine (5-EU) assay for nucleolar rRNA biogenesis to an accessible, miniaturized format. The 5-EU assay has been successfully used to quantify changes in

nucleolar transcriptional activity by several other groups in a variety of systems including human tissue culture cells (187, 189-196), primary neurons (197), porcine fetal fibroblasts (198), *Drosophila melanogaster* ovarian stem cells (199), and plant seedlings (200, 201). A key limitation in almost all of these studies is that total cellular or total nuclear 5-EU is quantified, rather than solely nucleolar 5-EU. Because only nucleolar signal corresponds to biogenesis of the primary pre-rRNA, quantifying total 5-EU leads to increased background from nascent transcription by RNA Polymerases besides RNAP1. Additionally, the computational methods used for image segmentation and quantification have varied widely and include custom MATLAB scripts, manual definition of regions-of-interest in ImageJ, and image multiplication in Adobe Photoshop, further limiting assay accessibility and reproducibility across research groups.

To improve upon these limitations, we present a miniaturized, high-throughput-ready 5-EU assay that selectively measures nucleolar rRNA biogenesis by co-staining for the nucleolar protein fibrillarin (FBL). In addition, we provide an analysis pipeline for the open-source image analysis software CellProfiler (202) that provides a facile and reproducible framework for quantifying nucleolar 5-EU levels. We validate our assay by depleting 68 known RB factors including core RNAP1 machinery, assembly factors, and RPs, demonstrating robust and reproducible results for specifically measuring nucleolar rRNA biogenesis. Strikingly, we find that nucleolar 5-EU incorporation is sensitive to defects not only in RNAP1 transcription (producing strong percent inhibition), but also to aberrant pre-rRNA processing and ribosome assembly (producing milder percent inhibition). We underscore that changes in pre-rRNA synthesis or in pre-rRNA stability

can affect nucleolar pre-rRNA accumulation, and therefore nucleolar rRNA biogenesis is sensitive to alterations in fundamental RB subprocesses. Our results prompt an expansion of the field's conceptualization of nucleolar 5-EU incorporation experiments in general, which, at measurable time points, report not only on RNAP1 transcription, but more broadly on nucleolar rRNA biogenesis. Overall, our miniaturized 5-EU assay expands the dimensionality of HTS experiments studying the nucleolus, and will accelerate the discovery of novel RB regulators and targeted therapeutics.

2.3. Results

2.3.1. A high-content assay to quantify nucleolar rRNA biogenesis

In order to achieve specific quantification of nucleolar rRNA biogenesis, we introduced a 5-EU labeling step into our previously established screening platform for counting nucleolar number (83), which utilizes CellProfiler (202) to segment nuclei and nucleoli in images of cells immunofluorescently stained for DNA and the nucleolar protein fibrillarin (FBL) (**Figure 2-1A**). In our new protocol, MCF10A breast epithelial cells are reverse-transfected with siRNA duplexes for 72 h. For one hour following the transfection period, the cells are treated with 1 mM 5-EU, which is incorporated into nascent transcripts. Since the bulk of cellular transcription occurs in the nucleolus, most of the 5-EU label is incorporated into nucleolar nascent pre-rRNA (**Figure 2-1A**). The cells are fixed and immunofluorescently stained for DNA and FBL, after which nascent

RNA is visualized *in situ* by performing a bio-orthogonal click reaction to covalently label the 5-EU alkyne moiety with an azide fluorophore (AF488 azide) (**Figure 2-1A**). The cells are then imaged and analyzed with CellProfiler to specifically quantify nucleolar rRNA biogenesis across all control and unknown wells. CellProfiler is known for its ease-of-use and modular adaptability (203, 204), making it suitable for inclusion in a standardized, broadly accessible protocol.

We optimized our 5-EU assay to use a non-targeting siRNA as a negative control (siNT), and an siRNA targeting *POLR1A*, the largest subunit of RNAP1 also known as RPA194, as a positive control (siPOLR1A) (**Figure 2-1B**). RNAP1 inhibition by POLR1A depletion strongly reduces the nucleolar 5-EU signal to a degree consistent with acute treatment with BMH-21, a potent small molecule inhibitor of RNAP1 (182, 205) (**Figure 2-1B-C**, compare siNT to siNT + BMH and siPOLR1A). However, it is clear that residual nucleoplasmic 5-EU signal remains even after RNAP1 inhibition (**Figure 2-1B**, siNT + BMH and siPOLR1A), emphasizing the importance of only quantifying 5-EU staining within the nucleolus via FBL co-staining.

To achieve nucleolar 5-EU quantification during analysis, images of DNA and FBL staining (**Figure 2-1C**, panels 1 and 2) were first used to segment nuclei and nucleoli by CellProfiler (**Figure 2-1C**, panels 3 and 4), respectively. Then, the median 5-EU signal within each nucleolus was measured (**Figure 2-1C**, panel 5), enabling aggregate quantification analysis per treatment condition across every nucleolus within each well (**Figure 2-1C**, panel 6). Final calculation of mean signals, percent inhibitions (by normalization to the negative and positive controls), and screening statistics

including signal-to-background (S/B) and Z' factor can be carried out in any standard data analysis software that can import the CellProfiler output CSV files, such as Microsoft Excel, JMP, R, or Python pandas.

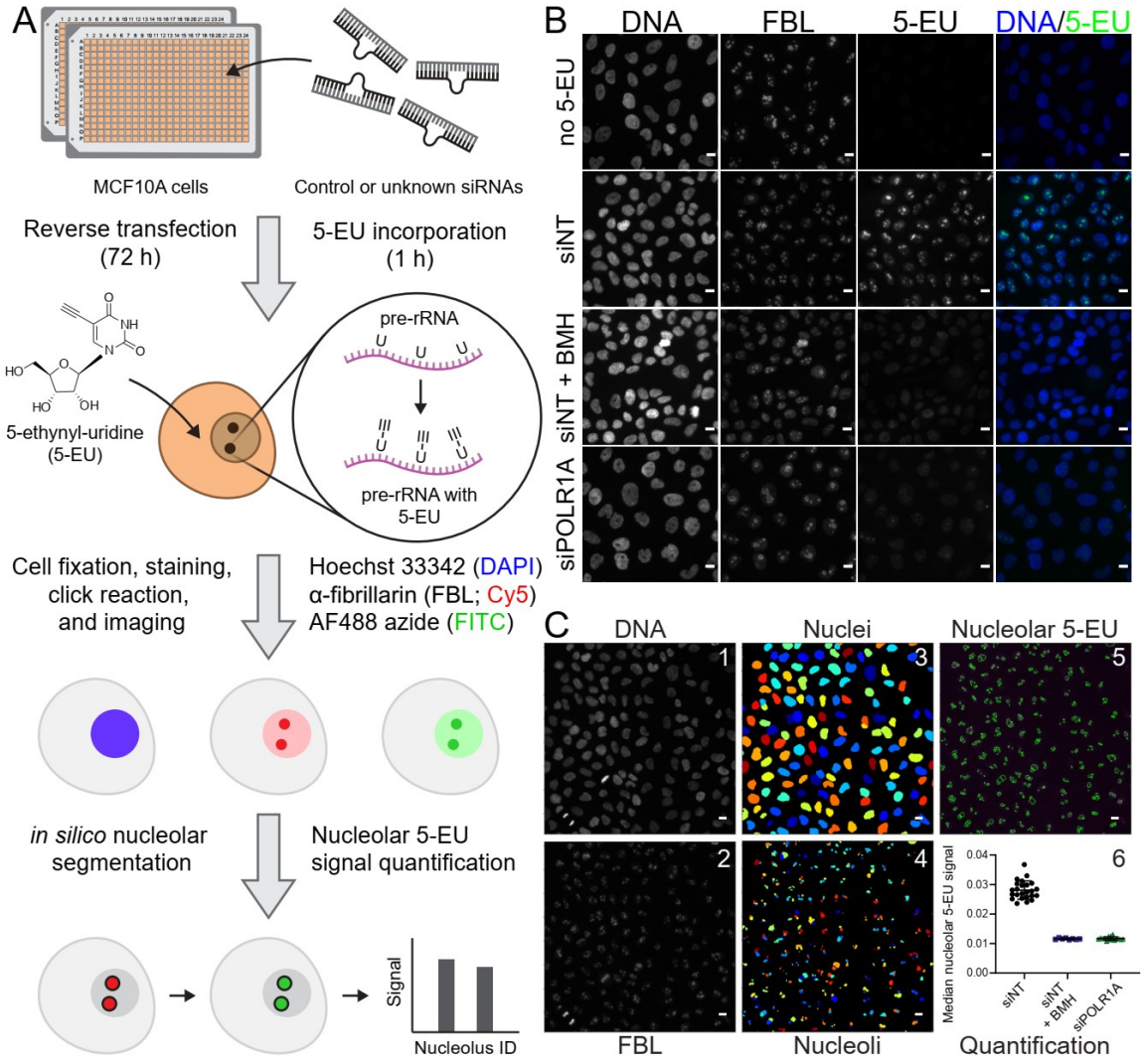

Figure 2-1. A high-throughput assay for nucleolar rRNA biogenesis using 5-ethynyl uridine (5-EU).

(A) Schematic of the 5-EU assay protocol. MCF10A cells are reverse-transfected in 384-well imaging plates with control or unknown siRNAs for 72 h. Following target depletion, 5-EU is incorporated into nascent RNA transcripts for 1 h, with the majority of label incorporated into nascent pre-ribosomal RNA (pre-rRNA). Treated cells are fixed and stained for DNA (Hoechst 33342, DAPI channel) and the nucleolar protein fibrillarin (FBL, Cy5 channel). 5-EU in nascent transcripts is conjugated to an azide fluorophore (AF488 azide, FITC channel) via a copper-catalyzed click reaction. After fluorescent imaging, cell nuclei and nucleoli are segmented *in silico* with CellProfiler, and nucleolar-specific 5-EU signal is quantified for each nucleolus object identified.

(B) RNAP1 inhibition specifically inhibits nucleolar 5-EU incorporation. No 5-EU, experiment without 1 h 5-EU incorporation. Treatment with a non-targeting siRNA (siNT) leads to high 5-EU signal within the nucleolus and moderate nucleoplasmic

background signal. Acute treatment with BMH-21 (siNT + BMH) or siRNA-mediated depletion of POLR1A (siPOLR1A) decreases nucleolar 5-EU signal, although nucleoplasmic background remains. DNA (Hoechst staining), FBL (fibrillarin staining), 5-EU (5-EU staining), DNA/5-EU (combined Hoechst and EU staining). Scale bars, 10 μm.

(C) Schematic of CellProfiler segmentation and nucleolar 5-EU quantification. Panels 1 and 2, raw images of DNA and FBL staining. Panels 3 and 4, nuclei or nucleoli segmented by CellProfiler from DNA or FBL staining, respectively. Rainbow coloring identifies object number. Panel 5, overlay of segmented nucleoli (green) on top of 5-EU staining (magenta). Panel 6, quantification of median nucleolar 5-EU signal for nucleoli in cells treated with siNT, siNT and BMH-21, or siPOLR1A. n = 24, 8, or 16 wells, respectively. Scale bars, 10 μm.

2.3.2. Optimization of the 5-EU assay for a miniaturized 384-well plate format

To adapt the 5-EU assay for use in high-throughput, we developed and optimized an optional 5-EU module that integrates into our existing nucleolar number screening platform. We first investigated the assay in MCF10A cells in the absence of siRNA knockdown or FBL co-staining, using the potent RNAP1 inhibitor BMH-21 or DMSO vehicle as positive or negative controls, respectively. For the first optimization experiments without FBL co-staining, median or maximum nuclear 5-EU signal was measured. We hypothesized that maximum nuclear 5-EU signal should track nucleolar function more accurately than the median, since a larger difference in the maximum value should be observed after RNAP1 inhibition. However, both metrics should decrease significantly upon BMH-21 treatment. Based on the original 5-EU method publication (206), we chose to label cells with 5-EU for 1 h, striking a balance between signal levels and incorporation time. By varying the 5-EU treatment concentration and click reaction time in wells treated without or with BMH-21, we discovered that treatment with 1 mM 5-EU for 1 h, followed by a 30 min click reaction was optimal (

Figure 2-2A). Specifically, these conditions achieved the highest S/B ratio for the controls for each metric (

Figure 2-2B).

Next, we introduced steps to enable nucleolar segmentation including blocking with a 10% (volume-per-volume, or v/v) FBS/PBS solution and immunofluorescent staining for FBL. We utilized blocking and staining parameters that were previously optimized for our original screening platform (83). Using BMH-21, we found the highest control S/B and Z' factor occurred when measuring maximum 5-EU signal in nuclei that had been blocked but not stained for FBL (

Figure 2-2C, second group). To specifically quantify nucleolar 5-EU incorporation, we also measured median nucleolar 5-EU signal. We selected the median metric because, compared to the maximum, it is more robust to outliers that may occur from staining artifacts or other abnormalities. When segmenting nucleoli, a comparable Z' factor was achieved when measuring median 5-EU signal in nucleoli (

Figure 2-2C, fourth group).

Interestingly, we also noted that acute treatment with 1 μM BMH-21 during our 1 h 15 min treatment period caused increased nucleoplasmic FBL staining, presumably from FBL dispersion following RNAP1 inhibition (**Figure 2-1B**, siNT + BMH, FBL panel). We hypothesized that there may be a more optimal BMH-21 concentration where nucleolar FBL localization remains intact, but nucleolar rRNA biogenesis is still significantly inhibited.

To pursue the effects of acute BMH-21 treatment on 5-EU incorporation and FBL dispersion in more detail, we performed dose response experiments with our optimized protocol (**Figure 2-3**). We utilized fourteen BMH-21 concentrations ranging from 2 nM to 20 μM to ensure sufficient capture of response dynamics. We probed BMH-21's ability to inhibit nucleolar rRNA biogenesis by quantifying both median nucleolar 5-EU signal and maximum nuclear 5-EU signal (**Figure 2-3A-B**). For these measurement schemes, we discovered an IC_{50} value of 300 ± 30 nM or 350 ± 30 nM, respectively, following BMH-21 action upon nucleolar rRNA biogenesis (**Figure 2-3B**, **Table 2-1**).

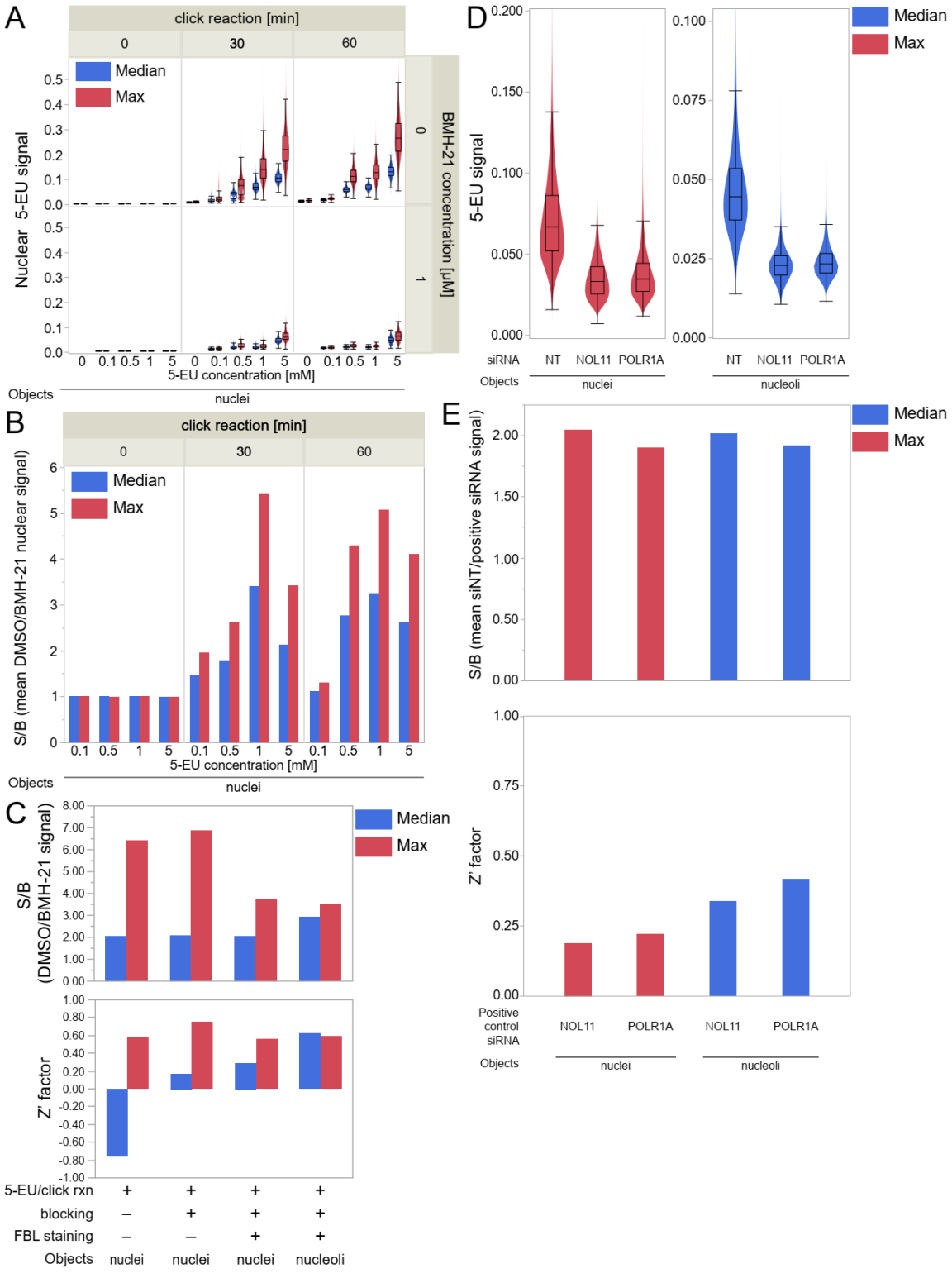
A
click reaction [min]
0
30
60
Median
Max
Nuclear 5-EU signal
BMH-21 concentration [µM]
0
1
0 0.1 0.5 1 5 0 0.1 0.5 1 5 0 0.1 0.5 1 5
5-EU concentration [mM]
Objects
nuclei
B
click reaction [min]
S/B (mean DMSO/BMH-21 nuclear signal)
0.1 0.5 1 5 0.1 0.5 1 5 0.1 0.5 1 5
5-EU concentration [mM]
Objects
nuclei
C
S/B (DMSO/BMH-21 signal)
Z' factor
5-EU/click rxn + + + +
blocking – + + +
FBL staining – – + +
Objects nuclei nuclei nuclei nucleoli
D
5-EU signal
siRNA NT NOL11 POLR1A NT NOL11 POLR1A
Objects
nuclei
nucleoli
E
S/B (mean siNT/positive siRNA signal)
Z' factor
Positive control siRNA
NOL11 POLR1A NOL11 POLR1A
Objects
nuclei
nucleoli

Figure 2-2. Optimization of the miniaturized 5-EU assay for nucleolar rRNA biogenesis.

(A) Median (blue) or maximum (red) nuclear 5-EU signal for cells treated across a range of 5-EU concentrations and click reaction times, without or with BMH-21 treatment at 1 μM. n ≥ 20,000 cells per condition.

(B) Control signal-to-background (S/B) ratios for treatment conditions in Panel A. Control S/B is calculated as the ratio of mean DMSO-treated nuclear 5-EU signal divided by mean BMH-21-treated nuclear 5-EU signal, for each combination of 5-EU concentration and click reaction time. Median nuclear 5-EU signal (blue), maximum nuclear 5-EU signal (red).

(C) Control S/B and Z' factor values for nuclei or nucleoli objects with only 5-EU visualization, 5-EU plus blocking with 10% (v/v) FBS/PBS, or 5-EU plus blocking and FBL co-staining. Median 5-EU signal (blue), maximum 5-EU signal (red).

(D) Maximum nuclear 5-EU signal (red) or median nucleolar 5-EU signal (blue) for cells treated with siNT, siNOL11, or siPOLR1A. n ≥ 130,000 cells per siRNA.

(E) Control S/B and Z' factor values for cells (from Panel D) treated with siNOL11 or siPOLR1A as the positive control. Control S/B is calculated as the ratio of mean siNT-treated 5-EU signal divided by mean siNOL11- or siPOLR1A-treated 5-EU signal. Maximum nuclear 5-EU signal (red), median nucleolar 5-EU signal (blue).

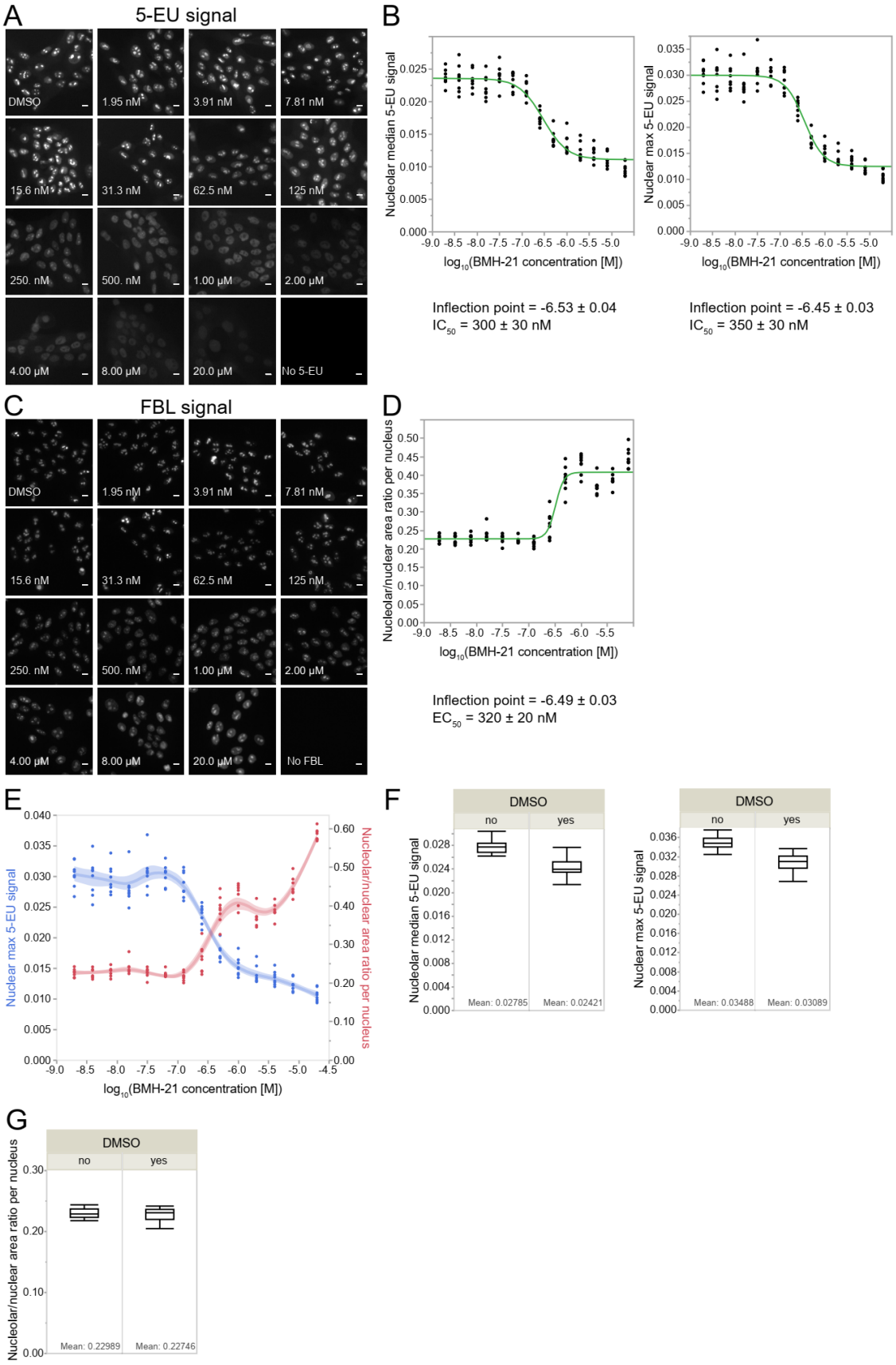
A
5-EU signal
DMSO
1.95 nM
3.91 nM
7.81 nM
15.6 nM
31.3 nM
62.5 nM
125 nM
250. nM
500. nM
1.00 µM
2.00 µM
4.00 µM
8.00 µM
20.0 µM
No 5-EU
B
Nucleolar median 5-EU signal
log10(BMH-21 concentration [M])
Inflection point = -6.53 ± 0.04
IC50 = 300 ± 30 nM
Nuclear max 5-EU signal
log10(BMH-21 concentration [M])
Inflection point = -6.45 ± 0.03
IC50 = 350 ± 30 nM
C
FBL signal
DMSO
1.95 nM
3.91 nM
7.81 nM
15.6 nM
31.3 nM
62.5 nM
125 nM
250. nM
500. nM
1.00 µM
2.00 µM
4.00 µM
8.00 µM
20.0 µM
No FBL
D
Nucleolar/nuclear area ratio per nucleus
log10(BMH-21 concentration [M])
Inflection point = -6.49 ± 0.03
EC50 = 320 ± 20 nM
E
Nuclear max 5-EU signal
Nucleolar/nuclear area ratio per nucleus
log10(BMH-21 concentration [M])
F
DMSO
no
yes
Nucleolar median 5-EU signal
Mean: 0.02785
Mean: 0.02421
DMSO
no
yes
Nuclear max 5-EU signal
Mean: 0.03488
Mean: 0.03089
G
DMSO
no
yes
Nucleolar/nuclear area ratio per nucleus
Mean: 0.22989
Mean: 0.22746

Figure 2-3. Dose response experiments reveal similar potencies of BMH-21 on inhibiting nucleolar rRNA biogenesis and FBL dispersion from nucleoli.

(A) Representative images of 5-EU signal across a 14-point BMH-21 dilution series, plus DMSO vehicle only and "No 5-EU" staining conditions.

(B) Dose response curves for 5-EU signal inhibition following BMH-21 treatment. Curve fits for median nucleolar 5-EU signal (left) and maximum nuclear 5-EU signal (right) are presented, and inflection point and IC_{50} estimates with standard error are shown below each graph respectively. n = 8 wells per dose, representing at least 13,000 cells per dose.

(C). Representative images of FBL signal across a 14-point BMH-21 dilution series, plus DMSO vehicle only and "No FBL" staining conditions.

(D) Dose response curves for FBL dispersion following BMH-21 treatment. A curve fit for nucleolar/nuclear area ratio is presented, and inflection point and EC_{50} estimates with standard error are shown below the graph. The FBL dispersion dose response curve was fit for all doses except 20 μM due to non-asymptotic behavior at that dose. n = 8 wells per dose, representing at least 13,000 cells per dose.

(E) Overlay graph illustrating simultaneous 5-EU inhibition and FBL dispersion effects from increasing BMH-21 dose. Maximum nuclear 5-EU signal (left axis, blue) and nucleolar/nuclear area ratio (right axis, red) are overlaid. Shading represents fit 95% confidence intervals. Well data are the same as presented in **B** and **D**.

(F) Treatment with DMSO (2% [v/v]) causes a decrease in median nucleolar (left) and maximum nuclear (right) 5-EU signal. n = 16 wells per condition, representing at least 25,000 cells per condition. **G.** Treatment with DMSO (2% [v/v]) does not significantly alter FBL localization as measured by nucleolar/nuclear area ratio. n = 16 wells per condition, representing at least 25,000 cells per condition.

Table 2-1. BMH-21 dose response IC50 and EC50 estimates for nucleolar rRNA biogenesis assay.

Curve	Parameter	Estimate	Std Error
Nucleolar median 5-EU signal	IC50 [molar]	3.0E-07	3E-08
Nuclear max 5-EU signal	IC50 [molar]	3.5E-07	3E-08
Nucleolar/nuclear area ratio per nucleus	EC50 [molar]	3.2E-07	2E-08

We next investigated the extent to which BMH-21 decreases nucleolar-specific FBL localization (**Figure 2-3C-D**). To quantify FBL dispersion, we calculated the ratio of total area segmented as nucleoli (using FBL staining) to total area segmented as nucleus (using Hoechst staining), on a per-nucleus basis. In other words, this nucleolar/nuclear area ratio represents the percentage of each nucleus that is segmented as nucleolar by CellProfiler. We hypothesized that, as BMH-21 concentration increases and FBL disperses into the nucleoplasm, the nucleolar/nuclear area ratio would increase relative to vehicle or low concentration treatment conditions. Consistent with our hypothesis, we observed an increase in the nucleolar/nuclear area ratio from approximately 23% at low BMH-21 concentrations to approximately 41% at high BMH-21 concentrations, with an EC_{50} value of 320 ± 20 nM (**Figure 2-3D**, **Table 2-1**). We find that in response to increasing BMH-21 concentration, nucleolar rRNA biogenesis is inhibited in concert with FBL dispersion, and that BMH-21's potency in both processes is approximately equivalent (**Figure 2-3B, Figure 2-3D, Figure 2-3E**, and **Table 2-1**). Thus, in our system, there is not a concentration of BMH-21 where nucleolar rRNA biogenesis is strongly inhibited that retains normal nucleolar localization of FBL. This is consistent

with reports of RNAP1 inhibition resulting in nucleolar disintegration, including FBL dispersion, following acute BMH-21 treatment (182).

During our dose response experiments, we also investigated how DMSO treatment affects nucleolar rRNA biogenesis and FBL localization. Importantly, we find that treatment with 1 μL of DMSO vehicle (approximately 2% [v/v]) decreases median nucleolar 5-EU signal and maximum nuclear 5-EU signal by 10-15% (**Figure 2-3F**). This inhibitory effect of DMSO is not unexpected, as low-dose DMSO treatment has been shown to alter RNA structure *in vitro* (207), and to reduce viability and induce apoptosis after 24 h *in vivo* (208). Following DMSO treatment, we did not notice an effect on FBL localization as reported by nucleolar/nuclear area ratio (**Figure 2-3G**).

We caution that the accuracy of nucleolar segmentation should be closely monitored by calculating nucleolar/nuclear area ratio, if using BMH-21 or another potent RNAP1 inhibitor that causes FBL dispersion. Aberrancies in FBL staining could lead to inaccurate segmentation, affecting results obtained by calculating median nucleolar 5-EU signal. In these situations, maximum nuclear 5-EU signal can be monitored in addition to or in place of median nucleolar 5-EU signal. If using the assay to study the effects of DMSO-solubilized small molecules, care should also be taken to treat all wells with equal volumes of vehicle, as DMSO treatment does slightly affect 5-EU incorporation.

In the final phase of optimization, we studied how siRNA knockdown of known RB factors affected nuclear and nucleolar 5-EU signal. We chose to deplete NOL11, a small subunit processome factor critical for pre-rRNA transcription (85), or POLR1A,

the largest subunit of the RNAP1 complex, as positive controls. We verified robust knockdown of *NOL11* or *POLR1A* mRNA transcripts using RT-qPCR (**Figure 2-4**). Compared to treatment with siNT, depletion of NOL11 or POLR1A decreased maximum nuclear signal and median nucleolar signal by roughly 50% in each case (**Figure 2-3D**), corresponding to control S/B values of 1.9-2.0 for each control (**Figure 2-3E**, top). However, measuring median nucleolar signal had lower object-to-object variability, resulting in more favorable Z' factors than when measuring maximum nuclear signal (**Figure 2-3E**, bottom). Thus, both NOL11 and POLR1A are excellent positive controls for inhibiting nucleolar rRNA biogenesis in the 5-EU assay, when median nucleolar signal is measured. In follow-up validation studies (see below), we confirmed that measuring the median nucleolar 5-EU signal provides the most robust Z' factors, despite the nucleolar 5-EU standard deviation metric having a higher control S/B ratio (**Figure 2-5**). From these results, we recommend measuring maximum nuclear 5-EU when using treatments that cause FBL dispersion, such as BMH-21. We also conclude that measuring median nucleolar 5-EU signal, which corresponds only to nucleolar rRNA biogenesis, is the optimal 5-EU assay endpoint under conditions where FBL has sufficiently specific nucleolar localization, as optimized by the assay user for a given combination of experimental variables including cell line and treatment conditions.

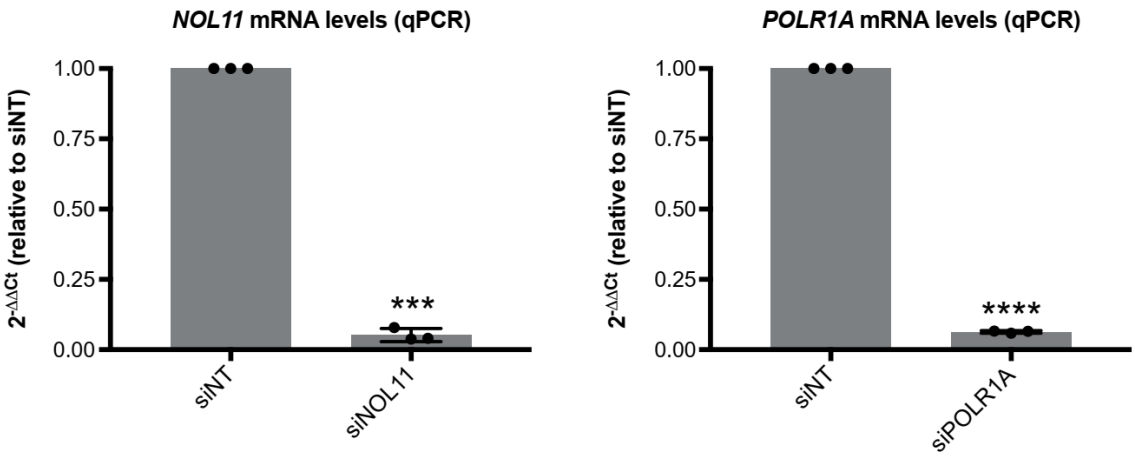

Figure 2-4. Positive control siRNAs targeting *NOL11* (left) or *POLR1A* (right) mRNAs achieve robust knockdown by RT-qPCR.

Statistical significance was calculated by two-tailed paired t-test using GraphPad Prism. n = 3 biological replicates with 3 technical replicates each. *** $p < 0.001$, **** $p < 0.0001$.

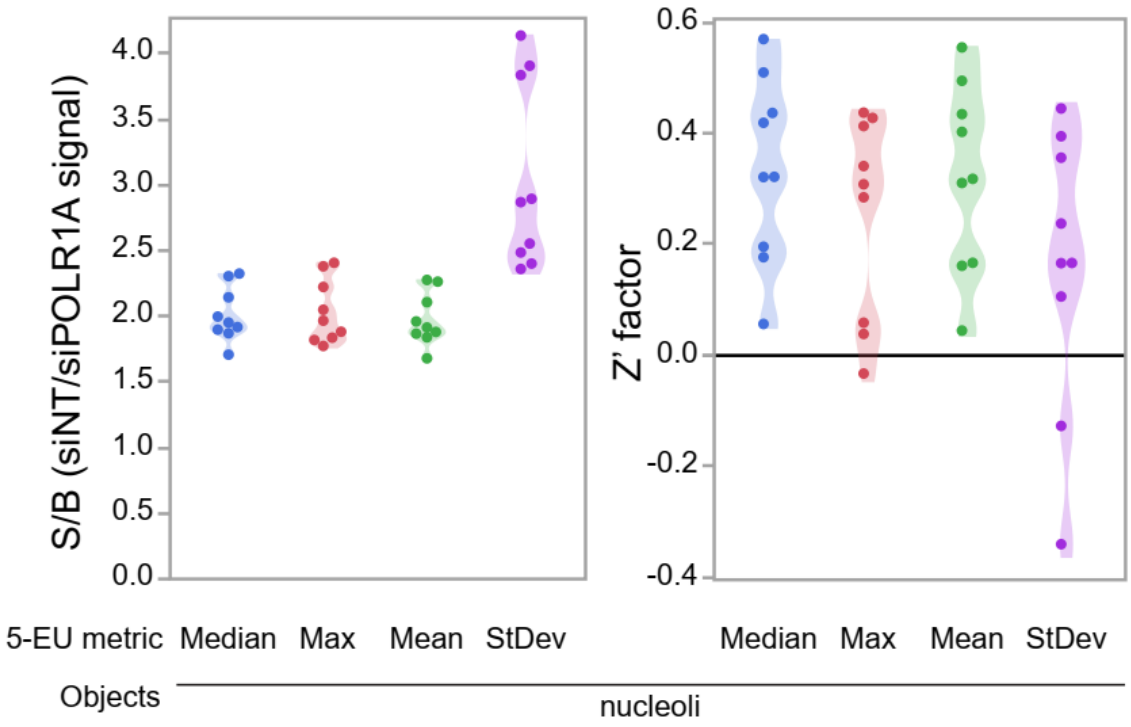

Figure 2-5. Control S/B and Z' factor values for validation assay replicates.

Control S/B is calculated as the ratio of mean siNT-treated 5-EU signal divided by mean siPOLR1A-treated 5-EU signal. Median (blue), maximum (red), mean (green), or standard deviation (purple) of nucleolar 5-EU signal. n = 9 replicates.

2.3.3. Validation of the high-throughput 5-EU assay on 68 known ribosome biogenesis factors

After optimization, we validated the high-throughput 5-EU assay using a subset of 68 previously studied RB factors, including RPs and assembly factors for both ribosomal subunits, as well as core RNAP1 machinery and drivers of transcription such as MYC (**Figure 2-6A, Table 2-2**). We depleted each RB factor over 72 h using siRNA pools in accordance with our protocol, performing the assay in biological triplicate to ensure reproducibility. Strikingly, we found that depletion of 58/68 biogenesis factors led to a significant (≥ 50%) inhibition of nucleolar 5-EU signal after standardization to the controls (**Figure 2-6A**). Images of the assay controls illustrate typical signal levels observed for the negative control siNT, set at 0% inhibition, and the positive control siPOLR1A, set at 100% inhibition (**Figure 2-6B**, siNT and siPOLR1A). Furthermore, images from the RB factors tested demonstrate the sensitivity of the assay to RNAP1 inhibition, from extreme effects above 100% inhibition (*e.g.,* siMYC) to more moderate inhibitory effects (*e.g.,* siTRMT112) (**Figure 2-6B**). Full results from the assay validation are presented in **Figure 2-6C** and **Table 2-2**.

Strikingly, we observed 11 targets that resulted in stronger nucleolar rRNA biogenesis inhibition than the positive control, POLR1A; consistent with a mean percent inhibition greater than 100%, 7/11 of these targets are implicated in control of pre-rRNA transcription, including MYC (209), HEATR1/UTP10 (210-212), DNTTIP2/TdIF2 (213), SUPT6H (214), SUPT5H (83), EIF4A3/DDX48 (215), and POLR2E (49). Overall, 12/58 factors with a significant inhibition of nucleolar rRNA biogenesis have been implicated in transcription, also including the RNAP1 initiation

factor RRN3 (216-218), two other t-UTPs, NOL11/UTP8 (85) and UTP4 (219), and the proteins MDN1, a pre-60S assembly factor, and KIF11, a mitotic kinesin essential for RB (84).

Pre-rRNA processing and modification factors comprised a sizeable subset of factors with significant nucleolar rRNA biogenesis mean percent inhibition. In total, 19/58 factors that inhibited nucleolar rRNA biogenesis were critical for processing, including the t-UTPs HEATR1/UTP10, NOL11/UTP8, and UTP4 (85, 210-212, 219), the C/D box snoRNP scaffolds NOP56 and NOP58 (20), as well as other processing factors including DNTTIP2 (87), WBP11 (220), MDN1 (221), ESF1 (87, 222), BCCIP (223), RPP30 (87, 224), EXOSC9 (225), NUMA1 (83), MPHOSPH10 (226), TRMT112 (227), UTP20 (228), and NUDT16 (229). In addition, nucleolar rRNA biogenesis was moderately inhibited for the pre-rRNA modification factors TRMT112 (227), RPUSD2 (220), and NOLC1 (230, 231). Notably, factors involved in transcription had a higher mean percent inhibition than factors involved in processing (83.1% inhibition v. 74.9% inhibition, n = 15 v. n = 22); factors involved in both transcription and processing had a mean percent inhibition of 99.0% (n = 6).

Table 2-2. 68 ribosome biogenesis factors used to validate the miniaturized 5-EU assay.

HGNC Symbol	HGNC ID	RB function	Mean 5-EU percent inhibition
MYC	HGNC:7553	pre-rRNA transcription	119.20
HEATR1	HGNC:25517	pre-rRNA processing	116.44
DNTTIP2	HGNC:24013	pre-rRNA transcription	112.56
DDX19B	HGNC:2742	subunit export	111.08
RPL3	HGNC:10332	ribosomal protein	110.59
SUPT6H	HGNC:11470	pre-rRNA transcription	107.13
RPS28	HGNC:10418	ribosomal protein	106.23
SUPT5H	HGNC:11469	pre-rRNA transcription	105.92
RPL19	HGNC:10312	ribosomal protein	105.20
EIF4A3	HGNC:18683	pre-rRNA transcription	102.98
POLR2E	HGNC:9192	pre-rRNA transcription	100.42
DDX56	HGNC:18193	subunit export	99.60
RPS4X	HGNC:10424	ribosomal protein	98.49
RPS6	HGNC:10429	ribosomal protein	98.32
RPS8	HGNC:10441	ribosomal protein	96.80
RPS3A	HGNC:10421	ribosomal protein	95.89
RPS14	HGNC:10387	ribosomal protein	94.49
NOL11	HGNC:24557	pre-rRNA processing	93.78
RPS24	HGNC:10411	ribosomal protein	91.96
WBP11	HGNC:16461	pre-rRNA processing	91.90
RPS5	HGNC:10426	ribosomal protein	91.22
RPS7	HGNC:10440	ribosomal protein	91.08
MDN1	HGNC:18302	pre-rRNA processing	90.81
RPS16	HGNC:10396	ribosomal protein	89.96
ESF1	HGNC:15898	pre-rRNA processing	89.57
RPL18	HGNC:10310	ribosomal protein	88.51
RPL26	HGNC:10327	ribosomal protein	86.94
RPL17	HGNC:10307	ribosomal protein	86.78
RRN3	HGNC:30346	pre-rRNA transcription	84.51
RPS9	HGNC:10442	ribosomal protein	83.66
RPLP2	HGNC:10377	ribosomal protein	81.78
RPS13	HGNC:10386	ribosomal protein	81.74
RPL8	HGNC:10368	ribosomal protein	81.46
KIF11	HGNC:6388	pre-rRNA transcription	81.25
RPL35A	HGNC:10345	ribosomal protein	80.82
RPL23A	HGNC:10317	ribosomal protein	80.74
RPL24	HGNC:10325	ribosomal protein	80.69
BCCIP	HGNC:978	pre-rRNA processing	80.62

HGNC Symbol	HGNC ID	RB function	Mean 5-EU percent inhibition
RPL7	HGNC:10363	ribosomal protein	80.20
RPS11	HGNC:10384	ribosomal protein	79.62
NOP56	HGNC:15911	pre-rRNA processing	77.74
UTP4	HGNC:1983	pre-rRNA processing	77.17
RPS15A	HGNC:10389	ribosomal protein	77.09
RPP30	HGNC:17688	pre-rRNA processing	70.96
EXOSC9	HGNC:9137	pre-rRNA processing	69.71
RIOX2	HGNC:19441	ribosome assembly (RP hydroxylation)	68.48
RPS10	HGNC:10383	ribosomal protein	66.98
NUMA1	HGNC:8059	pre-rRNA processing	66.38
MPHOSPH10	HGNC:7213	pre-rRNA processing	65.55
NSA2	HGNC:30728	ribosome assembly	64.92
TRMT112	HGNC:26940	pre-rRNA modification	64.72
RPS21	HGNC:10409	ribosomal protein	64.56
NOP58	HGNC:29926	pre-rRNA processing	60.94
UTP20	HGNC:17897	pre-rRNA processing	58.89
RPUSD2	HGNC:24180	pre-rRNA modification	57.07
RRS1	HGNC:17083	ribosome assembly	56.68
NUDT16	HGNC:26442	pre-rRNA processing	53.72
NOLC1	HGNC:15608	pre-rRNA modification	51.33
NOL8	HGNC:23387	pre-rRNA processing	47.82
METTL15	HGNC:26606	mitochondrial pre-rRNA modification	46.47
SUV39H1	HGNC:11479	pre-rRNA transcription	46.09
XRCC5	HGNC:12833	pre-rRNA processing	44.37
ABCE1	HGNC:69	ribosome recycling	36.43
TTF1	HGNC:12397	pre-rRNA transcription	27.40
MPV17L2	HGNC:28177	mito-ribosome assembly	24.79
MAF1	HGNC:24966	pre-rRNA transcription	24.49
POLR1D	HGNC:20422	pre-rRNA transcription	16.69
TAF1D	HGNC:28759	pre-rRNA transcription	10.76

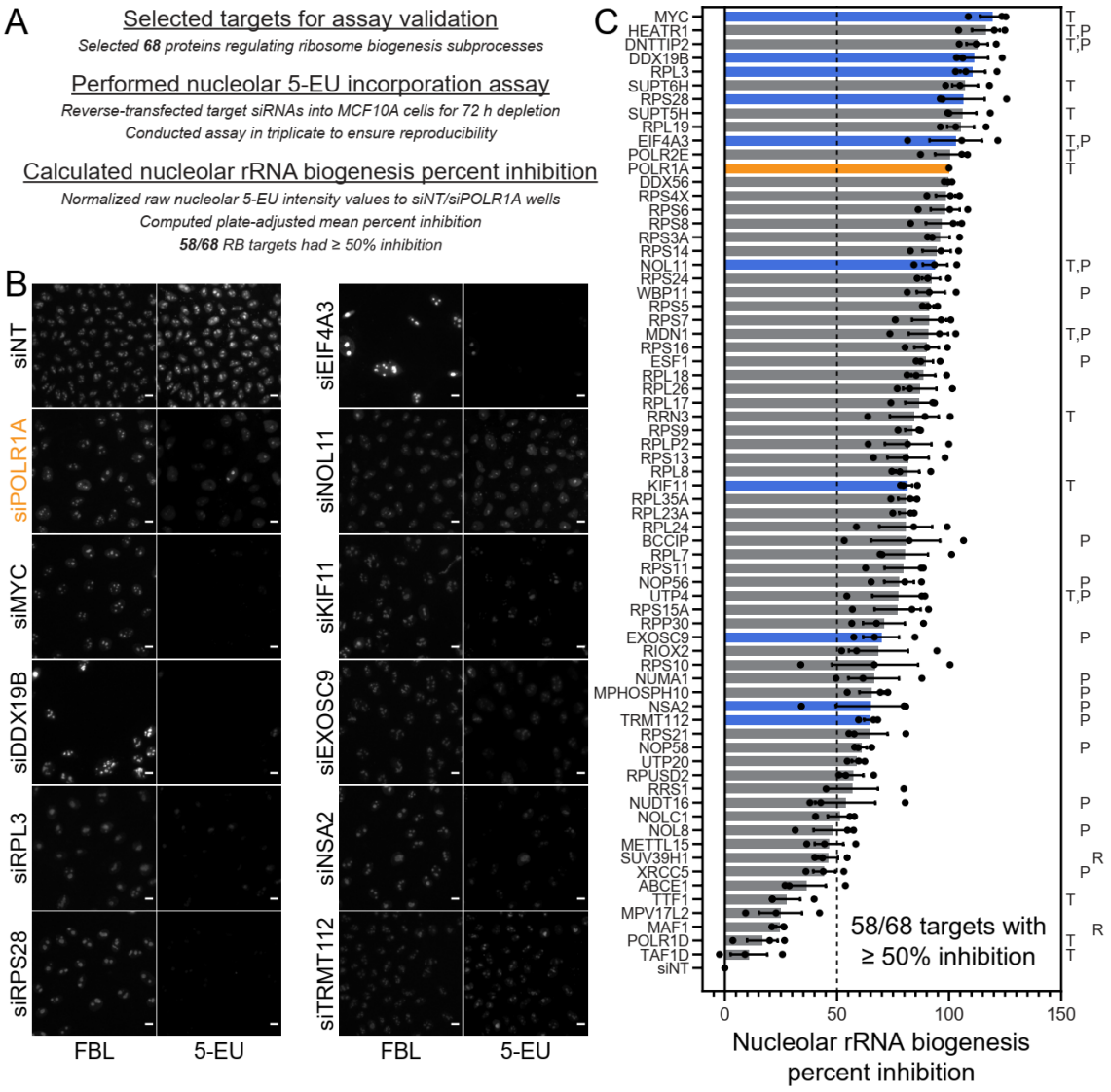

Figure 2-6. Validation of the 5-EU assay for nucleolar rRNA biogenesis on 68 known ribosome biogenesis factors.

(A) Outline of assay validation experiments. 68 proteins known to regulate ribosome biogenesis subprocesses, including RNAP1 transcription and pre-rRNA processing, modification, or stability, were selected for assay validation. The 5-EU assay was performed on cells depleted of these factors in biological triplicate, as described.

(B) Representative images of FBL staining and 5-EU visualization for cells treated with siNT (negative control), siPOLR1A (positive control, orange), or a subset of siRNAs targeting known RB factors.

(C) Nucleolar rRNA biogenesis percent inhibition values for cells depleted of each known RB factor. Black dots, individual percent inhibition values for one biological replicate. Solid bars, mean percent inhibition (n = 3). Orange bar, POLR1A positive control (percent inhibition = 100%). Blue bars, RB factors illustrated in Panel B. Letters to right indicate factors involved in RNAP1 transcription (T), pre-rRNA processing (P), or transcription repression (R).

We also noted significant percent inhibition averages for 28 RPs from both the 40S and 60S subunits. Almost all RPs are essential for pre-rRNA biogenesis in the yeast *Saccharomyces cerevisiae* (232, 233) and in human cells (74, 175), compatible with a concomitant observed decrease in nucleolar rRNA biogenesis following their depletion.

Furthermore, of the 10 factors that had a mean percent inhibition value under 50%, five factors were either inhibitors of pre-rRNA transcription, including SUV39H1 (234) and MAF1 (235, 236), mitochondrial ribosome biogenesis factors, including METTL15 (237, 238) and MPV17L2 (239), or ribosome recycling factors involved in translation, namely ABCE1 (240).

Surprisingly, the other five RB factors with a mean percent inhibition less than 50% are well-appreciated for playing roles in pre-rRNA transcription, including POLR1D (241), TAF1D (242), and TTF1 (243), and in pre-rRNA processing, including NOL8 (244) and XRCC5/Ku86, which also aids TTF1 during RNAP1 termination (245, 246). It is possible that these factors were not significantly depleted following transfection, or that, within our timeframe, the 5-EU assay cannot detect a significant change in nucleolar RNA levels as a result of non-concordant changes in both pre-rRNA transcription and stability.

2.4. Discussion

More precise, accessible methods for the study of nucleolar function are critical for illuminating novel ribosome biogenesis regulators and next-generation therapeutics for human disease states including cancer, aging, and rare ribosomopathies. Here, we developed an HT-ready, image-based assay that selectively measures nucleolar rRNA biogenesis in MCF10A breast epithelial cells. Building upon previous HTS techniques, we combined FBL staining of nucleoli and 5-EU incorporation into nascent RNA to measure only the 5-EU signal corresponding to nucleoli. We optimized the parameters of this assay using both small molecule inhibition (BMH-21) and acute siRNA depletion of essential RNAP1 transcription machinery (POLR1A and NOL11). Our detailed assay framework can be applied to studies of novel RNAP1 drug inhibitors and cellular regulators of nucleolar rRNA biogenesis, with the potential for adaptation to a variety of cell types. Our assay will increase the dimensionality and efficiency of future HTS campaigns focused on the nucleolus, accelerating the discovery of novel modulators of nucleolar function.

After optimizing the 5-EU assay for a miniaturized format, we validated its utility on 68 known RB factors including core RNAP1 components, small (pre-40S) or large (pre-60S) ribosomal subunit-specific processing and assembly factors, pre-rRNA modification factors, and RPs. As expected, all RB factors had a percent inhibition value greater than 0%. While a wide range of percent inhibition values were observed, 58/68 factors (85.5%) had a mean percent inhibition of at least 50%, signaling that the 5-EU assay robustly reports depletion conditions that interrupt nucleolar rRNA biogenesis.

Although our nucleolar 5-EU assay accurately reported the interruption of nucleolar rRNA biogenesis for the vast majority of RB factors studied, we note the following considerations and caveats regarding our method and results. First, nucleolar rRNA biogenesis can be affected by changes in one or more RB subprocesses including pre-rRNA transcription, processing, modification, and binding by RPs, which all occur co-geographically within the nucleolus. Since kinetic studies have defined the rates of human pre-rRNA transcription (247) and initial pre-rRNA processing steps (248) to be on the order of minutes, 5-EU label will be distributed across a population of partially-processed or folded nucleolar pre-rRNA intermediates at the end of the assay's 1 h labeling period. Therefore, nucleolar 5-EU incorporation over the course of 1 h cannot report solely on RNAP1 transcriptional activity, and additional mechanistic assays may be necessary to precisely define how an experimental treatment alters RB following the observation of a 5-EU defect. We highlight the importance of our discovery of the expanded ability of the 5-EU assay to report on defects in multiple RB steps in addition to RNAP1 transcription, which to our knowledge has not been previously considered.

Second, a treatment, like 72 h siRNA-mediated depletion of cultured human cells as we have done here, may also have opposing, compensatory effects on multiple RB subprocesses, leading to an artificially low percent inhibition and a false negative result. More broadly, as with any HTS study using RNAi-mediated target depletion, off-target effects or inefficient on-target depletion could lead to false positive or false negative results, respectively (249, 250). Second, we have empirically defined a percent inhibition significance cutoff of 50% inhibition because it minimizes the number of incorrectly

classified RB factors. However, it is still unclear if there is a more stringent percent inhibition cutoff that would correspond strictly to RB factors regulating RNAP1 transcriptional activity, or cutoffs for other RB subprocesses. Future studies may elucidate the relationship between the roles of a given RB factor and the nucleolar rRNA biogenesis percent inhibition value observed upon its depletion. Finally, close attention must be paid to the accuracy of nucleolar segmentation if median nucleolar 5-EU signal is being quantified; the maximum nuclear 5-EU signal metric can be used if treatment causes significant FBL dispersion, as we have observed with BMH-21 at 1 μM.

Our miniaturized 5-EU assay enables direct quantification of nucleolar rRNA biogenesis in high-throughput, providing clearer insight into how targets modulate RB and improving upon previous HTS techniques for studying nucleolar function. The 5-EU assay is also compatible with our previously published assay for nucleolar number (83), and is likely to be compatible with other high-content assays for ribosome biogenesis that monitor nucleolar architecture by co-staining for nucleolar proteins (187, 188). By extending the dimensionality and specificity of current state-of-the-art assays which indirectly track nucleolar function, our 5-EU assay will permit researchers to focus on the most promising screen candidates earlier, thereby increasing the efficiency of RB-directed screening campaigns. We anticipate that the miniaturized 5-EU assay will expedite the identification and definition of novel regulators of RB in basic or translational studies of nucleolar function.

2.5. Materials and Methods

2.5.1. Cell lines and culture conditions

Human MCF10A breast epithelial cells (ATCC CRL-10317) were cultured in DMEM/F-12 (Gibco 11330032) with 5% horse serum (Gibco 16050122), 10 μg/mL insulin (MilliporeSigma I1882), 0.5 μg/mL hydrocortisone (MilliporeSigma H0135), 20 ng/mL epidermal growth factor (Peprotech AF-100-15), and 100 ng/mL cholera toxin (MilliporeSigma C8052). Cells were incubated at 37 °C in a humidified atmosphere with 5% CO2.

2.5.2. RNAi depletion by reverse-transfection

RNAi depletion was conducted in MCF10A cells as previously reported (83, 84). MCF10A cells were reverse-transfected into an arrayed 384-well plate library containing small interfering RNA (siRNA) constructs (Horizon Discovery, see **Table 2-3**. Assay-ready plates containing 10 μL of 100 nM ON-TARGET siRNAs resuspended in 1X siRNA buffer (Horizon Discovery B-002000-UB-100) were prepared from master library 384-well plates (Horizon Discovery, 0.1 nmol scale) and stored at -80 C. Plates were thawed at room temperature for 30 min and briefly centrifuged at 300 RPM. siRNA controls (**Table 2-3**) were freshly diluted in 1X siRNA buffer to 100 nM from a 50 μM frozen stock, and 10 μL of 100 nM control siRNAs were manually pipetted into the assay-ready plates. To each well, 10 μL of a 1:100 (v/v) RNAiMAX:OptiMEM solution was added (Invitrogen 13778-150, Gibco 31985070), after which the plates

were briefly centrifuged at 300 RPM and incubated at room temperature for 30 min. MCF10A cells at 70%-80% confluency were trypsinized for 15 min with 0.05% trypsin (Gibco 25300054), resuspended in culture media, counted with a hemacytometer, and diluted in culture medium to a density of 100,000 cells/mL. Thirty μL of cells were dispensed into assay plates using a Multidrop Combi Reagent Dispenser (Thermo Scientific), to achieve a seeding density of 3000 cells/well, a final volume of 50 μL, and a final siRNA concentration of 20 nM. Seeded assay plates were briefly centrifuged at 300 RPM and incubated at 37 °C for 72 h. Ribosome biogenesis factors were screened in triplicate.

Table 2-3. Horizon Discovery (Dharmacon) siRNAs used for 72 h target knockdown.

HGNC Symbol	HGNC ID	Horizon Discovery Catalog Number
Non-targeting ctrl	N/A	D-001810-10
POLR1A ctrl	HGNC:17264	M-013983-01
NOL11 ctrl	HGNC:24557	M-016695-01
ABCE1	HGNC:69	L-008702-00
BCCIP	HGNC:978	L-013030-00
DDX19B	HGNC:2742	L-013471-01
DDX56	HGNC:18193	L-020410-01
DNTTIP2	HGNC:24013	L-020513-01
EIF4A3	HGNC:18683	L-020762-00
ESF1	HGNC:15898	L-015235-01
EXOSC9	HGNC:9137	L-019924-01
HEATR1	HGNC:25517	L-015939-02
KIF11	HGNC:6388	L-003317-00
MAF1	HGNC:24966	L-018603-01
MDN1	HGNC:18302	L-009786-00
METTL15	HGNC:26606	L-016943-01
MPHOSPH10	HGNC:7213	L-012128-01
MPV17L2	HGNC:28177	L-014959-02
MYC	HGNC:7553	L-003282-02
NOL11	HGNC:24557	L-016695-01
NOL8	HGNC:23387	L-016976-01
NOLC1	HGNC:15608	L-019843-00
NOP56	HGNC:15911	L-019143-01
NOP58	HGNC:29926	L-017973-01
NSA2	HGNC:30728	L-017043-01
NUDT16	HGNC:26442	L-016334-01
NUMA1	HGNC:8059	L-005272-00
POLR1D	HGNC:20422	L-020979-01
POLR2E	HGNC:9192	L-004739-01
RIOX2	HGNC:19441	L-016031-01
RPL17	HGNC:10307	L-013633-01
RPL18	HGNC:10310	L-011142-01
RPL19	HGNC:10312	L-010865-01
RPL23A	HGNC:10317	L-012863-00
RPL24	HGNC:10325	L-011144-02
RPL26	HGNC:10327	L-011132-01
RPL3	HGNC:10332	L-012975-01
RPL35A	HGNC:10345	L-013543-01

HGNC Symbol	HGNC ID	Horizon Discovery Catalog Number
RPL7	HGNC:10363	L-013727-00
RPL8	HGNC:10368	L-013721-02
RPLP2	HGNC:10377	L-004314-01
RPP30	HGNC:17688	L-015336-01
RPS10	HGNC:10383	L-011136-00
RPS11	HGNC:10384	L-013569-02
RPS13	HGNC:10386	L-011150-02
RPS14	HGNC:10387	L-013532-00
RPS15A	HGNC:10389	L-013542-01
RPS16	HGNC:10396	L-013627-00
RPS21	HGNC:10409	L-011153-00
RPS24	HGNC:10411	L-011155-00
RPS28	HGNC:10418	L-013679-02
RPS3A	HGNC:10421	L-013603-01
RPS4X	HGNC:10424	L-011138-00
RPS5	HGNC:10426	L-010498-00
RPS6	HGNC:10429	L-003024-00
RPS7	HGNC:10440	L-013700-01
RPS8	HGNC:10441	L-011140-01
RPS9	HGNC:10442	L-011131-00
RPUSD2	HGNC:24180	L-015920-01
RRN3	HGNC:30346	L-016947-00
RRS1	HGNC:17083	L-014077-01
SUPT5H	HGNC:11469	L-016234-00
SUPT6H	HGNC:11470	L-010540-00
SUV39H1	HGNC:11479	L-009604-00
TAF1D	HGNC:28759	L-014314-02
TRMT112	HGNC:26940	L-020786-01
TTF1	HGNC:12397	L-012378-00
UTP20	HGNC:17897	L-020215-00
UTP4	HGNC:1983	L-015011-00
WBP11	HGNC:16461	L-013343-00
XRCC5	HGNC:12833	L-010491-00

2.5.3. Analysis of mRNA knockdown by RT-qPCR

MCF10A cells were seeded at $1x10^5$ cells per well in 6-well plates and incubated at 37 °C for 24 h. Cells were reverse transfected with 20 nM siRNA controls (**Table 2-3**) using lipofectamine RNAiMAX per manufacturer's instructions for 72 h. RNA was harvested using TRIzol reagent (Life Technologies 15596018) per manufacturer's instructions. RNA used for cDNA synthesis had a minimum A_{260}/A_{230} ratio of 1.7. cDNA was synthesized from 1 μg total input RNA using iScript™ gDNA Clear cDNA Synthesis Kit (BioRad 1725035). qPCR was performed using SYBR Green reagent (BioRad 1725121) and gene-specific primers (**Table 2-4**). Cycling parameters were as follows: initial denaturation 95 ºC for 30 s, 40 cycles 95 ºC for 15 s and 60ºC for 30 s, melt curve analysis 60 ºC to 94.8 ºC in 0.3 ºC increment. Data analysis was completed using the comparative C_T method ($\Delta\Delta C_T$) using *ACTB* mRNA as an internal control.

Table 2-4. Primer sequences for RT-qPCR.

Target mRNA	Forward Primer Sequence (5' → 3')	Reverse Primer Sequence (5' → 3')
ACTB	ATT GGC AAT GAG CGG TTC	CGT GGA TGC CAC AGG ACT
NOL11	TCC AGG CAA GAA CGG TGT TT	GAA ACC TGC AGT CCT ACC CC
POLR1A	CTT CAT TCT TCC ACA GGG CA	CCG AAA GGA ACA CAA CAG CA

2.5.4. BMH-21 treatment and 5-ethynyl uridine incorporation

BMH-21 (MilliporeSigma SML1183) was resuspended in DMSO to a working concentration of 50 μM (50X) and stored at -20 C. 5-ethynyl uridine (5-EU, ClickChemistryTools 1261-100) was resuspended in ddH_2O from powder to a working

concentration of 50 mM (50X) and stored at -20 C. For BMH-21 treatment, reverse-transfected assay plates were treated 15 min before the end of the 72 h RNAi depletion period. One μL of either DMSO vehicle or of 50 μM BMH-21 was manually added directly to 50 μL medium in the appropriate wells of the assay plates, which were then briefly centrifuged at 300 RPM and incubated for 15 min before 5-EU incorporation and for the remaining 1 h 5-EU treatment period. For 5-EU incorporation into nascent RNA, reverse-transfected assay plates were treated for 1 h after the end of the 72 h RNAi depletion period. One μL of 50 mM 5-EU was manually added directly to 50 μL medium in each well of the assay plates, which were then briefly centrifuged at 300 RPM and incubated for 1 h.

2.5.5. Immunofluorescent staining and click fluorophore labeling

After 5-EU incorporation, cells were gently washed with 30 μL of PBS and fixed with 1% (v/v) paraformaldehyde (Electron Microscopy Sciences 15710-S) diluted in PBS at room temperature for 20 min. Cells were washed twice with 20 μL wash buffer consisting of PBS with 0.05% (v/v) TWEEN 20 (MilliporeSigma P1379), then permeabilized with 20 μL of 0.5% (v/v) Triton X-100 in PBS for 5 min. Cells were washed twice with 20 μL wash buffer and incubated with 20 μL of blocking buffer consisting of 10% (v/v) FBS (MilliporeSigma F0926) diluted in PBS for 1 h at room temperature. FBL primary antibody solution was prepared by diluting supernatant from the 72B9 hybridoma line (251) at 1:500 or 1:250 (v/v) in blocking buffer. After blocking, cells were incubated with 20 μL FBL primary antibody solution for 2 h at room

temperature. Cells were washed twice with 20 μL wash buffer and incubated with 20 μL secondary antibody solution, consisting of 1:1000 (v/v) goat anti-mouse AlexaFluor 647 (Invitrogen A-21236) and 3 μg/mL Hoechst 33342 dye in blocking buffer, for 1 h in the dark at room temperature. Immediately before the end of the secondary antibody incubation period, the click reaction cocktail was prepared in PBS by combining 5 μM AFDye 488 azide (ClickChemistryTools 1275-5), 0.5 mg/mL $CuSO_4$ (Acros Organics 197730010), and 20 mg/mL freshly-resuspended sodium ascorbate (Alfa Aesar A15613). Cells were washed twice with 20 μL wash buffer, then treated with 20 μL of click reaction cocktail for 30 min in the dark at room temperature. Cells were washed twice with 20 μL wash buffer, and soaked in 20 μL PBS containing 3 μg/mL Hoechst 33342 dye for 30 min in the dark at room temperature to dissociate excess AFDye 488 azide. Cells were washed twice with 20 μL wash buffer and 40 μL of PBS was added to each well before high-content imaging.

2.5.6. High-content imaging

Stained assay plates were imaged with a GE Healthcare IN Cell Analyzer 2200. Fields of view were acquired at 20X magnification with 2x2 pixel binning (665.63 μm^2) at 16-bit depth using Cy5, DAPI, and FITC channels for FBL, Hoechst, and 5-EU staining, respectively. Laser autofocus was used to automatically determine imaging Z-height. For publication, images were cropped, merged, and labeled with scale bars using ImageJ 1.53i (252).

2.5.7. CellProfiler pipeline and data analysis

Image analysis was conducted with a custom pipeline for CellProfiler 3.1.9 (202, 253). Briefly, nuclei and nucleoli objects were segmented from DAPI and Cy5 channels, respectively, using global two-class Otsu thresholding. Child nucleoli objects were linked to parent nuclei objects using the RelateObjects module. For both object classes, area was measured from DAPI or Cy5 images, and 5-EU intensity was measured from FITC images. Object-level normalized 5-EU intensity metrics including maximum, mean, median, and standard deviation were calculated by CellProfiler. Raw CellProfiler output CSV files including plate metadata were imported into and analyzed with JMP Pro 15.2.0 (SAS Institute). Per-well averages were computed for each 5-EU metric. For each plate, aggregate control well data were used to calculate signal-to-background (S/B) and Z' factor screening statistics. Nucleolar rRNA biogenesis percent inhibition values were calculated for each well as follows:

$$\text{Nucleolar rRNA biogenesis percent inhibition} = \left(1 - \frac{x_i - \bar{x}_{POLR1A}}{\bar{x}_{NT} - \bar{x}_{POLR1A}}\right) * 100\%$$

where x is the average 5-EU metric value over all objects in a well, x_i is the well metric value for a non-control well, $\bar{x}_{NT}$ and $\bar{x}_{POLR1A}$ are averages of all NT or POLR1A control well metric values respectively. Plate-adjusted percent inhibition values were calculated for non-control wells by subtracting the plate's median NT percent inhibition value from each non-control well percent inhibition (254). Nucleolar/nuclear area ratios

were calculated for each nucleus by summing the area of all child nucleoli for a given nucleus, then dividing by the area of the specified nucleus. Nucleoli without a valid parent nucleus (parent ID 0) were discarded. Per-well averages were then computed. Optimization data were graphed in JMP. Triplicate data from the ribosome biogenesis factor screen were averaged in JMP and graphed with GraphPad Prism 8 (GraphPad Software).

2.5.8. BMH-21 dose response treatment

A 14-point 50X dilution series ranging from 1 mM to 100 nM BMH-21 was created in DMSO vehicle from a 1 mM BMH-21 working stock. In a 384-well plate, 3000 MCF10A cells/well were plated in 50 μL of media on day 0. On day 1, columns 3-4 were treated with 1 μL of only vehicle and each column from 5-18 was treated with 1 μL of one concentration of the BMH-21 dilution series for 15 min at 37 °C, resulting in a 1X dilution series ranging from 20 μM to 2 nM at final concentration. Columns 1-2 were not treated with DMSO. Each well was treated with 1 μL of 50 mM 5-EU for a final concentration of 1 mM 5-EU for an additional 1 h at 37 °C. Cells were fixed and stained as detailed above. Rows A-H were stained only for FBL (no 5-EU click reaction), and rows I-P were stained for FBL and treated with the 5-EU click reaction. Cells were imaged as above and processed with the CellProfiler pipeline. Raw data were analyzed in JMP, and per-well averages were used to fit dose response curves using JMP's Logistic 4 Parameter Hill equation. Fit parameter estimates and errors are provided in **Table 2-5**. Summary data were graphed in JMP.

Table 2-5. BMH-21 dose response curve fitting parameter estimates for the Logistic 4 Parameter Hill equation in JMP.

Curve	Parameter	Estimate	Std Error	Wald ChiSquare	Prob > ChiSquare	Lower 95%	Upper 95%
Nucleolar median 5-EU signal	Growth Rate	-1.616562	0.2091874	59.719148	<.0001	-2.026562	-1.206562
Nucleolar median 5-EU signal	Inflection Point	-6.528818	0.0392489	27670.282	<.0001	-6.605745	-6.451892
Nucleolar median 5-EU signal	Lower Asymptote	0.011091	0.0003195	1204.7225	<.0001	0.0104647	0.0117172
Nucleolar median 5-EU signal	Upper Asymptote	0.0235976	0.0002631	8045.8384	<.0001	0.023082	0.0241132
Nuclear max 5-EU signal	Growth Rate	-2.023083	0.2612414	59.971259	<.0001	-2.535107	-1.511059
Nuclear max 5-EU signal	Inflection Point	-6.454994	0.0318318	41121.519	<.0001	-6.517383	-6.392605
Nuclear max 5-EU signal	Lower Asymptote	0.0124749	0.000403	958.45226	<.0001	0.0116851	0.0132647
Nuclear max 5-EU signal	Upper Asymptote	0.0300003	0.0003211	8730.8645	<.0001	0.029371	0.0306296
Nucleolar/nuclear area ratio per nucleus	Growth Rate	5.4023123	1.1717432	21.256635	<.0001	3.1057379	7.6988867
Nucleolar/nuclear area ratio per nucleus	Inflection Point	-6.489622	0.0293274	48965.739	<.0001	-6.547103	-6.432142
Nucleolar/nuclear area ratio per nucleus	Lower Asymptote	0.2272056	0.0037004	3770.0065	<.0001	0.2199529	0.2344582
Nucleolar/nuclear area ratio per nucleus	Upper Asymptote	0.4080419	0.0049142	6894.3767	<.0001	0.3984101	0.4176736

Chapter 3

Discovery of novel microRNA regulators of ribosome biogenesis

The contents of this chapter are being preprinted and submitted as follows:

Bryant CJ, McCool MA, Rosado-González GT, Abriola L, Surovtseva YV, Baserga SJ. Discovery of novel microRNA regulators of ribosome biogenesis.

3.1. Work Contributed

This manuscript has not yet been submitted for publication. I conceptualized the project with SJ Baserga. I conducted all experiments, data analysis, and figure preparation except for the following: 1) L Abriola and YV Surovtseva assisted with screen data analysis and conducted the microRNA hairpin inhibitor screen and siRNA deconvolution; 2) GT Rosado-González contributed several immunoblots for puromycin (global translation) and TP53 levels under my supervision; 3) MA McCool collected images from siON-TARGET screening of *RPS28* and *SPRR3* for changes in nucleolar number or nucleolar rRNA biogenesis. The manuscript was written by myself and SJ Baserga with very helpful input from our co-authors and other members of the Baserga lab.

3.2. Introduction

Ribosome biogenesis (RB) is the complex, essential process by which mature small and large ribosomal subunits are produced in all living organisms. Eukaryotes partition many RB steps into the nucleolus, a phase-separated membraneless organelle within the enveloped nucleus (44, 45, 255). In human cells, three of the four mature ribosomal RNAs (rRNAs), the 18S, 5.8S, and 28S rRNAs, are synthesized in the nucleolus as components of the polycistronic 47S primary pre-rRNA precursor transcript from tandem ribosomal DNA (rDNA) repeats by RNA Polymerase 1 (RNAP1) (173). The 5S rRNA is separately transcribed in the nucleus by RNA Polymerase 3 (RNAP3) (7, 256). A myriad of ribosome assembly factors (AFs) execute endo- and exonucleolytic

pre-rRNA processing and modification events to liberate the mature rRNAs from the 47S transcript, forming the small 40S and large 60S ribosomal subunits (2, 8, 257, 258). AFs also facilitate the binding of structurally-constitutive ribosomal proteins (RPs) and the folding of the maturing subunits at the macromolecular scale (3, 12, 13, 259-261). Defects in RB can trigger the nucleolar stress response during which labile members of the 5S RNP including RPL5 (uL18) or RPL11 (uL5) bind and sequester the TP53-specific E3 ligase MDM2, effectively stabilizing TP53 levels and leading to *CDKN1A* (*p21*) induction, cell cycle arrest, and apoptosis (71, 72, 262). At the organismal level, nucleolar stress resulting from RB defects can cause a class of rare human diseases called ribosomopathies (71, 139, 140, 263). Furthermore, cancer initiation and progression are strongly linked to aberrant RB (176-179, 264-266).

MicroRNAs comprise a class of non-coding (nc)RNAs of approximately 22 nt which can base pair with messenger (m)RNAs to post-transcriptionally reduce transcript stability or translation efficiency, acting as "sculptors of the transcriptome" to fine-tune gene expression (88, 89, 267). Like RB, microRNAs play critical roles in mediating human development, health, and disease including cancer (106, 268). How microRNAs regulate RB has yet to be explored systematically at the experimental level, yet there are some intriguing links between them. A handful of microRNAs have been experimentally described to affect RB subprocesses including RNAP1 transcription, 60S assembly, and RP gene transcription (53). Consistent with this, the microRNA biogenesis factors Drosha and Dicer are required for 28S and 5.8S maturation (269). AGO2, the microRNA-binding component of the active RISC complex (267), has been found in the

nucleolus (102) along with several microRNAs (98-100), though their precise biological function there remains unclear. Computational analysis has implicated microRNA-mediated control of RPs as a key potentiator of RB activity and disease progression (270), thereby necessitating additional *in vivo* experiments. Software packages have made some inroads towards accurate prediction of microRNA targets (271, 272) or functions (273) although abundant false positives limit their utility (270, 274). The limited amount of direct experimental evidence that microRNAs are involved in RB represents a significant gap in our understanding of the layers of regulation of nucleolar function in human cells.

Previously, our laboratory established a robust screening platform to identify novel regulators of RB by exploiting the close relationship between nucleolar number and function (83, 84). We discovered that either a decrease or increase in nucleolar number from 2-4 nucleoli per nucleus following genetic perturbation is strongly predictive of aberrant RB in human MCF10A breast epithelial cells. Our high-content screening platform leverages changes in nucleolar number to identify putative novel regulators of RB. For these genome-wide siRNA screens, we reverse-transfected MCF10A cells with an arrayed library of siRNAs for 72 h. Following treatment, we fixed and stained the cells for the nucleus and the nucleolus, conducted automated imaging, and used a custom CellProfiler pipeline to count the number of nucleoli per nucleus on a per-cell basis. Screening statistics were robust, with routine Z' factors above 0.5. Together, our laboratory's previous RNAi-based nucleolar number screening campaigns have successfully identified over 250 novel protein-coding regulators of RB (83, 84).

To date, no holistic, unbiased discovery campaign for microRNAs functioning in RB regulation has been conducted, and the full complement of microRNAs affecting RB remains poorly understood. We previously hypothesized that microRNAs may be a key, underappreciated conduit linking biochemical RB defects to the pathogenesis of diseases like ribosomopathies and cancer (53). To discover novel microRNAs negatively regulating RB, we conducted a high-content screen for changes in nucleolar number following microRNA mimic overexpression in human MCF10A cells. High-throughput screens using microRNA mimics have previously revealed mechanistic insight into microRNA-mediated regulation dynamics during cellular proliferation and signaling (275, 276), cardiac regeneration (277), viral infection (278), and cancer (279, 280).

Here, we identify 72 high-confidence mature human microRNA hits that disrupt RB, which are enriched for mRNA targets involved in cell cycle regulation, cellular proliferation, and localization within the nucleolus. We validate the roles of a subset of 15 hits in RB subprocesses including pre-rRNA transcription, pre-rRNA processing, and global protein synthesis. For the first time, we directly define the abilities of 12 microRNAs to inhibit pre-rRNA processing. Our work reveals that the MIR-28 family members, hsa-miR-28-5p and hsa-miR-708-5p, are strong inhibitors of pre-40S pre-rRNA processing by way of *RPS28* downregulation. The MIR-28 family also targets *SPRR3*, an understudied oncogene whose depletion causes a decrease in nucleolar number, and which we show is essential for pre-rRNA transcription and global protein synthesis, but not for pre-rRNA processing. Our screen's results underscore the broad

potential of microRNAs to dysregulate RB, and raise new questions regarding the extent to which microRNAs may connect RB and disease.

3.3. Results

3.3.1. A high throughput phenotypic screen for altered nucleolar number identifies 71 novel microRNAs that negatively regulate ribosome biogenesis

Following on the success of our previous nucleolar number-based screens for novel RB regulators (83, 84), we hypothesized that microRNAs could also be functioning as nodes of control for RB. To discover novel microRNA negative regulators of ribosome biogenesis, we screened an arrayed library of 2603 human mature microRNA mimics (Dharmacon/Horizon Discovery) for their ability to alter nucleolar number 72 h after transfection into human MCF10A cells (**Figure 3-1A**). While most MCF10A cells treated with a negative control non-targeting siRNA (siNT) display between two and four nucleoli, cells depleted of the tUTP NOL11 (siNOL11) have an increased probability of having one nucleolus per nucleus ("one-nucleolus phenotype"), while those depleted of the mitotic kinesin KIF11 (siKIF11) have an increased probability of having five or more nucleoli per nucleus ("5+ nucleoli phenotype") (**Figure 3-1B**, siNT, siNOL11, or siKIF11 panels). Using these siRNAs as controls, we employed our established high-throughput nucleolar number screening platform to count nucleolar number after overexpression of microRNAs by using the CellProfiler software to segment and enumerate FBL-stained nucleoli on a per-cell basis from images captured by an automated microscope.

We took several steps to ensure our screen's reproducibility and minimize false positives. We conducted the primary screen in biological triplicate, enabling robust

calculation of one-nucleolus percent effect and 5+ nucleoli percent effect for each microRNA mimic. To assist with hit selection, we also calculated the strictly standardized mean difference (SSMD) for each microRNA mimic. SSMD is a more robust estimator of hit effect size than percent effect alone, as it also incorporates information on sample size and reproducibility (variance) while simultaneously controlling the false positive and false negative rates (281). Using these two cutoffs in concert allowed us to pick the strongest, most replicable hits. The percent effect cutoff was set at the top 2.5% for the one-nucleolus effect and at the top 1.0% for the 5+ nucleoli effect; the SSMD cutoff was set at 1.645 for both phenotypes, which allows identification of hits that are at least fairly strong (254). The median signal-to-background (S/B) for the controls was 2.74 or 2.64 for the one-nucleolus screen or the 5+ nucleoli screen, respectively. The median Z' factor for the one-nucleolus screen was 0.41, although the median Z' factor for the 5+ nucleoli screen was unfavorable at -0.43. Despite poor separation of controls for the 5+ nucleoli screen, reflected in the low median Z' factor, we felt confident that imposing a stricter percent effect cutoff and maintaining the strong SSMD cutoff would enable us to identify hits with reproducible increases in nucleolar number.

Using stringent cutoffs for mean percent effect and SSMD, the nucleolar number primary screen identified 64 one-nucleolus hits and nine 5+ nucleoli hits (**Figure 3-1C-D, Table 3-1**). The SSMD cutoff approach allowed us to ignore a number of less reproducible hits with otherwise high mean percent effect values, mostly from the 5+ nucleoli side of the screen (**Figure 3-1C-D**, bottom right quadrant of each graph). This total of 73 hits equates to an overall 2.8% hit rate. Inspection of images from top hits

including hsa-miR-548an, hsa-miR-708-5p, and hsa-miR-629-3p (**Figure 3-1B**) confirmed that the relevant phenotype for each hit was observed. We performed a validation screen with replicates for the 73 hits, where each hit was picked from the original microRNA mimic library and rescreened on a new plate for a change in nucleolar number. Overall, 71/73 hits (97%) passed validation (**Figure 3-2**).

We also screened a library containing 2609 microRNA inhibitors (Dharmacon/Horizon Discovery) in biological triplicate to investigate whether any microRNAs expressed in MCF10A cells were positively regulating RB. This screen had overall fewer actives and greater variability among replicates. Therefore, no microRNAs were consistently identified to be positively regulating RB in this screening campaign in MCF10A cells. While it is possible that technical limitations such as poor library quality prevented the identification of hits from this screen, I believe this result is more likely to be attributed to cell-type specific microRNA expression, and that searching for novel microRNA positive regulators of RB in cell lines other than MCF10A may be worthwhile. I discuss the future prospects of finding such hits in **Chapter 0**.

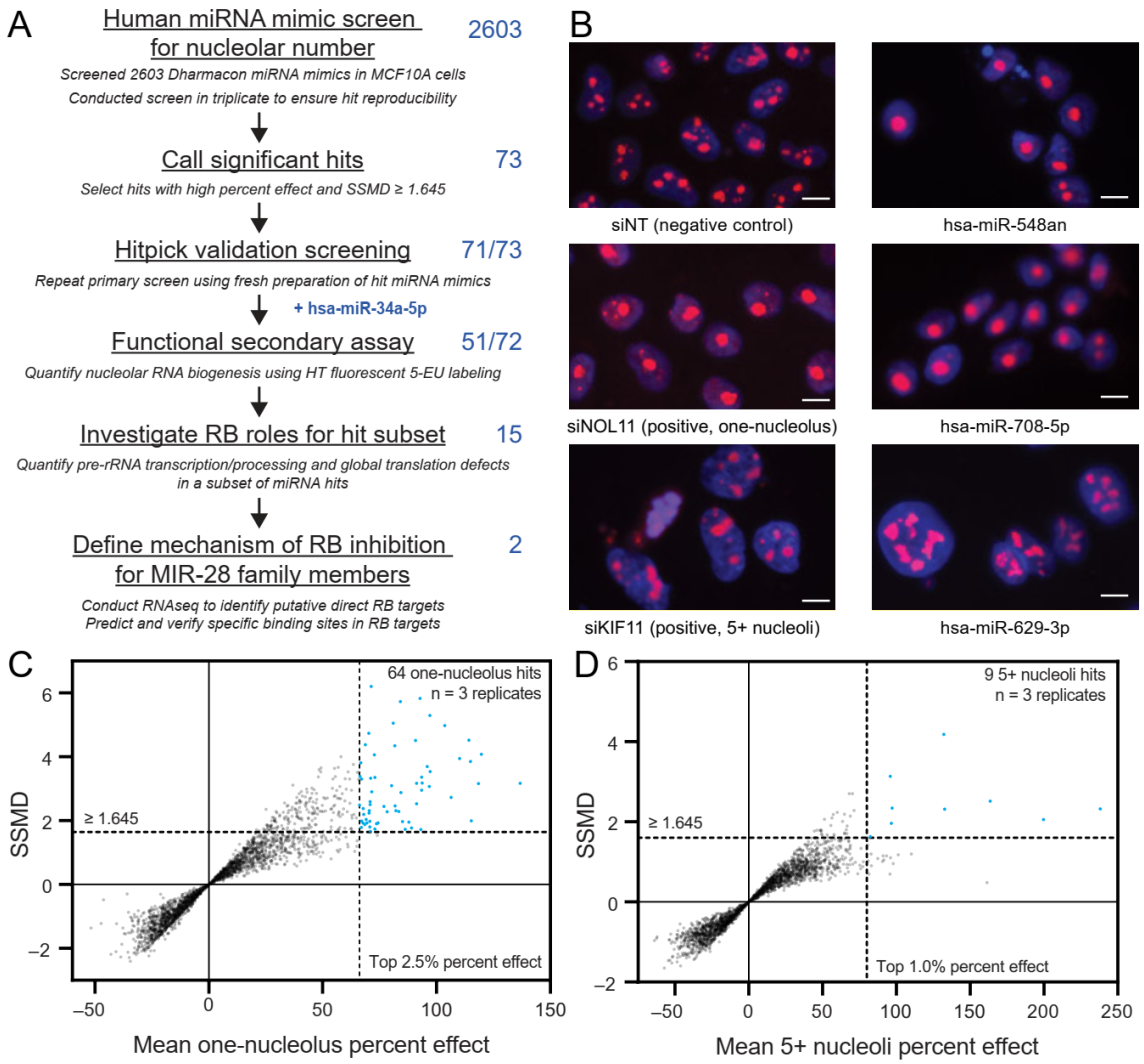

Figure 3-1. A screen for changes in nucleolar number reveals 71 novel microRNA mimic negative regulators of RB.

(**A**) Screening campaign pipeline. MCF10A cells were reverse-transfected into a library of 2,603 mature human microRNA mimics, then fixed and stained for DNA and FBL after 72 h in biological triplicate. The number of nucleoli was calculated using CellProfiler. Hits were called based on a decrease or increase in nucleolar number, respectively termed the one-nucleolus or 5+ nucleoli phenotypes. The primary screen identified 73 high-confidence hits, 71 of which passed hitpick validation screening. While not a primary screen hit, hsa-miR-34a-5p was included for further validation as described in the text. A functional secondary screen found that 51/73 hits strongly inhibited nucleolar rRNA biogenesis via 5-EU incorporation. Additional mechanistic assays for pre-rRNA transcription or processing, global translation, and nucleolar stress were carried out for a subset of 15 rigorously-selected hits. Further mechanistic studies were performed on two MIR-28 family siblings, hsa-miR-28-5p and hsa-miR-708-5p.

(**B**) Representative images from the screen showing 3 top hits alongside the negative control (non-targeting, siNT) and positive controls for the one-nucleolus (siNOL11) or 5+ nucleoli (siKIF11) phenotypes. hsa-miR-548-an and hsa-miR-708-5p are hits with the one-nucleolus phenotype while hsa-miR-629-3p is a hit with the 5+ nucleoli phenotype. The DNA stain (Hoechst) is shown in blue and fibrillarin (FBL) antibody detection is shown in red. Scale bars, 10 μm.

(**C**) Double flashlight plot for one-nucleolus hit selection. A total of 64 one-nucleolus hits were called using cutoffs for the top 2.5% of mean one-nucleolus percent effect and at least fairly strong hits where SSMD $\geq$ 1.645 as described in the text. Data were graphed in GraphPad Prism 8.

(**D**) Double flashlight plot for 5+ nucleoli hit selection. A total of nine 5+ nucleoli hits were called using cutoffs for the top 1.0% of mean 5+ nucleoli percent effect and the same SSMD cutoff as above. Hits are shown in blue. Data were graphed in GraphPad Prism 8.

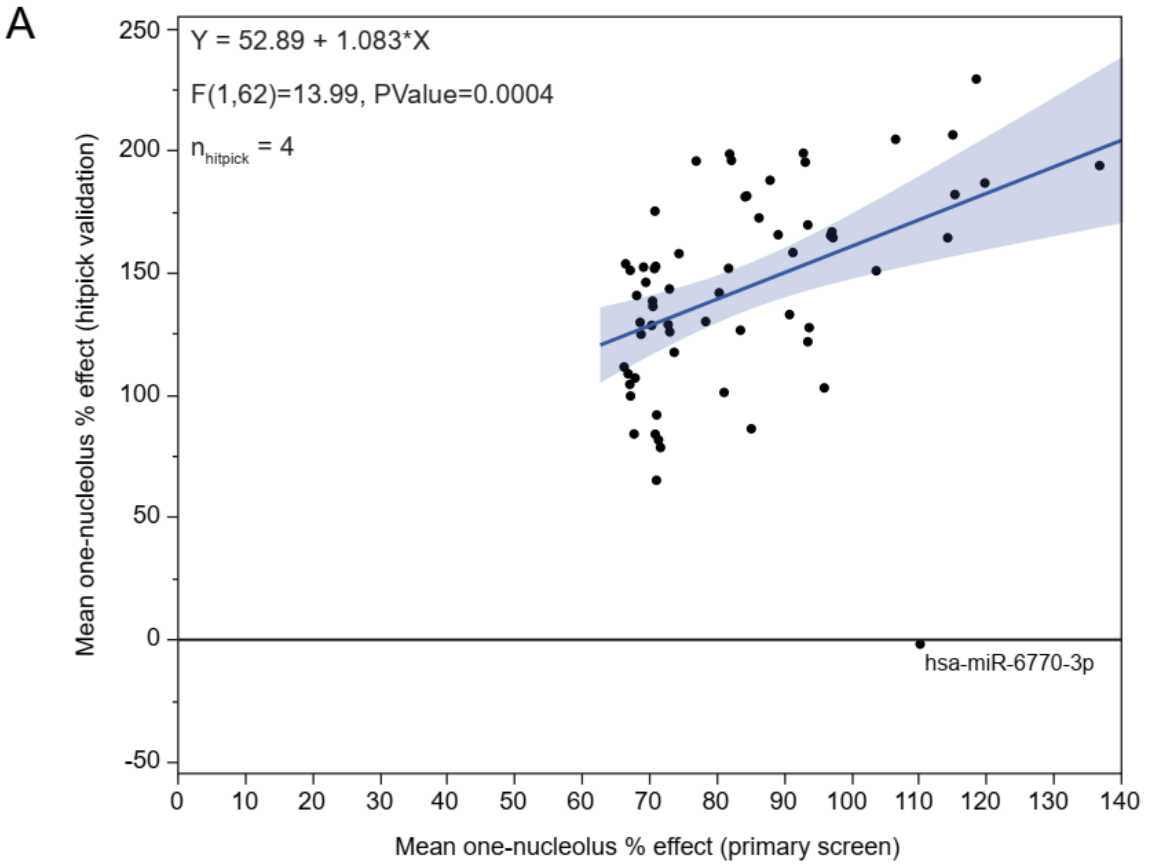
A
Y = 52.89 + 1.083*X
F(1,62)=13.99, PValue=0.0004
n hitpick = 4
hsa-miR-6770-3p
Mean one-nucleolus % effect (hitpick validation)
Mean one-nucleolus % effect (primary screen)
250
200
150
100
50
0
-50
0
10
20
30
40
50
60
70
80
90
100
110
120
130
140

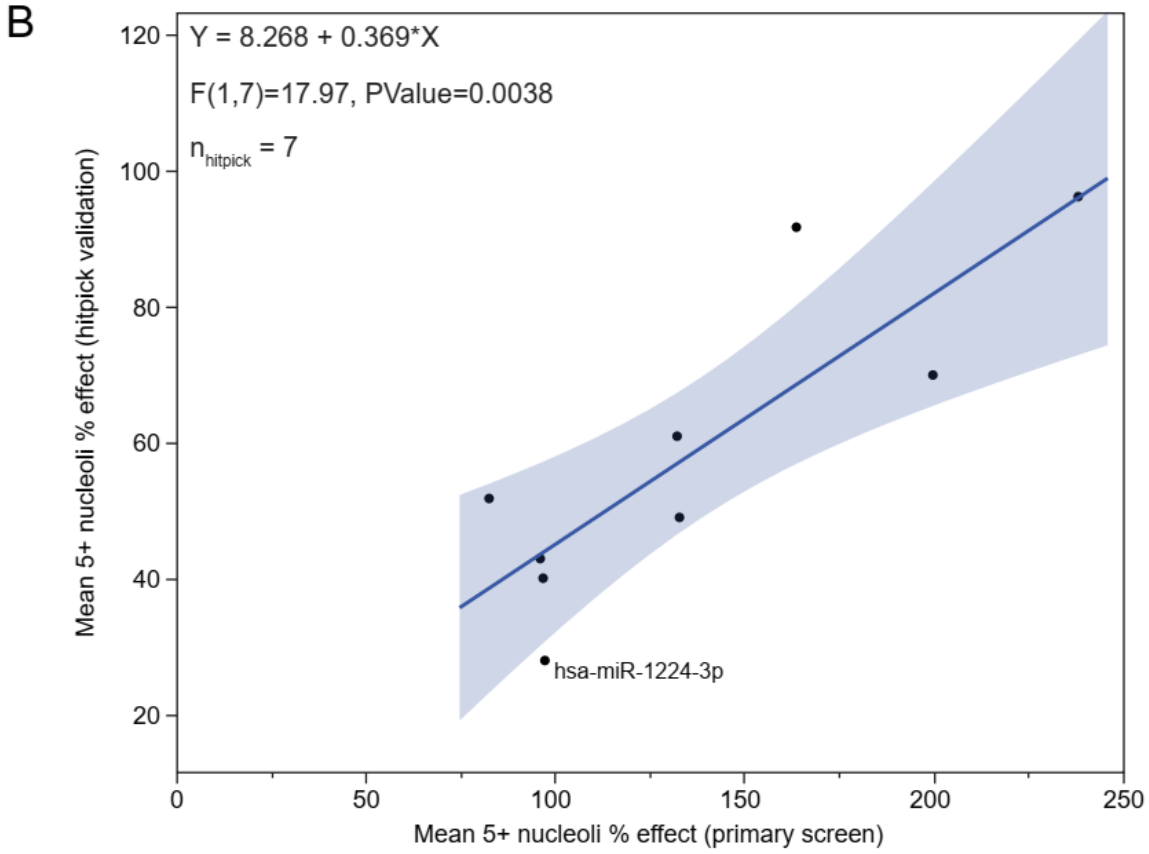
B
Y = 8.268 + 0.369*X
F(1,7)=17.97, PValue=0.0038
n hitpick = 7
hsa-miR-1224-3p
Mean 5+ nucleoli % effect (hitpick validation)
Mean 5+ nucleoli % effect (primary screen)
120
100
80
60
40
20
0
50
100
150
200
250

Figure 3-2. Primary screen hitpick validation excludes hsa-miR-6770-3p and hsa-miR-1224-3p.

(**A**) Comparison of mean one-nucleolus percent effects from primary screen (x-axis) or hitpick validation (y-axis) for 64 one-nucleolus hits. One-nucleolus hitpick was conducted with $n = 4$ replicates. hsa-miR-6770-3p was excluded from downstream analysis.

(**B**) Comparison of mean 5+ nucleoli percent effects from primary screen (x-axis) or hitpick validation (y-axis) for nine 5+ nucleoli hits. 5+ nucleoli hitpick was conducted with $n = 7$ replicates. Graphing and linear regression was performed in JMP. Blue shading represents the 95% confidence interval for the linear regression. hsa-miR-1224-3p was excluded from downstream analysis.

Table 3-1. Screen data from the microRNA mimic hits.

Mature Name	Mature Sequence	Hit type	Mean 1 nucleolus % effect (primary screen)	Mean 5+ nucleoli % effect (primary screen)	Mean % viability (primary screen)	Mean nucleolar rRNA biogenesis % inhibition (secondary screen)
hsa-miR-19b-1-5p	AGUUUUGCAGGUUUGCAUCCAGC	1nuc	76.8905	-41.5499	26.1811	30.6867
hsa-miR-25-5p	AGGCGGAGACUUGGGCAAUUG	1nuc	115.2847	-48.5213	29.4302	75.3336
hsa-miR-28-5p	AAGGAGCUCACAGUCUAUUGAG	1nuc	69.4171	-30.6874	39.0352	0.1798
hsa-miR-34a-5p	UGGCAGUGUCUUAGCUGGUUGU	5-EU only	11.2126	-14.4373	11.8626	72.1552
hsa-miR-34a-3p	CAAUCAGCAAGUAUACUGCCCU	1nuc	83.4515	-43.5020	25.6138	70.2136
hsa-miR-103b	UCAUAGCCCUGUACAAUGCUGCU	1nuc	72.9192	-32.5321	46.2277	47.6248
hsa-miR-124-3p	UAAGGCACGCGGUGAAUGCC	1nuc	70.4051	-14.4059	39.1479	61.8829
hsa-miR-147a	GUGUGUGGAAAUGCUUCUGC	1nuc	95.8985	-15.2537	18.3357	61.8420
hsa-miR-182-3p	UGGUUCUAGACUUGCCAACUA	1nuc	97.1881	-35.7837	17.5034	64.5551
hsa-miR-183-5p	UAUGGCACUGGUAGAAUUCACU	1nuc	81.0295	-23.9935	16.1631	33.4878
hsa-miR-192-3p	CUGCCAAUUCCAUAGGUCACAG	1nuc	70.4635	-40.7675	62.6596	67.1256
hsa-miR-212-5p	ACCUUGGCUCUAGACUGCUUACU	5+nuc	-30.8900	163.6195	27.8740	118.4006
hsa-miR-214-5p	UGCCUGUCUACACUUGCUGUGC	1nuc	93.4515	-42.1335	31.1500	-8.4825
hsa-miR-330-5p	UCUCUGGGCCUGUGUCUUAGGC	1nuc	67.1414	-22.3293	17.8441	65.2029
hsa-miR-378g	ACUGGGCUUGGAGUCAGAAG	1nuc	91.2407	-34.6224	16.7899	57.8991
hsa-miR-383-5p	AGAUCAGAAGGUGAUUGUGGCU	1nuc	68.7036	-26.7467	14.2377	0.9726
hsa-miR-431-3p	CAGGUCGUCUUGCAGGGCUUCU	1nuc	84.3927	-53.3944	35.2821	83.8315
hsa-miR-491-3p	CUUAUGCAAGAUUCCCUUCUAC	1nuc	73.6259	-51.5044	15.4532	63.6482
hsa-miR-493-3p	UGAAGGUCUACUGUGUGCCAGG	1nuc	72.9701	-34.2707	27.9966	69.2548
hsa-miR-526b-5p	CUCUUGAGGGAAGCACUUUCUGU	1nuc	71.2961	-54.4678	28.7207	130.2448
hsa-miR-548m	CAAAGGUAUUUGUGGUUUUUG	1nuc	68.5661	-40.8286	39.4094	4.1084

Mature Name	Mature Sequence	Hit type	Mean 1 nucleolus % effect (primary screen)	Mean 5+ nucleoli % effect (primary screen)	Mean % viability (primary screen)	Mean nucleolar rRNA biogenesis % inhibition (secondary screen)
hsa-miR-548an	AAAAGGCAUUGUGGUUUUUG	1nuc	136.7606	-52.5958	11.6122	65.7227
hsa-miR-605-3p	AGAAGGCACUAUGAGAUUUAGA	1nuc	66.4180	-49.9415	43.9197	65.0323
hsa-miR-629-3p	GUUCUCCCAACGUAAGCCCAGC	5+nuc	-34.5624	238.0865	38.5501	82.0529
hsa-miR-644a	AGUGUGGCUUUCUUAGAGC	1nuc	93.4518	-48.3585	34.9965	100.6519
hsa-miR-646	AAGCAGCUGCCUCUGAGGC	1nuc	70.6868	-42.6278	32.4484	130.3189
hsa-miR-708-5p	AAGGAGCUUACAAUCUAGCUGGG	1nuc	119.7255	-34.6331	27.9298	-26.2627
hsa-miR-1181	CCGUCGCCGCCACCCGAGCCG	5+nuc	-33.0869	96.7002	127.8444	86.9475
hsa-miR-1205	UCUGCAGGGUUUGCUUUGAG	1nuc	96.8437	-53.6603	20.5371	15.8211
hsa-miR-1224-3p	CCCCACCUCCUCUCUCCUCAG	not a hit	-25.7397	97.1706	86.6935	22.3652
hsa-miR-1273c	GGCGACAAAACGAGACCCUGUC	1nuc	106.4777	-32.6471	17.4055	31.5759
hsa-miR-1289	UGGAGUCCAGGAAUCUGCAUUUU	1nuc	78.2921	-51.7531	19.9980	68.0807
hsa-miR-1307-3p	ACUCGGCGUGGCGUCGGUCGUG	1nuc	66.1854	-50.4654	39.9432	100.3311
hsa-miR-1469	CUCGGCGCGGGGCGCGGGCUCC	1nuc	74.3347	-35.5461	29.9642	96.6575
hsa-miR-1908-5p	CGGCGGGGACGGCGAUUGGUC	1nuc	93.6562	-47.1934	40.6031	90.6213
hsa-miR-3126-3p	CAUCUGGCAUCCGUCACACAGA	1nuc	67.0451	-5.5614	9.1127	22.0878
hsa-miR-3139	UAGGAGCUCAACAGAUGCCUGUU	1nuc	84.1485	-23.5231	18.7614	5.8621
hsa-miR-3141	GAGGGCGGGUGGAGGAGGA	1nuc	72.7212	-29.4567	20.0734	51.1399
hsa-miR-3140-3p	AGCUUUUGGGAAUUCAGGUAGU	1nuc	91.3161	-25.8760	17.6869	6.4376
hsa-miR-3173-3p	AAAGGAGGAAAUAGGCAGGCCA	1nuc	67.6698	-35.7474	17.4723	86.4880
hsa-miR-3195	CGCGCCGGGCCCGGGUU	1nuc	82.1160	-31.0666	19.3988	51.5642
hsa-miR-3194-5p	GGCCAGCCACCAGGAGGGCUG	1nuc	81.8519	-36.9387	18.5734	22.9069
hsa-miR-3908	GAGCAAUGUAGGUAGACUGUUU	1nuc	89.0530	-34.4066	19.7717	7.3404
hsa-miR-3909	UGUCCUCUAGGGCCUGCAGUCU	1nuc	93.0802	-34.2190	25.5002	42.9342

Mature Name	Mature Sequence	Hit type	Mean 1 nucleolus % effect (primary screen)	Mean 5+ nucleoli % effect (primary screen)	Mean % viability (primary screen)	Mean nucleolar rRNA biogenesis % inhibition (secondary screen)
hsa-miR-3910	AAAGGCAUAAAACCAAGACA	1nuc	97.0357	-39.2190	11.9456	12.6747
hsa-miR-3911	UGUGUGGAUCCUGGAGGAGGCA	1nuc	70.2815	-46.9596	12.8721	53.8164
hsa-miR-3913-5p	UUUGGGACUGAUCUUGAUGUCU	5+nuc	-47.3333	132.1015	69.2233	84.5325
hsa-miR-4268	GGCUCCUCCUCUCAGGAUGUG	5+nuc	-15.5755	82.4269	41.5307	133.4294
hsa-miR-4278	CUAGGGGGUUUGCCCUUG	1nuc	67.0979	-35.5055	13.5478	45.5853
hsa-miR-4279	CUCUCCUCCCGGCUUC	1nuc	87.8508	-34.8641	14.1099	26.7648
hsa-miR-4287	UCUCCCUUGAGGGCACUUU	5+nuc	-43.0702	199.6889	65.9882	82.0778
hsa-miR-4325	UUGCACUUGUCUCAGUGA	1nuc	70.8107	-30.4466	15.7465	103.6378
hsa-miR-4468	AGAGCAGAAGGAUGAGAU	1nuc	66.7852	-43.5545	16.4727	102.3949
hsa-miR-4484	AAAAGGCGGGAGAAGCCCCA	1nuc	92.7922	-51.5909	11.9581	69.6034
hsa-miR-4527	UGGUCUGCAAAGAGAUGACUGU	1nuc	103.6077	-39.4285	12.2780	67.3410
hsa-miR-4667-5p	ACUGGGGAGCAGAAGGAGAACC	1nuc	67.8202	-15.4990	9.0654	81.1779
hsa-miR-4690-5p	GAGCAGGCGAGGCUGGGCUGAA	1nuc	70.7700	-41.0713	11.0638	100.5287
hsa-miR-4713-5p	UUCUCCCACUACCAGGCUCCCA	5+nuc	-12.0522	95.9440	32.9144	82.3596
hsa-miR-4730	CUGGCGGAGCCCAUUCCAUGCCA	1nuc	118.4596	-43.2291	18.2180	91.1100
hsa-miR-4761-3p	GAGGGCAUGCGCACUUUGUCC	1nuc	85.0680	-23.8814	19.9690	76.0168
hsa-miR-4790-3p	UGAAUGGUAAAGCGAUGUCACA	1nuc	71.5904	-42.5343	32.1782	105.1903
hsa-miR-5197-5p	CAAUGGCACAAACUCAUUCUUGA	1nuc	70.9915	-38.8861	22.6965	16.5107
hsa-miR-5589-5p	GGCUGGGUGCUCUUGUGCAGU	1nuc	71.0230	-4.5214	17.4247	70.0484
hsa-miR-5681a	AGAAAGGGUGGCAAUACCUCUU	1nuc	114.2165	-33.0949	8.2312	76.4446
hsa-miR-5681b	AGGUAUUGCCACCCUUUCUAGU	1nuc	90.7399	-35.5083	12.6968	66.0084
hsa-miR-6081	AGGAGCAGUGCCGGCCAAGGCGCC	1nuc	81.6949	-52.8988	22.8626	57.2548
hsa-miR-6500-5p	AGGAGCUAUCCACUCCAGGUGUCC	1nuc	70.8775	-33.0112	19.1631	61.3489

Mature Name	Mature Sequence	Hit type	Mean 1 nucleolus % effect (primary screen)	Mean 5+ nucleoli % effect (primary screen)	Mean % viability (primary screen)	Mean nucleolar rRNA biogenesis % inhibition (secondary screen)
hsa-miR-6516-5p	UUUGCAGUAACAGGUGUGAGCA	1nuc	80.2993	-40.5673	23.8130	48.6421
hsa-miR-6753-5p	CACCAGGGCAGAGCAGGGCUGA	1nuc	68.0572	-39.9846	14.9927	91.1626
hsa-miR-6770-3p	CUGGCGGCUGUGUCUUCACAG	not a hit	110.1270	-40.2447	18.3507	-8.8181
hsa-miR-6809-5p	UGGCAAGGAAAGAAGAGGAUCA	1nuc	114.9752	-45.7449	9.1460	69.8322
hsa-miR-6867-3p	CUCUCCCUCUUUACCCACUAG	5+nuc	-34.9736	132.7331	61.8130	71.1090
hsa-miR-6877-3p	CAGCCUCUGCCCUUGGCCUCC	1nuc	69.0770	-44.6557	28.9503	114.1757
hsa-miR-6888-5p	AAGGAGAUGCUCAGGCAGAU	1nuc	86.2097	-53.9600	31.0220	50.5858

3.3.2. Novel microRNA negative regulators of ribosome biogenesis preferentially target transcripts encoding proteins in the nucleolus or involved in cell cycle regulation

We hypothesized that the microRNA mimic hits from the primary screen would be more likely to target genes whose product is nucleolar or is involved in processes affecting the nucleolus. We sought to combine bioinformatic databases containing microRNA:target RNA pairs, MCF10A RNA expression data, and catalogs of known nucleolar proteins to test this hypothesis. To investigate the hits' targets, we utilized TarBase 8, a catalog of over 670,000 experimentally-validated microRNA:target RNA interactions collected from the literature (282). We filtered TarBase 8 to only include 373,890 human microRNA:target interactions with a "down" regulatory relationship (**Figure 3-3A**). We assembled an MCF10A RNA expression dataset from 4 independent RNAseq experiments (BioProject accessions PRJNA290557, PRJNA384982, PRJNA530983, PRJNA647393) to determine which RNAs were expressed in this cell line. We discovered 20,345 genes bearing one or more transcripts with a normalized (zTPM) expression value greater than -3 in at least one RNAseq experiment, supporting expression for each of these genes (283). We used our RNA expression dataset to further filter out all target genes that were not expressed in MCF10A cells from TarBase 8, after which 1,074 microRNAs and 351,983 microRNA:target interactions remained (**Figure 3-3A**). Furthermore, we merged three nucleolar protein databases (284-286) to create a nucleolar protein reference metadatabase containing 3,490 unique nucleolar proteins (**Figure 3-3A**). Using these three datasets, we labeled all microRNA:target interactions potentially present in MCF10A cells that contain targets encoding nucleolar proteins.

Only 32/71 (45.1%) of the microRNA hits had at least one experimentally-validated target in TarBase 8 (**Figure 3-3A**); however, this figure is consistent with the fact that only 1,074/2,603 (41.3%) microRNAs in the primary screening library are represented in TarBase 8.

To investigate our hypothesis that hit microRNAs preferentially target transcripts encoding nucleolar proteins, we compared the 32 hit microRNAs to the remaining 1,042 non-hit microRNAs in our filtered, annotated TarBase 8 database (**Figure 3-3B**). We counted the number of transcripts coding nucleolar proteins that are targeted by each microRNA. We find that the median number of nucleolar targets for the hit microRNAs is 54, compared to the median value of 40 for 1,042 non-hit microRNAs, confirming enrichment and supporting our hypothesis (**Figure 3-3B**). We also identified 262 genes expressed in MCF10As that are targeted by at least 5 of the novel microRNA hits, representing the top 3.7% of genes most frequently targeted by the hits (**Figure 3-3A**). GO analysis of these genes revealed enrichment for encoded functions in cell cycle regulation, TP53 signaling, cellular proliferation, and for localization within the nucleolus (**Figure 3-3C**). Altogether, these data support the hypothesis that the novel microRNA hits preferentially target transcripts encoding proteins localized to the nucleolus or involved in cell cycle regulation.

A

TarBase 8

Database of experimentally-validated miRNA:mRNA interactions
1,075 miRs and 520,410 validated interactions in Homo sapiens

↓

Filter based on MCF10A gene expression

Removed non-expressed targets using MCF10A RNAseq expression data
Expressed genes have a zTPM > -3 for at least one of four datasets
1,074 miRs and 351,983 validated interactions with expressed targets

↓

Overlap with nucleolar metadatabase

Labeled nucleolar proteins using a compendium of nucleolar databases
3,490 nucleolar genes

↓

Quantify number of validated nucleolar targets for non-hit and hit miRNAs (Fig. 2B)

Identified 32/71 hit miRNAs with expressed, validated targets in TarBase 8
Discovered that, on average, hit miRNAs target more nucleolar factors than non-hits

↓

Investigate most frequently targeted mRNAs for functional enrichment (Fig. 2C)

Identified 262 mRNAs (top 3.7%), targeted by 5 or more miRNA hits
Found that frequent mRNA targets are enriched for functions in cell cycle and proliferation, and for localization within the nucleolus

B

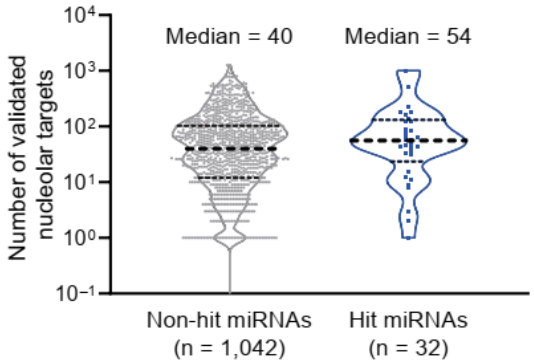

C

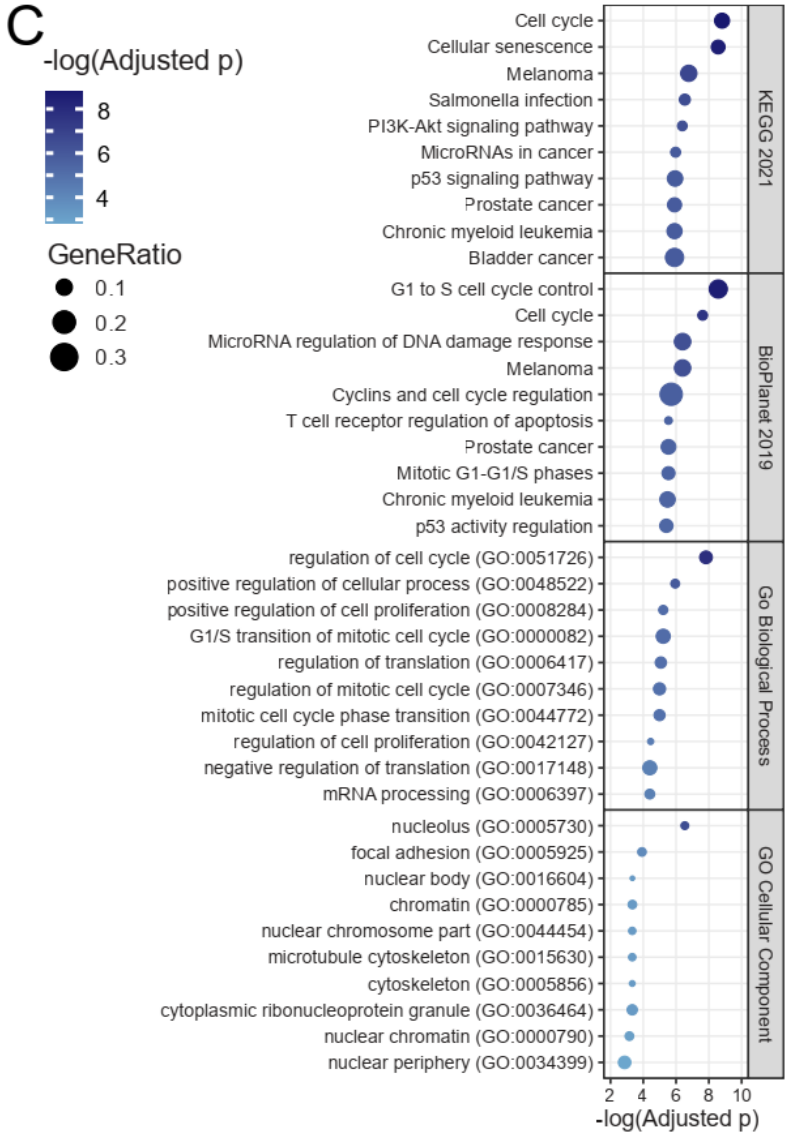

Figure 3-3. The novel microRNA hits preferentially target genes encoding proteins with nucleolar localization or with functions in cell cycle control.

(**A**) Bioinformatics workflow. TarBase 8 contained 520,410 validated microRNA:RNA target interactions across 1,075 mature human microRNAs. TarBase 8 was filtered for genes expressed in MCF10A cells, using a cutoff of more than -3 zTPM (normalized TPM), leaving 351,983 validated interactions. Targets were labeled for nucleolar localization based on our nucleolar proteome metadatabase containing 3,490 nucleolar proteins. MicroRNAs were grouped based on primary screen hit status, with 32/71 primary screen hits having one or more validated, expressed targets in MCF10A cells. The number of validated, expressed, nucleolar targets was calculated for hit and non-hit microRNAs. Conversely, the number of hit microRNAs targeting each gene was calculated, and all genes targeted by 5 or more hits (262, top 3.7%) were analyzed for enrichment.

(**B**) Log_{10}-scale plot indicating the number of validated nucleolar targets expressed in MCF10A cells for hit and non-hit microRNAs in TarBase 8. The median number of nucleolar targets per hit microRNA is 54, which is greater than the non-hit median of 40.

(**C**). Enrichment plots for 262 genes targeted by 5 or more of the microRNA hits. Plots indicate $-\log_{10}$(adjusted p) on the x-axis and marker color, and the gene ratio as the marker size. Enrichment analysis was conducted with Enrichr, and plots were made in R. Enrichment databases: Kyoto Encyclopedia of Genes and Genomes (KEGG) 2021; NCATS BioPlanet of Pathways 2019; Gene Ontology (GO) Biological Process 2018; GO Cellular Component 2018.

3.3.3. A majority of novel microRNA negative regulators of ribosome biogenesis strongly inhibit nucleolar rRNA biogenesis

To more directly determine the extent to which the novel microRNA hits can abrogate nucleolar function, we harnessed our laboratory's high-throughput assay for nucleolar rRNA biogenesis inhibition (287). Briefly, we previously optimized and miniaturized a nascent rRNA assay using 5-ethynyl uridine (5-EU) metabolic labeling to quantify changes in nucleolar 5-EU signal by co-staining for the nucleolar protein FBL/fibrillarin (**Figure 3-4A**). Our assay is sensitive to defects in pre-rRNA transcription, processing, or modification, which we collectively refer to as nucleolar rRNA biogenesis (287). We established an empirical cutoff for nucleolar rRNA biogenesis inhibition of 50%, as we discovered that depletion of almost all RB factors we tested during validation caused inhibition at or above this value (287). Furthermore, factors involved in both pre-rRNA transcription and processing typically caused the highest percent inhibition values, followed by factors only involved in pre-rRNA transcription, pre-rRNA processing, or pre-rRNA modification, respectively.

We conducted a secondary screen with five biological replicates for nucleolar rRNA biogenesis inhibition on all 71 microRNA mimics that passed primary screen validation as well as one additional microRNA mimic in the original library as a positive control, hsa-miR-34a-5p. We chose to include both hsa-miR-34a strands, as the *MIR34A* locus has been implicated in Wnt-mediated control of RB (288), and hsa-miR-34a-5p targets the *RMRP* RNA which is critical for pre-rRNA processing (289, 290). Following treatment, cells were fixed and stained for FBL and 5-EU incorporation

(**Figure 3-4B**), before image processing and quantification were completed with CellProfiler. As expected, MCF10A cells treated with siNT had robustly active nucleoli (**Figure 3-4B**, siNT panel), while positive control cells depleted of the RNAP1 subunit POLR1A (siPOLR1A) showed strongly decreased nucleolar rRNA biogenesis (**Figure 3-4B**, siPOLR1A panel) (287). Acute treatment with BMH-21, a known small molecular inhibitor of RNAP1 (182, 205), at 1 μM for 1 h also eliminated nucleolar 5-EU signal as expected (287) (**Figure 3-4B**, siNT + BMH panel). For the secondary screen replicates (n = 5), the median Z' factor was 0.27 and the median S/B was 1.88, indicating acceptable separation of controls.

Remarkably, the secondary screen indicated that 51/72 (70.8%) microRNA mimic hits assayed caused at least a 50% inhibition of nucleolar rRNA biogenesis (**Figure 3-4C, Table 3-1**). Notably, all eight 5+ hits tested strongly inhibited nucleolar rRNA biogenesis, with a mean percent inhibition of 92.6%. These data support the hypothesis that most microRNA hits from the primary screen significantly disrupt nucleolar rRNA biogenesis, the main function of the nucleolus.

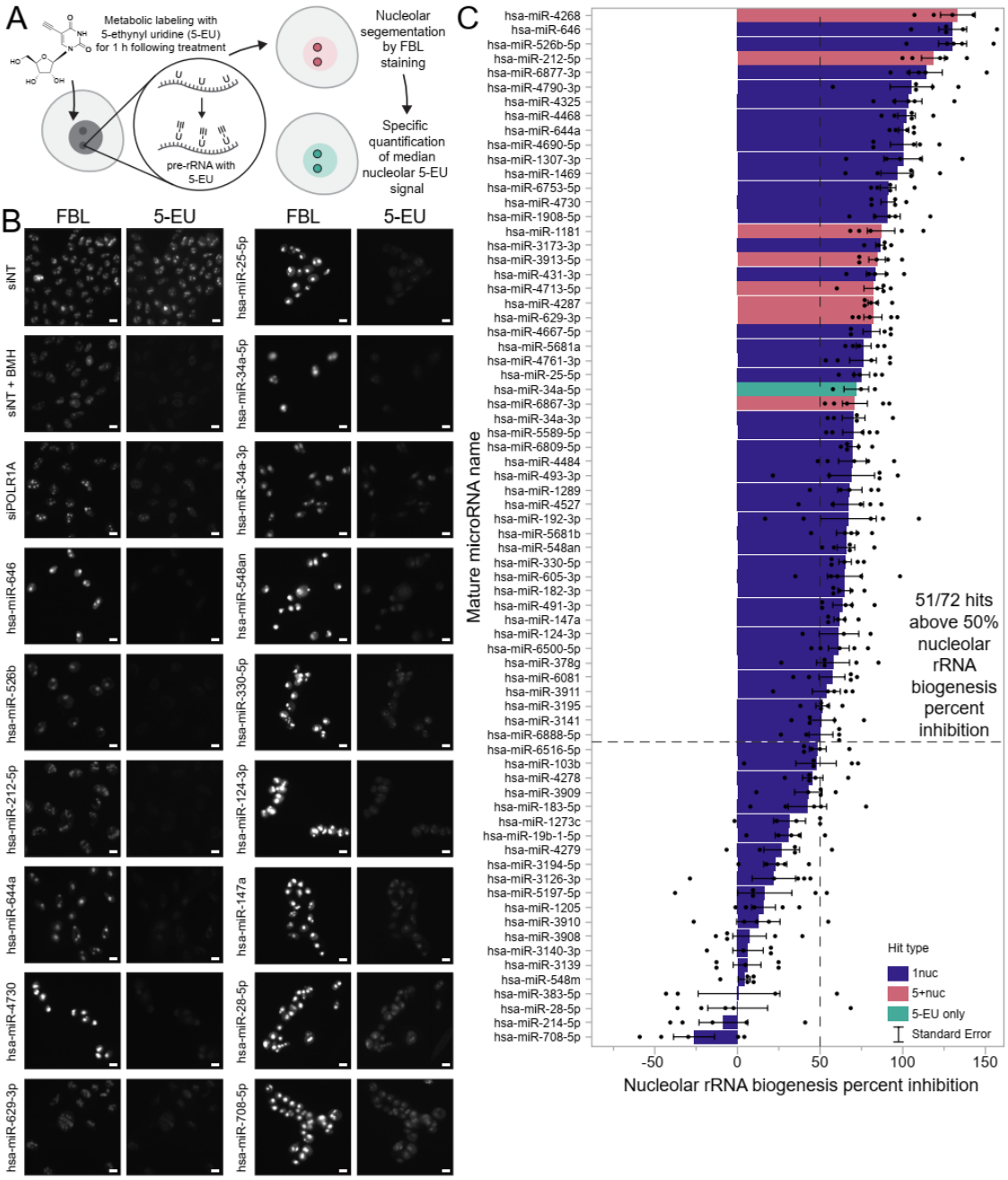

Figure 3-4. A secondary screen reveals 51/72 hits strongly inhibit nucleolar rRNA biogenesis.

(**A**). Schematic for the nucleolar rRNA biogenesis inhibition assay (287). Following 72 h of RNAi transfection, MCF10A cells were labeled for 1 h with 1 mM 5-ethynyl uridine (5-EU). Cells were fixed and immunostained for the nucleolar protein FBL and for 5-EU, then imaged. CellProfiler was used to segment nucleoli and calculate the median 5-EU intensity for all nucleoli per well, enabling calculation of the nucleolar rRNA biogenesis percent inhibition.

(**B**) Representative images of control- and hit-treated MCF10A cells following 5-EU incorporation. FBL immunostaining and 5-EU click labeling are shown as separate channels. Scale bars, 10 μm. siNT is the non-targeting negative control siRNA. siNT + BMH is siNT-transfected cells treated with 1 μM BMH-21 for 1 h before and during 5-EU incorporation. siPOLR1A is the POLR1A (RPA194) knockdown positive control.

(**C**). Nucleolar rRNA biogenesis percent inhibition values for 72 microRNA mimic hits. A total of 51/72 hits caused at least 50% inhibition of nucleolar rRNA biogenesis, surpassing the assay's empirical cutoff (287). siNT negative control is set to 0% inhibition, and siPOLR1A positive control is set to 100% inhibition. Hits are colored according to their primary screen phenotype; hsa-miR-34a-5p was not a primary screen hit but was included as described in the text. Mean ± SEM are shown alongside individual data points. Data were graphed in JMP.

3.3.4. A diverse subset of 15 microRNA hits was chosen for mechanistic follow-up

We chose a subset of 15 microRNA hits to further study for their specific effects on crucial RB subprocesses, including pre-rRNA transcription, pre-rRNA processing, and global protein synthesis. We prioritized selecting a diverse group of microRNAs that were representative of differences in key variables observed in the screening campaign, but also were considered to be authentic, valid microRNAs by sequencing and evolutionary analyses. To this end, we conducted principal component analysis to visualize screening and bioinformatic data in a dimension-reduced format (**Figure 3-5A-B**). A major cluster containing most one-nucleolus hits with relatively few validated nucleolar targets was apparent, accompanied by outliers that either were 5+ nucleoli hits or had a high number of validated nucleolar targets (**Figure 3-5A**). To minimize the potential for studying biological false positives, we also classified hits according to their evolutionary conservation, as cataloged by MirGeneDB (291), or their sequencing read quality consistency across 28,866 small RNAseq experiments (292). The MirGeneDB project, led by Fromm and collaborators, has thoroughly cataloged the microRNA gene sets in 75 species to-date using phylogenetic analysis and applying criteria ensuring conservation of (pre-)microRNA sequence and secondary structure features to avoid false positives (293, 294). MirGeneDB also traces microRNA orthologs to their point of evolutionary origin, emphasized by consistent gene/family nomenclature across clades, which has enabled reconstruction of previously-overlooked false negative microRNA genes (291, 294, 295). The results of MirGeneDB strongly support an upper bound on authentic, conserved human microRNA genes around 550 (291, 293). The latter

sequencing read quality analysis accounted for the compliance of small RNAseq reads with Dicer processing rules, particularly the minimal variability of microRNA sequences at the 5' terminus, and for coverage across the microRNA precursor transcriptome annotation.

For further mechanistic assay validation, we combined our PCA analysis, microRNA conservation data, and manual literature curation to select 12 one-nucleolus hits, two 5+ nucleoli hits, and hsa-miR-34a-5p, which was not a hit in the primary screen but did significantly inhibit nucleolar rRNA biogenesis (**Figure 3-5C**). The median nucleolar rRNA biogenesis percent inhibition of these hits was 72.2% with a range of -26.3% to 130.3%. Of these hits, 10 were recorded in MirGeneDB and were classified as "High Confidence" microRNAs annotated in miRBase (292), while 5 were not in MirGeneDB and were classified as "Low Confidence" microRNAs in miRBase. Additionally, 14/15 hits passed a tripartite filter for sequencing read quality consistency (292). Two microRNA hits from the MirGeneDB MIR-28 family (291), hsa-miR-28-5p and hsa-miR-708-5p, were included in the subset.

A

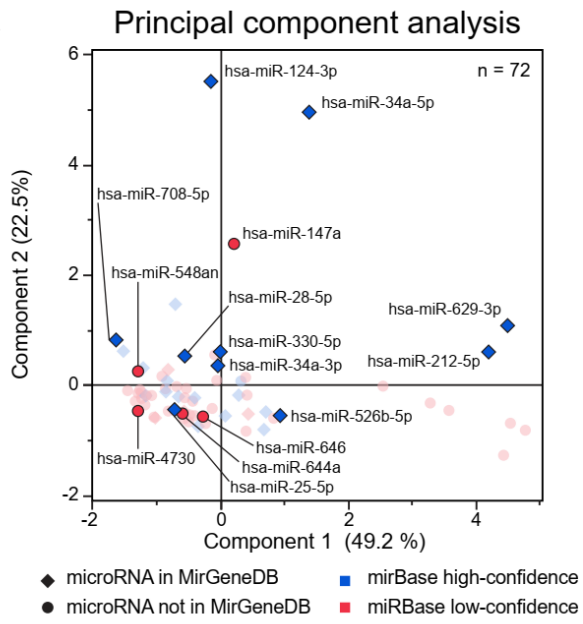

B

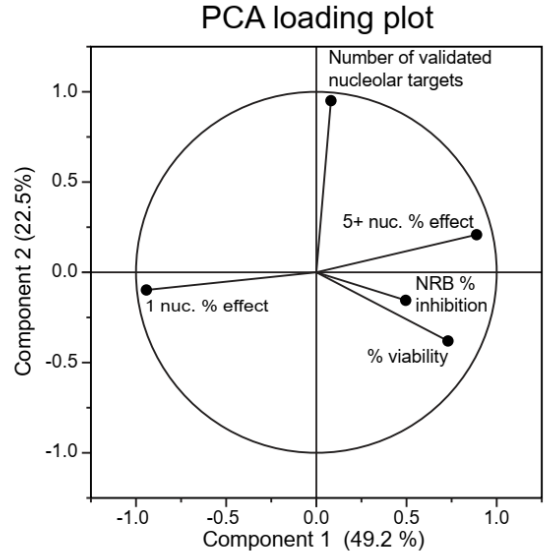

C

Mature microRNA name	miRBase accession
hsa-miR-25-5p	MIMAT0004498
hsa-miR-28-5p	MIMAT0000085
hsa-miR-34a-5p	MIMAT0004557
hsa-miR-34a-3p	MIMAT0000255
hsa-miR-124-3p	MIMAT0000422
hsa-miR-147a	MIMAT0000251
hsa-miR-212-5p	MIMAT0022695
hsa-miR-330-5p	MIMAT0004693
hsa-miR-526b-5p	MIMAT0002835
hsa-miR-548an	MIMAT0019079
hsa-miR-629-3p	MIMAT0003298
hsa-miR-644a	MIMAT0003314
hsa-miR-646	MIMAT0003316
hsa-miR-708-5p	MIMAT0004926
hsa-miR-4730	MIMAT0019852

Figure 3-5. A subset of 15 microRNA hits were rigorously selected for additional mechanistic validation.

(**A**) Principal component analysis (PCA) of 72 hits. The 15 selected subset hits are indicated with their mature microRNA name and are highlighted on the plot. Membership in MirGeneDB (291) or classification as high-confidence or low-confidence miRBase (292) is labeled with each hit's marker shape or color, respectively. Five variables were used for PCA including one-nucleolus and 5+ nucleoli percent effect, percent viability, nucleolar rRNA biogenesis (NRB) percent inhibition, and number of validated nucleolar targets for each hit in TarBase 8. Percentages in axis labels denote the proportion of variance explained by each PCA Component.

(**B**) Loading plot describing contribution of 5 quantitative variables to PCA Components 1 and 2 from above. In other words, this plot shows how 5 variables pertaining to the hits are represented by PCA Component 1 and 2 following dimension reduction. Percentages in axis labels denote the proportion of variance explained by each PCA Component.

(**C**) Table of 15 mature microRNA hits selected for further validation.

3.3.5. A subset of microRNA hits dysregulates pre-rRNA transcript levels and rDNA promoter activity

Since many microRNA hits caused strong inhibition of nucleolar rRNA biogenesis in the secondary 5-EU screen, we hypothesized that these hits might dysregulate pre-rRNA transcription directly by targeting the 47S primary transcript. This hypothesis predicts that microRNAs with few predicted 47S binding sites would cause low inhibition of nucleolar rRNA biogenesis, while microRNAs with many predicted 47S binding sites would strongly inhibit nucleolar rRNA biogenesis to levels consistent with interruption of pre-rRNA transcription (over 80% inhibition) (287). We tested this hypothesis by comparing the number of predicted canonical seed binding sites on the 47S pre-rRNA transcript (transcript NR_046235.3) for each of the 72 hits with its corresponding mean nucleolar rRNA biogenesis percent inhibition (**Figure 3-6A**). Surprisingly, we did not observe a strong correlation, with several hits having a high nucleolar rRNA biogenesis percent inhibition and zero predicted 47S binding sites. This result argues that the primary mechanism by which the microRNA hits inhibit RB is not by directly binding the primary pre-rRNA transcript.

To experimentally test the 15 subset hits' effects on RNAP1 transcription, we measured the steady-state levels of the 45S pre-rRNA transcript as a proxy for transcription after treatment with the subset of microRNA mimics or control siRNAs by RT-qPCR. (**Figure 3-6B**). While depletion of the transcription (t)UTP NOL11 led to a stark decrease in 45S levels versus siNT as expected (85), none of the microRNA hits statistically-significantly altered 45S levels (**Figure 3-6C**). However, 4 microRNA hits

(hsa-miR-34a-5p, hsa-miR-212-5p, hsa-miR-330-5p, hsa-miR-526b-5p) caused a mean decrease in 45S levels of at least 50% [less than -1 $\log_2$(45S transcript levels)]. However, considerable experimental noise with this assay may mask the true effect of these microRNA mimics on altering 45S transcript levels.

To further interrogate pre-rRNA transcription, we conducted a dual-luciferase reporter assay for RNAP1 promoter activity (296, 297) after microRNA mimic expression. The assay uses a firefly luciferase reporter under the control of the rDNA promoter and a *Renilla* luciferase reporter constitutively driven by a CMV promoter to normalize for transfection efficiency (**Figure 3-6D**). Strikingly, we found that treatment with the 15 microRNA hits had diverse effects on RNAP1 promoter activity: 3 microRNA mimics (hsa-miR-147a, hsa-miR-526b, hsa-miR-548an) caused a decrease in RNAP1 promoter activity; 5 microRNA mimics (hsa-miR-34a-5p, hsa-miR-124-3p, hsa-miR-330-5p, hsa-miR-629-3p, hsa-miR-646) caused an increase in RNAP1 promoter activity; and the other 7 microRNA mimics did not cause a significant effect (**Figure 3-6E**). Compared to mock and siNT negative controls, siNT treatment followed by 1 μM BMH-21 dosage significantly decreased RNAP1 promoter activity, while NOL11 depletion caused a modest but statistically-insignificant defect (**Figure 3-6E**). Conversely, depletion of the cytoplasmic RP RPL4 had no effect on RNAP1 promoter activity (**Figure 3-6E**). These results indicate that the microRNA hits do not reliably affect pre-rRNA transcription as measured by 5-EU incorporation or 45S transcript levels, while they may upregulate, downregulate, or have no effect on RNAP1 promoter

activity. Future experiments may be required to better understand the interplay between microRNA activity and pre-rRNA transcription.

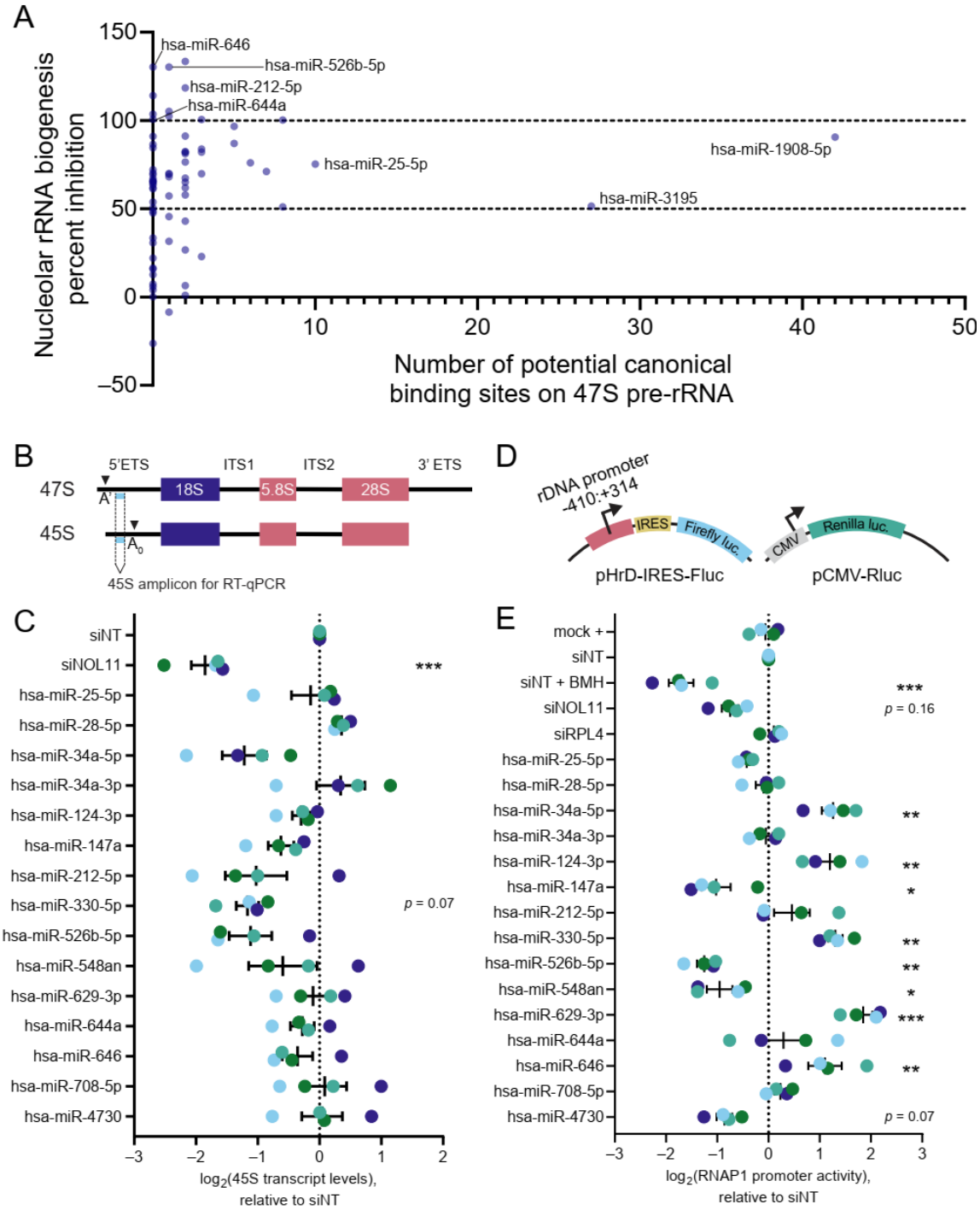

Figure 3-6. MicroRNA hits do not reliably alter RNAP1 transcription.

(**A**). Scatter plot comparing the number of potential canonical (seed) binding sites on the 47S pre-rRNA transcript to the nucleolar rRNA biogenesis percent inhibition for the 72 microRNA hits, as predicted by BLAST. A number of hits have close to 0 predicted canonical 47S binding sites but strong nucleolar rRNA biogenesis percent inhibition. Select hits are labeled, and labels for percent inhibition are shown at 50% inhibition

(empirical assay cutoff, consistent with pre-rRNA modification defect) and 100% inhibition (siPOLR1A positive control, consistent with pre-rRNA transcription defect) (287). The data were graphed in GraphPad Prism 8.

(**B**). Schematic indicating the amplicon (light blue) used for 45S pre-rRNA RT-qPCR, located between the A' and A_0 cleavage sites in the 5' ETS of the primary rRNA transcript. The location of the mature 18S, 5.8S and 28S rRNAs are indicated.

(**C**). RT-qPCR analysis of levels of the 45S pre-rRNA precursor transcript as a proxy for RNAP1 transcription. The monitored amplicon in the 5' ETS is described in (**B**). The mean ± SEM are shown alongside individual data points, colored by replicate (4 replicates). The data were normalized to 7SL RNA abundance as a loading control, then to siNT for comparison using the $\Delta\Delta C_T$ method. The data were analyzed by ordinary one-way ANOVA with multiple comparisons against siNT and Holm-Šídák correction in GraphPad Prism 8. *, $p < 0.05$; **, $p < 0.01$; ***, $p < 0.001$.

(**D**). Schematic for the dual-luciferase reporter assay for RNAP1 promoter activity (84, 297). MCF10A cells were co-transfected with pHrD-IRES-Fluc, in which a 724 bp fragment of the rDNA promoter and early 5' ETS drive firefly luciferase production, and pCMV-Rluc, in which the constitutive CMV promoter drives *Renilla* luciferase production.

(**E**). Dual-luciferase reporter assay for RNAP1 promoter activity. The mean ± SEM are shown alongside individual data points, colored by replicate (4 replicates). The data were analyzed by ordinary one-way ANOVA with multiple comparisons against siNT and Holm-Šídák correction in GraphPad Prism 8. *, $p < 0.05$; **, $p < 0.01$; ***, $p < 0.001$.

3.3.6. A subset of microRNA hits dysregulates maturation of the 30S pre-rRNA precursor

Given the inconclusive ability of the microRNA hit subset to consistently regulate pre-rRNA transcription, we also hypothesized that these hits could affect pre-rRNA processing, another component of nucleolar rRNA biogenesis (287). We carried out northern blotting for all 15 microRNA hits in the subset, probing for pre-rRNA processing intermediate molecules containing either ITS1 (P3 probe) or ITS2 (P4) probe (**Figure 3-7A**). Surprisingly, ITS1 blots broadly demonstrated that most microRNA hits dysregulated maturation of the 30S pre-rRNA precursor (**Figure 3-7B-C**). Ratio Analysis of Multiple Precursors calculations [RAMP, (298)] indicated 3 major clusters of pre-rRNA processing defects caused by the microRNA hits, namely, no change (n.c.), a 30S down cluster, and a 30S up/21S down cluster (**Figure 3-7C-D**). The last cluster contained two subclusters, one with hits causing a moderate 21S processing defect ("30S↑, 21S↓" in **Figure 3-7D**) and another with hsa-miR-28-5p and hsa-miR-708-5p which caused a severe 21S processing defect ("30S↑, 21S↓↓" in **Figure 3-7D**). Changes in levels of the primary pre-rRNA transcript ("47S") by northern blotting were consistent with changes observed by 45S RT-qPCR (**Figure 3-8**).

We also examined the extent to which ITS2 processing was dysregulated by the subset of microRNA hits (**Figure 3-9A**). We discovered that hsa-miR-708-5p and the two 5+ nucleoli hits, hsa-miR-212-5p and hsa-miR-629-3p, each caused a mild increase in 32S levels and a mild decrease in 12S levels; additionally, hsa-miR-330-5p mildly attenuated levels of the 32S and 12S precursors (**Figure 3-9B-C**). The remaining microRNA hits did not cause a significant change in ITS2-containing precursor levels.

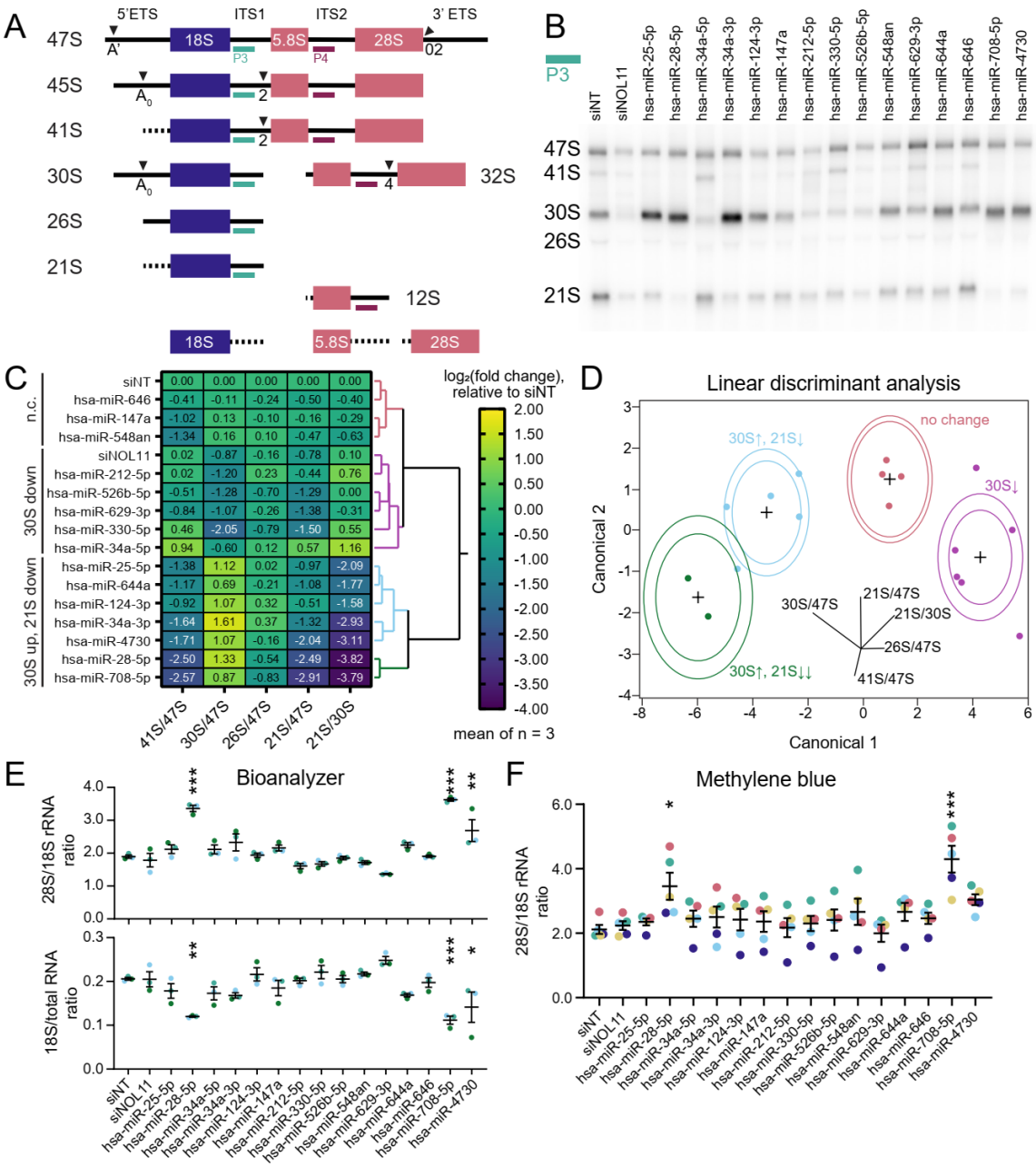

Figure 3-7. Most subset microRNA hits dysregulate pre-18S pre-rRNA processing.

(**A**) Simplified diagram of human pre-rRNA processing intermediates. Mature 18S, 5.8S, and 28S rRNA regions are shown as blue (pre-40S) or red (pre-60S) rectangles. Intermediate names are indicated on the left, and transcribed spacers (solid black lines) are labeled at the top. Cleavage sites are labeled with their name and represented with triangles. Dotted lines signify transcribed spacer regions digested by exonucleases. Northern blot probes P3 (teal, ITS1) or P4 (dark red, ITS2) are shown at each pre-rRNA intermediate that they bind.

(**B**) Representative ITS1 (probe P3) northern blot of 3 μg of total RNA isolated from

control- or hit-treated (as indicated) MCF10A cells. Pre-rRNA processing intermediates are labeled on the left. Images were quantified using Bio-Rad Image Lab. siNT is the non-targeting negative control and siNOL11 is the positive control.

(**C**) Clustered heatmap showing $\log_2$-transformed Ratio Analysis of Multiple Precursor [RAMP (298)] calculations for microRNA hits, normalized to siNT negative control. Values represent mean $\log_2$-scale RAMP ratio for $n = 3$. Clusters: no change (n.c., red); 30S down (magenta); 30S up, 21S down (mild defect, blue and severe defect, green). RAMP ratios were calculated in Microsoft Excel. Four clusters were assigned using hierarchical Ward clustering in JMP, and data were graphed in GraphPad Prism 8.

(**D**) Linear discriminant analysis (LDA) of four 30S pre-rRNA processing defect clusters from (**C**) above. Cluster colors are the same as in (**C**). Canonical component biplot rays are shown in the graph. Ellipses represent 50% (outer) and 95% (inner) confidence levels. Data were graphed in JMP.

(**E**) Bioanalyzer analysis for 1 μg of total RNA isolated from control- or hit-treated MCF10A cells. Top, the 28S/18S mature rRNA ratio; bottom, 18S mature rRNA/total RNA ratio. Mean ± SEM are shown alongside individual data points, colored by replicate. Data were graphed and analyzed by ordinary one-way ANOVA with multiple comparisons against siNT (non-targeting negative control) and Holm-Šídák correction in GraphPad Prism 8. *, $p < 0.05$; **, $p < 0.01$; ***, $p < 0.001$.

(**F**) Methylene blue (MB) analysis of the 28S/18S mature rRNA ratio. Northern blots from (**B-C**) were stained with MB, imaged, and quantified using Bio-Rad Image Lab. Mean ± SEM are shown alongside individual data points, colored by replicate. Data were graphed and analyzed by ordinary one-way ANOVA with multiple comparisons against siNT (non-targeting negative control) and Holm-Šídák correction in GraphPad Prism 8. *, $p < 0.05$; **, $p < 0.01$; ***, $p < 0.001$.

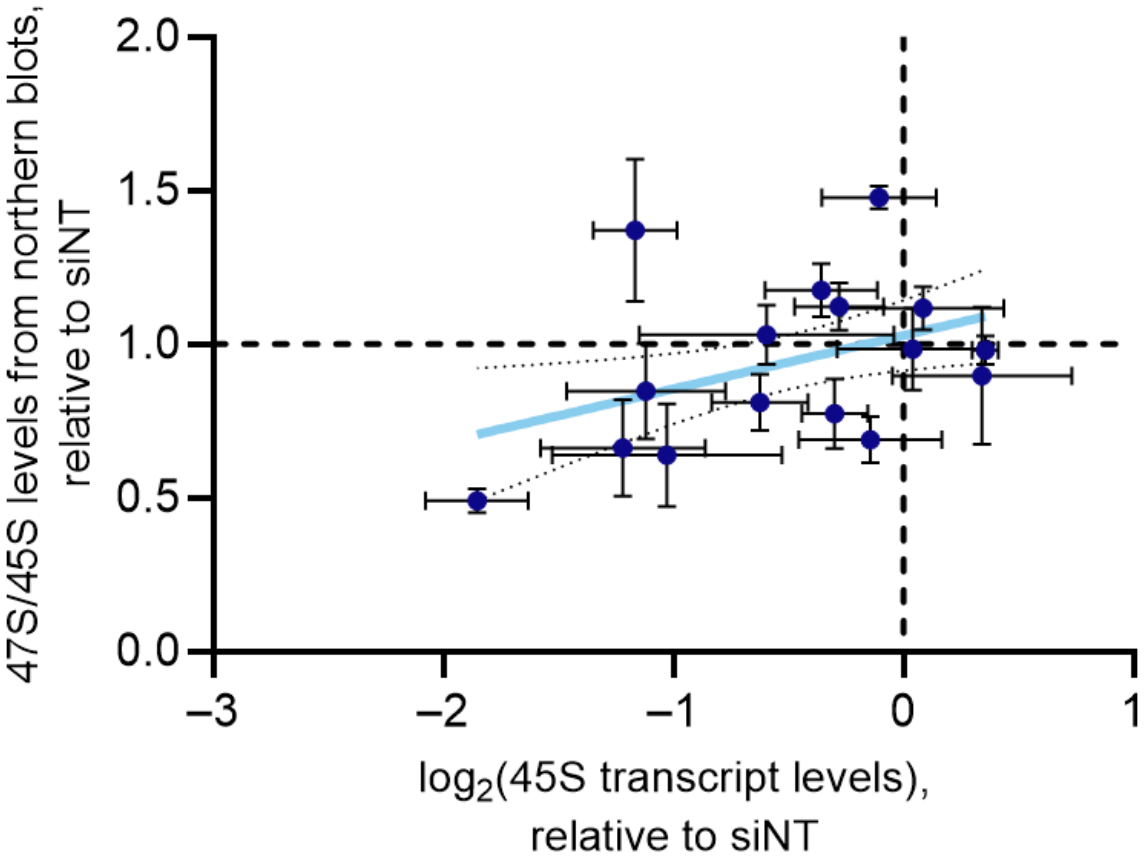

Figure 3-8. Primary pre-rRNA precursor levels are consistent between 45S qPCR and northern blotting techniques.

Data measuring pre-rRNA transcription via RT-qPCR (**Figure 3-6C**) or via northern blot (**Figure 3-7B-C**) are plotted on the x- or y-axis, respectively. Data points represent the mean ± SEM with 4 replicates for RT-qPCR and 3 replicates for northern blots. Line-of-best-fit is shown in light blue with 95% confidence intervals indicated by dotted black curves. Plotting and regression were conducted in GraphPad Prism 8.

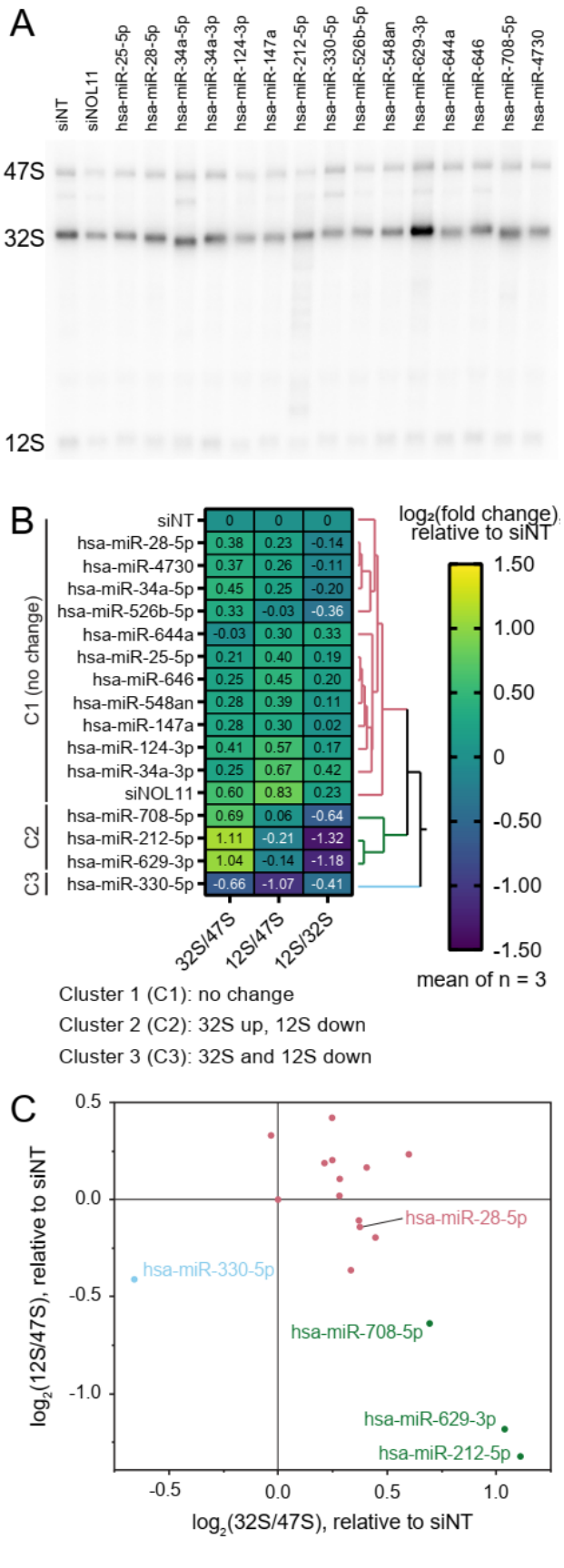
A
siNT
siNOL11
hsa-miR-25-5p
hsa-miR-28-5p
hsa-miR-34a-5p
hsa-miR-34a-3p
hsa-miR-124-3p
hsa-miR-147a
hsa-miR-212-5p
hsa-miR-330-5p
hsa-miR-526b-5p
hsa-miR-548an
hsa-miR-629-3p
hsa-miR-644a
hsa-miR-646
hsa-miR-708-5p
hsa-miR-4730
47S
32S
12S
B
log2(fold change) relative to siNT
1.50
1.00
0.50
0
-0.50
-1.00
-1.50
mean of n = 3
C1 (no change)
C2
C3
siNT 0 0 0
hsa-miR-28-5p 0.38 0.23 -0.14
hsa-miR-4730 0.37 0.26 -0.11
hsa-miR-34a-5p 0.45 0.25 -0.20
hsa-miR-526b-5p 0.33 -0.03 -0.36
hsa-miR-644a -0.03 0.30 0.33
hsa-miR-25-5p 0.21 0.40 0.19
hsa-miR-646 0.25 0.45 0.20
hsa-miR-548an 0.28 0.39 0.11
hsa-miR-147a 0.28 0.30 0.02
hsa-miR-124-3p 0.41 0.57 0.17
hsa-miR-34a-3p 0.25 0.67 0.42
siNOL11 0.60 0.83 0.23
hsa-miR-708-5p 0.69 0.06 -0.64
hsa-miR-212-5p 1.11 -0.21 -1.32
hsa-miR-629-3p 1.04 -0.14 -1.18
hsa-miR-330-5p -0.66 -1.07 -0.41
32S/47S
12S/47S
12S/32S
Cluster 1 (C1): no change
Cluster 2 (C2): 32S up, 12S down
Cluster 3 (C3): 32S and 12S down
C
log2(12S/47S), relative to siNT
log2(32S/47S), relative to siNT
0.5
0.0
-0.5
-1.0
-0.5
0.0
0.5
1.0
hsa-miR-28-5p
hsa-miR-330-5p
hsa-miR-708-5p
hsa-miR-629-3p
hsa-miR-212-5p

Figure 3-9. Four microRNA hits slightly interfere with ITS2 processing.

(**A**). Representative ITS2 (probe P4) northern blot of 3 μg of total RNA isolated from control- or hit-treated MCF10A cells. The pre-rRNA processing intermediates are labeled on the left according to the schematic in Figure 5A. The images were quantified using Bio-Rad Image Lab.

(**B**). Clustered heatmap showing $\log_2$-transformed Ratio Analysis of Multiple Precursor [RAMP, (298)] calculations for microRNA mimic hits, normalized to si non-targeting (siNT) negative control. Values represent mean $\log_2$-scale RAMP ratio for $n = 3$ replicates. Clusters: no change (C1, red); 32S up, 12S down (C2, green); both 32S and 12S down (C3, blue). The RAMP ratios were calculated in Microsoft Excel. Three clusters were assigned using hierarchical Ward clustering in JMP, and data were graphed in GraphPad Prism 8.

(**C**). Log_2-scale 32S/47S and 12S/47S pre-rRNA precursor RAMP ratios after subset microRNA mimic treatment, relative to a non-targeting (siNT). Cluster colors the same as in (**B**). The data were graphed in GraphPad Prism 8, with select hits labeled.

We conducted BioAnalyzer electrophoresis to define the ability of the microRNA hits to modulate steady-state levels of mature 28S and 18S rRNAs (**Figure 3-7A**). BioAnalyzer quantification revealed an increase in the mature 28S/18S rRNA ratios for 3 microRNA hits: hsa-miR-28-5p, hsa-miR-708-5p, and hsa-miR-4730 (**Figure 3-7E**), portending a defect in 18S maturation. Indeed, calculation of the ratio of mature 18S rRNA to total RNA from the electropherogram data showed stark decreases in 18S levels following treatment with any of these three microRNAs (**Figure 3-7E**). Methylene blue staining corroborated the increase in 28S/18S ratio for hsa-miR-28-5p and hsa-miR-708-5p (**Figure 3-7F**), although this technique has lower precision than BioAnalyzer quantification. All three microRNAs with deficient mature 18S rRNA levels were in the severe 21S processing defect cluster, consistent with the pre-rRNA processing pathway (**Figure 3-7A**), and hsa-miR-4730 clustered at the interface between the moderate and severe 30S defect subclusters (**Figure 3-7D**). The other 12 microRNA mimic hits did not cause a significant change in mature rRNA levels. Together these results reveal, for the first time, the dysregulatory potential of microRNAs to interfere with major steps in pre-rRNA processing.

3.3.7. A subset of microRNA hits decreases global translation

We also hypothesized that overexpression of the microRNA hits might repress global translation. We used the SUnSET puromycin labeling assay (299) to quantify the extent to which each microRNA hit could inhibit global protein synthesis. Following a 72 h transfection period, MCF10A cells were metabolically labeled for 1 h with 1 μM puromycin, which is incorporated into nascent peptides. Total puromycin was measured as a proxy for global translation rate by immunoblotting total protein with an α-puromycin primary antibody. Treatment with 14/15 (93.3%) of the microRNA hits significantly decreased global protein synthesis relative to the negative non-targeting siRNA control (**Figure 3-10A-B**). A similar decrease was observed for the positive control, an siRNA depleting the 60S subunit member RPL4 (**Figure 3-10A-B**). In total, these results indicate that nearly all of the subset microRNA hits inhibit global protein synthesis, the ultimate objective of ribosome biogenesis.

3.3.8. A subset of microRNA hits alters levels of TP53 or CDKN1A (p21)

Since treatment with many microRNA mimic hits significantly inhibited nucleolar rRNA biogenesis and normal pre-rRNA processing, we hypothesized that treatment with the hits may activate the nucleolar stress response via TP53 stabilization and *CDKN1A* (*p21*) upregulation. The nucleolar stress response is induced following disruption of RB subprocesses or the normal tripartite nucleolar structure (71, 72, 300). Mechanistically, 5S RNP proteins including the 60S RPs RPL5 or RPL11 can bind and sequester MDM2, the E3 ubiquitin ligase targeting TP53 for constitutive degradation.

Derepression of TP53 then upregulates *CDKN1A* (*p21*) expression, which acts in concert with TP53 to arrest the cell cycle and initiate apoptosis. We tested the first part of our hypothesis by immunoblotting for steady-state TP53 levels to assess how microRNA hit overexpression affected nucleolar stress response induction (**Figure 3-10C**). Six of the 15 microRNA hits stabilized TP53 levels, while surprisingly, hsa-miR-629-3p significantly decreased steady-state levels of TP53 (**Figure 3-10C-D**). The remaining 8/15 microRNAs did not cause significant dysregulation of TP53 levels. Depletion of either the tUTP factor NOL11 or the 60S RP RPL4 strongly stabilized TP53 as expected (**Figure 3-10C-D**).

We also investigated how the microRNA hits affected *CDKN1A* (p21) mRNA transcript levels by RT-qPCR. Again, depletion of the positive control NOL11 robustly increased *CDKN1A* levels as compared to siNT, while 11/15 microRNA mimics also upregulated *CDKN1A* to a statistically-significant degree (**Figure 3-10E**). These data largely concur, although there are two notable discrepancies. First, hsa-miR-28-5p and hsa-miR-708-5p caused strong TP53 stabilization yet did not elicit measurable *CDKN1A* upregulation, which we address in the next section. Second, hsa-miR-629-3p strongly decreased steady-state TP53 levels while simultaneously inducing *CDKN1A*. These results indicate that the hits have diverse abilities to induce the nucleolar stress response for cell cycle interruption via upregulation of TP53 or *CDKN1A*.

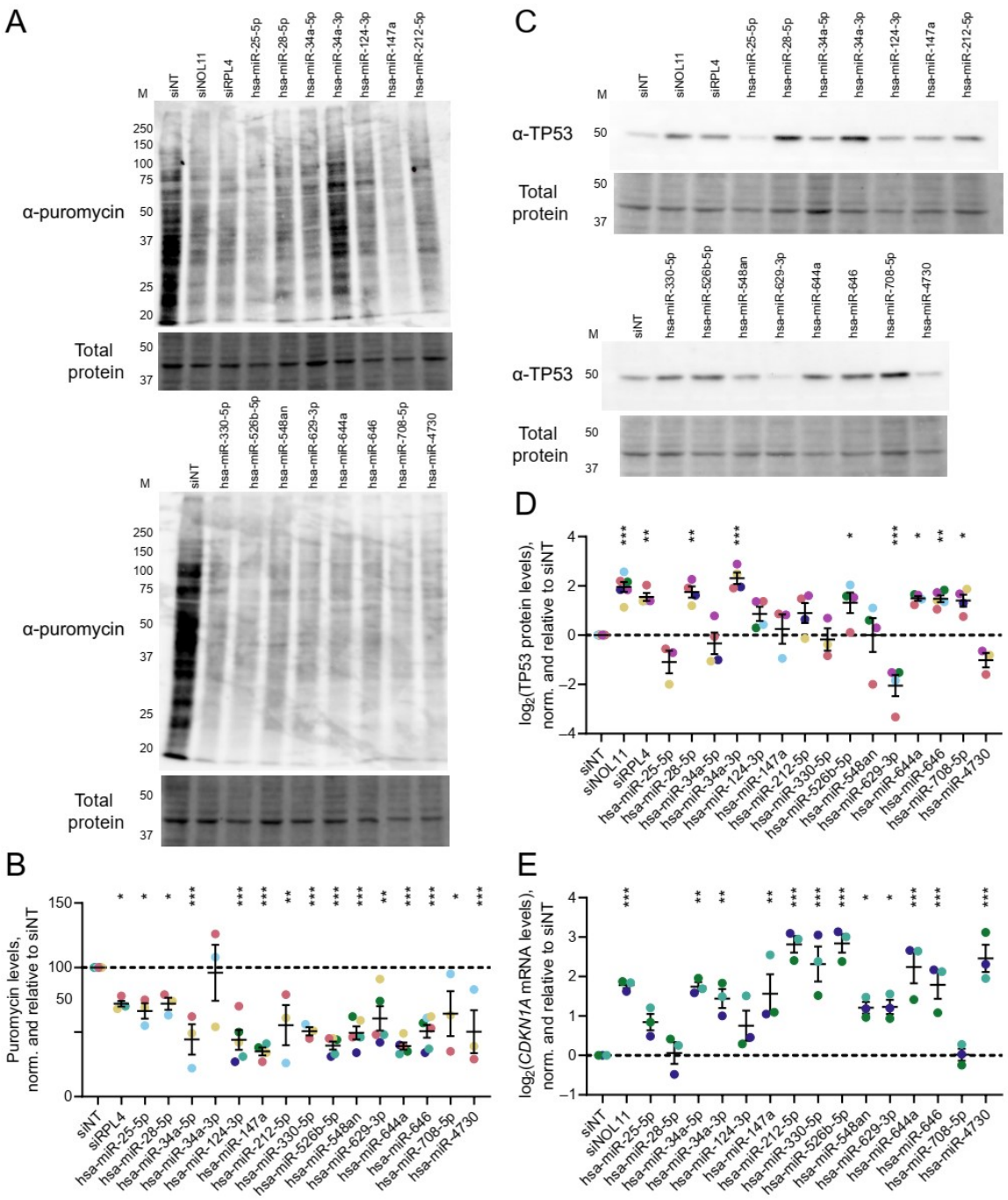

Figure 3-10. MicroRNA hits inhibit global protein synthesis and dysregulate levels of the cell cycle regulators TP53 and *CDKN1A*.

(**A**). Representative examples of the SUnSET puromycin incorporation assay (83, 299) immunoblots of total protein isolated from control- or hit-treated MCF10A cells. α-puromycin is an immunoblot for puromycin incorporation as a proxy for global protein synthesis. Total protein is the trichloroethanol total protein stain loading control. The images were quantified with Bio-Rad Image Lab.

(**B**). Quantification of global protein synthesis levels from (**A**) above. Mean ± SEM are shown alongside individual data points, colored by replicate (at least 3 replicates per condition, with all replicates shown in the graph). The data were normalized to siNT, then graphed and analyzed by ordinary one-way ANOVA with multiple comparisons against siNT and Holm-Šídák correction in GraphPad Prism 8. *, $p < 0.05$; **, $p < 0.01$; ***, $p < 0.001$.

(**C**). Representative examples of TP53 immunoblots of total protein isolated from control- or hit-treated MCF10A cells. α-TP53 is the blot for TP53. Total protein is the trichloroethanol total protein stain loading control.

(**D**). Log_2-scale quantification of TP53 protein levels from (**C**) above. Mean ± SEM are shown alongside individual data points, colored by replicate (at least 3 replicates per condition, with all replicates shown in the graph). Data were normalized to siNT, then graphed and analyzed by ordinary one-way ANOVA with multiple comparisons against siNT and Holm-Šídák correction in GraphPad Prism 8. *, $p < 0.05$; **, $p < 0.01$; ***, $p < 0.001$.

(**E**). Log_2-scale RT-qPCR analysis of *CDKN1A* (*p21*) mRNA levels from control- or hit-treated MCF10A cells. The data from 3 biological replicates were normalized to the 7SL RNA abundance as a loading control, then to siNT for comparison using the $\Delta\Delta C_T$ method. Mean ± SEM are shown alongside individual data points, colored by replicate. Data were analyzed by ordinary one-way ANOVA with multiple comparisons against siNT and Holm-Šídák correction in GraphPad Prism 8. *, $p < 0.05$; **, $p < 0.01$; ***, $p < 0.001$.

3.3.9. Two microRNA hits, hsa-miR-28-5p and hsa-miR-708-5p, are family members that each downregulate RPS28 and the oncogene SPRR3

During our mechanistic studies of the 15 microRNA hits, we hypothesized that the two included MIR-28 family members, hsa-miR-28-5p and hsa-miR-708-5p, would elicit similar results from each assay because of their identical seed sequences. These two microRNAs share the same 7 nt seed sequence (AGGAGCU) (**Figure 3-11A**) (291). Indeed, we observed similar cellular RB phenotypes following hsa-miR-28-5p or hsa-miR-708-5p treatment, including the same aberrant pre-rRNA processing signature and stark decreases in both mature 18S rRNA levels and global protein synthesis (**Figure 3-11A**). To uncover potential mechanisms for these phenotypic changes, we conducted RNAseq and differential expression analysis for cells treated with hsa-miR-28-5p or hsa-miR-708-5p versus non-targeting siRNA (siNT) to control for nonspecific effects of small RNA transfection (**Figure 3-11B**). We hypothesized that differential gene expression should correlate strongly between the two microRNA siblings on a per-gene basis, given that the microRNAs should be largely sharing targets due to their identical seed sequences. Remarkably, when graphing per-gene $\log_2$ expression changes for hsa-miR-708-5p (y-axis) versus hsa-miR-28-5p (x-axis) relative to the negative control, the line of best fit was close to y = 0 + 1x with an R^2 value of 0.61 (**Figure 3-11B**). Such a strong correlation indicates treatment with either hsa-miR-28-5p or hsa-miR-708-5p has a very similar effect on expression across the transcriptome, with the expression of individual genes increasing or decreasing, on average, to the same degree following treatment with either microRNA. These data strongly support the conclusion that

treatment with hsa-miR-28-5p or hsa-miR-708-5p have similar phenotypic effects on MCF10A cells, and also that both microRNA hits cause highly-similar changes to the transcriptome as expected for two microRNAs with the same seed sequence.

Using our differential expression analysis, we followed up on two genes, *RPS28* and *SPRR3*, strongly co-downregulated by each MIR-28 sibling microRNA (**Figure 3-11B-C**). RPS28 is a ribosomal protein component of the 40S subunit, and its depletion in human cells causes the same 30S up, 21S down aberrant pre-rRNA processing signature (175, 301) that we observed following treatment with hsa-miR-28-5p or hsa-miR-708-5p. SPRR3 is an oncogene in breast (302), colorectal (303, 304), kidney (305), brain (306), and lung tissues (307, 308) controlled by the onco-transcription factor *JUN* (308, 309). Our laboratory previously identified SPRR3 as a novel candidate protein regulator of ribosome biogenesis (83), but its precise mechanism of action in RB remains undefined. We validated the miR-induced downregulation of *RPS28* or *SPRR3* by each microRNA hit at the transcriptomic and proteomic levels (**Figure 3-11D-E**).

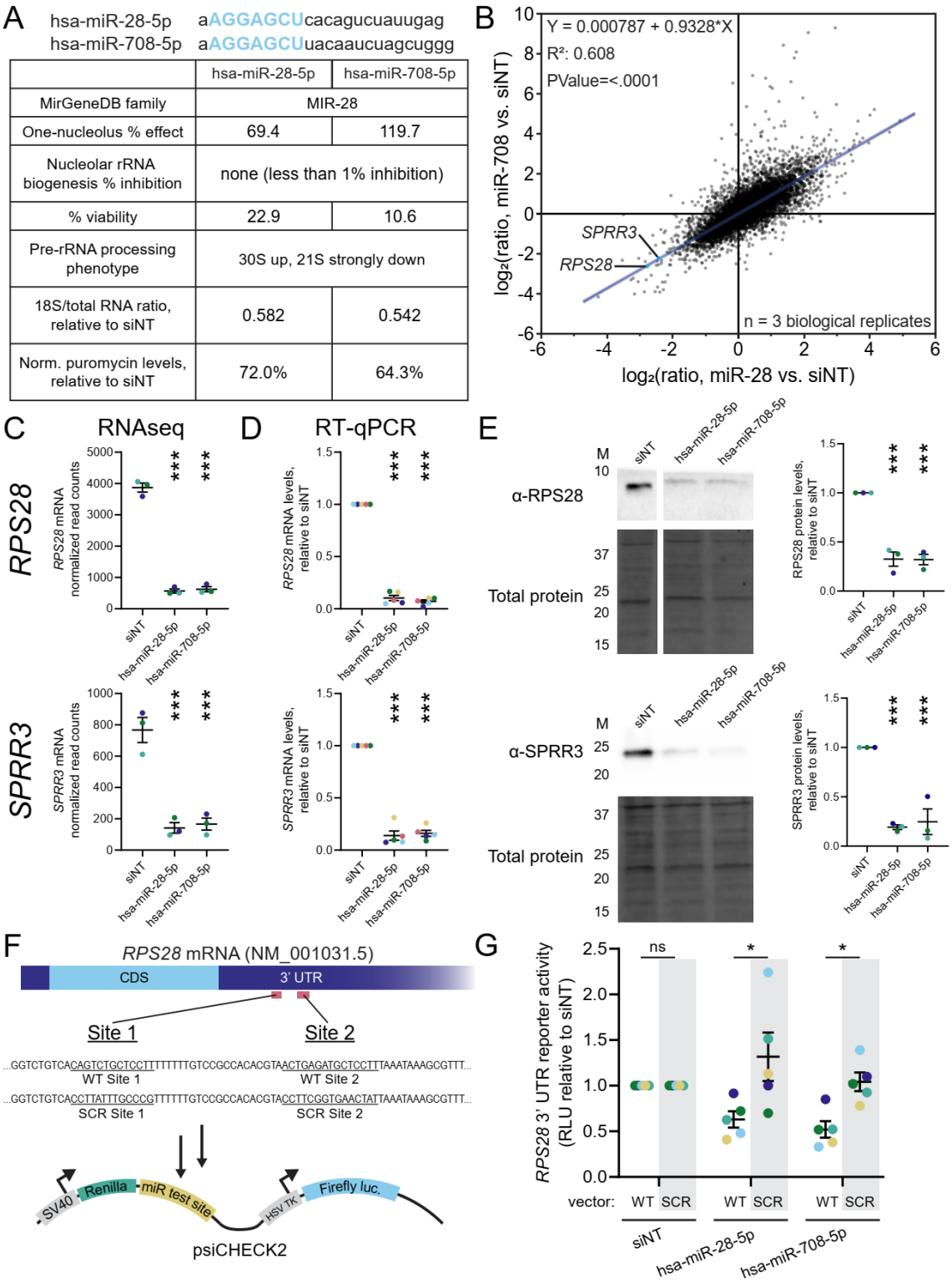

Figure 3-11. The MIR-28 siblings, hsa-miR-28-5p and hsa-miR-708-5p, directly target *RPS28* and downregulate *SPRR3*.

(**A**). Comparison of the MIR-28 family members, hsa-miR-28-5p and hsa-miR-708-

5p. The full mature microRNA sequence is shown for each sibling, with the common AGGAGCU seed sequence indicated in blue. The table compares the RB phenotypes observed in MCF10A cells following treatment with either microRNA mimic.

(**B**). Regression comparing $\log_2$-scale RNAseq differential expression profiles of MCF10A cells treated with either hsa-miR-28-5p or hsa-miR-708-5p, relative to siNT negative control. Each dot represents one mRNA, with *RPS28* and *SPRR3* labeled. The line-of-best-fit shown in blue, with equation, R^2 value, and *p* value for non-zero slope indicated in top left. The data from 3 biological replicates were graphed and analyzed in JMP.

(**C**). Normalized RNAseq read counts mapping to *RPS28* or *SPRR3*. The mean ± SEM are shown alongside individual data points, colored by replicate (3 replicates). The data were analyzed by ordinary one-way ANOVA with multiple comparisons against siNT and Holm-Šídák correction in GraphPad Prism 8. *, $p < 0.05$; **, $p < 0.01$; ***, $p < 0.001$.

(**D**). RT-qPCR analysis of *RPS28* or *SPRR3* mRNA levels from control- or hit-treated MCF10A cells. The data were normalized to 7SL RNA abundance as a loading control, then to siNT for comparison using the $\Delta\Delta C_T$ method. Mean ± SEM are shown alongside individual data points, colored by replicate (5 replicates). The data were analyzed by ordinary one-way ANOVA with multiple comparisons against siNT and Holm-Šídák correction in GraphPad Prism 8. *, $p < 0.05$; **, $p < 0.01$; ***, $p < 0.001$.

(**E**). Immunoblot analysis and quantification of RPS28 or SPRR3 protein levels from control- or hit-treated MCF10A cells. α-RPS28 or α-SPRR3, indicates the example immunoblot for each protein. Total protein, trichloroethanol total protein stain loading control. M, molecular weight marker lane. The images were quantified with Bio-Rad Image Lab. Mean ± SEM are shown alongside individual data points, colored by replicate (3 replicates). The data were normalized to siNT, then graphed and analyzed by ordinary one-way ANOVA with multiple comparisons against siNT and Holm-Šídák correction in GraphPad Prism 8. *, $p < 0.05$; **, $p < 0.01$; ***, $p < 0.001$.

(**F**). Schematic for 3' UTR luciferase reporter assay for testing direct the binding of the MIR-28 siblings to *RPS28*. Diagram for the *RPS28* mRNA transcript, indicating untranslated regions (UTR; dark blue) or coding sequence (CDS; light blue). Putative MIR-28 binding sites 1 and 2 are shown in red, and their wild-type (WT) sequence is given along with the design for scrambled MIR-28 sites (SCR) rescue construct. WT or SCR regions of the *RPS28* 3' UTR containing both putative MIR-28 sites were cloned into the 3' UTR of the *Renilla* luciferase expression cassette in the psiCHECK2 plasmid.

(**G**). Quantification of 3' UTR luciferase reporter assays as in (**F**) testing direct binding of MIR-28 siblings to *RPS28*. The vector construct is indicated as wild-type (WT) or scrambled (SCR) above the transfection treatment labels. The luciferase data were collected for each treatment and construct combination, then normalized to the siNT

treatment on a per-construct basis. Mean ± SEM are shown alongside individual data points, colored by replicate (5 replicates). The data were analyzed by unpaired two-sided Welch's *t*-tests between WT and SCR constructs in GraphPad Prism 8. *, $p < 0.05$; **, $p < 0.01$; ***, $p < 0.001$.

Given that both hsa-miR-28-5p and hsa-miR-708-5p treatment caused such a significant decrease in levels of *RPS28* or *SPRR3*, we hypothesized that transcripts of these genes may be directly targeted by the MIR-28 family. We identified two tandem putative MIR-28 family binding sites in the *RPS28* mRNA 3' UTR (**Figure 3-11F**). By conducting *in silico* binding experiments using the DuplexFold algorithm on the RNAstructure server (310), we confirmed that the seed regions of both MIR-28 family members could favorably interact with the candidate binding region in *RPS28* (**Figure 3-11F**, WT lowest energy in table; **Figure 3-12A-D**). Scrambling the sequence of both binding sites in the candidate region strongly abrogated the predicted interaction with hsa-miR-28-5p or hsa-miR-708-5p (**Figure 3-11F**, SCR lowest energy in table; **Figure 3-12E-H**). We also identified two putative MIR-28 sites in the 5' UTR or CDS region of *SPRR3*. Favorable binding was predicted between the *SPRR3* 5' UTR site and each MIR-28 sibling (**Figure 3-13A-B**). However, the *SPRR3* CDS region interactions predicted by DuplexFold showed interrupted seed binding (**Figure 3-13C-D**), lowering our confidence that interactions with the CDS would be functional in reducing *SPRR3* expression.

Next, we sought to test the extent to which the MIR-28 siblings could directly target these putative binding sites by using luciferase 3' UTR reporter assays (311, 312). Treatment with hsa-miR-28-5p or hsa-miR-708-5p inhibited reporter activity when the reporter contained the *RPS28* candidate region with WT putative binding sites (**Figure 3-11G**). Crucially, reporter assays carried out using the *RPS28* candidate region with scrambled putative binding sites completely rescued the microRNA-induced reporter

downregulation (**Figure 3-11G**), supporting the conclusion that each MIR-28 family microRNA hit directly targets the *RPS28* 3' UTR. In contrast, our reporter for the *SPRR3* 5' UTR did not show the MIR-28 mimics could directly bind to this region of *SPRR3* (**Figure 3-13E**).

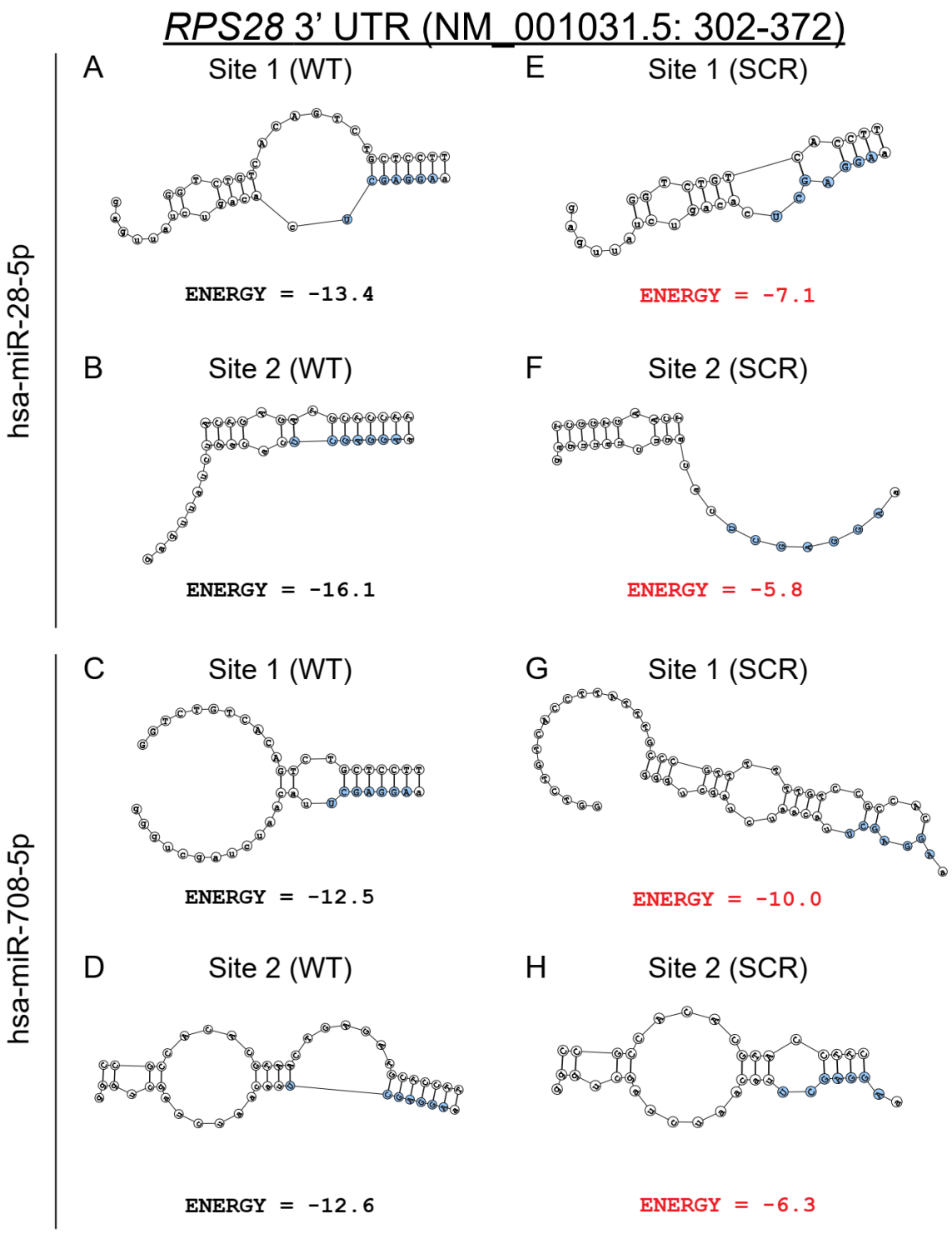

Figure 3-12. Predicted binding structures between MIR-28 siblings and putative binding sites in the *RPS28* 3' UTR.

(**A-D**). DuplexFold predicted structures between hsa-miR-28-5p (**A-B**) or hsa-miR-708-5p (**C-D**) to wild-type (WT) putative MIR-28 sites in the *RPS28* 3' untranslated

region (UTR). The seed sequence for each microRNA is shown in blue. The DuplexFold predicted binding energies are indicated for each structure. Transcriptomic coordinates for the binding region input are shown in the header. Extraneous target base pairs were removed for visualization.

(**E-H**). Corresponding DuplexFold predicted structures between hsa-miR-28-5p (**E-F**) or hsa-miR-708-5p (**G-H**) to seed site scrambled (SCR) putative MIR-28 sites in *RPS28* 3' untranslated region (UTR). Each binding energy (red) is reduced following seed scrambling. Extraneous target base pairs were removed for visualization.

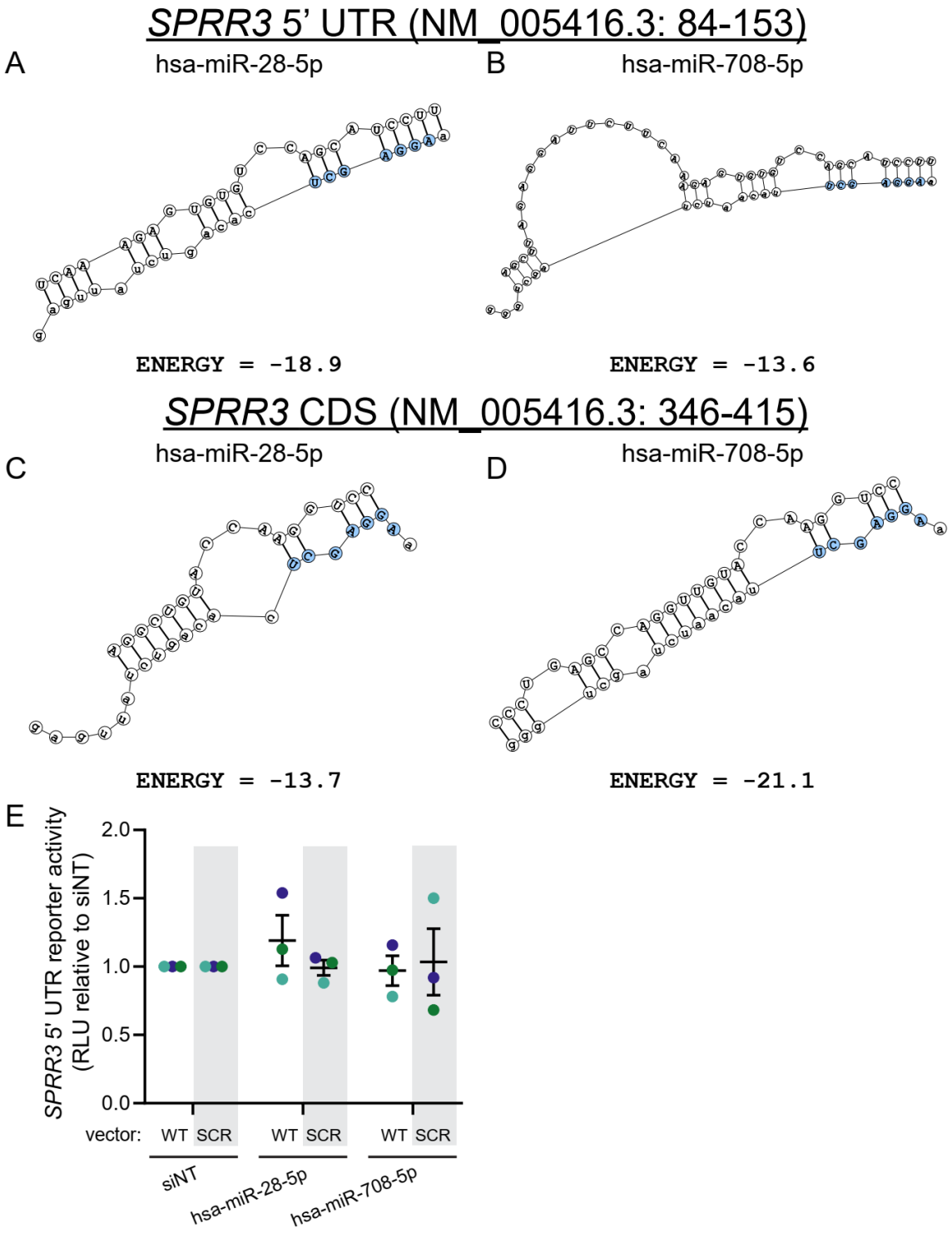

Figure 3-13. MIR-28 siblings do not directly target the *SPRR3* 5' UTR.

(**A-B**). DuplexFold predicted structures between hsa-miR-28-5p (**A**) or hsa-miR-708-5p (**B**) to wild-type (WT) putative MIR-28 sites in the *SPRR3* 5' untranslated region (UTR). The seed sequence for each microRNA is shown in blue. The DuplexFold

predicted binding energies are indicated for each structure. The transcriptomic coordinates for the binding region input are shown in the header. Extraneous target base pairs were removed for visualization.

(**C-D**). DuplexFold predicted structures between hsa-miR-28-5p (**C**) or hsa-miR-708-5p (**D**) to wild-type (WT) putative MIR-28 sites in the *SPRR3* coding sequence (CDS). The seeds do not appear to bind canonically. Other features as in (**A-B**).

(**E**). Quantification of luciferase reporter assays testing direct binding of MIR-28 siblings to the *SPRR3* 5' UTR. Vector construct indicated as wild-type (WT) or scrambled (SCR) above transfection treatment labels. Luciferase data were collected for each treatment and construct combination, then normalized to the non-targeting siRNA (siNT) treatment on a per-construct basis. The mean ± SEM are shown alongside individual data points, colored by replicate (3 replicates). The data were graphed in GraphPad Prism 8.

To search for other possible direct targets of the MIR-28 family, we pooled 10 million MCF10A cells each treated separately with either hsa-miR-28-5p or hsa-miR-708-5p mimics for 27 h to permit RISC loading and targeting, then conducted miR-eCLIP analysis for microRNA:mRNA target chimeras (313). Briefly, treated cells were UV crosslinked, pooled, and an AGO2 immunoprecipitation was performed to isolate microRNAs actively complexed to their targets. Despite limit of detection challenges from modest AGO2 enrichment, sequencing revealed 9,243 high-confidence reads consisting of microRNA:mRNA chimeras, representing functional target pairs. We uncovered 31 genes in our MIR-28 mimic RNAseq dataset bearing transcripts targeted by both MIR-28 siblings (**Figure 3-14A**), including *MYC* and *CDKN1A* (*p21*) (**Figure 3-15A-D**). An additional 113 genes in our MIR-28 mimic RNAseq dataset were targeted by either MIR-28 sibling (**Figure 3-14B**). MIR-28 family members therefore likely directly reduce *MYC* levels, providing another avenue of RB attenuation since MYC is an RNAP1 transcription factor (50). Targeting of *MYC* by the MIR-28 family has not previously been demonstrated in TarBase 8 (282). Furthermore, *CDKN1A* was directly targeted by the MIR-28 family, providing a logical explanation for the lack of change of *CDKN1A* mRNA levels in the face of TP53 upregulation that we observed (**Figure 3-10D-E**, hsa-miR-28-5p or hsa-miR-708-5p). *RPS28* or *SPRR3* were not observed to be direct targets of hsa-miR-28-5p or hsa-miR-708-5p by miR-eCLIP; however, these negative results do not preclude the possibility that functional binding could occur between the MIR-28 family and *SPRR3* transcripts, especially given the likelihood that the experimental results were incomplete due to subpar detection limits. Together, these

results provide strong evidence for the ability of the MIR-28 family to perturb the transcriptome identically, and to engage in direct post-transcriptional downregulation of the central RB regulator *MYC* and *RPS28*, an RP critical for normal 18S maturation.

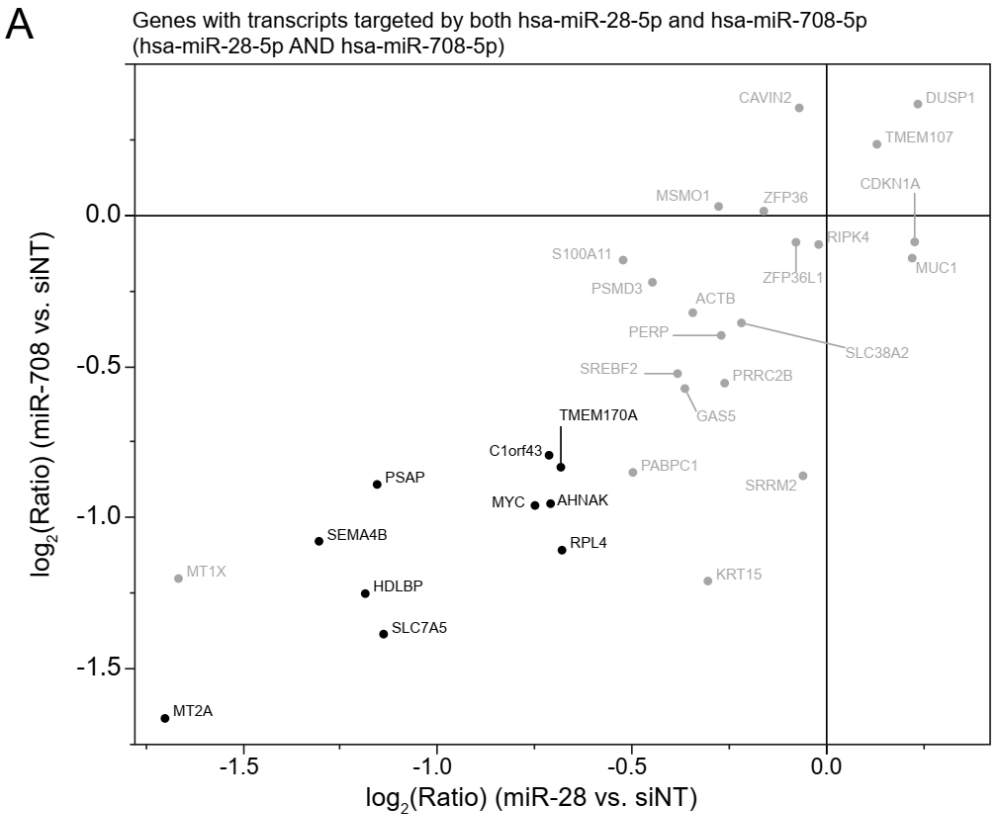
A
Genes with transcripts targeted by both hsa-miR-28-5p and hsa-miR-708-5p
(hsa-miR-28-5p AND hsa-miR-708-5p)
CAVIN2
DUSP1
TMEM107
MSMO1
ZFP36
CDKN1A
RIPK4
S100A11
MUC1
ZFP36L1
PSMD3
ACTB
PERP
SLC38A2
SREBF2
PRRC2B
GAS5
TMEM170A
C1orf43
PABPC1
SRRM2
PSAP
MYC
AHNAK
SEMA4B
RPL4
MT1X
KRT15
HDLBP
SLC7A5
MT2A
0.0
-0.5
-1.0
-1.5
log2(Ratio) (miR-708 vs. siNT)
log2(Ratio) (miR-28 vs. siNT)

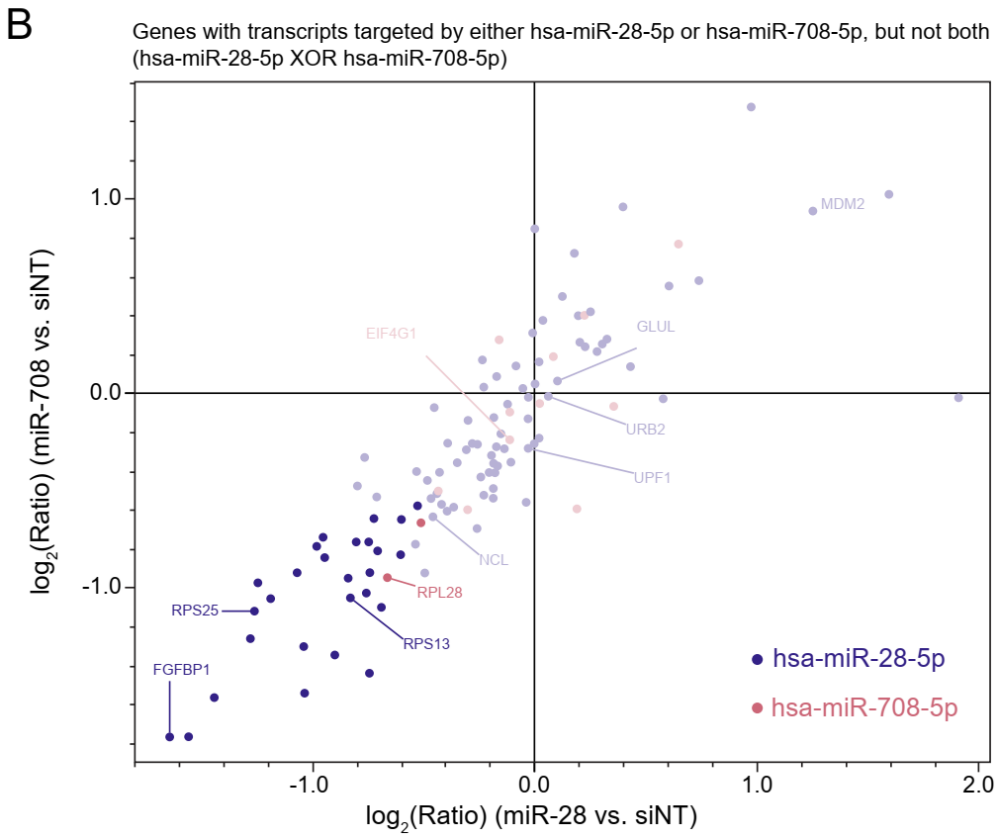
B
Genes with transcripts targeted by either hsa-miR-28-5p or hsa-miR-708-5p, but not both
(hsa-miR-28-5p XOR hsa-miR-708-5p)
MDM2
EIF4G1
GLUL
URB2
UPF1
NCL
RPL28
RPS25
RPS13
FGFBP1
hsa-miR-28-5p
hsa-miR-708-5p
1.0
0.0
-1.0
2.0
log2(Ratio) (miR-708 vs. siNT)
log2(Ratio) (miR-28 vs. siNT)

Figure 3-14. Direct targets of the MIR-28 siblings revealed by miR-eCLIP.

(**A**). Plot of genes with mRNA transcripts targeted by both hsa-miR-28-5p and hsa-miR-708-5p. The miR-eCLIP data were filtered for genes expressed in MCF10A cells, and RNAseq differential expression data following MIR-28 treatment is graphed for each gene on the x- and y-axes. Bolded points represent genes downregulated by both MIR-28 mimics by at least -0.5 $\log_2$ units, with a differential expression false discovery rate < 0.05 for both treatments. All genes are labeled with their HGNC symbol.

(**B**). Plot of genes with mRNA transcripts targeted exclusively (XOR) by either hsa-miR-28-5p or hsa-miR-708-5p. The miR-eCLIP data were filtered and graphed as above. The genes encoding mRNA transcripts are colored blue if bound by hsa-miR-28-5p or red if bound by hsa-miR-708-5p, according to miR-eCLIP data. Select genes are labeled with HGNC symbol.

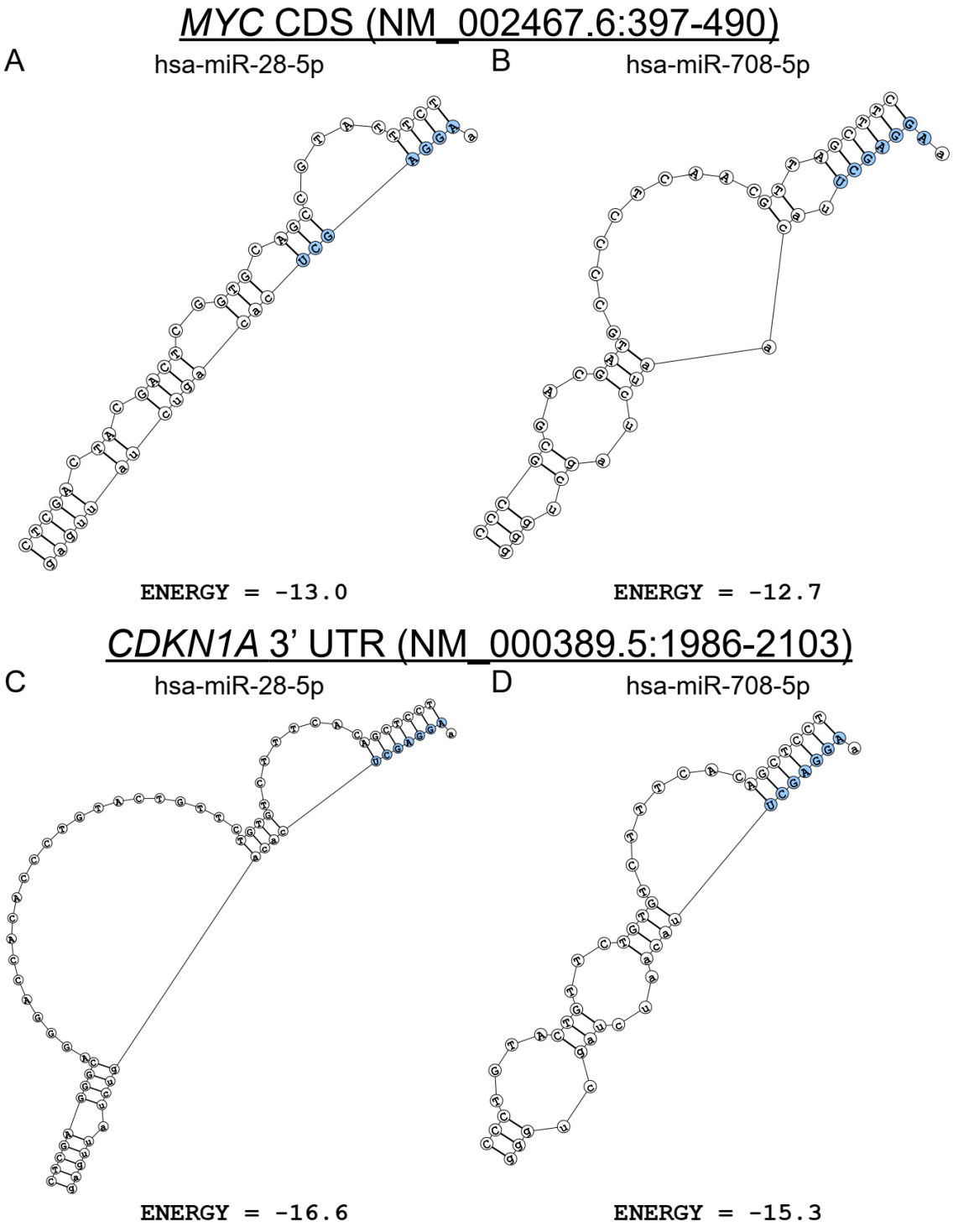

Figure 3-15. Predicted MIR-28 binding structures in the *MYC* CDS or *CDKN1A* (*p21*) 3' UTR.

(**A-B**). DuplexFold predicted structures between hsa-miR-28-5p (**A**) or hsa-miR-708-5p (**B**) and wild-type (WT) putative MIR-28 sites in the *MYC* coding sequence (CDS).

The seed sequence for each microRNA is shown in blue. The DuplexFold predicted binding energies are indicated for each structure. Transcriptomic coordinates for the binding region input are shown in the header. Extraneous target base pairs were removed for visualization.

(**C-D**). DuplexFold predicted structures between hsa-miR-28-5p (**C**) or hsa-miR-708-5p (**D**) and wild-type (WT) putative MIR-28 sites in *CDKN1A* (*p21*) 3' UTR. Other features as in (**A-B**).

3.3.10. SPRR3 is a novel positive regulator of RNAP1 transcription

Since our previous high-throughput screen identified SPRR3 as a putative novel regulator of RB (83), we first verified that SPRR3 depletion causes a change in nucleolar number. Indeed, treatment of MCF10A cells with a pool of four ON-TARGET siRNAs targeting *SPRR3* led to a significant decrease in nucleolar number relative to the siNT negative control, as was observed for positive controls siNOL11 and siRPS28 (**Figure 3-16A-B**). siRNA deconvolution revealed 3/4 individual *SPRR3* siRNAs in the pool also caused a significant decrease in nucleolar number (**Table 3-2**), strongly arguing against siRNA-induced off-target effects.

We hypothesized that SPRR3 depletion could inhibit RB subprocesses including nucleolar rRNA biogenesis, pre-rRNA transcription and processing, and global translation. We again utilized our 5-EU incorporation assay to test the extent to which RPS28 or SPRR3 depletion inhibits nucleolar rRNA biogenesis. Strikingly, depletion of either gene produced nucleolar rRNA biogenesis percent inhibition values above the positive control, siPOLR1A, set at 100% (**Figure 3-16A, C**). These results are consistent with the known role of RPS28 in ribosome assembly (175, 301), and further implicate SPRR3 as a novel regulator of RB.

For further RB assays, we utilized the original pool of four siGENOME siRNAs targeting *RPS28*. We also created a custom equimolar subpool of the two most potent individual *SPRR3* siRNAs (Horizon Discovery catalog J-019976-09 and J-019976-10). We verified that treatment with siRPS28 or the custom siSPRR3 subpool

significantly reduced mRNA and protein levels of each gene, respectively (**Figure 3-17A-D**).

We used 45S qPCR and the dual luciferase RNAP1 promoter activity reporter assay to determine how SPRR3 depletion altered RNAP1 transcription. Treatment with siSPRR3 significantly reduced 45S transcript levels by qPCR relative to siNT negative control (**Figure 3-16D**). siNOL11 transfection or 1 μM BMH-21 treatment following siNT transfection also decreased 45S levels, while siRPS28 transfection did not, as expected (**Figure 3-16D**). SPRR3 depletion also significantly abrogated RNAP1 promoter activity relative to mock or siNT transfection (**Figure 3-16E**). Again, treatment with siNOL11 or co-treatment with siNT and BMH-21 decreased RNAP1 promoter activity, while depletion of the cytosolic pre-60S maturation factor SBDS did not alter promoter activity levels (**Figure 3-16E**). Interestingly, depletion of RPS28 reduced RNAP1 promoter activity via this assay, although this did not appear to transmit functionally as 45S levels were not consequently reduced by siRPS28 (**Figure 3-16D-E**). Our observations that SPRR3 depletion strongly decreases nucleolar rRNA biogenesis, 45S transcript levels, and RNAP1 promoter activity support the conclusion that SPRR3 is a novel positive regulator of RNAP1 transcription.

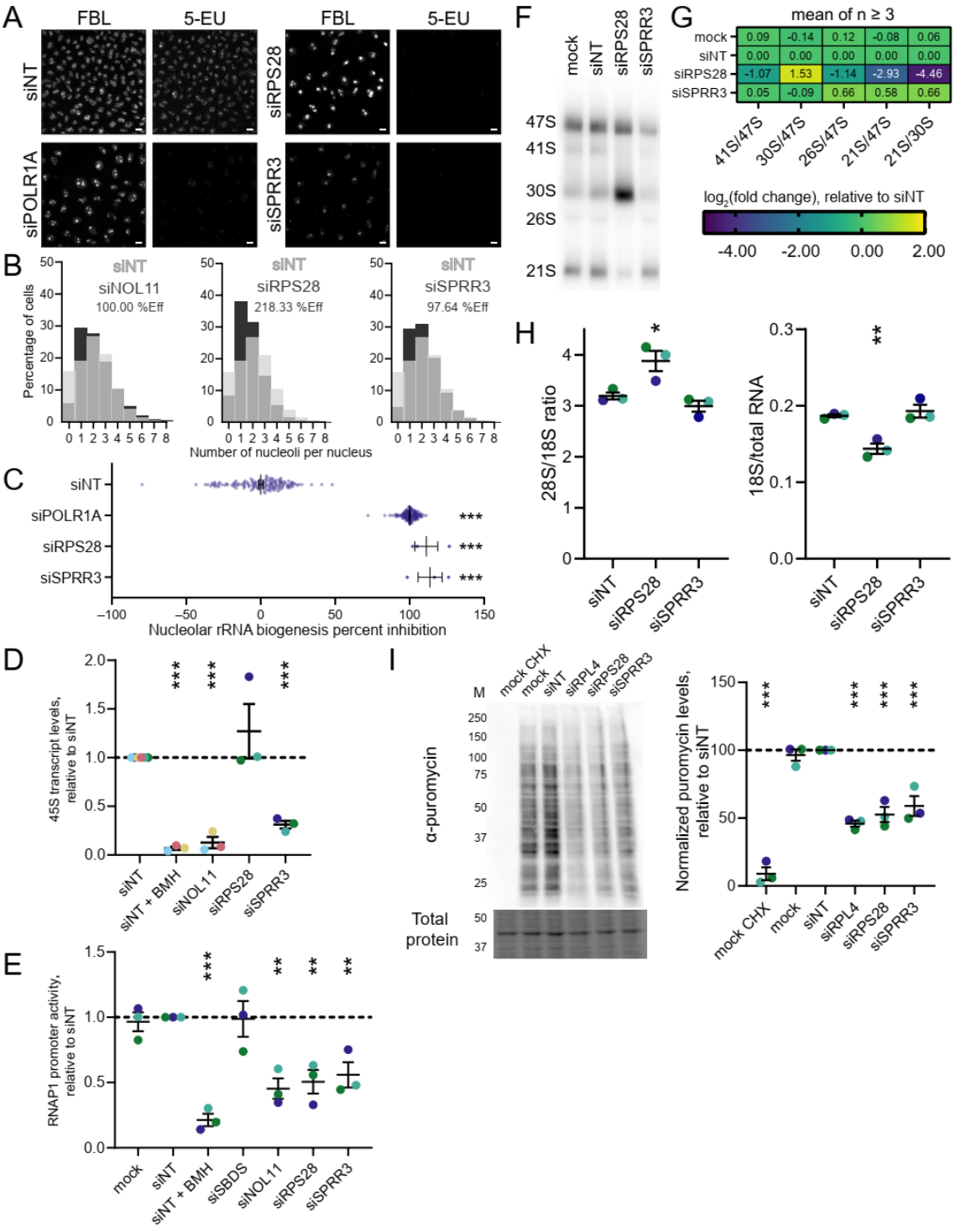

Figure 3-16. SPRR3 is a novel positive regulator of RNAP1 transcription.

(A) Representative images of control-treated, RPS28-depleted, or SPRR3-depleted MCF10A cells following fibrillarin (FBL) antibody staining and 5-EU incorporation. FBL immunostaining and 5-EU click labeling are shown as separate channels. Scale bars,

10 μm. siNT is a non-targeting negative control siRNA. siPOLR1A, POLR1A (RPA194) knockdown is a positive control.

(B) Quantification of nucleolar number following siRNA depletion of RPS28 or SPRR3. The histograms indicate the percentage of cells with a given number of nucleoli. The siNT negative control histogram is shown in light gray on all graphs for reference. Histograms from cells depleted of NOL11, RPS28, or SPRR3 are shown in black. siNOL11 is the positive control for decrease in nucleolar number. The one-nucleolus percent effect for black-labeled treatment is shown.

(C) Quantification of the percent inhibition of nucleolar rRNA biogenesis. The overall mean percent inhibition ± SEM is shown for each treatment, with each dot representing one well. The siNT negative control is set to 0% inhibition, and the siPOLR1A positive control is set to 100% inhibition. Data were analyzed by ordinary one-way ANOVA with multiple comparisons against siNT and Holm-Šídák correction in GraphPad Prism 8. *, $p < 0.05$; **, $p < 0.01$; ***, $p < 0.001$.

(D) RT-qPCR analysis of levels of the 45S pre-rRNA as a proxy for RNAP1 transcription. The mean ± SEM are shown alongside individual data points, colored by replicate (3 replicates). The data were normalized to 7SL RNA abundance as a loading control, then to siNT for comparison using the $\Delta\Delta C_T$ method. Data were analyzed by ordinary one-way ANOVA with multiple comparisons against siNT and Holm-Šídák correction in GraphPad Prism 8. *, $p < 0.05$; **, $p < 0.01$; ***, $p < 0.001$.

(E) Dual-luciferase reporter assay for RNAP1 promoter activity (84, 297). The mean ± SEM are shown alongside individual data points, colored by replicate (3 replicates). The data were analyzed by ordinary one-way ANOVA with multiple comparisons against siNT and Holm-Šídák correction in GraphPad Prism 8. *, $p < 0.05$; **, $p < 0.01$; ***, $p < 0.001$.

(F) Representative ITS1 (probe P3) northern blot of 3 μg of total RNA isolated from RPS28- or SPRR3-depleted MCF10A cells. siNT is the non-targeting control. Mock is mock transfected. The pre-rRNA processing intermediates are labeled on the left. The pre-rRNA processing schematic is as in Figure 5A. The images were quantified using Bio-Rad Image Lab.

(G) Heatmap showing $\log_2$-transformed Ratio Analysis of Multiple Precursor [RAMP (298)] calculations, normalized to the si non-targeting (siNT) negative control. The values represent mean RAMP ratio for $n = 4$ replicates, except $n = 3$ for mock. RAMP ratios were calculated in Microsoft Excel and data were graphed in GraphPad Prism 8.

(H) Bioanalyzer analysis for 1 μg of total RNA isolated from RPS28- or SPRR3-depleted MCF10A cells. Left, the 28S/18S mature rRNA ratio; right, the 18S mature rRNA/total RNA ratio. Mean ± SEM are shown alongside individual data points, colored

by replicate (3 replicates). The data were graphed and analyzed by ordinary one-way ANOVA with multiple comparisons against a non-targeting siRNA (siNT) and Holm-Šídák correction in GraphPad Prism 8. *, $p < 0.05$; **, $p < 0.01$; ***, $p < 0.001$.

(I) Representative examples of SUnSET puromycin incorporation assay (83, 299) immunoblots of total protein isolated from RPS28 or SPRR3-depleted MCF10A cells. α-puromycin is an example blot for puromycin incorporation as a proxy for global protein synthesis. Total protein is the trichloroethanol total protein stain loading control. Mock CHX is mock cells treated with cycloheximide. Images were quantified with Bio-Rad Image Lab. The mean ± SEM are shown alongside individual data points, colored by replicate (3 replicates). siRPL4 is the positive control. Data were normalized to a non-targeting siRNA (siNT), then graphed and analyzed by ordinary one-way ANOVA with multiple comparisons against siNT and Holm-Šídák correction in GraphPad Prism 8. *, $p < 0.05$; **, $p < 0.01$; ***, $p < 0.001$.

Table 3-2. SPRR3 siRNA deconvolution data.

Library siRNA	Duplex Catalog Number	HGNC Symbol	Gene Accession	Mean % viability	Mean one-nucleolus % effect	siNT +3 SD one-nucleolus % effect hit cutoff	Passed cutoff?
SPRR3-si1	J-019976-09	SPRR3	NM_005416	21.5214	62.2942	16.0373	1
SPRR3-si2	J-019976-10	SPRR3	NM_005416	22.2053	27.7435	16.0373	1
SPRR3-si3	J-019976-11	SPRR3	NM_005416	34.5195	18.3587	16.0373	1
SPRR3-si4	J-019976-12	SPRR3	NM_005416	92.5719	-4.4062	16.0373	0

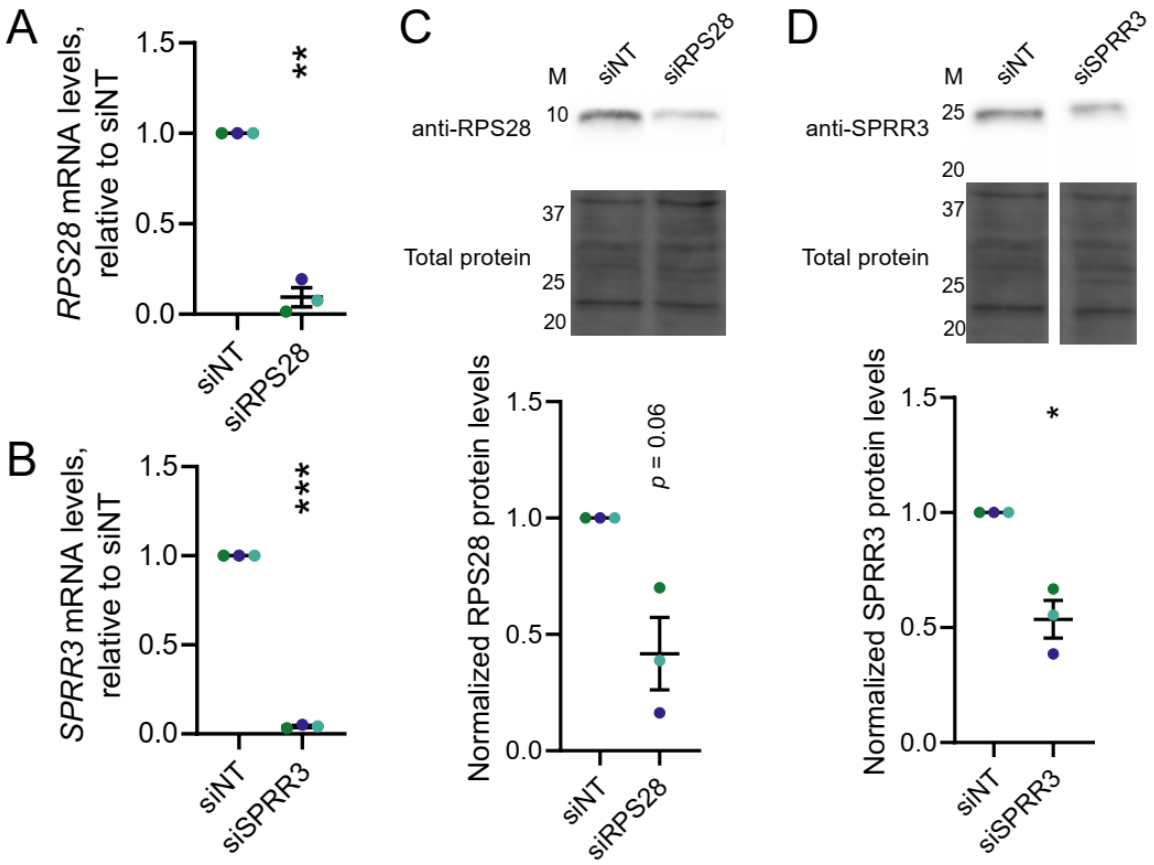

Figure 3-17. Validation of siRNA-mediated knockdown of RPS28 or SPRR3.

(A-B) RT-qPCR quantification of mRNA transcript levels following siRNA knockdown for *RPS28* (**A**) or *SPRR3* (**B**). The data were normalized to the 7SL RNA abundance as a loading control, then to a non-targeting siRNA (siNT) for comparison using the $\Delta\Delta C_T$ method. The mean ± SEM are shown alongside individual data points, colored by replicate (3 replicates). Data were analyzed by unpaired two-sided Welch's *t*-tests in GraphPad Prism 8. *, $p < 0.05$; **, $p < 0.01$; ***, $p < 0.001$.

(C-D) Immunoblot quantification of protein levels following siRNA knockdown for *RPS28* (**C**) or *SPRR3* (**D**). Anti-RPS28 or anti-SPRR3 antibodies shown in example immunoblots for the indicated protein. Total protein is the trichloroethanol total protein stain loading control. M, molecular weight marker lane. The images were quantified using Bio-Rad Image Lab. The mean ± SEM are shown alongside individual data points, colored by replicate (3 replicates). The data were graphed and analyzed by unpaired two-sided Welch's *t*-tests in GraphPad Prism 8. *, $p < 0.05$; **, $p < 0.01$; ***, $p < 0.001$.

We probed how depletion of RPS28 or SPRR3 could alter pre-rRNA processing patterns. While RPS28 depletion did not attenuate 45S transcript levels, it did cause very stark inhibition of nucleolar rRNA biogenesis, and has been previously shown to cause a 30S up, 21S down phenotype (175). We therefore hypothesized that the high nucleolar rRNA biogenesis inhibition observed after SPRR3 depletion could be caused not only by downregulation of pre-rRNA transcription but also by interruption of the pre-rRNA processing pathway. Northern blots confirmed that RPS28 depletion resulted in 30S stabilization and 21S destabilization, but pre-rRNA processing defects were not observed after siSPRR3 treatment (**Figure 3-16F-G**). Instead, SPRR3 depletion resulted in northern blots where all precursors are decreased, similar to what is observed upon NOL11 depletion (**Figure 3-7B-C**), consistent with inhibition of pre-rRNA transcription (85). Additionally, we quantified the 28S/18S mature rRNA ratio and 18S/total RNA ratio following RPS28 or SPRR3 depletion, finding that siRPS28 resulted in an increase in 28S/18S ratio caused by lower 18S levels while siSPRR3 did not alter ratios of mature rRNAs (**Figure 3-16H**). These results bolster the conclusion that SPRR3's primary novel role in RB control is to positively regulate pre-rRNA transcription.

We conducted puromycin incorporation experiments following depletion of RPS28 or SPRR3 to test the hypothesis that each of these factors is critical for maintaining normal global protein synthesis. Indeed, siRPS28 or siSPRR3 treatment significantly diminished puromycin incorporation versus the mock or siNT negative controls, at a magnitude similar to that observed following RPL4 depletion (**Figure 3-16I**). Altogether, our experiments are consistent with a model in which SPRR3 is

crucial for supporting pre-rRNA transcription, and thereby the intracellular supply of ribosomes and the process of cytoplasmic protein translation.

3.4. Discussion

Our work represents the first systematic foray into uncovering the complex roles of microRNAs as governors of ribosome biogenesis. Using our unbiased high-content screening platform for changes in nucleolar number, we have uncovered 72 novel microRNA negative regulators of RB. Strikingly, 51/72 hits strongly inhibited nucleolar rRNA biogenesis as measured by nucleolar 5-EU incorporation, supporting a role for the hits in antagonizing RB. Stringent selection and mechanistic validation of a subset of 15 novel microRNA hits unexpectedly revealed a major effect of hit overexpression to be dysregulation of 30S pre-rRNA processing; significantly, no specific microRNAs have yet been observed to directly affect pre-rRNA processing (53). While hits in the subset did not appear to reliably alter RNAP1 transcription, almost all subset hits inhibited global protein synthesis and caused upregulation of *CDKN1A* (*p21*), with nearly half increasing TP53 steady-state levels. We hypothesized that the microRNA hits were acting by binding to mRNAs required for nucleolar function and reducing their translatability. Bioinformatics of all the microRNA hits revealed that they were enriched for mRNA targets encoding proteins localized within the nucleolus or bearing functions in cell cycle progression, proliferation, or TP53 signaling, supporting our mechanistic hypothesis.

To further probe the hypothesis that microRNA mimic hits preferentially target nucleolar proteins, we focused on two MIR-28 family members, hsa-miR-28-5p and hsa-miR-708-5p. We chose them because they share the same 7 nt AGGAGCU seed sequence, and their overexpression causes the same RB defects, including a severe pre-18S rRNA processing defect. Comparison of RNAseq results following overexpression of either mimic resulted in identical transcriptomic profiles and revealed *RPS28* as a putative direct target. Indeed, we found these MIR-28 family members directly target the *RPS28* 3' UTR, providing a mechanistic explanation for the observed processing defect (175, 301) and supporting our hypothesis.

Transcriptomics also revealed SPRR3, a protein not previously known to regulate RB, as a candidate target of the MIR-28 family. Excitingly, we discovered that SPRR3 is essential for RNAP1 transcription. While we first identified SPRR3 as a candidate RB regulator in our genome-wide siRNA screen (83), our present work further defines its importance in facilitating RNAP1 promoter activity and normal accumulation of the 45S pre-rRNA precursor, as well as in enabling global translation. However, whether the MIR-28 siblings bind directly to *SPRR3* remains to be decisively determined. Consistent with a role in RNAP1 transcription, a recent report illustrated that SPRR3 is a positive regulator of pan-AKT phosphorylation (305), in turn likely driving RB as a key effector of the PI3K/AKT/mTOR axis that drives growth and proliferation. Pertinently, mTORC1 can activate UBTF (UBF) and RRN3 (TIF-1A) to enhance RNAP1 initiation, and can deactivate the RNAP3 inhibitor MAF1 to derepress synthesis of the 5S rRNA and tRNAs (50). We propose a model in which SPRR3 acts as a key pro-RB signal far

upstream of direct rDNA regulation, consistent with its reported cytoplasmic localization (309). This novel role agrees with SPRR3's known oncogenic function (302-307, 314). Our results elucidate the regulatory power held by a small oncogenic, cytoplasmic protein over the cellular nexus of translation in the nucleolus, underscoring the importance of non-nucleolar regulation of RB.

While our results point to the novel microRNA hits canonically acting to inhibit RB by post-transcriptionally downregulating target genes with nucleolar localization or functions in the cell cycle, we cannot exclude the possibility that these microRNAs may also have a more immediate role inside the nucleolus itself. A number of studies have defined nucleolar subsets of microRNAs in mammalian cells (98-101, 103), though the function of nucleolar microRNAs remains poorly understood. It has been suggested that the nucleolus may serve as a staging platform for microRNAs to complex with target mRNAs outside the competitive, mRNA-rich cytoplasm (101), or perhaps that efflux of microRNAs from the nucleolus may be part of a stress response to the invasion of foreign genetic material (99). Additionally, AGO2 has been observed to bind to regions of rDNA possibly via rRNA-mediated tethering (102), though more research is needed to fully understand the potential of microRNAs to directly downregulate the 45S transcript. Previous studies (99, 100) have observed the nucleolus to contain a number of our hits' families, including miR-19b, miR-25, miR-34a, miR-182, miR-183, miR-192, miR-330, and miR-629. However, in most cases, the microRNA strand was not indicated. Future investigation of nucleolar microRNAs may shed additional light on the potential direct impacts of the hits inside the nucleolus beyond the present scope.

Others have criticized the use of microRNA mimics (315), finding that they could perturb endogenous microRNA action (316). Our work did harness overexpression of microRNA mimics in tissue culture cells, which may have supraphysiological or gain-of-function effects relative to the normal human. Importantly, our hits did not overlap with hits of other microRNA mimic screens for cardiac regeneration (277) or G1-S transition and proliferation regulators (275), arguing against nonspecific dysregulatory effects on the transcriptome induced by pollution of cellular microRNAs by mimic overexpression. Furthermore, our 2.8% hit rate is on par with other screens, and we conducted thorough validation of a subset of 15 hits that lead to a wide range of RB-altered phenotypes. Tissue-specific differences may also have a confounding effect on hit observability of microRNA mimics or inhibitors, as microRNAs are often tuned for cell type specificity (317). While we acknowledge these technological shortcomings, we argue that systematic exploration of the role of this large set of human microRNAs has illuminated new regulatory roles for microRNAs in RB.

Based on the promiscuous nature of microRNA activity, screens with microRNA mimics have an increased scale and complexity of direct regulatory perturbation compared to previous RB screening campaigns (81-84, 87). While prior screens used siRNA technology to surgically deplete expression of a single gene, the transfection of a microRNA mimic may directly deplete tens to thousands of mRNAs. Simultaneous manipulation of multiple gene regulatory networks with microRNAs may lead to complex, potentially-discordant cellular phenotypes. This is because assay results report an integration of many more heterogeneous expression changes than in simpler single-

gene siRNA experiments. One key example from this work is that the MIR-28 siblings elevate TP53 protein levels without a concomitant increase in TP53's downstream target, *CDKN1A* (*p21*), as expected (318). Our miR-eCLIP data indicated that both MIR-28 microRNAs in fact directly target *CDKN1A in vivo*, as previously shown for hsa-miR-28-5p (319), resolving this discrepancy. While we found a straightforward explanation for this case, other discrepancies in our data likely remain. These results invite additional probing to improve our understanding of the complex functional perturbations associated with each microRNA hit.

Looking forward, we highlight our discovery of novel microRNA negative regulators of RB in the context of cancer. Differential regulation of many of the 72 hits has been observed in various tumors (289, 320-353), with hits including hsa-miR-28-5p and hsa-miR-708-5p (354-363) often acting as tumor suppressors. We emphasize the enrichment of the hits' targets for involvement in the cell cycle, which is tightly intertwined with RB, nucleolar formation, and tumorigenesis (84, 178, 364). Additionally, microRNA mimic therapeutics are a promising avenue in oncology (365), though roadblocks including delivery and dosage have impeded achieving success in the clinic (366). Combining mimics and small molecules may enable inhibition of multiple targets or decrease required microRNA dose (366), as seen in clinical trials for hepatitis C (367, 368). Given that cancer cells often hyperactivate ribosome production (264), our study underscores the potential of harnessing conserved microRNAs for chemotherapy as standalone therapeutics or in concert with other potent small molecule

inhibitors of RB like BMH-21 to simultaneously target pre-rRNA transcription and processing.

3.5. Materials and Methods

3.5.1. Cell lines and culture conditions

Human MCF10A breast epithelial cells (ATCC CRL-10317) were cultured in DMEM/F-12 (Gibco 11330032) with 5% horse serum (Gibco 16050122), 10 μg/mL insulin (MilliporeSigma I1882), 0.5 μg/mL hydrocortisone (MilliporeSigma H0135), 20 ng/mL epidermal growth factor (Peprotech AF-100-15), and 100 ng/mL cholera toxin (MilliporeSigma C8052). Cells were incubated at 37 °C in a humidified atmosphere with 5% CO2.

3.5.2. Chemical reagents

BMH-21 (Sigma-Aldrich SML1183; CAS 896705-16-1) was diluted to a working stock concentration of 50 μM in DMSO for direct dosing of cells in 384-well plates.

3.5.3. RNAi depletion and microRNA expression by reverse-transfection

RNAi depletion was conducted in MCF10A cells as previously reported (83, 84, 287). Briefly, MCF10A cells were reverse-transfected into an arrayed 384-well plate

library containing small interfering RNA (siRNA) or miRIDIAN microRNA mimic constructs (Horizon Discovery) using Opti-MEM (Gibco 31985070) and Lipofectamine RNAiMAX transfection reagent (Invitrogen 13778150). Assay-ready plates containing 10 μL of 100 nM microRNA mimics resuspended in 1X siRNA buffer (Horizon Discovery B-002000-UB-100) were prepared from master library 384-well plates (Horizon Discovery, 0.1 nmol scale) and stored at -80 C. Plates were prepared with control siRNAs (siNT, siNOL11, siKIF11, or siPOLR1A) for reverse-transfection at a final 20 nM siRNA/microRNA mimic concentration as described (287), at a seeding density of 3000 MCF10A cells/well. The miRIDIAN microRNA hairpin inhibitor library (Horizon Discovery) was screened using the same protocol. siRNA deconvolution for SPRR3 was conducted as previously reported (296).

3.5.4. 5-ethynyl uridine labeling; staining and high-content imaging

5-ethynyl uridine (5-EU; ClickChemistryTools 1261-100, CAS 69075-42-9) was used to label cells at a 1 mM final concentration. Staining, click chemistry, and high-content imaging were performed as previously described (287).

3.5.5. CellProfiler pipeline and data analysis

Image analysis and data processing were conducted using a custom pipeline for CellProfiler 3.1.9 as previously described (83, 84, 202, 253, 287). Strictly-standardized mean difference (SSMD) values were calculated from plate-adjusted one-nucleolus or 5+ nucleoli percent effect values using the uniformly minimal variance unbiased estimate

(UMVUE), equation A5 in (254). Data from the primary or secondary screen were averaged in JMP and graphed with JMP or GraphPad Prism 8 (GraphPad Software).

3.5.6. MCF10A RNA expression dataset

Deposited reads from four RNAseq experiments from MCF10A cells (**Table 3-3**) quantifying transcript levels without treatment (negative control conditions; see table below) were re-analyzed using Partek Flow. Reads were aligned to the hg38 genome with HISAT2 2.1.0 and quantified using the Ensembl Transcripts version 99 annotation with the Partek E/M algorithm module. Normalized transcripts per million (zTPM) for genes in each experiment was calculated in R as described (283). For each dataset, a given gene was categorized as expressed if its zTPM was greater than -3, as described in (283).

Table 3-3. BioProjects accessed to construct the MCF10A RNA expression dataset.

BioProject accession	**GEO samples used**	**Reference**
PRJNA290557	GSM1829628	(369)
PRJNA384982	GSM2593351, GSM2593352, GSM2593353	(370)
PRJNA530983	GSM3711368, GSM3711369	N/A
PRJNA647393	GSM4667014, GSM4667015, GSM4667016	(371)

3.5.7. Nucleolar protein metadatabase

Three nucleolar protein databases were merged to create a nucleolar protein metadatabase. The Human Protein Atlas subcellular localization database (v. 20.0) (286,

proteinatlas.org) containing 1350 unique nucleolar proteins was retrieved, and HGNC gene names were updated based on Ensembl Gene ID using BioMart. Proteins labeled with the GO terms “Nucleoli”, “Nucleoli fibrillar center”, or “Nucleoli rim” were considered to be nucleolar. The T-cell nucleolar proteome (285) containing 880 unique nucleolar proteins was retrieved, and HGNC gene names were updated based on NCBI Entrez Gene ID using BioMart. An archived copy of NOPdb 3.0 (284) containing 2242 unique nucleolar proteins was retrieved, and HGNC gene names were updated based on International Protein Index (IPI) ID using the latest IPI database release (v. 3.87) and BioMart. The three databases were merged on updated HGNC name, resulting in a metadatabase of 3490 unique nucleolar proteins.

3.5.8. Bioinformatic target enrichment analysis

TarBase 8 (282) was utilized to identify experimentally-validated microRNA:mRNA interactions. Genes were filtered for the *Homo sapiens* species, for true positive microRNA:mRNA interactions, and for interactions where the microRNA caused reduced levels of the mRNA. Next, genes were annotated with zTPM expression data from the MCF10A expression dataset (see above), for nucleolar localization using the nucleolar protein metadatabase (see above), and 89 cytosolic RP genes were labeled based on HGNC gene groups (35 “S ribosomal proteins”, HGNC gene group 728; 54 “L ribosomal proteins”, HGNC gene group 729). The number of genes targeted by each microRNA was calculated in JMP, and confirmed hit microRNAs were labeled. Subset tabulations were also carried out to determine the number of genes coding for nucleolar

proteins targeted by each microRNA, and the number of genes coding for RPs targeted by each microRNA. Mean and median values for each category were calculated with JMP for hit microRNAs and non-hit microRNAs. Conversely, the number of microRNAs targeting each gene was also calculated with JMP, and all 262 genes targeted by 5 or more microRNA hits were analyzed for enrichment using Enrichr (372-374).

3.5.9. RNA isolation following RNAi transfection

MCF10A cells were seeded at 100,000 cells per well in 2 mL of media in 6-well plates and incubated at 37 °C for 24 h. Cells were transfected with 30 nM siRNAs or microRNA mimics using Lipofectamine RNAiMAX (Invitrogen 13778-150) and Opti-MEM (Gibco 31985070) per manufacturer's instructions for 72 h. Cells were washed with 1X PBS, then collected with 1 mL of TRIzol reagent (Invitrogen 15596026). Total RNA was purified following the manufacturer's protocol.

3.5.10. PolyA+ RNAseq following overexpression of hsa-miR-28-5p or hsa-miR-708-5p

MCF10A cells were treated with siNT, hsa-miR-28-5p, or hsa-miR-708-5p, and RNA was isolated as above. One μg of total RNA was resuspended in nuclease-free H_2O and submitted to the Yale Center for Genomic Analysis (West Haven, CT) for polyA+ library preparation and sequencing. All samples had an RNA Integrity Number (RIN) of at least 9.6. 35-50 million 100 bp paired-end reads were collected per sample using a NovaSeq 6000 Sequencing System (Illumina). RNAseq was conducted in biological

triplicate. Partek Flow was used to process, align, and quantify reads. Reads were trimmed of adapters, then aligned to the hg38 genome with HISAT2 2.1.0. Reads were quantified using the RefSeq Transcripts version 93 annotation with the Partek E/M algorithm module. Differential expression analysis was conducted with DESeq2 (375). Raw reads are available on NCBI under BioProject accession PRJNA919164.

3.5.11. Analysis of RNA transcript levels by RT-qPCR

MCF10A cells were treated with control siRNAs or microRNA mimics, and RNA was isolated as above. cDNA was synthesized from 1 μg total input RNA using iScript™ gDNA Clear cDNA Synthesis Kit (Bio-Rad 1725035). In a qPCR plate (Bio-Rad MLL9601), 1 μL of cDNA was dispensed, followed by 19 μL of a qPCR master mix containing iTaq Universal SYBR Green Supermix (Bio-Rad 1725121), 500 nM forward primer, 500 nM reverse primer, and water. Primers sequences are given in **Table 3-4**. The plate was briefly centrifuged and assayed using a Bio-Rad CFX96 Touch Real-Time PCR Detection System. Amplification parameters were: initial denaturation 95 ºC for 30 s; 40 cycles 95 ºC denaturation for 15 s, 60 ºC annealing and extension for 30 s. Melt curve analysis parameters were: 60 ºC to 94.8 ºC in 0.3 ºC increment. Data analysis was completed using the comparative C_T method ($\Delta\Delta C_T$) using 7SL RNA as an internal loading control.

Table 3-4. Primer sequences for RT-qPCR analysis.

Target RNA	Forward primer (5' → 3')	Reverse primer (5' → 3')	Ref.
45S pre-rRNA	GAACGGTGGTGTGTCGTTC	CGTCTCGTCTCGTCTCACTC	(376)
7SL RNA	ATCGGGTGTCCGCACTAAGTT	CAGCACGGGAGTTTTGACCT	(377)
CDKN1A (p21)	TGGAGACTCTCAGGGTCGAAA	GGCGTTTGGAGTGGTAGAAATC	(378)
RPS28	GGTCTGTCACAGTCTGCTCC	CATCTCAGTTACGTGTGGCG	(379)
SPRR3	AGCAGGTCCAGCATCCTTTGA	CTCCTTGGTTGTGGGAACAAAT	(314)

3.5.12. Analysis of mature rRNAs

MCF10A cells were treated with control siRNAs or microRNA mimics, and RNA was isolated as above. One μg of total RNA was resuspended in nuclease-free H_2O and submitted to the Yale Center for Genomic Analysis for electropherogram analysis. Each experiment was conducted with either a Bioanalyzer 2100 or a Fragment Analyzer 5300 (Agilent). Mature rRNA ratios and mature rRNA relative peak areas were taken from the output reports. The data were graphed and analyzed by ANOVA followed by Holm-Šídák post-hoc testing in GraphPad Prism.

3.5.13. Northern blot analysis of pre-rRNA processing

MCF10A cells were treated with siRNAs or microRNA mimics, and RNA was isolated as above. Northern blots were performed using 3 μg of total RNA as published (83, 84) using probes in **Table 3-5**, and were performed in at least biological triplicate. Blots were quantified with Image Lab 6.0.1 (Bio-Rad). RAMP [Ratio Analysis of Multiple Precursors, (298)] ratios were calculated in Microsoft Excel, and heatmaps were

made using the mean $\log_2$ RAMP ratio for each treatment relative to siNT in GraphPad Prism. The following DNA oligonucleotides were radiolabeled for blotting:

Table 3-5. Probe sequences for northern blotting.

Probe name	Probe sequence (5' → 3')	Ref.
P3 (ITS1)	AAGGGGTCTTTAAACCTCCGCGCCGGAACGCGCTAGGTAC	(83)
P4 (ITS2)	CGGGAACTCGGCCCGAGCCGGCTCTCTCTTTCCCTCTCCG	(83)

3.5.14. Dual-luciferase assay for RNAP1 promoter activity

MCF10A cells were seeded at 30,000 cells per well in 1 mL of media in 12-well plates and incubated at 37 °C for 24 h. Cells were transfected with 30 nM siRNAs or microRNA mimics as above for 48 h. Cells were then transfected with 1 μg of pHrD-IRES-Fluc and 1 ng of CMV-Rluc reporter plasmids (296) using Lipofectamine 3000 (Invitrogen L3000015). Concurrently, cells were treated with 3.5 μL of DMSO vehicle or 300 μM BMH-21, to achieve a final concentration of 1 μM BMH-21. After another 24 h, treated cells were washed once with 1X PBS and lysed with 250 μL of 1X Passive Lysis Buffer (Promega E1941) at room temperature for at least 30 minutes. In a solid white 96-well plate (Greiner Bio-One 655074), 20 μL of lysate from each sample was dispensed into a well. Samples were assayed using a Promega GloMax plate reader with dual injectors, using the Dual-Luciferase Reporter Assay System (Promega E1910) per manufacturer's instructions. Sixty μL of LAR II or Stop & Glo substrate were injected with a 2 s delay and a 10 s read time. Data were analyzed by calculating the Fluc/Rluc ratio for each well, then normalizing to the Fluc/Rluc ratio for siNT. Data import was

carried out in Microsoft Excel, calculations were performed in JMP, and normalized data were graphed and analyzed by ANOVA followed by Holm-Šídák post-hoc testing in GraphPad Prism.

3.5.15. Protein isolation, SDS-PAGE analysis, and immunoblotting

MCF10A cells were seeded at 100,000 cells per well in 2 mL of media in 6-well plates and incubated at 37 °C for 24 h. Cells were transfected with a final concentration of 30 nM siRNAs or microRNA mimics in a total volume of 2250 μL as above for 72 h. Following treatment, cells were washed twice with cold 1X PBS, manually dislodged using cell scrapers (Falcon 353085), collected in 1 mL of cold 1X PBS, centrifuged at 1100 RCF for 5 minutes at 4 °C, then lysed in AZ lysis buffer (50 mM Tris pH 7.5, 250 mM NaCl, 1% Igepal, 0.1% SDS, 5 mM EDTA pH 8.0) with 1X complete protease inhibitors (cOmplete Protease Inhibitor Cocktail, Roche 11697498001) by vortexing. Cell debris was pelleted at 21000 RCF for 15 minutes. A Bradford assay was used to determine supernatant total protein concentration. Protein aliquots were made using 5X Laemmli buffer, then boiled at 95°C for 3 minutes and loaded onto a gel or frozen at -20°C. Handcast SDS-PAGE gels (8%, 10%, 15%, or 4-18% gradient) containing 0.5% (v/v) trichloroethanol (Acros Organics 139441000) for stain-free imaging (380) were used to separate total protein at 110 V for 2 h. Total protein was imaged using the ChemiDoc stain-free imaging protocol (Bio-Rad) to ensure even loading at the gel stage. Gels were UV-activated for 5 min in the ChemiDoc. Following membrane transfer with the Trans-Blot Turbo system (Bio-Rad), blots were imaged again for total protein; these

images are presented and quantified as blot loading controls. Immunoblotting was carried out using 5% (w/v) Omniblok dry milk (American Bio AB10109) in 1X PBST (1X PBS containing 5% (v/v) Tween) with primary antibodies listed in **Table 3-6** followed by 1:5000 peroxidase-linked anti-mouse or anti-rabbit IgG (Amersham NXA931 or NA934) as appropriate. Blots were developed using low- or high-sensitivity ECL reagent (Millipore WBKLS0500, Thermo Scientific 34094) for 5 minutes, then dried and imaged with the ChemiDoc. Images from the ChemiDoc were quantified using Image Lab 6.0.1 (Bio-Rad). Data were graphed and analyzed by ANOVA followed by Holm-Šídák post-hoc testing in GraphPad Prism.

Table 3-6. Primary antibodies used for immunoblotting.

Target molecule	Primary antibody manufacturer and catalog number	Dilution
FBL	Abcam ab226178	1:1000
POLR1A (RPA194)	Santa Cruz Biotechnology sc-48385 (clone C-1)	1:1000
Puromycin	Kerafast EQ0001 (clone 3RH11)	1:5000
RPS28	Invitrogen PA5-45721	1:500
SPRR3	Proteintech 11742-1-AP	1:500
TP53	Santa Cruz Biotechnology sc-126 HRP (clone DO-1)	1:5000
UBTF	Santa Cruz Biotechnology sc-13125	1:500

3.5.16. Puromycin incorporation for SUnSET global translation assay

After the 72 h transfection period in 2250 μL in six-well plates, MCF10A cells were treated with an additional 750 μL of media containing 3 μM puromycin (Mirus Bio 5940), achieving a final concentration of 1 μM (0.5 μg/mL) puromycin and final

volume of 3 mL (83, 84, 296, 299). Cells were incubated 1 h at 37 °C, then washed with cold 1X PBS. Protein was isolated and analyzed as above.

3.5.17. Identification of putative microRNA binding sites

Candidate microRNA binding sites in transcripts coding for nucleolar proteins were identified using databases including TarBase 8 (282), TargetScan 7.2 (381), and miRWalk 3 (382). Binding sites were computationally tested using the bimolecular DuplexFold algorithm on the RNAStructure Web Server (310). The sequence of either hsa-miR-28-5p or hsa-miR-708-5p was tested for *in silico* binding to 70 bp regions of target transcripts containing putative microRNA binding sites. Transcript regions bearing a scrambled binding site were also tested for binding by either mature microRNA sequence. Computed binding energies from DuplexFold are reported in this manuscript.

3.5.18. Molecular cloning of psiCHECK-2 plasmids for microRNA UTR assays

The psiCHECK-2 plasmid was acquired as a gift from P. Pawlica and J. A. Steitz (Yale University) (311). Transcriptomic regions of approximately 200 bp containing putative microRNA binding sites were cloned from MCF10A genomic DNA, which was isolated using the DNeasy Blood & Tissue Kit (Qiagen 69504). Primers for generating XhoI-NotI amplicons were designed using Geneious 8.1.9 (Biomatters Ltd.) (**Table 3-7**). Amplicons were restriction cloned into psiCHECK-2. Target WT seed sequences were scrambled by site-directed mutagenesis overlap cloning (383). Plasmids were verified by Sanger sequencing (GENEWIZ, Inc./Azenta Life Sciences).

Table 3-7. Primer sequences for microRNA UTR construct cloning.

Primer name	Purpose	Sequence
RPS28_3UTR_XhoF	Restriction cloning putative MIR-28 binding region into psiCHECK2	ACTGCTCGAGGCTTGGCTGCTCGCTGGGTCTTGGATGTCGGGTTCG
RPS28_3UTR_NotR	Restriction cloning putative MIR-28 binding region into psiCHECK2	ACTGGCGGCCGCACCGCCTGGGAGCC
RPS28_3UTR_SCR-1F	Site-directed mutagenic overlap cloning to scramble RPS28 3' UTR WT site 1	CCTTCGGTGAACTATTAAATAAAGCGTTTGTGTTTCAAGT
RPS28_3UTR_SCR-1R	Site-directed mutagenic overlap cloning to scramble RPS28 3' UTR WT site 1	ATAGTTCACCGAAGGTACGTGTGGCGGACAAAAAA
RPS28_3UTR_SCR-2F	Site-directed mutagenic overlap cloning to scramble RPS28 3' UTR WT site 2	CCTTATTTGCCCGTTTTTTGTCCGCCACACGTA
RPS28_3UTR_SCR-2R	Site-directed mutagenic overlap cloning to scramble RPS28 3' UTR WT site 2	CGGGCAAATAAGGTGACAGACCATTCCCATCGG
SPRR3_5UTR_XhoF	Restriction cloning putative MIR-28 binding region into psiCHECK2	ACTGCTCGAGACCAGATCCCAGAGGCTGAACACCTCGACCTTCTCTGCACAGCAGATGATCCCTGAGCAGCTGAAGACCA
SPRR3_5UTR_NotR	Restriction cloning putative MIR-28 binding region into psiCHECK2	ACTGGCGGCCGCGCTTCAAAGGATGCTGGACACACTCTTTGAAGAATCCTCTAAGCTCCTG
SPRR3_5UTR_SCR_NotR	Restriction cloning scrambled MIR-28 binding region into psiCHECK2 (used with SPRR3_5UTR_XhoF)	ACTGGCGGCCGCGCTTCACCGGAGTGACATAAATTCCGAAAAATGTCCGTCATGTCTCCTGAATTAAGCAGAAAGTCTTAGTGGC

3.5.19. MicroRNA UTR assays testing for direct interaction of microRNA mimics with putative mRNA targets

MCF10A cells were seeded at 40,000 cells per well in 1 mL of media in 24-well plates and incubated at 37 °C for 24 h. Cells were co-transfected for 24 h with 30 nM siRNA or microRNA mimic, 10 ng of psiCHECK-2 plasmid, and 1 μg of salmon sperm carrier DNA using Lipofectamine 3000 (Invitrogen L3000015) according to manufacturer protocol. Following treatment, cells were washed with 1 mL of 1X PBS and incubated in 100 μL of 1X Passive Lysis Buffer (Promega E1941) at room temperature for at least 30 minutes. The dual-luciferase assay was carried out as detailed above. Data were analyzed by calculating the Rluc/Fluc ratio for each well, then normalizing to the Rluc/Fluc ratio for siNT. Data import was carried out in Microsoft Excel, calculations were performed in JMP, and normalized data were graphed and analyzed by ANOVA followed by Holm-Šídák post-hoc testing in GraphPad Prism.

3.5.20. miR-eCLIP analysis for identifying direct targets of MIR-28 family members

miR-eCLIP was performed as detailed in (313). Briefly, 3.5 million MCF10A cells were seeded into 15 cm tissue culture dishes and incubated for 48 h in 10 mL media. Cells were transfected with either hsa-miR-28-5p or hsa-miR-708-5p microRNA mimics at 30 nM using RNAiMAX (see above). After 27 h, cells were washed with 15 mL 1X PBS, covered with 5 mL 1X PBS, UV crosslinked with 254 nm light at 400 mJ/cm^2, and collected by scraping. Approximately 10 million crosslinked cells from each microRNA mimic treatment were pooled and processed for miR-eCLIP sequencing and

data analysis (Eclipse Bioinnovations, San Diego, CA). Raw reads for the AGO2 immunoprecipitation (IP) and the size-matched input are available at NCBI under BioProject accession PRJNA923105.

3.5.21. Statistical testing

Statistical tests are outlined above and in the Figure Legends. Biological replicates are shown in the figures and sample sizes are noted in the Figure Legends. Statistical tests were conducted in JMP or GraphPad Prism 8. Unless otherwise stated in the Figure Legends, tests were conducted using siNT as the comparator, and p value magnitude is represented as *, $p < 0.05$; **, $p < 0.01$; ***, $p < 0.001$.

Chapter 4

Biallelic splicing variants in the nucleolar 60S assembly factor RBM28 cause the ribosomopathy, ANE syndrome

Bryant CJ*, Lorea CF*, de Almeida HL, Jr., Weinert L, Vedolin L, Vairo FP†, Baserga SJ†. Biallelic splicing variants in the nucleolar 60S assembly factor RBM28 cause the ribosomopathy ANE syndrome. Proc Natl Acad Sci U S A. 2021;118(19). doi: 10.1073/pnas.2017777118. PubMed PMID: 33941690; PMCID: 8126767.

* *These authors contributed equally as co-first-authors.*

† *These authors contributed equally as co-contributing authors.*

4.1. Work Contributed

This manuscript was published in 2021. A team of Brazilian medical researchers led by FP Vairo (including Lorea CF, de Almeida HL, Jr., Weinert L, and Vedolin L) approached SJ Baserga in 2018 regarding the patient discussed in the paper. The medical researcher team investigated the patient's genotype and clinical features to produce all the data in **Figure 4-1**, which I assembled. SJ Baserga and I conceptualized the yeast experiments to test functionality of the novel Nop4/RBM28 variant proteins, as well as the minigene assays testing splicing. I conducted all experiments and data analysis outside of **Figure 4-1**, and assembled all figures. The manuscript was co-written by all authors.

4.2. Introduction

Ribosome biogenesis (RB) is the essential cellular process in which the complex macromolecular ribosomal machinery is manufactured and assembled, enabling protein translation (1, 8, 260, 384). Both ribosomal RNA (rRNA) and ribosomal protein (RP) components must be correctly synthesized, processed, modified, folded, translocated, and ultimately joined in the cytoplasm to engage in global protein synthesis (1, 8, 260). For eukaryotes, 4 rRNA molecules (1, 172) and about 80 RPs (1, 385, 386) form the core of the mature 40S and 60S ribosomal subunits. The demand for ribosomes during the cell cycle is immense: in a growing yeast cell more than 30 ribosomes are synthesized per second (39), while in a growing Hela cell this figure balloons to 125 ribosomes per

second (41). Over 200 *trans*-acting assembly factors (AFs) are necessary to achieve the fast and accurate ribosome assembly required to meet this tremendous cellular translational demand (1).

Given that up to 80% of cellular metabolism is devoted to ribosome biogenesis (387), it is unsurprising that defects in RB factors are causative of a class of human diseases known as ribosomopathies (1, 139, 140, 142, 143, 388, 389). Though not fully-understood, tissue-specific defects are the hallmark of ribosomopathies (139, 141). Tissues formed from hematopoietic or neural crest cell lineages are disproportionately affected, resulting in anemia, neutropenia, leukemia, and bone marrow failure diseases including Diamond-Blackfan Anemia (119, 145, 390-393) and Shwachman-Diamond syndrome (146, 394, 395), or craniofacial, dermatological, and neurological diseases including Treacher Collins syndrome (150-152), postaxial acrofacial dysostosis (396), and alopecia, neurologic defects, and endocrinopathy (ANE) syndrome (155-157, 160).

ANE syndrome (OMIM:612079) (155, 397) is a rare ribosomopathy defined by heterogeneous clinical features of variable severity including alopecia, neurological deformities and intellectual disability, and hormonal deficiencies with pubertal delay. In the only ANE syndrome case report published to-date, Nousbeck and coworkers studied five brothers of consanguineous parentage with variable ANE syndrome features, finding that ANE syndrome patient tissue samples had quantifiably fewer ribosomes and qualitatively dysmorphological rough endoplasmic reticula versus healthy control samples (155). All five patients were found to carry a homozygous missense variant (p.(Leu351Pro); L>P) in *RBM28* (155), a known essential large ribosomal subunit

(60S) assembly factor homologous to yeast Nop4 (166, 167, 398, 399). Follow-up studies further defined the clinical extent of endocrinopathy (156) and the biochemical mechanisms of hair and skin defects (157) or of inhibited ribosome biogenesis (160, 400) due to impaired function of RBM28 or its yeast homolog, Nop4. However, due to the rarity of the disease and lack of sufficient animal model studies, further investigation of ANE syndrome has been limited.

We report a female pediatric patient in the second family of ANE syndrome to date, unrelated to the family in the original case report (155). The novel ANE syndrome patient has a clinical presentation consistent with the definition of ANE syndrome but possesses differing genetic variants and molecular pathology. Using *in vivo* techniques, we demonstrate that the patient's novel compound heterozygous splicing variants in *RBM28* create one hypomorphic (ΔE5) and one null (ΔE8) allele with respect to overall growth and 60S pre-rRNA processing functions. By elucidating the pathology of a novel ANE syndrome patient, our results bolster and extend our understanding of this rare ribosomopathy, and reinforce the importance of proper nucleolar function in human health and disease.

4.3. Results

4.3.1. A novel female pediatric patient with alopecia, neurologic defects, and endocrinopathy (ANE) syndrome possesses biallelic splicing variants in RBM28

A Brazilian girl was born at term to nonconsanguineous parents with birth weight of 2,735 g (5th centile), head circumference (HC) of 32 cm (2nd centile) and Apgar score 10/10. No delays were noted in the first months of life. She started babbling at 12 months of age and she walked at 16 months. Her weight and height remained steadily at the 5th centile. She was born with sparse hair that fell out in the following few days and has not regrown. On physical examination, she has a branchial cleft cyst and mild facial dysmorphism, including prominent ears and very few sparse terminal hairs (**Figure 4-1A-C**). We observed dermatological features including an unexpected hypomelanosis guttata on the feet resembling hypomelanosis guttata idiopathica seen in adults in sun-exposed areas (**Figure 4-1D**), and a verrucous nevus accompanied by hypertrichosis on the right scapular region (**Figure 4-1E**). Compared to normal control hairs with a regular distribution of cuticular scales (**Figure 4-1F**), patient hairs examined using scanning electron microscopy displayed a very irregular cuticle (**Figure 4-1G**).

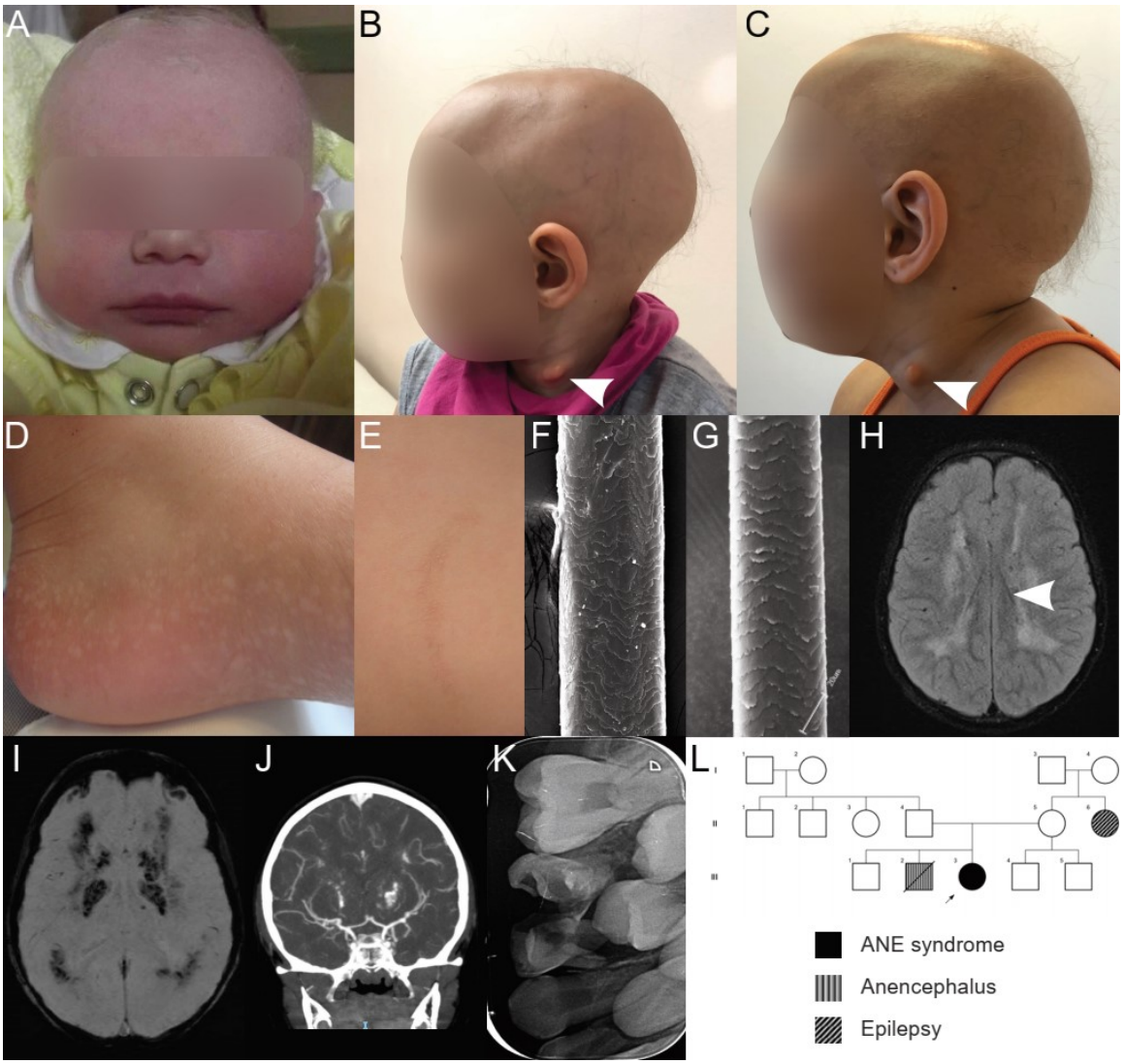

Figure 4-1. Clinical presentation and analysis of a novel female pediatric ANE syndrome patient.

(A) Patient during the newborn period.

(B-C) Patient at 3 years (**B**) and 6 years (**C**) of age. Note the sparse hair, branchial cleft cist on the neck (white arrowhead), and prominent ears.

(D-E) Dermatological features including acral gutate hypomelanosis on the feet (**D**) and verrucous nevus on the right scapular region (**E**).

(F-G) Scanning electron microscopy of a normal control hair (**F**) versus a hair from the patient (**G**), which displays an irregular hair cuticle. Micrographs were imaged with 500X magnification.

(H) Fluid-attenuated inversion recovery (FLAIR) image showing diffuse white matter lesions and periventricular cysts (arrowhead).

(I) Susceptibility weighted imaging (SWI) MRI indicating diffuse calcifications affecting basal ganglia and subcortical white matter.

(J) Angiotomography image showing middle cerebral artery stenosis and presence of collateral circulation.

(K) Premolars with double roots.

(L) Patient family pedigree. One of the proband's siblings died *in utero* diagnosed with anencephaly; no necropsy or genetic testing was performed.

The patient also presented with aberrant brain features but normal metabolite and endocrine levels. At four years of age, a brain magnetic resonance exam (MRI) with proton spectroscopy was performed and showed a slightly hypoplastic anterior hypophysis, mild volumetric reduction of white matter, small cysts in frontal and parietal white matter, and diffuse symmetric predominantly supratentorial and subcortical leukoencephalopathy with surrounding calcifications (**Figure 4-1H-I**). Proton spectroscopy was considered normal. At six years of age, brain vascular malformations were evidenced by computed angiotomography (**Figure 4-1J**). Chromosomal microarray and metabolic testing including biotinidase activity, plasma amino acids, urinary organic acids, and plasma acylcarnitines profiling were essentially normal. Endocrinological evaluation was first performed at three years of age. She was at 10th percentile for height (predicted height was at 25th percentile), her growth velocity was 6 cm/year and she had prepubertal sexual characteristics. Bone age was 2 years and 10 months when the chronological age was 3 years and 10 months (bone age was projected at the 50^{th} percentile of the stature growth chart). Full morning pituitary hormonal tests were normal and a stimulation test with 1 μg of ACTH excluded adrenal insufficiency. Pituitary hormone reevaluations at four, five and six years of age also yielded normal results (**Table 4-1**). Her growth velocity has been 6 cm/year in the last 3 years. Parathyroid hormone and calcium metabolism were also evaluated and results were considered normal for the patient's age.

Table 4-1. Novel ANE syndrome patient pituitary hormone evaluations.

Hormone	3 years	6 years	Reference Range	Units
Thyrotropin	2.7	2.5	0.35 – 4.94	μIU/mL
Free Thyroxin	1.02	0.83	0.70 – 1.48	ng/dL
Insulin like growth factor-1	58	89	3 years: 13 – 187; 6 years: 35 – 232	ng/mL
Growth Hormone	3.27	0.08	< 6	ng/mL
Morning Cortisol	9.4	15.1	> 18*	μg/dL
Corticotropin	1.0	12.1	7.2 - 63.3	pg/mL
Stimulation test with 1 mcg of ACTH	0: 4.3; 30′: 24.4; 60′: 23.0		> 18	μg/dL
Prolactin	6.36	53	5.18 – 26.53	ng/mL
Luteinizing hormone	0.16	<0.01	< 0.3	mIU/mL
Follicle stimulating hormone	2.7	0.83	1.0 – 4.2	mIU/mL
Estradiol	< 10	< 10	< 10	pg/mL

* Values above 18 μg/dL exclude adrenal insufficiency; values below 3 μg/dL confirm insufficiency. Values between 3 and 18 μg/dL should be referred to stimulation test.

A follow-up evaluation indicated the patient had persistent craniofacial and neurological defects. At six years of age, she had been treated for six dental caries and she had two teeth broken due to bruxism. Tooth root malformations were observed after dental extractions (**Figure 4-1K**). She has microcephaly (HC = 48.3 cm; < 3rd centile), limited speech capacity, and has no sphincter control. She is very active, but has underdeveloped fine motor skills. No other family members were identified with the same phenotype. It was her mother's fifth pregnancy, but the third from this couple (**Figure 4-1L**). The second pregnancy of this couple was interrupted due to anencephaly; the fetus was male and did not undergo any genetic testing (**Figure 4-1L**, striped box). Considering the patient's complex phenotype, whole exome sequencing (WES) was performed and revealed compound heterozygous variants in *RBM28* (NM_018077.2:c.[541+1_541+2delinsA]; [946G>T]). The first variant occurs in the canonical 5' splice site of exon 5 and is classified as pathogenic following the American College of Medical Genetics (ACMG) and the Association for Molecular Pathology (AMP) joint guidelines (401) (**Figure 4-2A**, top left). While the second variant was initially classified as a variant of uncertain significance (VUS) (NP_060547.2:p.(Ala316Ser)) and deemed benign or tolerated by PolyPhen2 (402) and SIFT (403), this variant is predicted to negatively impact splicing by the SpliceAI algorithm (404) due to its location at the 5' splice site of exon 8 (**Figure 4-2A**, top right). Each variant allele was inherited from an unaffected parent, as confirmed by Sanger sequencing, and neither variant was present in population-based databases including gnomAD (405). After taking the patient's clinical features and *RBM28*

genotype into consideration, she was ultimately diagnosed with ANE syndrome. **Table 4-2** compares characteristics of this patient to those previously reported (155).

Table 4-2. Comparison of clinical characteristics with previously reported cases.

	Nousbeck *et al.* (ref. (155))	**This report**
Sex	Male (5/5)	Female
Age (years)	20-39	4
Intellectual deficiency	+	+
Alopecia/hypotrichosis	+	+
Microcephaly	3/5	+
Dental caries	+	+
Hypodontia	3/5	Not present at this time
Limb contractures	4/5	-
Central adrenal insufficiency	5/5	Not present at this time
Brain MRI	Hypoplastic pituitary (only performed in one patient)	Hypoplastic pituitary and other findings described in the text
Branchial cleft cyst	-	+
Hypochromic spots	-	+

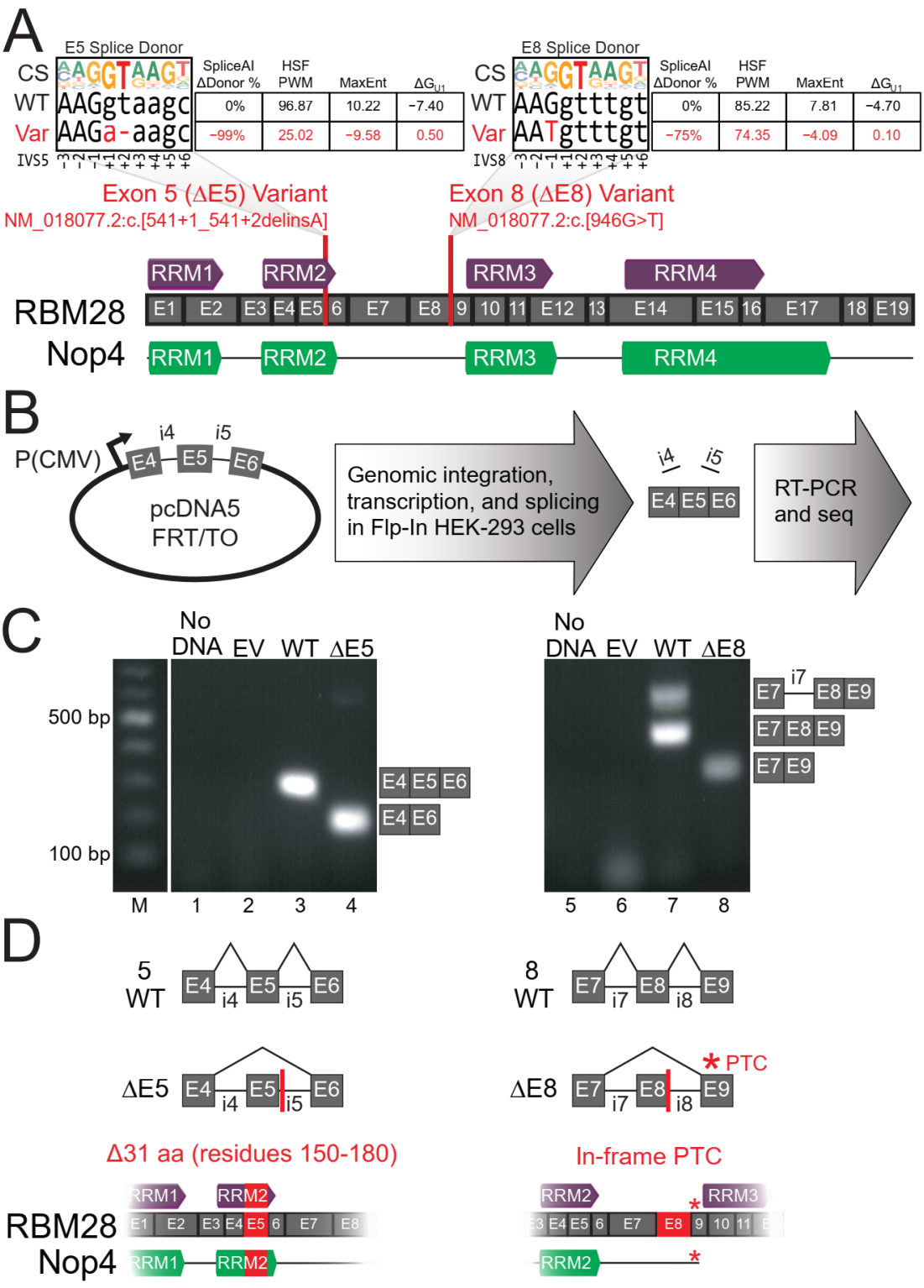
A
E5 Splice Donor
CS
WT AAGgtaagc
Var AAGa-aagc
IVS5
SpliceAI ΔDonor %
HSF PWM
MaxEnt
ΔG U1
0% 96.87 10.22 −7.40
−99% 25.02 −9.58 0.50
E8 Splice Donor
CS
WT AAGgtttgt
Var AATgtttgt
IVS8
0% 85.22 7.81 −4.70
−75% 74.35 −4.09 0.10
Exon 5 (ΔE5) Variant
NM_018077.2:c.[541+1_541+2delinsA]
Exon 8 (ΔE8) Variant
NM_018077.2:c.[946G>T]
RBM28
Nop4
RRM1 RRM2 RRM3 RRM4
E1 E2 E3 E4 E5 6 E7 E8 9 10 11 E12 13 E14 E15 16 E17 18 E19
B
P(CMV)
i4 i5
E4 E5 E6
pcDNA5
FRT/TO
Genomic integration, transcription, and splicing in Flp-In HEK-293 cells
RT-PCR and seq
C
No DNA EV WT ΔE5
500 bp
100 bp
E4 E5 E6
E4 E6
M 1 2 3 4
No DNA EV WT ΔE8
i7
E7 E8 E9
E7 E8 E9
E7 E9
5 6 7 8
D
5 WT
E4 i4 E5 i5 E6
ΔE5
E4 i4 E5 i5 E6
8 WT
E7 i7 E8 i8 E9
ΔE8
E7 i7 E8 i8 E9
* PTC
Δ31 aa (residues 150-180)
In-frame PTC
RBM28
Nop4
RRM1 RRM2
E1 E2 E3 E4 E5 6 E7 E8
RRM2 RRM3
E4 E5 6 E7 E8 9 10 11
Loss of Exon 5:
Predicted partial deletion in RRM2. Impairment of RNA binding and LSU assembly.
Loss of Exon 8:
Predicted in-frame PTC and truncation or NMD. Loss of crucial protein-protein interaction domains.

Figure 4-2. *In silico* analyses and cellular minigene splicing assays reveal that only the exon 5 variant *RBM28* allele will have residual function.

(A) Computational splicing prediction algorithms predict that patient variants negatively impact the function of the WT 5' splice site. Analysis of 5' splice site function without and with patient variant at exon 5 (**left**) or exon 8 (**right**). 5' splice site consensus sequence (CS) (406) is shown above WT and variant (Var, red) sequences at each exon's 5' splice site. Exonic nucleotides (IVS−3 to IVS−1) are capitalized and intronic nucleotides (IVS+1 to IVS+6) are in lowercase. Splicing algorithm scores are tabulated for SpliceAI (SpliceAI ΔDonor %), HumanSplicingFinder position weight matrices (HSF PWM), maximum entropy (MaxEnt), and free energy of base pairing to the U1 snRNA (ΔG, AnalyzerSpliceTool). 5' splice sites are considered broken if the decrease in SpliceAI Donor %, PWM, or MaxEnt scores upon mutation exceeds a variation threshold (>50% decrease for SpliceAI Donor %, >10% decrease for PWM, >30% decrease for MaxEnt), or if the ΔG of U1 snRNA base pairing is unfavorable ($\Delta G_{U1} > 0$). (**Bottom**) Location of exons (gray), RNA recognition motif (RRM) protein domains (purple or green), and patient variants (red) at exons 5 and 8 in human *RBM28* and yeast Nop4.

(B) Schematic of minigene splicing assay for a generic transcript containing three exons and two introns. The gene fragment of interest (minigene, gray) was cloned into the CMV expression cassette of the pcDNA5 FRT/TO vector. After genomic integration into HEK-293 Flp-In T-REx cells, the fragment is transcribed and spliced by the cellular machinery. Total RNA is isolated and analyzed by RT-PCR and sequencing.

(C) RT-PCR and sequencing results of WT and variant (Var) exon 5 and exon 8 minigene constructs. WT and patient variant *RBM28* minigenes were constructed from a genomic library clone using PCR and site-directed mutagenesis. Spliced transcripts were amplified from total cDNA and separated by agarose gel electrophoresis. No DNA (Lanes 1 and 5) and empty pcDNA5 vector (EV, Lanes 2 and 6) PCR controls were run. Sequencing results are diagrammed to the right of each image. M, 1 kb+ ladder marker.

(D) Deleterious effects on proteins translated from patient variant transcripts. Location of exons (gray), RNA recognition motif (RRM) protein domains (purple and green) for RBM28 and Nop4, and variant positions (red). (**Left**) Skipping exon 5 creates an in-frame partial deletion of RRM2, which is predicted to impair RNA binding and large subunit (LSU) assembly. Critical protein interaction domains necessary for LSU biogenesis are retained (RRM3 and RRM4). (**Right**) Skipping exon 8 creates a frame shift and premature termination codon (PTC, red asterisk) in exon 9, resulting in protein truncation or mutant transcript degradation via nonsense-mediated decay. Critical protein interaction domains necessary for LSU biogenesis are lost (RRM3 and RRM4).

4.3.2. In silico predictions and in vivo splicing assays show that patient RBM28 splice variants ablate wild-type splicing

The novel ANE syndrome patient has biallelic splicing variants at exon 5 and exon 8 of *RBM28*, which disrupt nucleotides in the 5' splice site consensus sequence (406) that are conserved in wild-type (WT) *RBM28*. The GT deleted from the exon 5 splice donor corresponds to the invariant GT in the 5' splice site consensus sequence (**Figure 4-2A**, top left), while the G>T variant in exon 8 alters the highly-conserved G at the IVS−1 position (**Figure 4-2A**, top right). The relative locations of each variant and the exons and protein domains of RBM28 and its well-conserved yeast ortholog Nop4 (26% identity) are also illustrated in **Figure 4-2A**. Because splice site sequence is essential for proper pre-mRNA processing and downstream translation of the RBM28 protein, we sought to discover what new or aberrant patterns of splicing might occur in the presence of either variant. In the absence of patient transcriptomic or proteomic data, we utilized both computational splicing prediction software packages and *in vivo* minigene splicing assays to determine the outcomes of the novel *RBM28* exon 5 (∆E5) or exon 8 (∆E8) splicing variants.

In silico splicing prediction algorithms predicted that the 5' splice site functionality of each of the exon 5 and exon 8 variants is severely impaired, and that only the exon 5 (∆E5) variant allele is likely to retain residual function. Overall, four different computational metrics [calculated with SpliceAI (404), HumanSplicingFinder (407), and AnalyzerSpliceTool (408)] predicted that each patient variant will negatively impact

the function of the corresponding WT *RBM28* 5' splice site (**Figure 4-2A**, inset tables). We hypothesize that each variant will disrupt WT splicing of exons 5 and 8 to the downstream exon, and any splicing that does occur will most likely use a different 5' splice site. Furthermore, holistic analysis of potential substituting splice sites using NNSplice (409) and COSSMO (410) (**Table 4-3**) predicted five possible exon 5 substitute splice sites (∆E5) that would create an in-frame partial deletion; these are predicted to be functional. In contrast, all predicted exon 8 (∆E8) substitute splice sites would contain premature termination codons, rendering ∆E8 a non-functional allele.

In order to determine which of the predicted substitute splice events predominate *in vivo*, we conducted minigene splicing assays in human HEK-293 cells followed by RT-PCR and sequencing analysis (**Figure 4-2B**). Wild-type minigene constructs predominately resulted in the expected WT spliced product containing three exons (**Figure 4-2C**, lanes 3 and 7). For the WT E8 construct, we also observed a minor band resulting from retention of intron 7 (**Figure 4-2C**, lane 7). Strikingly, introduction of the patient variants into exon 5 and exon 8 minigene constructs caused a complete shift from WT spliced products to splice products that cleanly skipped the variant exons (**Figure 4-2C**, lanes 4 and 8). This observation was experimentally verified in triplicate (**Figure 4-3A**). Since splice events upstream of exon 4 were predicted for the ∆E5 variant allele (**Table 4-3**), a longer minigene fragment spanning exon 1 through exon 6 was also analyzed for substitute splice events upon incorporation of the ∆E5 variant (**Figure 4-3B**). Splicing of the WT exon 1-6 minigene was normal, and introduction of the ∆E5 variant caused specific exon 5 skipping in the final splice product, consistent with results

from the shorter minigene (**Figure 4-3B**). The splice event observed for the ΔE5 variant corresponds to the predicted Δ31 partial deletion splice (removing amino acids 150-180) in **Figure 4-3A** (**Table 4-3** [ID 5.08]). Surprisingly, the exon 8 skipping event was not predicted by NNSplice or COSSMO, although it would still create a PTC in exon 9 and cause protein truncation or nonsense-mediated degradation (NMD) of the transcript.

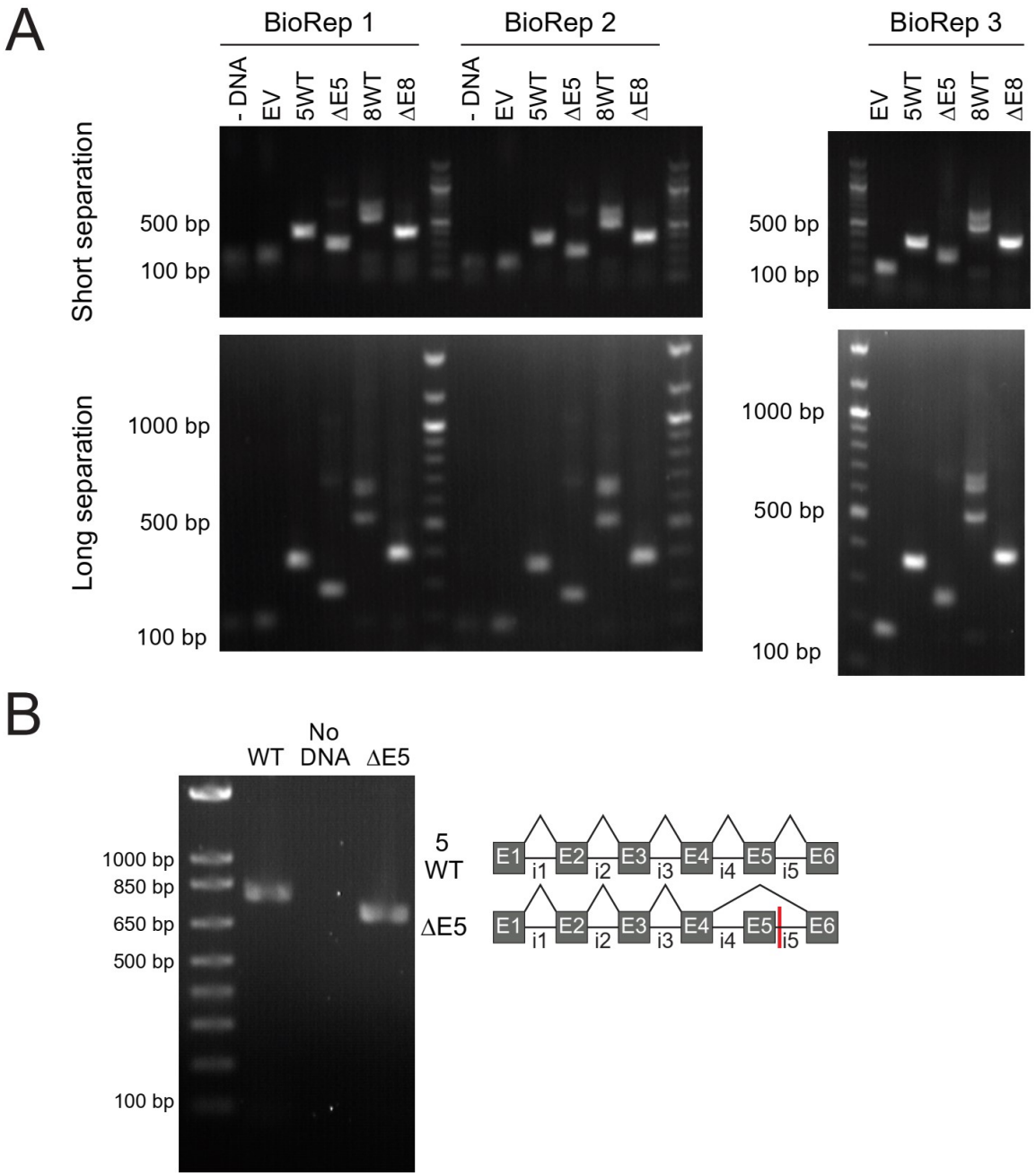

Figure 4-3. Patient variants cause aberrant 5' splice site choice.

(A) Cellular small minigene splicing assays show that each patient variant results in an aberrantly-spliced transcript, as compared to WT. Short and long gel separation times are shown for three biological replicates of the minigene assay. – DNA, no DNA control lane. EV, empty vector PCR control. 5WT and ΔE5, exon 5 WT and patient variant constructs. 8WT and ΔE8, exon 8 WT and patient variant constructs.

(B) Cellular long minigene splicing assay indicates the exon 5 patient variant specifically

causes only exon 5 skipping. WT and ΔE5, exon 5 WT and patient variant constructs. No DNA, no DNA control lane. Sequencing results are diagrammed to the right of the image.

Table 4-3. Predicted *RBM28* splicing events after the introduction of the exon 5 or exon 8 variant.

ID	Desc	GRCh37.p13 Position	NNSplice	COSSMO PSI	Product Length	Outcome
5.01	Exon 1	127,983,729		0.06856	618	Deletion 141aa from RRM 1 and 2, AA 40-180
	Intron 1 PTC	127,983,559				
5.02	Early Intron 1	127,982,873		0.01183	96	NMD
5.03	Mid Intron 1	127,981,343		0.04852	96	NMD
5.04	Mid Intron 1	127,981,171		0.02278	96	NMD
5.05	Mid Exon 2	127,979,755		0.08815	648	Deletion 111aa from RRM 1 and 2, AA 70-180
5.06	Exon 2	127,979,686		0.02423	671	Deletion 88aa from RRM 2, AA 93-180
5.07	Exon 3	127,979,280		0.01043	147	Frameshift, PTC in Exon 6, NMD
5.08	Exon 4	127,978,779		0.0267	728	Deletion 31aa in middle of RRM 2, AA 150-180
	Intron 4 PTC	127,978,741				
5.09	Mid Intron 4	127,978,538		0.02261	162	NMD
5.1	Mid Exon 5	127,978,342	0.91			Deletion of 13 residues in RRM 2, AA 168-180
5.11	Exon 5 (WT)	127,978,303	1	0.51287	759	WT
5.11-Mut	Exon 5 (Mutant)	127,978,303	N/A			
	Intron 5 PTC	127,978,253				
5.12	Intron 5	127,978,179	0.4		197	NMD
5.13	Intron 5	127,978,095	0.92		197	NMD
5.14	Intron 5	127,978,032	0.79		197	NMD
5.15	Intron 5	127,977,908	0.76		197	NMD
5.16	Intron 5	127,977,856	0.23		197	NMD
5.17	Intron 5	127,977,842	0.66		197	NMD
5.18	Intron 5	127,977,770	0.74		197	NMD
5.19	Intron 5	127,977,582	0.93	0.05968	197	NMD
5.2	Intron 5	127,977,483	0.77		197	NMD
5.21	Intron 5	127,977,435	0.29		197	NMD

ID	Desc	GRCh37.p13 Position	NNSplice	COSSMO PSI	Product Length	Outcome
5.22	Intron 5	127,977,307	0.94		197	NMD
8.01	Exon 8 (WT)	127,975,596	0.85	0.09691	759	WT
8.01-Mut	Exon 8 (Mutant)	127,975,596	0.01	N/A		
	Intron 8 PTC	127,975,579				
8.02	Intron 8	127,975,592		0.01037	321	NMD
8.03	Intron 8	127,975,428		0.02601	321	NMD
8.04	Intron 8	127,975,388	0.63		321	NMD
8.05	Intron 8	127,975,278	0.98	0.27868	321	NMD
8.06	Intron 8	127,975,070	0.44		321	NMD
8.07	Intron 8	127,974,954	0.48		321	NMD
8.08	Intron 8	127,974,818	0.23		321	NMD
8.09	Intron 8	127,974,804	0.27		321	NMD
8.1	Intron 8	127,974,782	0.29		321	NMD
8.11	Intron 8	127,974,747		0.01143	321	NMD
8.12	Intron 8	127,974,676	0.19		321	NMD
8.13	Intron 8	127,974,582	0.98		321	NMD
8.14	Intron 8	127,974,303	0.1		321	NMD
8.15	Intron 8	127,974,259	0.2		321	NMD
8.16	Intron 8	127,974,220	0.96		321	NMD
8.17	Intron 8	127,974,159	0.14	0.48842	321	NMD
8.18	Intron 8	127,974,042	0.12		321	NMD
8.19	Intron 8	127,973,845	0.87		321	NMD
8.2	Intron 8	127,973,694	0.31		321	NMD
8.21	Intron 8	127,973,646	0.25		321	NMD
8.22	Intron 8	127,973,553	0.61		321	NMD

4.3.3. Only the exon 5 (∆E5) patient variant allele retains residual function in large ribosome subunit RNA biogenesis in yeast

Since RBM28 and its well-conserved yeast homolog Nop4 have been shown to be essential in human CRISPR knockout screens (411-413), animal models (414), and in yeast (167, 398), we reasoned that the novel ANE syndrome patient must possess some gene product functionality from the *RBM28* locus. Taken together, these results led us to hypothesize that the exon 8 variant allele (∆E8) has minimal functional potential and is effectively null, while the exon 5 variant allele (∆E5) retains residual functional potential and is likely hypomorphic. This model is consistent with the observation that each variant allele was inherited from different unaffected parents, assuming that development of ANE syndrome only occurs when total RBM28 function is less than 50% of the wild-type.

To test the hypothesis that the exon 5 variant is hypomorphic and the exon 8 variant is null, we constructed a yeast model in which loss of endogenous yeast Nop4 function could be tested for growth complementation by variant Nop4 or the orthologous RBM28 proteins (**Figure 4-4A**). Previously, the yeast homolog of human RBM28 known as Nop4 was used to study the impacts of the classical Leu>Pro ANE syndrome mutation on large subunit biogenesis and the LSU processome network (160). Nop4 and RBM28 were reported to be 26% identical and contain four aligning RRM domains (160). For completeness, we tested the functionality of both Nop4 and RBM28 variant proteins in the absence of endogenous Nop4. The variant proteins for RBM28 were generated directly from the coding sequence, while Nop4 variant proteins were rationally

designed by alignment (**Figure 4-4B**). For each wild-type protein, previously-generated Leu>Pro (L>P) variants mirroring the original case report were utilized (Leu306Pro in Nop4 and Leu351Pro in RBM28) (155, 160) while exon 5 and exon 8 deletion variants (∆E5 and ∆E8) were generated by Gibson cloning. Variant protein coding sequences were shuttled into the GPD-promoter expression cassette of the p414-GPD vector. Plasmids were transformed into a previously-constructed *P(GAL)::3HA-NOP4* strain, for which endogenous HA-tagged Nop4 expression is repressed in dextrose-containing media while FLAG-tagged rescue protein variants are constitutively expressed regardless of carbon source (**Figure 4-4A**). We biochemically verified that each strain exhibits carbon source-dependent expression of endogenous HA-Nop4 and carbon source-independent expression of extrachromosomal FLAG-tagged variant proteins via immunoblot (**Figure 4-4C**).

We assayed the ability of each variant protein to restore vegetative growth in the absence of endogenous Nop4. We chose to rescue at the optimal yeast growth temperature (30°C) as well as temperatures both lower (17°C and 23°C) and higher (37°C) than the optimum. Because ribosome biogenesis is an energy-intensive, kinetically-limited process (1, 415), restricting ambient energy via temperature decrease exacerbates any subtle defects that might exist between wild-type and mutant proteins, facilitating defect detection (cold-sensitive). Investigation of a higher temperature enabled us to detect the extent to which variants were energetically destabilized compared to the wild-type conformational fold (temperature-sensitive).

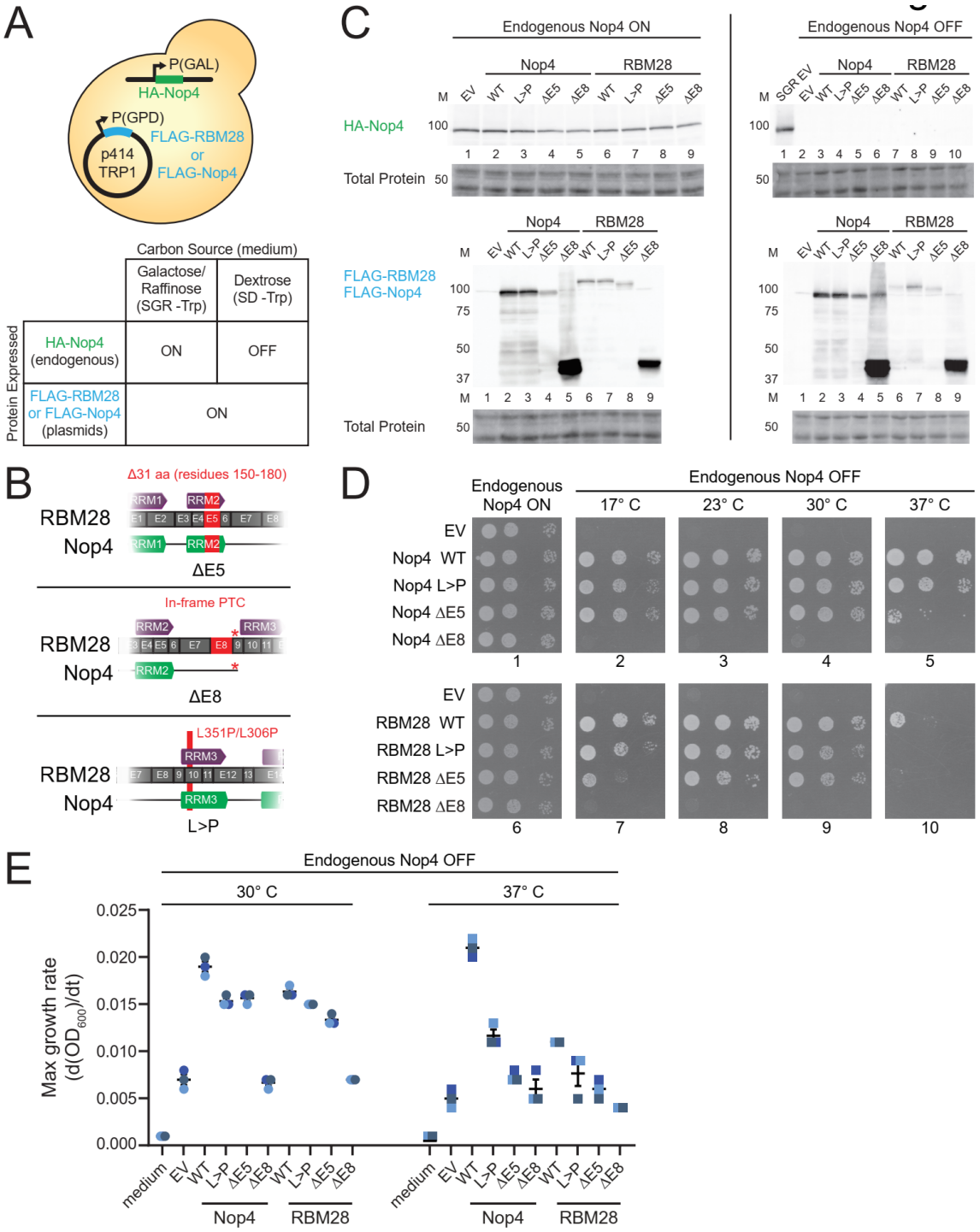

Figure 4-4. Variant Nop4 and RBM28 inhibit vegetative growth in a yeast model.

(A) Diagram of yeast model containing endogenous HA-tagged Nop4 under a repressible P(GAL) promoter (green) with plasmid-borne constitutively-expressed FLAG-tagged versions of Nop4 or RBM28 (blue). Endogenous HA-Nop4 is produced in SGR -Trp but repressed in SD -Trp; conversely, FLAG-Nop4 or FLAG-RBM28 is expressed in both conditions.

(B) Diagrams of patient variant protein constructs for RBM28 or Nop4. ΔE5, novel exon 5 variant; ΔE8, novel exon 8 variant; L>P, classical Leu>Pro variant (p.(Leu306Pro) in Nop4, p.(Leu351Pro) in *RBM28*). Modifications of the WT construct for each variant are noted in red. aa, amino acids; PTC (*), premature termination codon.

(C) Biochemical validation of the yeast model via immunoblotting. Strains were grown to log phase in liquid SGR -Trp (**left**, Endogenous Nop4 ON) or SD -Trp (**right**, endogenous Nop4 OFF) and protein was harvested for immunoblot analysis of either HA- or FLAG-tagged species. Note the presence of a faint, unrelated cross-reacting band present in all lanes around 100 kDa. Total protein loading controls were imaged for each blot. M, protein ladder size marker.

(D) Tenfold serial dilutions of each yeast strain were grown on SGR -Trp at 30 °C (**left**, Endogenous Nop4 ON) or SD -Trp between 17 and 37 °C (**right**, Endogenous Nop4 OFF). Strains were grown between 3 and 12 days, depending on temperature. EV, empty vector. L>P, Leu to Pro mutation (p.(Leu306Pro) in Nop4, p.(Leu351Pro) in *RBM28*). ΔE5 and ΔE8, proteins resulting from deletion of exon 5 or exon 8 respectively.

(E) Summary of the maximum growth rate attained by each strain using OD_{600} absorbance from an automated plate reader. Strains were grown in triplicate for 24 h at either 30 °C (**left**) or 37 °C (**right**) in SD -Trp (Endogenous Nop4 OFF). Individual values per experiment are overlaid on the mean ± SEM and are shown in **Table 4-4**. Data were analyzed using two-way ANOVA followed by Tukey's multiple comparisons test with all possible comparisons within each family.

First, we examined the functionality of WT and variant Nop4 proteins. Tenfold serial dilutions of strains on solid media illustrate that co-expression of endogenous Nop4 with all of the Nop4 constructs did not alter normal vegetative growth at 30°C, indicating no dominant negative effects on growth of the variant Nop4 proteins (**Figure 4-4D**, panel 1). Furthermore, WT, L>P, and ΔE5 variants of Nop4 largely support vegetative growth in the absence of endogenous Nop4 function, while empty vector (EV) plasmids or ΔE8 Nop4 exhibit severe growth defects at all temperatures examined (**Figure 4-4D**, panels 2-5). The Nop4 ΔE5 variant was sensitive to high temperatures (37°C) in this system (**Figure 4-4D**, panel 5), and the L>P and ΔE5 variants were slightly sensitive to low temperatures (17°C and 23°C) (**Figure 4-4D**, panels 2, 3).

Similarly, we probed the ability of human WT and variant RBM28 to complement Nop4 depletion in yeast. Again, co-expression of endogenous Nop4 with the RBM28 constructs did not alter normal vegetative growth at 30°C (**Figure 4-4D**, panel 6). Mirroring the Nop4 constructs, the WT, L>P, and ΔE5 RBM28 proteins supported growth in the absence of endogenous Nop4 at 23°C and 30°C (**Figure 4-4D**, panels 8-9). These variants also had increasingly limited ability to complement Nop4 depletion at 17°C (**Figure 4-4D**, panel 7). EV (empty vector) and ΔE8 RBM28 failed to rescue growth at all temperatures examined (**Figure 4-4D**, panels 6-10). Surprisingly, baseline WT RBM28 complementation was significantly impaired at 37°C (**Figure 4-4D**, panel 10), suggesting that human RBM28 sequence or structure may have diverged enough from Nop4 to fail to effectively complement Nop4 at 37°C. WT RBM28 was the only RBM28 construct to rescue some growth at 37°C, indicating

RBM28 variant proteins have impaired function compared to WT RBM28 (**Figure 4-4D**, panel 10). The failure of RBM28 constructs to complement Nop4 depletion at 37 °C versus at 30 °C was not attributable to diminished protein expression levels, as the expression of each protein was comparable at both 30 °C and 37 °C (**Figure 4-5A**). However, we hypothesize that the lower expression of the RBM28 constructs compared to the Nop4 constructs (**Figure 4-4C**, Endogenous Nop4 OFF) is due to suboptimal codon usage, limiting the potential for RBM28-mediated Nop4 complementation in this system. We conclude that the variant constructs for Nop4 and RBM28 rescue growth in our yeast model to differing degrees.

To verify these results, we collected growth curve data at absorbance OD_{600} using an automated plate reader (**Figure 4-5B-C**) and calculated the maximum growth rate for each strain (**Figure 4-4E, Table 4-4**). We found that within either the Nop4 or RBM28 construct family, the WT construct was the fittest, while the corresponding L>P and ΔE5 constructs were hypomorphic and the corresponding ΔE8 construct matched the growth of the null EV strain (**Figure 4-4E**, **Figure 4-5B-C**) at both 30 °C and 37 °C. As before, RBM28 strains demonstrated stark failure to complement the endogenous Nop4 at 37 °C. Altogether, our serial dilution results on plates and growth curve results in liquid culture indicate that ultimately, each variant cannot rescue growth as well as its WT counterpart in the absence of endogenous Nop4 across all temperatures tested, and in particular, both ΔE8 variants completely fail to rescue growth.

Table 4-4. Maximum growth rates for Nop4/RBM28 yeast strains at 30 and 37 °C.

Experiment	Media	Strain	Replicate	N Timepoints	Max(d(OD600)/dt)
30 C	SD -Trp	none	1	145	0.001
30 C	SD -Trp	none	2	145	0.001
30 C	SD -Trp	none	3	145	0.001
30 C	SD -Trp	EV	1	145	0.008
30 C	SD -Trp	EV	2	145	0.006
30 C	SD -Trp	EV	3	145	0.007
30 C	SD -Trp	Nop4 WT	1	145	0.019
30 C	SD -Trp	Nop4 WT	2	145	0.018
30 C	SD -Trp	Nop4 WT	3	145	0.02
30 C	SD -Trp	Nop4 LP	1	145	0.015
30 C	SD -Trp	Nop4 LP	2	145	0.015
30 C	SD -Trp	Nop4 LP	3	145	0.016
30 C	SD -Trp	Nop4 E5	1	145	0.016
30 C	SD -Trp	Nop4 E5	2	145	0.015
30 C	SD -Trp	Nop4 E5	3	145	0.016
30 C	SD -Trp	Nop4 E8	1	145	0.007
30 C	SD -Trp	Nop4 E8	2	145	0.006
30 C	SD -Trp	Nop4 E8	3	145	0.007
30 C	SD -Trp	RBM28 WT	1	145	0.016
30 C	SD -Trp	RBM28 WT	2	145	0.017
30 C	SD -Trp	RBM28 WT	3	145	0.016
30 C	SD -Trp	RBM28 LP	1	145	0.015
30 C	SD -Trp	RBM28 LP	2	145	0.015
30 C	SD -Trp	RBM28 LP	3	145	0.015
30 C	SD -Trp	RBM28 E5	1	145	0.013
30 C	SD -Trp	RBM28 E5	2	145	0.013
30 C	SD -Trp	RBM28 E5	3	145	0.014
30 C	SD -Trp	RBM28 E8	1	145	0.007
30 C	SD -Trp	RBM28 E8	2	145	0.007
30 C	SD -Trp	RBM28 E8	3	145	0.007
30 C	SGR -Trp	none	1	145	0
30 C	SGR -Trp	none	2	145	0.001
30 C	SGR -Trp	none	3	145	0
30 C	SGR -Trp	EV	1	145	0.01
30 C	SGR -Trp	EV	2	145	0.009
30 C	SGR -Trp	EV	3	145	0.009
30 C	SGR -Trp	Nop4 WT	1	145	0.01
30 C	SGR -Trp	Nop4 WT	2	145	0.009

Experiment	Media	Strain	Replicate	N Timepoints	Max(d(OD600)/dt)
30 C	SGR -Trp	Nop4 WT	3	145	0.008
30 C	SGR -Trp	Nop4 LP	1	145	0.009
30 C	SGR -Trp	Nop4 LP	2	145	0.009
30 C	SGR -Trp	Nop4 LP	3	145	0.009
30 C	SGR -Trp	Nop4 E5	1	145	0.009
30 C	SGR -Trp	Nop4 E5	2	145	0.01
30 C	SGR -Trp	Nop4 E5	3	145	0.009
30 C	SGR -Trp	Nop4 E8	1	145	0.009
30 C	SGR -Trp	Nop4 E8	2	145	0.009
30 C	SGR -Trp	Nop4 E8	3	145	0.009
30 C	SGR -Trp	RBM28 WT	1	145	0.01
30 C	SGR -Trp	RBM28 WT	2	145	0.01
30 C	SGR -Trp	RBM28 WT	3	145	0.009
30 C	SGR -Trp	RBM28 LP	1	145	0.009
30 C	SGR -Trp	RBM28 LP	2	145	0.01
30 C	SGR -Trp	RBM28 LP	3	145	0.009
30 C	SGR -Trp	RBM28 E5	1	145	0.01
30 C	SGR -Trp	RBM28 E5	2	145	0.009
30 C	SGR -Trp	RBM28 E5	3	145	0.009
30 C	SGR -Trp	RBM28 E8	1	145	0.01
30 C	SGR -Trp	RBM28 E8	2	145	0.01
30 C	SGR -Trp	RBM28 E8	3	145	0.009
30 C	water	none		3480	0.002
30 C	water	none	1	580	0.001
30 C	water	none	2	580	0.001
30 C	water	none	3	580	0.001
37 C	SD -Trp	none	1	145	0.001
37 C	SD -Trp	none	2	145	0.001
37 C	SD -Trp	none	3	145	0.001
37 C	SD -Trp	EV	1	145	0.006
37 C	SD -Trp	EV	2	145	0.004
37 C	SD -Trp	EV	3	145	0.005
37 C	SD -Trp	Nop4 WT	1	145	0.02
37 C	SD -Trp	Nop4 WT	2	145	0.022
37 C	SD -Trp	Nop4 WT	3	145	0.021
37 C	SD -Trp	Nop4 LP	1	145	0.011
37 C	SD -Trp	Nop4 LP	2	145	0.013
37 C	SD -Trp	Nop4 LP	3	145	0.011
37 C	SD -Trp	Nop4 E5	1	145	0.008
37 C	SD -Trp	Nop4 E5	2	145	0.007

Experiment	Media	Strain	Replicate	N Timepoints	Max(d(OD600)/dt)
37 C	SD -Trp	Nop4 E5	3	145	0.007
37 C	SD -Trp	Nop4 E8	1	145	0.008
37 C	SD -Trp	Nop4 E8	2	145	0.005
37 C	SD -Trp	Nop4 E8	3	145	0.005
37 C	SD -Trp	RBM28 WT	1	145	0.011
37 C	SD -Trp	RBM28 WT	2	145	0.011
37 C	SD -Trp	RBM28 WT	3	145	0.011
37 C	SD -Trp	RBM28 LP	1	145	0.009
37 C	SD -Trp	RBM28 LP	2	145	0.009
37 C	SD -Trp	RBM28 LP	3	145	0.005
37 C	SD -Trp	RBM28 E5	1	145	0.007
37 C	SD -Trp	RBM28 E5	2	145	0.006
37 C	SD -Trp	RBM28 E5	3	145	0.005
37 C	SD -Trp	RBM28 E8	1	145	0.004
37 C	SD -Trp	RBM28 E8	2	145	0.004
37 C	SD -Trp	RBM28 E8	3	145	0.004
37 C	SGR -Trp	none	1	145	0.001
37 C	SGR -Trp	none	2	145	0.001
37 C	SGR -Trp	none	3	145	0.001
37 C	SGR -Trp	EV	1	145	0.012
37 C	SGR -Trp	EV	2	145	0.012
37 C	SGR -Trp	EV	3	145	0.012
37 C	SGR -Trp	Nop4 WT	1	145	0.012
37 C	SGR -Trp	Nop4 WT	2	145	0.012
37 C	SGR -Trp	Nop4 WT	3	145	0.009
37 C	SGR -Trp	Nop4 LP	1	145	0.012
37 C	SGR -Trp	Nop4 LP	2	145	0.011
37 C	SGR -Trp	Nop4 LP	3	145	0.013
37 C	SGR -Trp	Nop4 E5	1	145	0.012
37 C	SGR -Trp	Nop4 E5	2	145	0.013
37 C	SGR -Trp	Nop4 E5	3	145	0.012
37 C	SGR -Trp	Nop4 E8	1	145	0.013
37 C	SGR -Trp	Nop4 E8	2	145	0.012
37 C	SGR -Trp	Nop4 E8	3	145	0.009
37 C	SGR -Trp	RBM28 WT	1	145	0.018
37 C	SGR -Trp	RBM28 WT	2	145	0.009
37 C	SGR -Trp	RBM28 WT	3	145	0.009
37 C	SGR -Trp	RBM28 LP	1	145	0.016
37 C	SGR -Trp	RBM28 LP	2	145	0.01
37 C	SGR -Trp	RBM28 LP	3	145	0.01

Experiment	Media	Strain	Replicate	N Timepoints	Max(d(OD600)/dt)
37 C	SGR -Trp	RBM28 E5	1	145	0.012
37 C	SGR -Trp	RBM28 E5	2	145	0.01
37 C	SGR -Trp	RBM28 E5	3	145	0.009
37 C	SGR -Trp	RBM28 E8	1	145	0.015
37 C	SGR -Trp	RBM28 E8	2	145	0.012
37 C	SGR -Trp	RBM28 E8	3	145	0.012
37 C	water	none		3480	0.001
37 C	water	none	1	580	0.001
37 C	water	none	2	580	0.001
37 C	water	none	3	580	0.001

A

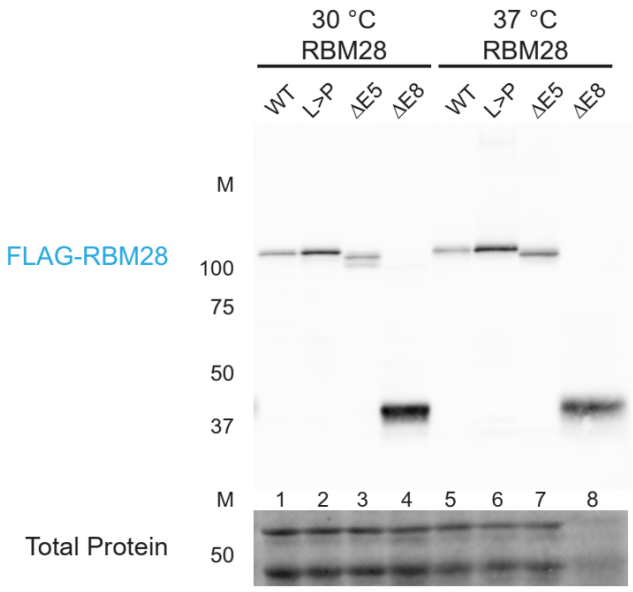
30 °C
RBM28
37 °C
RBM28
WT
L>P
ΔE5
ΔE8
WT
L>P
ΔE5
ΔE8
FLAG-RBM28
M
100
75
50
37
M
1
2
3
4
5
6
7
8
Total Protein
50

B

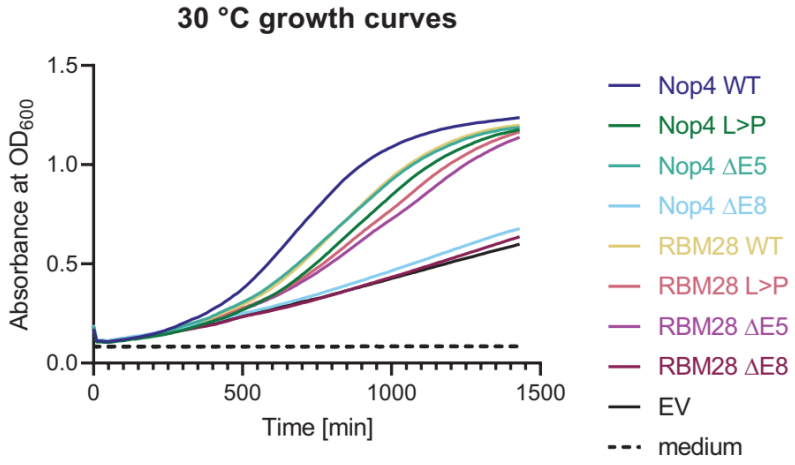
30 °C growth curves
Absorbance at OD600
1.5
1.0
0.5
0.0
0
500
1000
1500
Time [min]
Nop4 WT
Nop4 L>P
Nop4 ΔE5
Nop4 ΔE8
RBM28 WT
RBM28 L>P
RBM28 ΔE5
RBM28 ΔE8
EV
medium

C

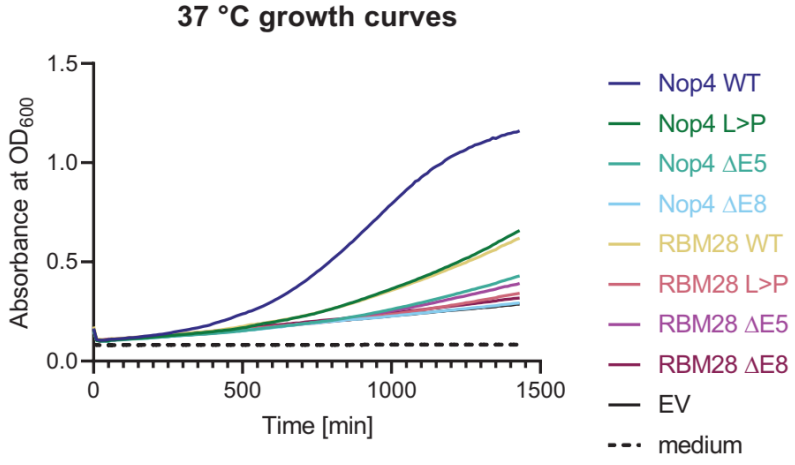
37 °C growth curves
Absorbance at OD600
1.5
1.0
0.5
0.0
0
500
1000
1500
Time [min]
Nop4 WT
Nop4 L>P
Nop4 ΔE5
Nop4 ΔE8
RBM28 WT
RBM28 L>P
RBM28 ΔE5
RBM28 ΔE8
EV
medium

Figure 4-5. Verification of exogenous RBM28 expression, and yeast complementation growth assays.

(A) *RBM28* constructs are expressed at similar levels at 30 °C and 37 °C. FLAG-RBM28 construct-expressing yeast strains were cultured in SD -Trp at the indicated temperature, and total protein was extracted and immunoblotted. Total protein loading controls were imaged for the blot. M, protein ladder size marker.

(B-C) Yeast strain growth curves indicate the L>P and ΔE5 variant constructs are hypomorphic, while the ΔE8 constructs are functionally null. Average OD_{600} absorbance values for three technical replicates are plotted for growth curves taken over 24 h at either 30 °C (**B**) or 37 °C (**C**).

Finally, we assayed the ability of each protein construct to rescue ribosome biogenesis in the absence of endogenous Nop4. Given Nop4's established roles in early endonucleolytic cleavage of the pre-rRNA precursor, mature 25S rRNA biogenesis, and as a hub protein in the LSU processome (160, 166, 167, 398, 416), we hypothesized that the patient variant proteins would only partially rescue levels of mature 25S rRNA and pre-rRNA precursor intermediates. In particular, we expected that the 35S primary pre-rRNA transcript would accumulate at the expense of large subunit rRNAs in precursor (27S, 7S) or mature (25S) form (**Figure 4-6A**), as previously observed (160, 167, 398, 416).

Harnessing a previously successful strategy for examining hypomorphic alleles (160), we depleted each strain of endogenous HA-Nop4 for 48 h at 23°C, after which total RNA was isolated and purified. Using methylene blue staining for mature rRNAs, we observed that the 25S/18S rRNA ratios remained unchanged in the presence of endogenous Nop4 (**Figure 4-6B**, odd-numbered lanes). In contrast, we found sharp decreases in the 25S/18S ratios for the empty vector, the null ΔE8 Nop4, and null ΔE8 RBM28 variant proteins, indicating that they are unable to fully complement Nop4's role in mature large ribosomal subunit RNA production (**Figure 4-6B**, lanes 2, 10, 18).

We probed the extent to which pre-rRNA processing was interrupted upon complementation of Nop4 depletion by each variant protein. Northern blots using the ITS2 probe Oligo E (**Figure 4-6A**) revealed that pre-rRNA processing intermediate accumulation was not disrupted in a dominant negative manner when endogenous Nop4 and extrachromosomal protein constructs are co-expressed, consistent with our growth

and mature rRNA assays (**Figure 4-6C**, odd-numbered lanes). However, we observed abnormal accumulation of pre-rRNA processing intermediates for all protein variants compared to WT Nop4. Specifically, steady-state levels of the 27S precursor decreased relative to the 35S primary transcript, consistent with the previously-reported importance of Nop4 in early ITS1 cleavage (**Figure 4-6C**, even-numbered lanes) (160, 167, 398, 416). Compared to WT Nop4, the Nop4 variants all yielded decreased 27S/35S ratios on northern blots. Interestingly, WT human RBM28 only partially rescued pre-rRNA processing compared to Nop4 WT (**Figure 4-6C**, lane 12); however, the RBM28 variants also exhibited decreased 27S/35S ratios compared to RBM28 WT (**Figure 4-6C**, lanes 14, 16, 18). Thus, while L>P and ΔE5 constructs were able to rescue growth and mature rRNA production, these mutants failed to completely rescue pre-rRNA processing according to the more sensitive northern blotting assay.

We also examined 7S RNA precursor levels relative to the 35S primary transcript. While mean 7S/35S ratios for all mutants and WT RBM28 decreased by 20 to 80% compared to Nop4 WT, these comparisons were not statistically significant due to high variability from three outlier measurements (**Figure 4-7**). Additionally, stark failure of WT and variant human RBM28 to rescue 7S RNA precursor levels indicates that RBM28 cannot complement in the C_2 cleavage step in ITS2 (**Figure 4-6A, Figure 4-6C, Figure 4-7**). Together, these data demonstrate that patient variants of Nop4 and RBM28 cause aberrant large subunit pre-rRNA processing, and in the most severe cases, significantly impair LSU biogenesis and growth of yeast.

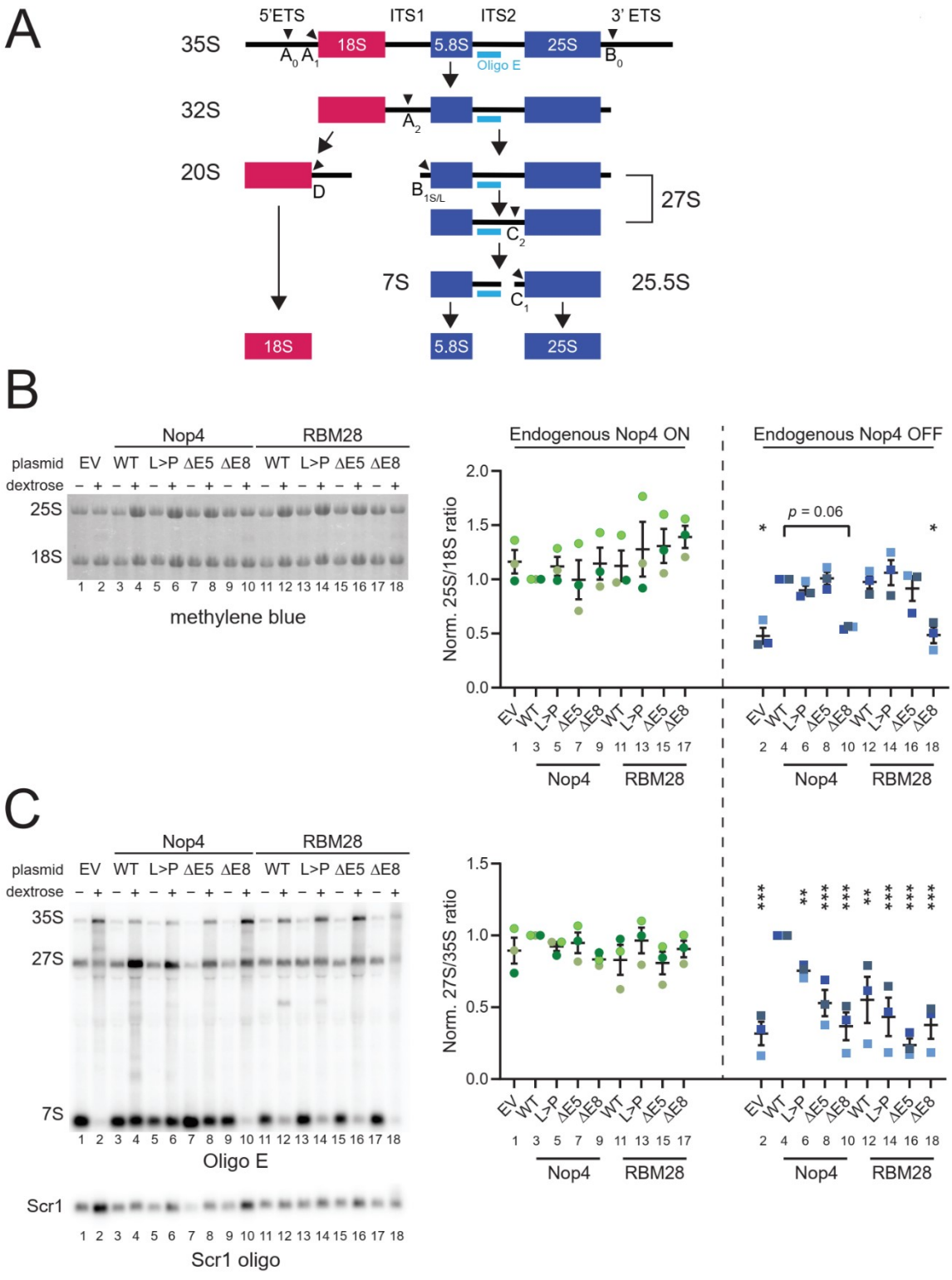

Figure 4-6. Nop4 and RBM28 variants fail to rescue mature 25S production and pre-ribosomal RNA processing in ITS2.

(A) Diagram of pre-ribosomal RNA (pre-rRNA) processing in *Saccharomyces cerevisiae*.

The 35S primary transcript undergoes endonucleolytic cleavage steps (arrowheads) and exonuclease trimming to render three of the four mature rRNAs. Nonfunctional spacer regions (ETS and ITS segments) and pre-rRNA intermediates are labeled. The small subunit 18S rRNA is shown in red, while the large subunit 5.8S and 28S rRNAs are shown in dark blue. Oligo E is shown in light blue next to every intermediate detected by Oligo E via northern blot.

(B-C) Methylene blue staining of mature rRNAs (**B**) and northern blotting of pre-rRNA intermediates detected by Oligo E (**C**). Three μg of RNA from each strain was run side-by-side for samples with endogenous Nop4 ON or OFF (- or + dextrose, respectively). Blotting for Scr1 serves as a loading control for the northern blot. Quantification of three experiments is presented on the right. 25S/18S ratio is calculated in **B**, and 27S/35S ratio is calculated in **C**. Values are normalized to Nop4 WT for each endogenous Nop4 level. Individual values per experiment are overlaid on the mean ± SEM. Data were analyzed by repeated measures using two-way ANOVA followed by Dunnett's post-hoc test with comparison to Nop4 WT for each media condition. $p < 0.05$ (*), $p < 0.01$ (**), $p < 0.001$ (***).

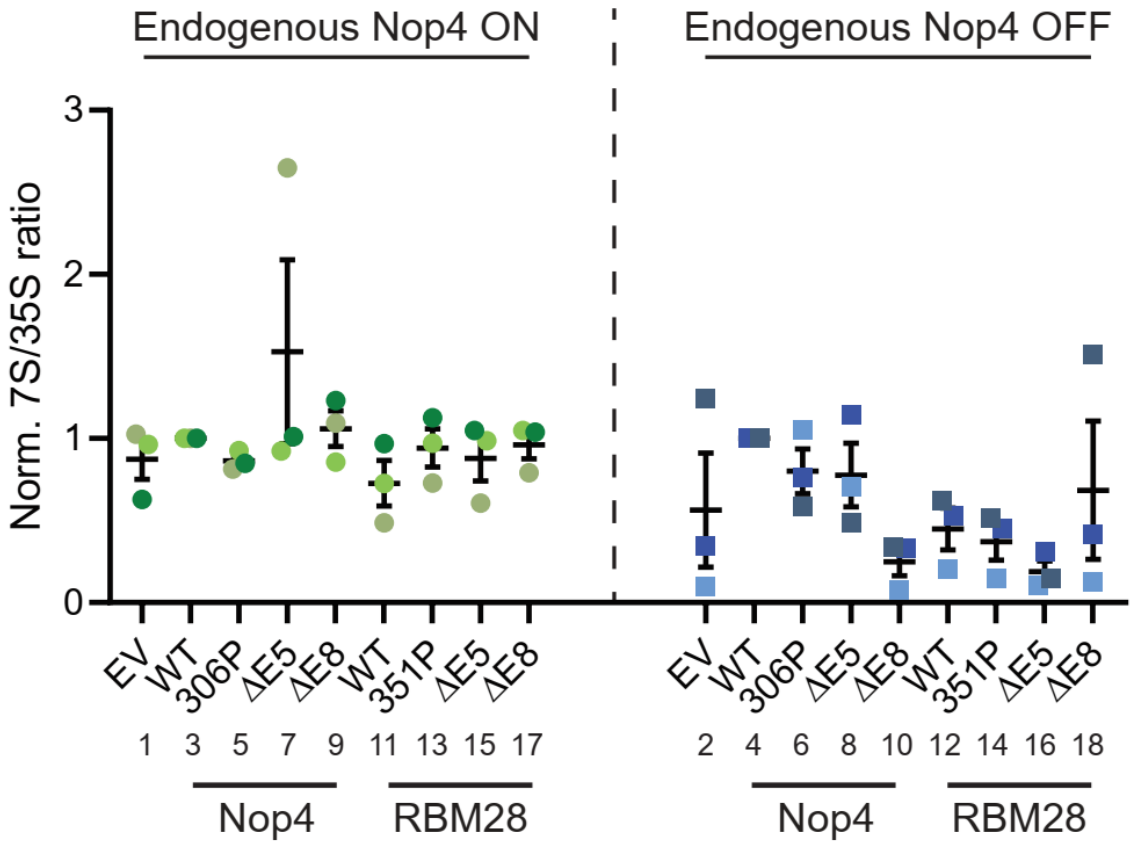

Figure 4-7. In yeast, patient variant proteins do not cause a statistically-significant decrease in 7S pre-rRNA precursor levels.

Northern blot quantification of the 7S/35S ratio for endogenous Nop4 ON or OFF levels. Three biological replicates are shown. Data were analyzed by repeated measures using two-way ANOVA followed by Dunnett's post-hoc test with comparison to Nop4 WT for each media condition. However, due to high variability for some samples, no significant differences were detected after testing.

4.4. Discussion

This is the second family with ANE syndrome, a rare ribosomopathy, reported to date and the first case of ANE syndrome in a female pediatric patient. ANE syndrome is caused by defects in the essential large ribosomal subunit assembly factor RBM28 (Nop4 in yeast). This ANE syndrome patient has a clinical presentation that is similar to that observed in the initial presentation of the disease (155), but harbors a novel molecular pathology featuring deleterious biallelic splicing variants affecting two different exons of the *RBM28* gene. *In silico* and *in vivo* experiments demonstrate that the exon 5 (ΔE5) variant results in a hypomorphic partial deletion in the RRM2 domain of RBM28, while the exon 8 (ΔE8) variant creates a premature stop resulting in a functionally null transcript. Both variants result in reduced growth and aberrant 60S-specific pre-rRNA processing in yeast, consistent with RBM28's known essential role as a large ribosomal subunit assembly factor. The identification of a second occurrence of ANE syndrome underscores the important role of the nucleolar RBM28 protein in maintaining human health and normal development.

This novel ANE syndrome patient broadly shares a clinical presentation and a recessive genetic etiology of disease with the first ANE syndrome case report (155), while her specific genetic pathology featuring biallelic splicing variants is new. Consistent with the established definition of ANE syndrome (155, 397), this patient's clinical features include alopecia, craniofacial defects, hypoplastic pituitary, and hair and skin defects. Unlike the previous ANE syndrome patients (155, 156), hormonal irregularities were not observed, although they may develop closer to the pubertal transition given the

presence of a hypoplastic pituitary. Both sets of cases are caused by recessive genetic variants in *RBM28*, a large ribosomal subunit assembly factor crucial for mature 28S rRNA production. However, while the previous ANE syndrome patients are homozygous for the RBM28 p.(Leu351Pro) (L>P) missense variant, this novel patient possesses compound heterozygous 5' splice site variants at exon 5 and exon 8 of *RBM28*. Additionally, one of the patient's unaffected parents bears the null exon 8 allele, demonstrating that ANE syndrome is not a disease of haploinsufficiency. Like Shwachman-Diamond syndrome (395) and Bowen-Conradi syndrome (388, 417), which are caused by recessive variants in the assembly factors SBDS and EMG1 respectively, ANE syndrome has an autosomal recessive pathology that contrasts with well-described dominant haploinsufficient ribosomopathies such as Diamond-Blackfan Anemia (DBA) and 5q- syndrome (140, 143, 390, 392).

The finding that RBM28 function is impaired by both the ∆E5 and ∆E8 variants is in line with the biochemical role of RBM28 (human) and Nop4 (yeast) in ribosome biogenesis (160, 166, 167, 398-400). Consistent with the discovery that the novel patient's ∆E5 allele is hypomorphic for growth and large subunit pre-rRNA processing, mutation of the Nop4 RRM2 RNP1 RNA binding motif causes reduced 60S subunit levels and impaired polysome formation (166). Likewise, nullity of the ∆E8 allele in RBM28 is consistent with the previous finding (160, 166) that the C-terminal half of Nop4 containing RRM3, RRM4, and the carboxy terminus is essential. Moreover, transcripts from the ∆E8 allele will contain a premature termination codon (PTC) and are likely degraded by NMD after a pioneer round of translation, which increases the

likelihood that this allele is null. In combination, these alleles comprise the molecular basis of this patient's ANE syndrome pathology.

We observe only subtle differences in yeast growth between WT and the hypomorphic L>P or ΔE5 variants, even at reduced temperatures where ribosome biogenesis is restrictive. Although one might expect hypomorphic variants of an essential ribosome assembly factor to yield greater impairment in growth, we emphasize that when coupled with the null ΔE8 allele in the novel patient, the hypomorphic ΔE5 variant retains enough residual function to support life. This result underscores that partially functional, but not completely null, mutations in *RBM28* are a hallmark of ANE syndrome.

While several yeast pre-60S cryo-EM structural models are now available (162-164), Nop4 is conspicuously absent in them, perhaps due to the transient nature of its interaction as demonstrated by proteomics experiments (165). Failure to localize Nop4 in pre-60S structures obscures its direct *in vivo* RNA and protein interactions, precluding structural insight into how ANE syndrome genetic variants interfere with normal Nop4 RNA binding and hub protein functions. In addition to affinity purification of early pre-60S particles, cryo-EM methods utilizing cross-linking (418, 419) or powerful *in silico* purification (420, 421) may enable localization of Nop4 and its contact partners in the pre-LSU complex. Careful mutational studies could also reveal the structural consequences of ANE syndrome variants on LSU biogenesis. Additional structural studies of early pre-60S particles containing Nop4 will more fully define Nop4's role in ribosome biogenesis and the structural consequences of ANE syndrome genetic variants.

In the future, we anticipate that identification of additional cases of ANE syndrome and realization of more advanced models of disease will facilitate better understanding of the pathophysiology of ANE syndrome. As awareness increases about rare diseases affecting ribosome biogenesis and as exome or genome sequencing bears more fruit in the clinic, additional cases of ANE syndrome will likely be identified. As in our study, modeling novel variants of uncertain significance in biological systems will continue to aid in variant classification. Furthermore, since the study of ANE syndrome variants in a strictly cellular context cannot directly reveal the neurological and developmental consequences of the disease, investigating *RBM28* variants in animal models will illuminate how brain development is differentially impaired by each of the three known ANE syndrome variants. Additional clinical and basic scientific studies will allow us to better grasp the developmental consequences of ANE syndrome and its underlying molecular mechanisms.

4.5. Materials and Methods

4.5.1. Patient evaluation

The patient in this report was 2 years old at the start of data collection. She was evaluated by specialists in clinical genetics, endocrinology, dermatology, pediatric neurology, phonoaudiology, and physical therapy at the Teaching Hospital of the Federal University of Pelotas, Brazil. She underwent complementary clinical diagnostic tests,

including pituitary hormonal evaluation and two brain MRIs, at ages four and six. Molecular diagnosis was obtained by clinical exome sequencing. A hair sample was analyzed by electron microscopy. The patient's family signed study approvals for all testing and for the publication of this report. The present study was approved by the institutional review board of Federal University of Pelotas.

4.5.2. In silico *splicing prediction algorithms*

Web interfaces for HumanSplicingFinder [HSF (407)] and AnalyzerSpliceTool [AST (408)] were used to calculate the severity of each novel *RBM28* patient variant. SpliceAI (404) was run from a command line in a UNIX environment to evaluate the strength of a novel splice site. The COSSMO web interface (410) was used to identify possible splice sites that could substitute for the patient's defective WT splice sites. Analyses were executed for the splice acceptors of exon 6 and exon 9.

4.5.3. Oligonucleotide design and synthesis; sequencing

All primer oligonucleotides for cloning and sequencing were designed in the Geneious Prime software package (version 2019.0.4, Biomatters, Ltd., Auckland, NZ) and prepared by Yale Keck Oligonucleotide Synthesis (New Haven, CT). DNA sequencing was performed by GENEWIZ (Boston, MA).

4.5.4. Image acquisition and analysis

Images of agarose gels were acquired on an Alpha Innotech AlphaImager 2200. Chemiluminescent immunoblots and methylene blue-stained RNA blots were imaged with a Bio-Rad ChemiDoc, and radiolabeled RNA blots were imaged with an Amersham Typhoon IP Biomolecular Imager. Image quantification of gels and blots was conducted with ImageJ version 1.51j8. All quantifications were made using unaltered, uncompressed original image files. Entire images presented in the manuscript may be adjusted for lightness or contrast for better clarity and consistency. No data was obscured by such processing. All data analysis was conducted on unaltered raw images.

4.5.5. Molecular cloning and plasmid preparation

Minigene fragments were cloned into the empty pcDNA5/TO/FRT vector from the RP11-640G20 clone of the RPCI-11 Human Male bacterial artificial chromosome library (BACPAC Genomics). Primers spanning exon 4-exon 6, exon 7-exon 9, and exon 1-exon 6 (**Table 4-5**) were used to amplify DNA by PCR with Q5 High-Fidelity DNA Polymerase (New England Biolabs M0491S). Amplicons were restriction endonuclease cloned into pcDNA5 empty vector (KpnI-HF and NotI-HF, New England Biolabs). Site-directed mutagenesis was carried out via PCR with Q5 DNA polymerase and partially-overlapping mutagenic primers (383) (**Table 4-5**) to introduce patient mutations into the wildtype minigene constructs.

Table 4-5. Primers for minigene cloning.

Plasmid	Reaction type	Starting plasmid/clone	Backbone plasmid	F primer	R primer
pcDNA5/FRT/TO - E5	Restriction cloning	RP11-640G20 (BACPAC)	pcDNA5/FRT/TO	ACTGGGTACCTGTTC AGAAGATGACTTGAA GACAG	ACTGGCGGCCGCCT ATAGCAGAAACAGA CTGTGTATCTTTA
pcDNA5/FRT/TO - E8	Restriction cloning	RP11-640G20 (BACPAC)	pcDNA5/FRT/TO	ACTGGGTACCGTGA GGAAAAGAGCCATGA ATCTA	ACTGGCGGCCGCCT GATAAAAACAGTTT TCCCTTCATTC
pcDNA5/FRT/TO - Exon1-6	Restriction cloning	RP11-640G20 (BACPAC)	pcDNA5/FRT/TO	ACTGGGTACCACTTC CGGAATCTCTCGGC	ACTGGCGGCCGCCT ATAGCAGAAACAGA CTGTGTATC
pcDNA5/FRT/TO - E5 Insert GT>A	Site-directed mutagenesis overlap PCR	pcDNA5/FRT/TO - E5		GATAAAAGAAAGCTT TCTATACCCATATCA TTGACCCAGATATTT	GAAAGCTTTCTTTT ATCTCTTTCATGTT CATGCCTTTGAGAG
pcDNA5/FRT/TO - E8 Insert G>T	Site-directed mutagenesis overlap PCR	pcDNA5/FRT/TO - E8		AGGATAAATGTTTGT TTGGATTTTCATAAA TGTCTTTAGACTTTA	AAACAAACATTTAT CCTCTTGCTCCTCA GTGCTGG
pcDNA5/FRT/TO - Exon1-6 GT>A	Site-directed mutagenesis overlap PCR	pcDNA5/FRT/TO - Exon1-6		GATAAAAGAAAGCTT TCTATACCCATATCA TTGACCCAGATATTT	GAAAGCTTTCTTTT ATCTCTTTCATGTT CATGCCTTTGAGAG

Coding sequences for wild-type or Leu>Pro (L>P) versions of Nop4 (p.(Leu306Pro)) or RBM28 (160) (p.(Leu351Pro)) were shuttled into the p414GPD-3xFLAG vector. Gibson cloning was used to generate exon 5 and exon 8 deletion plasmids for RBM28 directly, or for Nop4 by alignment and rational design in Geneious. Constructs were verified by DNA sequencing.

4.5.6. Mammalian minigene splicing assays

Flp-In T-REx HEK293 cells (Invitrogen R75007) were a generous gift from P. Gallagher, Yale School of Medicine. Cells were grown in DMEM (Gibco 11965092) with 10% FBS (Gibco 16050122) and 15 μg/mL blasticidin S (Alfa Aesar J67216XF), and were incubated at 37 °C in a humidified atmosphere with 5% CO_2. To genomically integrate each minigene construct, cells were transfected with OptiMEM (Gibco 31985070), Lipofectamine 3000 (Invitrogen L3000015), and a 9:1 mass ratio of pOG44:pcDNA5 vectors according to the manufacturer's protocol. Approximately 11.6 μg pOG44 and 1.3 μg pcDNA5 were used to transfect cells in 10 cm dishes with each minigene construct. Cells were split to less than 25% confluency and 200 μg/mL hygromycin B (Gibco 10687010) was introduced to the media for selection. Selective media was changed every 2 days until confluency, when polyclonal populations were harvested. Genomic DNA was isolated from each line with DNeasy Blood & Tissue kits (QIAGEN 69504), PCR amplified, and sequenced to validate transfection and integration.

To isolate total RNA, clonal cell lines were seeded in 6-well plates and 1 μg/mL tetracycline was added after 24 h to induce minigene transcription. After 48 h, total RNA was harvested using TRIzol (Invitrogen 15596018). cDNA was synthesized from 1 μg total RNA using random hexamer primers with the iScript cDNA synthesis kit (Bio-Rad 1708890). cDNA was PCR amplified using Taq DNA Polymerase with ThermoPol buffer (New England Biolabs M0267S) using primers located in **Table 4-6**. The reaction products were separated on a 1.0% agarose gel containing ethidium bromide. For DNA sequencing, products were column purified; single band products were sequenced directly while products with multiple bands were TOPO-TA cloned before sequencing (Invitrogen 450030).

Table 4-6. Primers for minigene RT-PCR and sequencing.

Primer	**Primer sequence**
P5_seqF2	ATAGAAGACACCGGGACCGA
BGH_R_2	TAGAAGGCACAGTCGAGGCT

4.5.7. Yeast growth media, transformation, serial dilutions, and automated growth curve collection

Yeast-peptone (YP) media supplemented with 2% (w/v) dextrose (YPD) or 1% (w/v) galactose/1% (w/v) raffinose (YPGR) was used to grow YPH499 and *P(GAL)::3HA-NOP4* strains (160). Minimal media with either dextrose or galactose/raffinose sugar sources was supplemented with -Trp dropout mix to grow strains transformed with p414-GPD vectors (Takara Bio USA 630411, 630420, and

630413). Dextrose -Trp media is abbreviated as SD -Trp and galactose/raffinose -Trp media is abbreviated as SGR -Trp. Strains were depleted of endogenous HA-tagged Nop4 by first growing liquid cultures to log phase in SGR -Trp at 30°C and then starting SD -Trp cultures for depletion of HA-Nop4 using a 1:100 dilution of the SGR -Trp culture. Cultures were grown for 24 h at 30 °C or 37 °C, and 48 h at 23 °C. Cells were harvested for protein or RNA isolation in log phase, where OD_{600} was between 0.2 and 0.8.

A previously-constructed *P(GAL)::3HA-NOP4* background strain generated from a YPH499 parental strain (160) was transformed with p414-GPD plasmids containing Nop4 and RBM28 variants described above. The high-efficiency transformation protocol described by Gietz (422) was utilized to transform the background strain.

Tenfold serial dilutions to test growth were performed as previously described (160).

To collect growth curve data, a saturated culture of each strain was pelleted, washed with ddH_2O, resuspended in ddH_2O, measured at a 1:100 dilution at OD_{600} on a spectrophotometer, and diluted to 0.1 OD_{600} in either SGR -Trp or SD -Trp. The inner wells of a sterile 96-well microplate (Greiner Bio-One 655185, wells B2 to G11) were inoculated with 200 uL of medium or diluted yeast strain in technical triplicate for each medium condition, and sterile water was used to fill the outside perimeter wells to prevent medium evaporation. The lidded microplate was loaded onto a BioTek Synergy H1 Hybrid Multi-Mode Microplate Reader set to maintain temperature at 30 °C or 37

°C, as indicated, and whole-plate OD_{600} measurements were taken every 10 minutes for 24 h. Raw OD_{600} data was exported, and point-to-point OD_{600} differences were calculated in Excel as an approximation for the first-order derivative. Maximum growth rates for each strain replicate were calculated from these derivative calculations in JMP Pro 15, and data were graphed and analyzed by two-way ANOVA with Tukey's multiple comparisons test in GraphPad Prism 8.

4.5.8. Protein isolation and analysis

Total protein was isolated from yeast cells as previously described (423). Briefly, 15 mL of yeast in log phase (OD_{600} between 0.2 and 0.8) were harvested, centrifuged, washed in 1 mL ddH_2O, and resuspended in 1 mL cold 1.0 M lithium acetate on ice for 5 minutes. Cells were centrifuged again and lysed in 1 mL cold 400 mM sodium hydroxide on ice for 5 minutes. Cells were pelleted and all supernatant was removed before resuspension in 100 μL of 2.5X SDS loading buffer. Protein was boiled at 95°C for 3 minutes, centrifuged at maximum speed, and loaded onto a gel or frozen at -20°C. Handcast 8% SDS-PAGE gels containing 0.5% (v/v) trichloroethanol (Acros Organics 139441000) were used to separate total protein at 110 V for 2 h. Total protein was imaged using the ChemiDoc stain-free imaging protocol (Bio-Rad) to ensure even loading at the gel stage. Following membrane transfer with the Trans-Blot Turbo system (Bio-Rad), blots were imaged again for total protein without crosslinking to ensure transfer quality; these images are presented as blot loading controls. Immunoblotting was carried out using 5% (w/v) Omniblok dry milk (American Bio AB10109) in PBST (5%

(v/v) Tween) with 1:30,000 Monoclonal ANTI-FLAG® M2-Peroxidase (HRP) (Sigma A8592), or 1:2,000 mouse anti-HA (clone 12CA5) followed by 1:10,000 sheep peroxidase-linked anti-mouse IgG (GE Healthcare NXA931V).

4.5.9. RNA isolation and analysis

Human cell line total RNA isolation is described above. RNA was isolated from yeast cells following the protocol of Shedlovskiy, *et al.* (424) after depletion of endogenous HA-Nop4 (see above in Materials and Methods). Briefly, 15 mL of yeast in log phase (OD_{600} between 0.2 and 0.8) were washed in ddH_2O and pelleted, then resuspended in 400 μL FAE (formamide/EDTA, consisting of 98% (v/v) formamide and 2% (v/v) 0.5 M EDTA). Yeast were incubated for at least 10 minutes at 70°C and vortexed for 10 seconds before pelleting and supernatant collection. Extracted RNA was precipitated with 3 M sodium acetate and washed thrice with 75% ethanol. Three μg of purified total RNA was separated on a denaturing formaldehyde agarose gel, transferred to a Hybond-XL membrane (GE Healthcare), methylene blue-stained and imaged, and blotted with radiolabeled Oligo E or Scr1 as previously described (160).

4.6. Afterword

In this Afterword, I will provide additional commentary to further contextualize my work in the clinical diagnosis of rare diseases including ribosomopathies, and to introduce two novel RBM28 variants observed since our publication.

The observation that ribosomopathies often cause tissue-specific defects is well-appreciated but remains poorly-understood. In particular, several ribosomopathies

specifically affect cells derived from hematopoietic or neural crest lineages (139, 141, 143). Multiple mechanisms could be contributing to the tissue specificity associated with ribosomopathies, including cell-type sensitivity to TP53 stabilization or requirement for translation of cell-specific mRNA isoforms, as well as the presence of ribosome heterogeneity (139, 141). RB interruption can trigger the nucleolar stress response, leading to TP53 stabilization and induction of apoptosis (71). In animal models, inhibiting this TP53-mediated apoptosis in a ribosomopathy genetic background has been shown to often (partially) rescue aberrant differentiation and development of these tissues (153, 425-428), supporting tissue-dependent TP53 sensitivity as a mechanism. Next, the ribosome concentration hypothesis posits that a decrease in mature ribosomes following impaired RB may lead to stark changes in translation depending on the transcriptomic composition in a highly cell-dependent manner (139, 140, 429). In other words, the mRNA transcripts in a particular tissue may exist as specific isoforms with specific translation efficiencies, and therefore may have differential translational sensitivities to changes in ribosome concentration across tissues, which may have a causative role in ribosomopathy pathogenesis. However, current evidence conflicts on how exactly transcript elements, *e.g.*, 5' UTR length and structure, may contribute to the sensitivity of translation efficiency to changes in ribosome concentration (139, 430, 431). Lastly, heterogeneity in ribosome composition ("specialized ribosomes") across tissues could also contribute to tissue-specific translation efficiency leading to ribosomopathies (139, 432). Evidence is growing to support the functional existence of ribosomes differing in RP or rRNA composition, in both developmental and oncological

contexts (432). For ANE syndrome, an animal model could be key for evaluating the relative contributions of these mechanisms to the disease's pathogenesis. A mouse model would be most appropriate, as a primary clinical feature of ANE syndrome is alopecia, although hair-lacking zebrafish or *Xenopus tropicalis* models would enable facile examination of the craniofacial defects associated with this ribosomopathy.

In our patient's clinical story, inheritance of two different pathogenic splicing variants in *RBM28* were found to be causative of ANE syndrome. This contrasts with the current state of genetic knowledge about ribosomopathies, in which protein-coding missense variants or gene deletions of RPs or AFs have most often been attributed with causation. However, it is estimated that 15-60% of disease-causing variants may affect splicing (433). Therefore, additional pathogenic splicing variants affecting *RBM28* or other RB factors may be linked to ribosomopathies in the future. Although the majority of splicing variants affect the invariant GT or AG dinucleotides in the 5' or 3' splice site respectively, up to 30-40% of splice-disrupting variants affect conserved but non-essential nucleotides surrounding the invariant bases (433-436). Furthermore, in an analysis of somatic pan-cancer splicing variants, 46% of intronic variants were found to affect "deep" intronic sequences away from the canonical splice sites, resulting in activation of cryptic splice sites or polypyrimidine tracts, or disruption of authentic polypyrimidine tracts, branch points, or splicing enhancer or silencer elements (437). These data illustrate the high likelihood of missing functional splicing variants during medical genetic diagnosis.

While it is difficult to provide precise estimates for how many pathogenic splicing variants may currently be overlooked, combining whole genome or exome sequencing with advanced *in silico* splicing prediction algorithms and confirmatory RNA assays may improve detection of novel pathogenic splicing variants. Whole genome sequencing (WGS) was found to be slightly more sensitive for detecting exonic pathogenic variants and to have more uniform coverage than whole exome sequencing (WES) (438, 439). Since WES enriches for exonic reads rather than reads that may contain intronic variants in 5' or 3' splice sites, splicing enhancers or repressors, or the splicing branch point, WGS should be the new diagnostic standard given its rapidly decreasing marginal cost relative to WES (440). Ideally, WGS data would then be analyzed using advanced deep learning splicing algorithms (410, 441, 442) to quickly identify likely pathogenic splicing variants, followed by RNAseq or RT-PCR assays to corroborate functional impact on splicing in tissue.

At least two additional novel RBM28 variants have been observed since my publication, although both are missense variants of uncertain clinical significance. First, an R582Q variant [NM_018077.3(RBM28):c.1745G>A (p.Arg582Gln), ClinVarID 1028085] was evaluated by Baylor Genetics in 2019, first available on ClinVar in 2021. This variant occurs in the C-terminus of the RBM28 RRM4 domain. Second, a T728S variant [NM_018077.3(RBM28):c.2182A>T (p.Thr728Ser), ClinvarID 2435384] was evaluated by PerkinElmer Genomics in 2021, first available in ClinVar in 2023. This variant occurs at the far C-terminal end of the RBM28 protein, downstream of the RRM4 domain. Given that both variants were classified as variants of uncertain

significance (VUS) according to the 2015 American College of Medical Genetics guidelines, the effect of these variants on RBM28's function in RB and in human development are unclear. Future *in vivo* experiments in yeast, human cells, or an animal model system could test the degree to which novel RBM28 variants impair RB.

Chapter 5

Perspectives and Future Directions

5.1. Introduction

In this thesis, I present three aspects of my doctoral work which simultaneously advance the field of RB in the areas of methodology, basic science, and clinical molecular pathology. I developed a refined high-throughput assay for specifically measuring nucleolar rRNA biogenesis, a direct readout of nucleolar function, in **Chapter 2**. **Chapter 3** describes my systematic exploration of microRNAs, leading to the discovery of 72 novel microRNA negative regulators of RB and revealing microRNAs' potential to interrupt pre-rRNA processing for the first time. Finally, I relay findings from my international collaborative effort with CF Lorea, FP Vairo, and colleagues regarding a novel molecular basis for the rare ribosomopathy ANE syndrome involving *RBM28* biallelic splicing variants in **Chapter 4**.

While my work has answered a number of critical questions pertaining to the (mis)regulation of RB in humans, several new avenues have been paved for further exploration. Here in **Chapter 5**, I will discuss how my work invites inquiry into four continuing areas of research:

5.2 To what extent might ncRNAs impact nucleolar function in other ways?

5.3 How can the novel microRNA hits be studied with other techniques?

5.4 Why does nucleolar number change in MCF10A cells upon RB inhibition?

5.5 What is the precise nature of Nop4/RBM28's interaction with early pre-60S particles?

5.2. To what extent might ncRNAs impact nucleolar function in other ways?

Perhaps most importantly, my hypothesis that ncRNAs are the next frontier in RB regulation (**Chapter 1**) and my subsequent studies of microRNA mimics as modulators of nucleolar function (**Chapter 3**) raise many additional questions about how ncRNAs may govern the nucleolus. While I defined how 15 microRNA mimic hits affected RB using a battery of mechanistic assays in **Chapter 3**, the precise effects of the other 57 hits on nucleolar output remain unprobed. The scope of my study only allowed for examination of the hits in one cell line, MCF10A, but other cell lines could be probed in the future. Furthermore, the extent to which microRNA mimics may dysregulate pre-rRNA transcription is still unclear (**Figure 3-6**), and time constraints prevented me from investigating the hits' effects on other RB subprocesses, most notably pre-rRNA modification and pre-ribosome nuclear export. These questions merit future investigation.

While I was only able to test the extent to which the microRNA hits inhibited RB in MCF10A cells, future investigations could test how the hits affect RB in other cell lines. Given that most hits inhibited nucleolar rRNA biogenesis and that many hits within the 15-hit subset strongly interfered with pre-rRNA processing and global translation, the microRNA hits appear to target the conserved process of RB, which is likely to be essentially identical across human cell types. Time permitting, these hits should be tested in at least one additional non-cancerous cell line and one cancer cell line. First, I would use hTERT-immortalized, non-transformed human retinal pigment epithelial (RPE-1) cells, which have a nearly-diploid karyotype like MCF10A cells as well

as intact DNA damage checkpoints; the McStay group has extensively studied the NORs and nucleolar stress response of this line and has genetically manipulated entire chromosome-scale rDNA arrays to probe nucleolar formation (63, 443, 444). hTERT RPE-1 cells were also used in recent work by the Gerton laboratory that defined a novel, extreme nucleolar stress phenotype following CDK9 inhibition (77). The chromosomal normality and thorough study of RPE-1 cells in ribosome biogenesis make them an excellent secondary testbed for the novel microRNA hits. Second, I would test the microRNA hits in a cancerous cell line, likely one derived from melanoma. Nucleolar number and size are strongly associated with melanoma tumor thickness and mitogenicity, and these nucleolar features are often used to score melanoma tumor aggressiveness (445, 446). Furthermore, therapeutic RB inhibition has been studied in melanoma by multiple groups (183, 184, 205, 447). An analysis of 42 melanoma cell lines found COLO 849 to be the line most similar to patient tumors, while commonly-used A375 cells ranked fourth (448). Either of these lines would be appropriate for investigating the novel microRNA hits in an oncology context.

Are there cellular settings in which microRNAs promote RB? This line of inquiry is compelling because two microRNA biogenesis enzymes, Drosha and Dicer, are known to be essential for maintaining normal levels of global translation and pre-60S pre-rRNA processing in addition to microRNA production (123, 269). Moreover, Drosha is required for Microprocessor complex-mediated upregulation of RP transcripts (449), and at least one microRNA, miR-10a, can promote RP translation (122); both mechanisms are attributed to the 5' TOP motifs common in the 5' UTR of RP transcripts

(450). These results suggest that, in normal physiological conditions, production of microRNAs may enhance ribosome production on average.

Therefore, other microRNAs may play yet-undiscovered roles as promoters of RB. Although my collaborators, L Abriola and YV Surovtseva, conducted a complementary microRNA hairpin inhibitor screen in MCF10A cells, only ≈5 candidate hits were observed — and each would require further examination (**Table 5-1**). A single one-nucleolus hit was identified (hsa-miR-149-3p), along with a handful of putative 5+ nucleoli hits including two members of the miR-520/MIR-430 family (hsa-miR-520d-3p, hsa-miR-520h, hsa-miR-638, hsa-miR-4291, hsa-miR-6724-5p). Notably, the novel microRNA negative RB regulator, hsa-miR-526b, is also a member of the MirGeneDB MIR-430 family. Given that these hits were identified from a microRNA inhibitor screen, further study may reveal them as novel positive regulators of RB. However, because microRNA expression depends on cell type (451), additional work in cell lines besides MCF10A may reveal other candidate microRNA positive regulators of RB. Thus, microRNA-mediated regulation of RB remains a fertile field for further inquiry. In **Chapter 5.3**, I discuss other techniques that may be useful in these future studies.

LncRNAs comprise another important class of ncRNAs that have yet to be systematically explored for functions in RB regulation (53). Like microRNAs, a handful of lncRNAs are already known to modulate RB, primarily at the steps of pre-rRNA transcription and processing (53, 452). For example, the lncRNAs LoNA (453), pRNA (454), PAPAS (455), and EPB41L4A-AS1 (456) all inhibit rDNA transcription (53,

452). While ascertaining a mechanism-of-action for lncRNA-mediated RB modulation may require more creativity and effort compared to microRNAs, whose mechanism is well-understood, the proven ability of lncRNAs to regulate RB encourages their further study.

Table 5-1. Possible hits from microRNA hairpin inhibitor screen.

Mature Name	Mature Sequence	n replicates above cutoff (one-nucleolus)	n replicates above cutoff (5+ nucleoli)	Average one-nucleolus % effect	Average 5+ nucleoli % effect	Average % viability
hsa-miR-149-3p	AGGGAGGGACGGGGGCUGUGC	2/3	0/3	9.2	9.3	70.1
hsa-miR-520d-3p	AAAGUGCUUCUCUUUGGUGGGU	0/3	1/3	-11.7	80.4	98.3
hsa-miR-520h	ACAAAGUGCUUCCCUUUAGAGU	0/3	1/3	-10.0	96.4	94.3
hsa-miR-559	UAAAGUAAAUAUGCACCAAAA	0/3	1/3	-8.8	73.9	104.1
hsa-miR-638	AGGGAUCGCGGGCGGGUGGCGGCCU	0/3	2/3	-4.4	88.9	74.6
hsa-miR-4291	UUCAGCAGGAACAGCU	0/3	2/3	-14.5	82.7	93.5
hsa-miR-6724-5p	CUGGGCCCGCGGCGGGCGUGGGG	1/3	2/3	3.6	92.2	44.6

Other classes of ncRNAs may also play regulatory roles in RB. In addition to being translational templates, circular (circ)RNAs may function as binding sponges for microRNAs or RNA binding proteins (457), and therefore could influence ribosome production. Vault RNAs are constituents of vault particles, the largest known ribonucleoprotein structures in the eukaryotic cell (458). Vault particles may affect cellular signaling, DNA damage repair, or the formation and operability of the nuclear pore complex (458), which is crucial for nuclear export of maturing pre-ribosomes (80, 260). Lastly, cleavage-inducing tiny (city)RNAs as small as 10-18 nt may target cellular transcripts for destruction via AGO/RISC, like their longer microRNA relatives (459). Original strategies would be required to engineer suitable arrayed screening libraries for these ncRNAs, if the MCF10A nucleolar number assay platform is to be used to identify putative RB regulators. Overall, further investigations of ncRNAs are necessary to uncover the full extent of mammalian RB regulation.

5.3. How can the novel microRNA hits be studied with other techniques?

In **Chapter 3.4**, I discuss several limitations associated with using microRNA mimics to study biological microRNA function. While I argue against non-specific effects resulting from pollution of the cellular microRNAome, the principal remaining issue at hand is that transfection of microRNA mimics may cause supraphysiological overexpression levels of the microRNA. Recent work by McGeary and coworkers (460) suggests to me that this exogenous augmentation may saturate knockdown of strong (high-complementarity) microRNA targets, or enable the microRNA mimic to

downregulate weaker (low-complementarity) targets that may not normally be affected by milder endogenous microRNA expression.

Ideally, finer control of microRNA expression from endogenous genomic loci could be employed in future work. One obvious technique for this would be CRISPR activation (CRISPRa) or inhibition (CRISPRi), depending on whether gain- or loss-of-function at a given microRNA locus is sought (461, 462). These approaches harness the precise genome-binding ability of the CRISPR-Cas9 system; however, rather than making genomic edits, a dead (d)Cas9 protein fused to either an engineered transcriptional activator (VP64, p65, and RTA comprising a "VPR" domain) or repressor (KRAB domain) is delivered to a target gene promoter, modulating its activity accordingly (462). Though costly, arrayed libraries of CRISPR guide RNAs are commercially-available (463), and would be necessary for high-content screens such as the cell-based nucleolar number assay so that phenotypes could unequivocally be attributed to specific guide RNAs/target genes.

To support the causality and specificity of microRNA modulation of RB, expression of a smaller number candidate microRNAs should also be titrated in dose-response experiments. While the magnitude of CRISPR activity on target loci has not traditionally been controllable, recent studies have achieved tunability by introducing mismatches into guide RNAs or altering the distance of between guide binding and the target gene (464-466). Inducible, titratable expression of either CRISPR guide RNAs or (pri-)microRNA transcripts from exogenous plasmids could feasibly act as an acceptable alternative.

One lingering issue with this strategy is that transcription of the entire primary microRNA would be upregulated, possibly leading to results confounded by upregulation of both 5p and 3p strands of the target microRNA. Additionally, some microRNAs are clustered in the genome, and broad transcriptional activation may induce expression of multiple primary microRNA transcripts. For example, 47 microRNA loci of the MirGeneDB MIR-430 family are clustered within 122 kb on chr19, with interlocus distances as small as 200 bp. Exogenous microRNA inhibitors or sponges could be used to minimize overexpression of non-target microRNA strands, or genome editing could be used to destabilize RISC selection or targeting capability of those strands. However, sufficient and careful controls would be needed to mitigate confounding variables in such experiments.

5.4. Why does nucleolar number change in MCF10A cells upon RB inhibition?

While our lab has used, to great effect, the observation that interrupting RB in MCF10A cells often leads to a change in nucleolar number, several questions remain about the mechanism and biological significance of this phenomenon. It is notable that such a change in nucleolar number following RB inhibition has only been observed in MCF10A cells (58, 83-85) as well as human HT1080 fibrosarcoma cells (upon 8-chloro-cAMP treatment) (58, 467) and mouse embryonic fibroblasts (following *Ubtf* inactivation) (58, 86). Interestingly, a slight decrease in nucleolar number was observed in human RPE-1 cells upon *MYC* overexpression, which activates RB (468). At least in

MCF10A cells, it is unclear if multiple NORs coalesce in the one-nucleolus phenotype, or whether at least one NOR is present in each nucleolus in the 5+ nucleoli phenotype. This question could be addressed by rDNA FISH following induction of a change in nucleolar number. It was also observed that one or more mitosis events (*i.e.*, dissolution and reformation of the nucleoli) are likely necessary to observe a change in nucleolar number; this stems from unpublished data collected following siRNA depletion of RB factors for 24, 48, or 72 h during optimization of the nucleolar number assay introduced in (83). The essentiality of mitosis for the phenotypes suggests a defect in machinery required for re-establishing nucleolar form and function may be at play.

Differences between the one-nucleolus and 5+ nucleoli phenotypes in MCF10A are also not well-understood. While mitosis and nucleolar reformation appear to be required for the genesis of either phenotype, inhibition of mitosis via siRNA depletion or small molecule treatment was strongly associated with an increase in nucleolar number and a decrease in pre-rRNA transcription with minimal inhibition of pre-rRNA processing (84). However, this increase in nucleolar number may be at least partially due to failures in G2/M progression and cytokinesis, resulting in cells with 4n DNA content (84). Conversely, Farley-Barnes *et al.* observed that 16/20 one-nucleolus hits tested inhibited pre-rRNA processing, while only 7/20 interrupted pre-rRNA transcription (83). Therefore, it may be the case that one-nucleolus hits are more likely to affect pre-rRNA processing, while 5+ nucleoli hits are more likely to affect pre-rRNA transcription. This hypothesis is consistent with my observations in **Chapter 3**, where most primary screen hits were one-nucleolus hits, and 12/15 hits tested caused interruption of pre-

rRNA processing. Augmenting nucleolar number data by simultaneously measuring nucleolar rRNA biogenesis could lead to development of a more accurate multi-class classifier for inhibition of specific RB subprocesses, compared to nucleolar number alone.

Ogawa McLean observed a dose-dependent effect on nucleolar number in MCF10As following treatment with the compound mitomycin C, wherein low concentrations (250 nM) caused an increase in nucleolar number while high concentrations (3.5–14 μM) caused a decrease in nucleolar number, suggesting a potential link or spectrum between each phenotype (469). It is tempting to speculate that under some regime of concomitant inhibition of RB and mitosis, nucleolar number increases, while different combinatorial levels of inhibition cause the one-nucleolus phenotype. However, due to the tightly-intertwined co-regulatory relationship between RB and the cell cycle, these rules may be difficult to tease out. A good first step would be conducting (super-resolution) fluorescence microscopy to probe changes in NOR occupancy (via rDNA FISH) or search for the presence of nucleolar stress caps, which form upon RNAP1 inhibition. Though technically challenging, live-cell microscopy across multiple mitosis events could also shed light onto the development of each nucleolar number phenotype.

5.5. What is the precise nature of Nop4/RBM28's interaction with early pre-60S particles?

As noted in **Chapter 4**, yeast Nop4/human RBM28 is an essential pre-60S AF critical for pre-rRNA processing. While Nop4's ability to bind several pre-60S factors including itself has been demonstrated by yeast two-hybrid assays (160, 400), its precise location and direct interaction partners within the maturing large subunit remain unknown, precluding full mechanistic understanding of 60S assembly. In the RCSB Protein Data Bank, Nop4 is absent from all 38 pre-60S structural models collected in *S. cerevisiae* and RBM28 does not appear in the 4 available human pre-60S structures. In fact, the only model of either protein is a solution nuclear magnetic resonance (NMR) structure of the murine ortholog, Rbm28, made public in 2005 by He and colleagues but never included in a published manuscript (PDB ID: 1X4H). This structure was used to model the disruptive effect of the classical ANE syndrome variant L351P on RBM28 RRM3 structure (160).

Unfortunately, yeast Nop4 may continue to elude structural triangulation for two reasons. First, mass spectrometry of tandem affinity purified pre-60S particles identified Nop4 as a transient component of nucleolar Noc2 particles containing the early 27S-A_2 pre-rRNA intermediate (165). Nop4 transiently interacts with these early pre-60S particles, as opposed to other factors that are more permanently bound including Nop16 and Rrp5 (165). Several other high-confidence Nop4 interactors found by yeast two-hybrid are also in these Noc2 particles, such as Noc2 itself, Ebp2, Nop12, Mak5, Has1, Drs1, and Nog1 (165, 400). Nop4 was not observed in later pre-60S particles

containing Nsa1 (late nucleolar), Rix1 (nucleoplasmic), or Arx1 (nucleoplasmic/cytoplasmic) (165). Second, Nop4 may also act as a hub protein, scaffolding other pre-60S AFs to remodel maturing pre-ribosomes (160, 400). In this way, its transient interaction with pre-60S particles might be indirectly mediated through binding partners. Given these factors, it may be unlikely that Nop4 will be identified in native yeast pre-60S subunits.

While hope for structurally locating Nop4 is dwindling, researchers may still have success with human RBM28. Only one group has reported human pre-60S structures to-date (161), though the earliest particles seen were nucleoplasmic, not nucleolar. New cutting-edge advances in biallelic gene tagging (470) and nucleolar pre-ribosome purification (471) may accelerate collection of tagged nucleolar human pre-60S structures containing RBM28. Complicating matters, RBM28 may have acquired additional functions in pre-mRNA splicing and direct TP53 regulation in humans (472, 473), perhaps altering the nature of its interactions with pre-60S particles or AFs. Ultimately, continued modeling of early large subunit human pre-ribosomes may yet illuminate RBM28's precise function in RB, yielding new insights into pathogenesis of the rare ribosomopathy, ANE syndrome.

References

1. Woolford JL, Jr., Baserga SJ. Ribosome biogenesis in the yeast Saccharomyces cerevisiae. Genetics. 2013;195(3):643-81. doi: 10.1534/genetics.113.153197. PubMed PMID: 24190922; PMCID: 3813855.

2. Bassler J, Hurt E. Eukaryotic Ribosome Assembly. Annu Rev Biochem. 2019;88:281-306. doi: 10.1146/annurev-biochem-013118-110817. PubMed PMID: 30566372.

3. Pena C, Hurt E, Panse VG. Eukaryotic ribosome assembly, transport and quality control. Nat Struct Mol Biol. 2017;24(9):689-99. doi: 10.1038/nsmb.3454. PubMed PMID: 28880863.

4. Hershey JW, Sonenberg N, Mathews MB. Principles of translational control: an overview. Cold Spring Harb Perspect Biol. 2012;4(12). doi: 10.1101/cshperspect.a011528. PubMed PMID: 23209153; PMCID: 3504442.

5. Noller HF, Hoffarth V, Zimniak L. Unusual Resistance of Peptidyl Transferase to Protein Extraction Procedures. Science. 1992;256(5062):1416-9. doi: DOI 10.1126/science.1604315. PubMed PMID: WOS:A1992HX33700026.

6. Ban N, Nissen P, Hansen J, Moore PB, Steitz TA. The complete atomic structure of the large ribosomal subunit at 2.4 A resolution. Science. 2000;289(5481):905-20. doi: 10.1126/science.289.5481.905. PubMed PMID: 10937989.

7. Panov KI, Hannan K, Hannan RD, Hein N. The Ribosomal Gene Loci-The Power behind the Throne. Genes (Basel). 2021;12(5). doi: 10.3390/genes12050763. PubMed PMID: 34069807; PMCID: 8157237.

8. Henras AK, Plisson-Chastang C, O'Donohue MF, Chakraborty A, Gleizes PE. An overview of pre-ribosomal RNA processing in eukaryotes. Wiley Interdiscip Rev RNA. 2015;6(2):225-42. doi: 10.1002/wrna.1269. PubMed PMID: 25346433; PMCID: 4361047.

9. Scull CE, Schneider DA. Coordinated Control of rRNA Processing by RNA Polymerase I. Trends Genet. 2019;35(10):724-33. doi: 10.1016/j.tig.2019.07.002. PubMed PMID: 31358304; PMCID: 6744312.

10. Leidig C, Thoms M, Holdermann I, Bradatsch B, Berninghausen O, Bange G, Sinning I, Hurt E, Beckmann R. 60S ribosome biogenesis requires rotation of the 5S ribonucleoprotein particle. Nature Communications. 2014;5. doi: ARTN 3491

10.1038/ncomms4491. PubMed PMID: WOS:000334301700002.

11. Fedoriw AM, Starmer J, Yee D, Magnuson T. Nucleolar association and transcriptional inhibition through 5S rDNA in mammals. PLoS Genet. 2012;8(1):e1002468. doi: 10.1371/journal.pgen.1002468. PubMed PMID: 22275877; PMCID: 3261910.

12. de la Cruz J, Karbstein K, Woolford JL, Jr. Functions of ribosomal proteins in assembly of eukaryotic ribosomes in vivo. Annu Rev Biochem. 2015;84:93-129. doi: 10.1146/annurev-biochem-060614-033917. PubMed PMID: 25706898; PMCID: 4772166.

13. Espinar-Marchena FJ, Babiano R, Cruz J. Placeholder factors in ribosome biogenesis: please, pave my way. Microb Cell. 2017;4(5):144-68. doi: 10.15698/mic2017.05.572. PubMed PMID: 28685141; PMCID: 5425277.

14. Melnikov S, Ben-Shem A, Garreau de Loubresse N, Jenner L, Yusupova G, Yusupov M. One core, two shells: bacterial and eukaryotic ribosomes. Nat Struct Mol Biol. 2012;19(6):560-7. doi: 10.1038/nsmb.2313. PubMed PMID: 22664983.

15. Xue S, Barna M. Specialized ribosomes: a new frontier in gene regulation and organismal biology. Nat Rev Mol Cell Biol. 2012;13(6):355-69. doi: 10.1038/nrm3359. PubMed PMID: 22617470; PMCID: 4039366.

16. Genuth NR, Barna M. The Discovery of Ribosome Heterogeneity and Its Implications for Gene Regulation and Organismal Life. Mol Cell. 2018;71(3):364-74. doi: 10.1016/j.molcel.2018.07.018. PubMed PMID: 30075139; PMCID: 6092941.

17. Henras AK, Soudet J, Gerus M, Lebaron S, Caizergues-Ferrer M, Mougin A, Henry Y. The post-transcriptional steps of eukaryotic ribosome biogenesis. Cell Mol Life Sci. 2008;65(15):2334-59. doi: 10.1007/s00018-008-8027-0. PubMed PMID: 18408888.

18. Kressler D, Hurt E, Bassler J. Driving ribosome assembly. Biochim Biophys Acta. 2010;1803(6):673-83. doi: 10.1016/j.bbamcr.2009.10.009. PubMed PMID: 19879902.

19. Meier UT. The daunting task of modifying ribosomal RNA. RNA. 2022. doi: 10.1261/rna.079391.122. PubMed PMID: 36109161.

20. Watkins NJ, Bohnsack MT. The box C/D and H/ACA snoRNPs: key players in the modification, processing and the dynamic folding of ribosomal RNA. Wires Rna. 2012;3(3):397-414. doi: 10.1002/wrna.117. PubMed PMID: WOS:000302995100007.

21. Bowman JC, Petrov AS, Frenkel-Pinter M, Penev PI, Williams LD. Root of the Tree: The Significance, Evolution, and Origins of the Ribosome. Chem Rev.

2020;120(11):4848-78. doi: 10.1021/acs.chemrev.9b00742. PubMed PMID: 32374986.

22. Koonin EV. Comparative genomics, minimal gene-sets and the last universal common ancestor. Nat Rev Microbiol. 2003;1(2):127-36. doi: 10.1038/nrmicro751. PubMed PMID: 15035042.

23. Harris JK, Kelley ST, Spiegelman GB, Pace NR. The genetic core of the universal ancestor. Genome Res. 2003;13(3):407-12. doi: 10.1101/gr.652803. PubMed PMID: 12618371; PMCID: 430263.

24. Charlebois RL, Doolittle WF. Computing prokaryotic gene ubiquity: rescuing the core from extinction. Genome Res. 2004;14(12):2469-77. doi: 10.1101/gr.3024704. PubMed PMID: 15574825; PMCID: 534671.

25. Tirumalai MR, Rivas M, Tran Q, Fox GE. The Peptidyl Transferase Center: a Window to the Past. Microbiol Mol Biol Rev. 2021;85(4):e0010421. doi: 10.1128/MMBR.00104-21. PubMed PMID: 34756086; PMCID: 8579967.

26. Prosdocimi F, Zamudio GS, Palacios-Perez M, Torres de Farias S, M VJ. The Ancient History of Peptidyl Transferase Center Formation as Told by Conservation and Information Analyses. Life (Basel). 2020;10(8). doi: 10.3390/life10080134. PubMed PMID: 32764248; PMCID: 7459865.

27. Parks MM, Kurylo CM, Batchelder JE, Theresa Vincent C, Blanchard SC. Implications of sequence variation on the evolution of rRNA. Chromosome Res. 2019;27(1-2):89-93. doi: 10.1007/s10577-018-09602-w. PubMed PMID: 30719681; PMCID: 6505490.

28. Arnheim N, Krystal M, Schmickel R, Wilson G, Ryder O, Zimmer E. Molecular evidence for genetic exchanges among ribosomal genes on nonhomologous chromosomes in man and apes. Proc Natl Acad Sci U S A. 1980;77(12):7323-7. doi: 10.1073/pnas.77.12.7323. PubMed PMID: 6261251; PMCID: 350495.

29. Smit S, Widmann J, Knight R. Evolutionary rates vary among rRNA structural elements. Nucleic Acids Res. 2007;35(10):3339-54. doi: 10.1093/nar/gkm101. PubMed PMID: 17468501; PMCID: 1904297.

30. Bose T, Fridkin G, Davidovich C, Krupkin M, Dinger N, Falkovich AH, Peleg Y, Agmon I, Bashan A, Yonath A. Origin of life: protoribosome forms peptide bonds and links RNA and protein dominated worlds. Nucleic Acids Res. 2022;50(4):1815-28. doi: 10.1093/nar/gkac052. PubMed PMID: 35137169; PMCID: 8886871.

31. Gilbert W. Origin of Life - the RNA World. Nature. 1986;319(6055):618-. doi: DOI 10.1038/319618a0. PubMed PMID: WOS:A1986A079600021.

32. Cech TR. The RNA worlds in context. Cold Spring Harb Perspect Biol. 2012;4(7):a006742. doi: 10.1101/cshperspect.a006742. PubMed PMID: 21441585; PMCID: 3385955.

33. Noller HF. Evolution of protein synthesis from an RNA world. Cold Spring Harb Perspect Biol. 2012;4(4):a003681. doi: 10.1101/cshperspect.a003681. PubMed PMID: 20610545; PMCID: 3312679.

34. Agmon IC. Could a Proto-Ribosome Emerge Spontaneously in the Prebiotic World? Molecules. 2016;21(12). doi: 10.3390/molecules21121701. PubMed PMID: 27941673; PMCID: 6274258.

35. Ebersberger I, Simm S, Leisegang MS, Schmitzberger P, Mirus O, von Haeseler A, Bohnsack MT, Schleiff E. The evolution of the ribosome biogenesis pathway from a yeast perspective. Nucleic Acids Res. 2014;42(3):1509-23. doi: 10.1093/nar/gkt1137. PubMed PMID: 24234440; PMCID: 3919561.

36. Juttner M, Ferreira-Cerca S. Looking through the Lens of the Ribosome Biogenesis Evolutionary History: Possible Implications for Archaeal Phylogeny and Eukaryogenesis. Molecular Biology and Evolution. 2022;39(4). doi: ARTN msac054

10.1093/molbev/msac054. PubMed PMID: WOS:000780307900001.

37. Ramesh M, Woolford JL, Jr. Eukaryote-specific rRNA expansion segments function in ribosome biogenesis. RNA. 2016;22(8):1153-62. doi: 10.1261/rna.056705.116. PubMed PMID: 27317789; PMCID: 4931108.

38. Gerbi SA. Expansion segments: regions of variable size that interrupt the universal core secondary structure of ribosomal RNA. In: Zimmermann RA, Dahlberg AE, editors. Ribosomal RNA structure, evolution, processing, and function in protein biosynthesis. Boca Raton, FL: Telford-CRC Press; 1996. p. 71-87.

39. Warner JR. The economics of ribosome biosynthesis in yeast. Trends Biochem Sci. 1999;24(11):437-40. doi: 10.1016/s0968-0004(99)01460-7. PubMed PMID: 10542411.

40. Raue U, Oellerer S, Rospert S. Association of protein biogenesis factors at the yeast ribosomal tunnel exit is affected by the translational status and nascent polypeptide sequence. J Biol Chem. 2007;282(11):7809-16. doi: 10.1074/jbc.M611436200. PubMed PMID: 17229726.

41. Lewis JD, Tollervey D. Like attracts like: getting RNA processing together in the nucleus. Science. 2000;288(5470):1385-9. doi: 10.1126/science.288.5470.1385. PubMed PMID: 10827942.

42. Duncan R, Hershey JW. Identification and quantitation of levels of protein synthesis initiation factors in crude HeLa cell lysates by two-dimensional polyacrylamide gel electrophoresis. J Biol Chem. 1983;258(11):7228-35. PubMed PMID: 6853516.

43. Wolf SF, Schlessinger D. Nuclear metabolism of ribosomal RNA in growing, methionine-limited, and ethionine-treated HeLa cells. Biochemistry. 1977;16(12):2783-91. doi: 10.1021/bi00631a031. PubMed PMID: 889788.

44. Lafontaine DLJ, Riback JA, Bascetin R, Brangwynne CP. The nucleolus as a multiphase liquid condensate. Nat Rev Mol Cell Biol. 2021;22(3):165-82. doi: 10.1038/s41580-020-0272-6. PubMed PMID: 32873929.

45. Correll CC, Bartek J, Dundr M. The Nucleolus: A Multiphase Condensate Balancing Ribosome Synthesis and Translational Capacity in Health, Aging and Ribosomopathies. Cells. 2019;8(8). doi: 10.3390/cells8080869. PubMed PMID: 31405125.

46. Németh A. The Nucleolus2016.

47. Thiry M, Lafontaine DL. Birth of a nucleolus: the evolution of nucleolar compartments. Trends Cell Biol. 2005;15(4):194-9. doi: 10.1016/j.tcb.2005.02.007. PubMed PMID: 15817375.

48. Potapova TA, Gerton JL. Ribosomal DNA and the nucleolus in the context of genome organization. Chromosome Res. 2019;27(1-2):109-27. doi: 10.1007/s10577-018-9600-5. PubMed PMID: 30656516.

49. Goodfellow SJ, Zomerdijk JC. Basic mechanisms in RNA polymerase I transcription of the ribosomal RNA genes. Subcell Biochem. 2013;61:211-36. doi: 10.1007/978-94-007-4525-4_10. PubMed PMID: 23150253; PMCID: 3855190.

50. Piazzi M, Bavelloni A, Gallo A, Faenza I, Blalock WL. Signal Transduction in Ribosome Biogenesis: A Recipe to Avoid Disaster. Int J Mol Sci. 2019;20(11). doi: 10.3390/ijms20112718. PubMed PMID: 31163577.

51. Mayer C, Grummt I. Ribosome biogenesis and cell growth: mTOR coordinates transcription by all three classes of nuclear RNA polymerases. Oncogene. 2006;25(48):6384-91. doi: 10.1038/sj.onc.1209883. PubMed PMID: 17041624.

52. Denissov S, Lessard F, Mayer C, Stefanovsky V, van Driel M, Grummt I, Moss T, Stunnenberg HG. A model for the topology of active ribosomal RNA genes. EMBO Rep. 2011;12(3):231-7. doi: 10.1038/embor.2011.8. PubMed PMID: 21331097; PMCID: 3059908.

53. McCool MA, Bryant CJ, Baserga SJ. MicroRNAs and long non-coding RNAs as novel regulators of ribosome biogenesis. Biochem Soc Trans. 2020;48(2):595-612. doi: 10.1042/BST20190854. PubMed PMID: 32267487; PMCID: 7200637.

54. Mamontova V, Trifault B, Boten L, Burger K. Commuting to Work: Nucleolar Long Non-Coding RNA Control Ribosome Biogenesis from Near and Far. Noncoding RNA. 2021;7(3). doi: 10.3390/ncrna7030042. PubMed PMID: 34287370; PMCID: 8293466.

55. Cockrell AJ, Gerton JL. Nucleolar Organizer Regions as Transcription-Based Scaffolds of Nucleolar Structure and Function. Results Probl Cell Differ. 2022;70:551-80. doi: 10.1007/978-3-031-06573-6_19. PubMed PMID: 36348121.

56. Ide S, Miyazaki T, Maki H, Kobayashi T. Abundance of ribosomal RNA gene copies maintains genome integrity. Science. 2010;327(5966):693-6. doi: 10.1126/science.1179044. PubMed PMID: 20133573.

57. Conconi A, Widmer RM, Koller T, Sogo JM. Two different chromatin structures coexist in ribosomal RNA genes throughout the cell cycle. Cell. 1989;57(5):753-61. PubMed PMID: 2720786.

58. Farley KI, Surovtseva Y, Merkel J, Baserga SJ. Determinants of mammalian nucleolar architecture. Chromosoma. 2015;124(3):323-31. doi: 10.1007/s00412-015-0507-z. PubMed PMID: WOS:000360288200004.

59. Grummt I, Langst G. Epigenetic control of RNA polymerase I transcription in mammalian cells. Biochim Biophys Acta. 2013;1829(3-4):393-404. doi: 10.1016/j.bbagrm.2012.10.004. PubMed PMID: 23063748.

60. Zillner K, Komatsu J, Filarsky K, Kalepu R, Bensimon A, Nemeth A. Active human nucleolar organizer regions are interspersed with inactive rDNA repeats in normal and tumor cells. Epigenomics. 2015;7(3):363-78. doi: 10.2217/epi.14.93. PubMed PMID: 26077426.

61. McStay B, Grummt I. The epigenetics of rRNA genes: from molecular to chromosome biology. Annu Rev Cell Dev Biol. 2008;24:131-57. doi: 10.1146/annurev.cellbio.24.110707.175259. PubMed PMID: 18616426.

62. Hao Q, Liu M, Daulatabad SV, Gaffari S, Srivastava R, Song YJ, Bhaskar S, Moitra A, Mangan H, Tseng E, Gilmore RB, Freier SM, Chen X, Wang C, Huang S, Chamberlain S, Jin H, Korlach J, McStay B, Sinha S, Janga SC, Prasanth SG, Prasanth KV. Monoallelically-expressed Noncoding RNAs form nucleolar territories on NOR-containing chromosomes and regulate rRNA expression. bioRxiv. 2022:2022.07.04.498693. doi: 10.1101/2022.07.04.498693.

63. van Sluis M, van Vuuren C, Mangan H, McStay B. NORs on human acrocentric chromosome p-arms are active by default and can associate with nucleoli independently of rDNA. Proc Natl Acad Sci U S A. 2020. doi: 10.1073/pnas.2001812117. PubMed PMID: 32332163.

64. van Sluis M, Gailin MO, McCarter JGW, Mangan H, Grob A, McStay B. Human NORs, comprising rDNA arrays and functionally conserved distal elements, are located within dynamic chromosomal regions. Genes Dev. 2019;33(23-24):1688-701. Epub 2019/11/14. doi: 10.1101/gad.331892.119. PubMed PMID: 31727772; PMCID: 6942050.

65. McStay B. Nucleolar organizer regions: genomic 'dark matter' requiring illumination. Genes Dev. 2016;30(14):1598-610. doi: 10.1101/gad.283838.116. PubMed PMID: 27474438; PMCID: 4973289.

66. Nurk S, Koren S, Rhie A, Rautiainen M, Bzikadze AV, Mikheenko A, Vollger MR, Altemose N, Uralsky L, Gershman A, Aganezov S, Hoyt SJ, Diekhans M, Logsdon GA, Alonge M, Antonarakis SE, Borchers M, Bouffard GG, Brooks SY, Caldas GV, Chen NC, Cheng H, Chin CS, Chow W, de Lima LG, Dishuck PC, Durbin R, Dvorkina T, Fiddes IT, Formenti G, Fulton RS, Fungtammasan A, Garrison E, Grady PGS, Graves-Lindsay TA, Hall IM, Hansen NF, Hartley GA, Haukness M, Howe K, Hunkapiller MW, Jain C, Jain M, Jarvis ED, Kerpedjiev P, Kirsche M, Kolmogorov M, Korlach J, Kremitzki M, Li H, Maduro VV, Marschall T, McCartney AM, McDaniel J, Miller DE, Mullikin JC, Myers EW, Olson ND, Paten B, Peluso P, Pevzner PA, Porubsky D, Potapova T, Rogaev EI, Rosenfeld JA, Salzberg SL, Schneider VA, Sedlazeck FJ, Shafin K, Shew CJ, Shumate A, Sims Y, Smit AFA, Soto DC, Sovic I, Storer JM, Streets A, Sullivan BA, Thibaud-Nissen F, Torrance J, Wagner J, Walenz BP, Wenger A, Wood JMD, Xiao C, Yan SM, Young AC, Zarate S, Surti U, McCoy RC, Dennis MY, Alexandrov IA, Gerton JL, O'Neill RJ, Timp W, Zook JM, Schatz MC, Eichler EE, Miga KH, Phillippy AM. The complete sequence of a human genome. Science. 2022;376(6588):44-53. doi: 10.1126/science.abj6987. PubMed PMID: 35357919; PMCID: 9186530.

67. Tartakoff AM, Chen L, Raghavachari S, Gitiforooz D, Dhinakaran A, Ni CL, Pasadyn C, Mahabeleshwar GH, Pasadyn V, Woolford JL, Jr. The nucleolus as a polarized coaxial cable in which the rDNA axis is surrounded by dynamic subunit-specific phases. Curr Biol. 2021;31(12):2507-19 e4. doi: 10.1016/j.cub.2021.03.041. PubMed PMID: 33862007; PMCID: 8222187.

68. LaPeruta AJ, Micic J, Woolford JL, Jr. Additional principles that govern the release of pre-ribosomes from the nucleolus into the nucleoplasm in yeast. Nucleic Acids Res. 2022. doi: 10.1093/nar/gkac430. PubMed PMID: 35736211.

69. Musacchio A. On the role of phase separation in the biogenesis of membraneless compartments. EMBO J. 2022;41(5):e109952. doi: 10.15252/embj.2021109952. PubMed PMID: 35107832; PMCID: 8886532.

70. Tartakoff A, DiMario P, Hurt E, McStay B, Panse VG, Tollervey D. The dual nature of the nucleolus. Genes Dev. 2022;36(13-14):765-9. doi: 10.1101/gad.349748.122. PubMed PMID: 36342833; PMCID: 9480854.

71. Lafita-Navarro MC, Conacci-Sorrell M. Nucleolar stress: From development to cancer. Semin Cell Dev Biol. 2022. doi: 10.1016/j.semcdb.2022.04.001. PubMed PMID: 35410715.

72. James A, Wang Y, Raje H, Rosby R, DiMario P. Nucleolar stress with and without p53. Nucleus. 2014;5(5):402-26. doi: 10.4161/nucl.32235. PubMed PMID: 25482194; PMCID: 4164484.

73. Zhang Y, Lu H. Signaling to p53: ribosomal proteins find their way. Cancer Cell. 2009;16(5):369-77. doi: 10.1016/j.ccr.2009.09.024. PubMed PMID: 19878869; PMCID: 4369769.

74. Nicolas E, Parisot P, Pinto-Monteiro C, de Walque R, De Vleeschouwer C, Lafontaine DL. Involvement of human ribosomal proteins in nucleolar structure and p53-dependent nucleolar stress. Nat Commun. 2016;7:11390. doi: 10.1038/ncomms11390. PubMed PMID: 27265389; PMCID: 4897761.

75. Hannan KM, Soo P, Wong MS, Lee JK, Hein N, Poh P, Wysoke KD, Williams TD, Montellese C, Smith LK, Al-Obaidi SJ, Nunez-Villacis L, Pavy M, He JS, Parsons KM, Loring KE, Morrison T, Diesch J, Burgio G, Ferreira R, Feng ZP, Gould CM, Madhamshettiwar PB, Flygare J, Gonda TJ, Simpson KJ, Kutay U, Pearson RB, Engel C, Watkins NJ, Hannan RD, George AJ. Nuclear stabilization of p53 requires a functional nucleolar surveillance pathway. Cell Rep. 2022;41(5):111571. doi: 10.1016/j.celrep.2022.111571. PubMed PMID: 36323262; PMCID: 9647041.

76. van Sluis M, McStay B. Nucleolar reorganization in response to rDNA damage. Curr Opin Cell Biol. 2017;46:81-6. doi: 10.1016/j.ceb.2017.03.004. PubMed PMID: 28431265.

77. Potapova TA, Unruh JR, Conkright-Fincham J, Banks CAS, Florens L, Schneider DA, Gerton JL. Distinct states of nucleolar stress induced by anti-cancer drugs. bioRxiv. 2022:2022.11.18.517150. doi: 10.1101/2022.11.18.517150.

78. Stage-Zimmermann T, Schmidt U, Silver PA. Factors affecting nuclear export of the 60S ribosomal subunit in vivo. Mol Biol Cell. 2000;11(11):3777-89. doi: 10.1091/mbc.11.11.3777. PubMed PMID: 11071906; PMCID: 15036.

79. Wade CH, Umbarger MA, McAlear MA. The budding yeast rRNA and ribosome biosynthesis (RRB) regulon contains over 200 genes. Yeast. 2006;23(4):293-306. doi: 10.1002/yea.1353. PubMed PMID: 16544271.

80. Wild T, Horvath P, Wyler E, Widmann B, Badertscher L, Zemp I, Kozak K, Csucs G, Lund E, Kutay U. A protein inventory of human ribosome biogenesis reveals an essential function of exportin 5 in 60S subunit export. PLoS Biol. 2010;8(10):e1000522. doi: 10.1371/journal.pbio.1000522. PubMed PMID: 21048991; PMCID: 2964341.

81. Badertscher L, Wild T, Montellese C, Alexander LT, Bammert L, Sarazova M, Stebler M, Csucs G, Mayer TU, Zamboni N, Zemp I, Horvath P, Kutay U. Genome-wide RNAi Screening Identifies Protein Modules Required for 40S Subunit Synthesis in Human Cells. Cell Rep. 2015;13(12):2879-91. doi: 10.1016/j.celrep.2015.11.061. PubMed PMID: 26711351.

82. Dörner K, Badertscher L, Horvath B, Hollandi R, Molnar C, Fuhrer T, Meier R, Sarazova M, van den Heuvel J, Zamboni N, Horvath P, Kutay U. Genome-wide RNAi screen identifies novel players in human 60S subunit biogenesis including key enzymes of polyamine metabolism. Nucleic Acids Res. 2022;50(5):2872-88. doi: 10.1093/nar/gkac072. PubMed PMID: 35150276; PMCID: 8934630.

83. Farley-Barnes KI, McCann KL, Ogawa LM, Merkel J, Surovtseva YV, Baserga SJ. Diverse Regulators of Human Ribosome Biogenesis Discovered by Changes in Nucleolar Number. Cell Rep. 2018;22(7):1923-34. doi: 10.1016/j.celrep.2018.01.056. PubMed PMID: 29444442; PMCID: 5828527.

84. Ogawa LM, Buhagiar AF, Abriola L, Leland BA, Surovtseva YV, Baserga SJ. Increased numbers of nucleoli in a genome-wide RNAi screen reveal proteins that link the cell cycle to RNA polymerase I transcription. Mol Biol Cell. 2021;32(9):956-73. doi: 10.1091/mbc.E20-10-0670. PubMed PMID: 33689394; PMCID: 8108525.

85. Freed EF, Prieto JL, McCann KL, McStay B, Baserga SJ. NOL11, implicated in the pathogenesis of North American Indian childhood cirrhosis, is required for pre-rRNA transcription and processing. PLoS Genet. 2012;8(8):e1002892. doi: 10.1371/journal.pgen.1002892. PubMed PMID: 22916032; PMCID: 3420923.

86. Hamdane N, Stefanovsky VY, Tremblay MG, Nemeth A, Paquet E, Lessard F, Sanij E, Hannan R, Moss T. Conditional inactivation of Upstream Binding Factor reveals its epigenetic functions and the existence of a somatic nucleolar precursor body. PLoS Genet. 2014;10(8):e1004505. doi: 10.1371/journal.pgen.1004505. PubMed PMID: 25121932; PMCID: 4133168.

87. Tafforeau L, Zorbas C, Langhendries JL, Mullineux ST, Stamatopoulou V, Mullier R, Wacheul L, Lafontaine DL. The complexity of human ribosome biogenesis revealed by systematic nucleolar screening of Pre-rRNA processing factors. Mol Cell. 2013;51(4):539-51. doi: 10.1016/j.molcel.2013.08.011. PubMed PMID: 23973377.

88. Bartel DP. Metazoan microRNAs. Cell. 2018;173(1):20-51. doi: 10.1016/j.cell.2018.03.006. PubMed PMID: 29570994; PMCID: 6091663.

89. Gebert LFR, MacRae IJ. Regulation of microRNA function in animals. Nat Rev Mol Cell Biol. 2019;20(1):21-37. doi: 10.1038/s41580-018-0045-7. PubMed PMID: 30108335; PMCID: 6546304.

90. Lambert M, Benmoussa A, Provost P. Small non-Coding RNAs derived from eukaryotic ribosomal RNA. Noncoding RNA. 2019;5(1). doi: 10.3390/ncrna5010016. PubMed PMID: 30720712; PMCID: 6468398.

91. Yoshikawa M, Fujii YR. Human ribosomal RNA-derived resident microRNAs as the transmitter of information upon the cytoplasmic cancer stress. Biomed Res Int. 2016;2016:7562085. doi: 10.1155/2016/7562085. PubMed PMID: 27517048; PMCID: 4969525.

92. Wei H, Zhou B, Zhang F, Tu Y, Hu Y, Zhang B, Zhai Q. Profiling and identification of small rDNA-derived RNAs and their potential biological functions. PLoS One. 2013;8(2):e56842. doi: 10.1371/journal.pone.0056842. PubMed PMID: 23418607; PMCID: 3572043.

93. Locati MD, Pagano JFB, Abdullah F, Ensink WA, van Olst M, van Leeuwen S, Nehrdich U, Spaink HP, Rauwerda H, Jonker MJ, Dekker RJ, Breit TM. Identifying small RNAs derived from maternal- and somatic-type rRNAs in zebrafish development. Genome. 2018;61(5):371-8. doi: 10.1139/gen-2017-0202. PubMed PMID: 29425468.

94. Mangrauthia SK, Sailaja B, Pusuluri M, Jena B, Prasanth VV, Agarwal S, Senguttuvel P, Sarla N, Ravindra Babu V, Subrahmanyam D, Voleti SR. Deep sequencing of small RNAs reveals ribosomal origin of microRNAs in Oryza sativa and their regulatory role in high temperature. Gene Reports. 2018;11:270-8. doi: 10.1016/j.genrep.2018.05.002.

95. Wang Y, Li H, Sun Q, Yao Y. Characterization of small RNAs derived from tRNAs, rRNAs and snoRNAs and their response to heat stress in wheat seedlings. PLoS One. 2016;11(3):e0150933. doi: 10.1371/journal.pone.0150933. PubMed PMID: 26963812; PMCID: 4786338.

96. Shi Y, Duan X, Xu G, Wang X, Wei G, Dong S, Xie G, Liu D. A ribosomal DNA-hosted microRNA regulates zebrafish embryonic angiogenesis. Angiogenesis. 2019;22(2):211-21. doi: 10.1007/s10456-019-09663-3. PubMed PMID: 30656567.

97. Locati MD, Pagano JFB, Girard G, Ensink WA, van Olst M, van Leeuwen S, Nehrdich U, Spaink HP, Rauwerda H, Jonker MJ, Dekker RJ, Breit TM. Expression of distinct maternal and somatic 5.8S, 18S, and 28S rRNA types during zebrafish

development. RNA. 2017;23(8):1188-99. doi: 10.1261/rna.061515.117. PubMed PMID: 28500251; PMCID: 5513064.

98. Politz JC, Hogan EM, Pederson T. MicroRNAs with a nucleolar location. RNA. 2009;15(9):1705-15. doi: 10.1261/rna.1470409. PubMed PMID: 19628621; PMCID: 2743059.

99. Li ZF, Liang YM, Lau PN, Shen W, Wang DK, Cheung WT, Xue CJ, Poon LM, Lam YW. Dynamic localisation of mature microRNAs in Human nucleoli is influenced by exogenous genetic materials. PLoS One. 2013;8(8):e70869. doi: 10.1371/journal.pone.0070869. PubMed PMID: 23940654; PMCID: 3735495.

100. Bai B, Liu H, Laiho M. Small RNA expression and deep sequencing analyses of the nucleolus reveal the presence of nucleolus-associated microRNAs. FEBS Open Bio. 2014;4:441-9. doi: 10.1016/j.fob.2014.04.010. PubMed PMID: 24918059; PMCID: 4050192.

101. Reyes-Gutierrez P, Ritland Politz JC, Pederson T. A mRNA and cognate microRNAs localize in the nucleolus. Nucleus. 2014;5(6):636-42. doi: 10.4161/19491034.2014.990864. PubMed PMID: 25485975; PMCID: 4615376.

102. Atwood BL, Woolnough JL, Lefevre GM, Saint Just Ribeiro M, Felsenfeld G, Giles KE. Human Argonaute 2 is tethered to ribosomal RNA through microRNA interactions. J Biol Chem. 2016;291(34):17919-28. doi: 10.1074/jbc.M116.725051. PubMed PMID: 27288410; PMCID: 5016180.

103. Politz JC, Zhang F, Pederson T. MicroRNA-206 colocalizes with ribosome-rich regions in both the nucleolus and cytoplasm of rat myogenic cells. Proc Natl Acad Sci U S A. 2006;103(50):18957-62. doi: 10.1073/pnas.0609466103. PubMed PMID: 17135348; PMCID: 1748159.

104. Catalanotto C, Cogoni C, Zardo G. MicroRNA in control of gene expression: an overview of nuclear functions. Int J Mol Sci. 2016;17(10). doi: 10.3390/ijms17101712. PubMed PMID: 27754357; PMCID: 5085744.

105. Lin S, Gregory RI. MicroRNA biogenesis pathways in cancer. Nat Rev Cancer. 2015;15(6):321-33. doi: 10.1038/nrc3932. PubMed PMID: 25998712; PMCID: 4859809.

106. Acunzo M, Romano G, Wernicke D, Croce CM. MicroRNA and cancer--a brief overview. Adv Biol Regul. 2015;57:1-9. doi: 10.1016/j.jbior.2014.09.013. PubMed PMID: 25294678.

107. Derenzini M, Montanaro L, Trere D. Ribosome biogenesis and cancer. Acta Histochem. 2017;119(3):190-7. doi: 10.1016/j.acthis.2017.01.009. PubMed PMID: 28168996.

108. Bublik DR, Bursac S, Sheffer M, Orsolic I, Shalit T, Tarcic O, Kotler E, Mouhadeb O, Hoffman Y, Fuchs G, Levin Y, Volarevic S, Oren M. Regulatory module involving FGF13, miR-504, and p53 regulates ribosomal biogenesis and supports cancer cell survival. Proc Natl Acad Sci U S A. 2017;114(4):E496-E505. doi: 10.1073/pnas.1614876114. PubMed PMID: 27994142; PMCID: 5278483.

109. Challagundla KB, Sun XX, Zhang X, DeVine T, Zhang Q, Sears RC, Dai MS. Ribosomal protein L11 recruits miR-24/miRISC to repress c-Myc expression in response to ribosomal stress. Mol Cell Biol. 2011;31(19):4007-21. doi: 10.1128/MCB.05810-11. PubMed PMID: 21807902; PMCID: 3187350.

110. Liao JM, Zhou X, Gatignol A, Lu H. Ribosomal proteins L5 and L11 co-operatively inactivate c-Myc via RNA-induced silencing complex. Oncogene. 2014;33(41):4916-23. doi: 10.1038/onc.2013.430. PubMed PMID: 24141778; PMCID: 4026346.

111. Li Y, Challagundla KB, Sun XX, Zhang Q, Dai MS. MicroRNA-130a associates with ribosomal protein L11 to suppress c-Myc expression in response to UV irradiation. Oncotarget. 2015;6(2):1101-14. doi: 10.18632/oncotarget.2728. PubMed PMID: 25544755; PMCID: 4359220.

112. Zhou X, Hao Q, Liao JM, Liao P, Lu H. Ribosomal protein S14 negatively regulates c-Myc activity. J Biol Chem. 2013;288(30):21793-801. doi: 10.1074/jbc.M112.445122. PubMed PMID: 23775087; PMCID: 3724636.

113. Rao S, Lee SY, Gutierrez A, Perrigoue J, Thapa RJ, Tu Z, Jeffers JR, Rhodes M, Anderson S, Oravecz T, Hunger SP, Timakhov RA, Zhang R, Balachandran S, Zambetti GP, Testa JR, Look AT, Wiest DL. Inactivation of ribosomal protein L22 promotes transformation by induction of the stemness factor, Lin28B. Blood. 2012;120(18):3764-73. doi: 10.1182/blood-2012-03-415349. PubMed PMID: 22976955; PMCID: 3488889.

114. Reza A, Choi YJ, Yuan YG, Das J, Yasuda H, Kim JH. MicroRNA-7641 is a regulator of ribosomal proteins and a promising targeting factor to improve the efficacy of cancer therapy. Sci Rep. 2017;7(1):8365. doi: 10.1038/s41598-017-08737-w. PubMed PMID: 28827731; PMCID: 5566380.

115. Coleman O, Suda S, Meiller J, Henry M, Riedl M, Barron N, Clynes M, Meleady P. Increased growth rate and productivity following stable depletion of miR-7 in a mAb producing CHO cell line causes an increase in proteins associated with the Akt pathway and ribosome biogenesis. J Proteomics. 2019. doi: 10.1016/j.jprot.2019.01.003. PubMed PMID: 30641232.

116. Connolly M, Paul R, Farre-Garros R, Natanek SA, Bloch S, Lee J, Lorenzo JP, Patel H, Cooper C, Sayer AA, Wort SJ, Griffiths M, Polkey MI, Kemp PR. miR-424-5p reduces ribosomal RNA and protein synthesis in muscle wasting. J Cachexia Sarcopenia

Muscle. 2018;9(2):400-16. doi: 10.1002/jcsm.12266. PubMed PMID: 29215200; PMCID: 5879973.

117. Alkhatabi HA, McLornan DP, Kulasekararaj AG, Malik F, Seidl T, Darling D, Gaken J, Mufti GJ. RPL27A is a target of miR-595 and may contribute to the myelodysplastic phenotype through ribosomal dysgenesis. Oncotarget. 2016;7(30):47875-90. doi: 10.18632/oncotarget.10293. PubMed PMID: 27374104; PMCID: 5216985.

118. Starczynowski DT, Kuchenbauer F, Argiropoulos B, Sung S, Morin R, Muranyi A, Hirst M, Hogge D, Marra M, Wells RA, Buckstein R, Lam W, Humphries RK, Karsan A. Identification of miR-145 and miR-146a as mediators of the 5q- syndrome phenotype. Nat Med. 2010;16(1):49-58. doi: 10.1038/nm.2054. PubMed PMID: 19898489.

119. Wan Y, Zhang Q, Zhang ZJ, Song BF, Wang XM, Zhang YC, Jia Q, Cheng T, Zhu XF, Leung AYH, Yuan WP, Jia HB, Fang XD. Transcriptome analysis reveals a ribosome constituents disorder involved in the RPL5 downregulated zebrafish model of Diamond-Blackfan anemia. Bmc Med Genomics. 2016;9. doi: ARTN 13

10.1186/s12920-016-0174-9. PubMed PMID: WOS:000372098800002.

120. Vasudevan S, Tong Y, Steitz JA. Switching from repression to activation: microRNAs can up-regulate translation. Science. 2007;318(5858):1931-4. doi: 10.1126/science.1149460. PubMed PMID: 18048652.

121. Bukhari SIA, Truesdell SS, Lee S, Kollu S, Classon A, Boukhali M, Jain E, Mortensen RD, Yanagiya A, Sadreyev RI, Haas W, Vasudevan S. A specialized mechanism of translation mediated by FXR1a-associated microRNP in cellular quiescence. Mol Cell. 2016;61(5):760-73. doi: 10.1016/j.molcel.2016.02.013. PubMed PMID: 26942679; PMCID: 4811377.

122. Orom UA, Nielsen FC, Lund AH. MicroRNA-10a binds the 5'UTR of ribosomal protein mRNAs and enhances their translation. Mol Cell. 2008;30(4):460-71. doi: 10.1016/j.molcel.2008.05.001. PubMed PMID: 18498749.

123. Srikantan S, Marasa BS, Becker KG, Gorospe M, Abdelmohsen K. Paradoxical microRNAs: individual gene repressors, global translation enhancers. Cell Cycle. 2011;10(5):751-9. doi: 10.4161/cc.10.5.14825. PubMed PMID: 21311220; PMCID: 3100788.

124. Mei Y, Wu M. Noncoding RNAs regulating p53 and c-Myc signaling. Adv Exp Med Biol. 2016;927:337-65. doi: 10.1007/978-981-10-1498-7_13. PubMed PMID: 27376742.

125. van Riggelen J, Yetil A, Felsher DW. MYC as a regulator of ribosome biogenesis and protein synthesis. Nat Rev Cancer. 2010;10(4):301-9. doi: 10.1038/nrc2819. PubMed PMID: 20332779.

126. Lessard F, Brakier-Gingras L, Ferbeyre G. Ribosomal proteins control tumor suppressor pathways in response to nucleolar stress. Bioessays. 2019:e1800183. doi: 10.1002/bies.201800183. PubMed PMID: 30706966.

127. Zhou X, Hao Q, Liao J, Zhang Q, Lu H. Ribosomal protein S14 unties the MDM2-p53 loop upon ribosomal stress. Oncogene. 2013;32(3):388-96. doi: 10.1038/onc.2012.63. PubMed PMID: 22391559; PMCID: 3736832.

128. Balzeau J, Menezes MR, Cao S, Hagan JP. The LIN28/let-7 pathway in cancer. Front Genet. 2017;8:31. doi: 10.3389/fgene.2017.00031. PubMed PMID: 28400788; PMCID: 5368188.

129. Wang X, Cao L, Wang Y, Wang X, Liu N, You Y. Regulation of let-7 and its target oncogenes (Review). Oncol Lett. 2012;3(5):955-60. doi: 10.3892/ol.2012.609. PubMed PMID: 22783372; PMCID: 3389667.

130. Zhao J, Tao Y, Zhou Y, Qin N, Chen C, Tian D, Xu L. MicroRNA-7: a promising new target in cancer therapy. Cancer Cell Int. 2015;15:103. doi: 10.1186/s12935-015-0259-0. PubMed PMID: 26516313; PMCID: 4625531.

131. Giles KM, Brown RA, Ganda C, Podgorny MJ, Candy PA, Wintle LC, Richardson KL, Kalinowski FC, Stuart LM, Epis MR, Haass NK, Herlyn M, Leedman PJ. microRNA-7-5p inhibits melanoma cell proliferation and metastasis by suppressing RelA/NF-kappaB. Oncotarget. 2016;7(22):31663-80. doi: 10.18632/oncotarget.9421. PubMed PMID: 27203220; PMCID: 5077967.

132. Shi Y, Luo X, Li P, Tan J, Wang X, Xiang T, Ren G. miR-7-5p suppresses cell proliferation and induces apoptosis of breast cancer cells mainly by targeting REGgamma. Cancer Lett. 2015;358(1):27-36. doi: 10.1016/j.canlet.2014.12.014. PubMed PMID: 25511742.

133. Yin CY, Kong W, Jiang J, Xu H, Zhao W. miR-7-5p inhibits cell migration and invasion in glioblastoma through targeting SATB1. Oncol Lett. 2019;17(2):1819-25. doi: 10.3892/ol.2018.9777. PubMed PMID: 30675243; PMCID: 6341908.

134. Zhu W, Wang Y, Zhang D, Yu X, Leng X. MiR-7-5p functions as a tumor suppressor by targeting SOX18 in pancreatic ductal adenocarcinoma. Biochem Biophys Res Commun. 2018;497(4):963-70. doi: 10.1016/j.bbrc.2018.02.005. PubMed PMID: 29408481.

135. Vasudevan S, Tong Y, Steitz JA. Cell-cycle control of microRNA-mediated translation regulation. Cell Cycle. 2008;7(11):1545-9. doi: 10.4161/cc.7.11.6018. PubMed PMID: 18469529; PMCID: 2556257.

136. Cockman E, Anderson P, Ivanov P. TOP mRNPs: Molecular Mechanisms and Principles of Regulation. Biomolecules. 2020;10(7). doi: 10.3390/biom10070969. PubMed PMID: 32605040; PMCID: 7407576.

137. Hein N, Sanij E, Quin J, Hannan KM, Ganley A, Hannan RD. The nucleolus and ribosomal genes in aging and senescence. In: Nagata T, editor. Senescence: IntechOpen; 2012. p. 171-208.

138. Polymenis M, Kennedy BK. Unbalanced growth, senescence and aging. Adv Exp Med Biol. 2017;1002:189-208. doi: 10.1007/978-3-319-57127-0_8. PubMed PMID: 28600787; PMCID: 6345385.

139. Farley-Barnes KI, Ogawa LM, Baserga SJ. Ribosomopathies: Old Concepts, New Controversies. Trends Genet. 2019. doi: 10.1016/j.tig.2019.07.004. PubMed PMID: 31376929.

140. Mills EW, Green R. Ribosomopathies: There's strength in numbers. Science. 2017;358(6363). doi: 10.1126/science.aan2755. PubMed PMID: 29097519.

141. Yelick PC, Trainor PA. Ribosomopathies: Global process, tissue specific defects. Rare Dis. 2015;3(1):e1025185. doi: 10.1080/21675511.2015.1025185. PubMed PMID: 26442198; PMCID: 4590025.

142. McCann KL, Baserga SJ. Genetics. Mysterious ribosomopathies. Science. 2013;341(6148):849-50. doi: 10.1126/science.1244156. PubMed PMID: 23970686; PMCID: 3893057.

143. Narla A, Ebert BL. Ribosomopathies: human disorders of ribosome dysfunction. Blood. 2010;115(16):3196-205. doi: 10.1182/blood-2009-10-178129. PubMed PMID: 20194897; PMCID: 2858486.

144. Ebert B, Lipton JM. Diamond Blackfan Anemia and Ribosome Biogenesis: Introduction. Semin Hematol. 2011;48(2):73-4. doi: 10.1053/j.seminhematol.2011.01.003. PubMed PMID: WOS:000289037800001.

145. Gazda HT, Sheen MR, Vlachos A, Choesmel V, O'Donohue MF, Schneider H, Darras N, Hasman C, Sieff CA, Newburger PE, Ball SE, Niewiadomska E, Matysiak M, Zaucha JM, Glader B, Niemeyer C, Meerpohl JJ, Atsidaftos E, Lipton JM, Gleizes PE, Beggs AH. Ribosomal Protein L5 and L11 Mutations Are Associated with Cleft Palate and Abnormal Thumbs in Diamond-Blackfan Anemia Patients. American Journal of Human Genetics. 2008;83(6):769-80. doi: 10.1016/j.ajhg.2008.11.004. PubMed PMID: WOS:000261822100012.

146. Levin TL, Makitie O, Berdon WE, Lachman RS. Shwachman-Bodian-Diamond syndrome: metaphyseal chondrodysplasia in children with pancreatic insufficiency and neutropenia. Pediatr Radiol. 2015;45(7):1066-71. doi: 10.1007/s00247-014-3231-6. PubMed PMID: WOS:000357044200016.

147. Ravera S, Dufour C, Degan P, Cappelli E. Fanconi anemia: from DNA repair to metabolism. European Journal of Human Genetics. 2018;26(4):475-6. doi: 10.1038/s41431-017-0046-6. PubMed PMID: WOS:000429542400005.

148. Wang AT, Smogorzewska A. SnapShot: Fanconi Anemia and Associated Proteins. Cell. 2015;160(1-2). doi: 10.1016/j.cell.2014.12.031. PubMed PMID: WOS:000347923200032.

149. Farley KI, Baserga SJ. Probing the mechanisms underlying human diseases in making ribosomes. Biochem Soc T. 2016;44:1035-44. doi: 10.1042/Bst20160064. PubMed PMID: WOS:000392728300009.

150. Dauwerse JG, Dixon J, Seland S, Ruivenkamp CAL, van Haeringen A, Hoefsloot LH, Peters DJM, Boers ACD, Daumer-Haas C, Maiwald R, Zweier C, Kerr B, Cobo AM, Toral JF, Hoogeboom AJM, Lohmann DR, Hehr U, Dixon MJ, Breuning MH, Wieczorek D. Mutations in genes encoding subunits of RNA polymerases I and III cause Treacher Collins syndrome. Nat Genet. 2011;43(1):20-2. doi: 10.1038/ng.724. PubMed PMID: WOS:000285683500009.

151. Valdez BC, Henning D, So RB, Dixon J, Dixon MJ. The Treacher Collins syndrome (TCOF1) gene product is involved in ribosomal DNA gene transcription by interacting with upstream binding factor. P Natl Acad Sci USA. 2004;101(29):10709-14. doi: 10.1073/pnas.0402492101. PubMed PMID: WOS:000222842700041.

152. Gonzales B, Henning D, So RB, Dixon J, Dixon MJ, Valdez BC. The Treacher Collins syndrome (TCOF1) gene product is involved in pre-rRNA methylation. Hum Mol Genet. 2005;14(14):2035-43. doi: 10.1093/hmg/ddi208. PubMed PMID: WOS:000230205800012.

153. Griffin JN, Sondalle SB, Del Viso F, Baserga SJ, Khokha MK. The ribosome biogenesis factor Nol11 is required for optimal rDNA transcription and craniofacial development in Xenopus. PLoS Genet. 2015;11(3):e1005018. doi: 10.1371/journal.pgen.1005018. PubMed PMID: 25756904; PMCID: 4354908.

154. Betard C, Rasquin-Weber A, Brewer C, Drouin E, Clark S, Verner A, Darmond-Zwaig C, Fortin J, Mercier J, Chagnon P, Fujiwara TM, Morgan K, Richter A, Hudson TJ, Mitchell GA. Localization of a recessive gene for North American Indian childhood cirrhosis to chromosome region 16q22 - and identification of a shared haplotype. American Journal of Human Genetics. 2000;67(1):222-8. doi: Doi 10.1086/302993. PubMed PMID: WOS:000088926900025.

155. Nousbeck J, Spiegel R, Ishida-Yamamoto A, Indelman M, Shani-Adir A, Adir N, Lipkin E, Bercovici S, Geiger D, van Steensel MA, Steijlen PM, Bergman R, Bindereif A, Choder M, Shalev S, Sprecher E. Alopecia, neurological defects, and endocrinopathy syndrome caused by decreased expression of RBM28, a nucleolar protein associated with ribosome biogenesis. Am J Hum Genet. 2008;82(5):1114-21. doi: 10.1016/j.ajhg.2008.03.014. PubMed PMID: 18439547; PMCID: 2427309.

156. Spiegel R, Shalev SA, Adawi A, Sprecher E, Tenenbaum-Rakover Y. ANE syndrome caused by mutated RBM28 gene: a novel etiology of combined pituitary hormone deficiency. Eur J Endocrinol. 2010;162(6):1021-5. doi: 10.1530/EJE-10-0077. PubMed PMID: 20231366.

157. Warshauer E, Samuelov L, Sarig O, Vodo D, Bindereif A, Kanaan M, Gat U, Fuchs-Telem D, Shomron N, Farberov L, Pasmanik-Chor M, Nardini G, Winkler E, Meilik B, Petit I, Aberdam D, Paus R, Sprecher E, Nousbeck J. RBM28, a protein deficient in ANE syndrome, regulates hair follicle growth via miR-203 and p63. Exp Dermatol. 2015;24(8):618-22. doi: 10.1111/exd.12737. PubMed PMID: 25939713.

158. Bryant CJ, Lorea CF, de Almeida HL, Jr., Weinert L, Vedolin L, Pinto EVF, Baserga SJ. Biallelic splicing variants in the nucleolar 60S assembly factor RBM28 cause the ribosomopathy ANE syndrome. Proc Natl Acad Sci U S A. 2021;118(19). doi: 10.1073/pnas.2017777118. PubMed PMID: 33941690; PMCID: 8126767.

159. Gerton JL. Faulty ribosome biogenesis underlies the ribosomopathy alopecia, neurological defects, endocrinopathy (ANE) syndrome. Proc Natl Acad Sci U S A. 2021;118(24). doi: 10.1073/pnas.2107030118. PubMed PMID: 34035178; PMCID: 8214674.

160. McCann KL, Teramoto T, Zhang J, Tanaka Hall TM, Baserga SJ. The molecular basis for ANE syndrome revealed by the large ribosomal subunit processome interactome. Elife. 2016;5. doi: 10.7554/eLife.16381. PubMed PMID: 27077951; PMCID: 4859800.

161. Liang X, Zuo MQ, Zhang Y, Li N, Ma C, Dong MQ, Gao N. Structural snapshots of human pre-60S ribosomal particles before and after nuclear export. Nat Commun. 2020;11(1):3542. doi: 10.1038/s41467-020-17237-x. PubMed PMID: 32669547; PMCID: 7363849.

162. Sanghai ZA, Miller L, Molloy KR, Barandun J, Hunziker M, Chaker-Margot M, Wang J, Chait BT, Klinge S. Modular assembly of the nucleolar pre-60S ribosomal subunit. Nature. 2018;556(7699):126-9. doi: 10.1038/nature26156. PubMed PMID: 29512650.

163. Kater L, Thoms M, Barrio-Garcia C, Cheng J, Ismail S, Ahmed YL, Bange G, Kressler D, Berninghausen O, Sinning I, Hurt E, Beckmann R. Visualizing the Assembly

Pathway of Nucleolar Pre-60S Ribosomes. Cell. 2017;171(7):1599-610 e14. doi: 10.1016/j.cell.2017.11.039. PubMed PMID: 29245012; PMCID: 5745149.

164. Ma C, Wu S, Li N, Chen Y, Yan K, Li Z, Zheng L, Lei J, Woolford JL, Jr., Gao N. Structural snapshot of cytoplasmic pre-60S ribosomal particles bound by Nmd3, Lsg1, Tif6 and Reh1. Nat Struct Mol Biol. 2017;24(3):214-20. doi: 10.1038/nsmb.3364. PubMed PMID: 28112732; PMCID: 5555584.

165. Zisser G, Ohmayer U, Mauerhofer C, Mitterer V, Klein I, Rechberger GN, Wolinski H, Prattes M, Pertschy B, Milkereit P, Bergler H. Viewing pre-60S maturation at a minute's timescale. Nucleic Acids Res. 2018;46(6):3140-51. doi: 10.1093/nar/gkx1293. PubMed PMID: 29294095; PMCID: 5888160.

166. Sun C, Woolford JL, Jr. The yeast nucleolar protein Nop4p contains four RNA recognition motifs necessary for ribosome biogenesis. J Biol Chem. 1997;272(40):25345-52. PubMed PMID: 9312154.

167. Sun C, Woolford JL, Jr. The yeast NOP4 gene product is an essential nucleolar protein required for pre-rRNA processing and accumulation of 60S ribosomal subunits. EMBO J. 1994;13(13):3127-35. PubMed PMID: 8039505; PMCID: 395203.

168. Ambros V. MicroRNAs and developmental timing. Curr Opin Genet Dev. 2011;21(4):511-7. doi: 10.1016/j.gde.2011.04.003. PubMed PMID: 21530229; PMCID: 3149784.

169. Chen J, Wang DZ. microRNAs in cardiovascular development. J Mol Cell Cardiol. 2012;52(5):949-57. doi: 10.1016/j.yjmcc.2012.01.012. PubMed PMID: 22300733; PMCID: 3721071.

170. Aubert M, O'Donohue MF, Lebaron S, Gleizes PE. Pre-Ribosomal RNA Processing in Human Cells: From Mechanisms to Congenital Diseases. Biomolecules. 2018;8(4). doi: 10.3390/biom8040123. PubMed PMID: 30356013; PMCID: 6315592.

171. Pederson T. The nucleolus. Cold Spring Harb Perspect Biol. 2011;3(3). doi: 10.1101/cshperspect.a000638. PubMed PMID: 21106648; PMCID: 3039934.

172. Moss T, Langlois F, Gagnon-Kugler T, Stefanovsky V. A housekeeper with power of attorney: the rRNA genes in ribosome biogenesis. Cell Mol Life Sci. 2007;64(1):29-49. doi: 10.1007/s00018-006-6278-1. PubMed PMID: 17171232.

173. Sharifi S, Bierhoff H. Regulation of RNA Polymerase I Transcription in Development, Disease, and Aging. Annu Rev Biochem. 2018;87:51-73. doi: 10.1146/annurev-biochem-062917-012612. PubMed PMID: 29589958.

174. Sloan KE, Warda AS, Sharma S, Entian KD, Lafontaine DLJ, Bohnsack MT. Tuning the ribosome: The influence of rRNA modification on eukaryotic ribosome biogenesis and function. RNA Biol. 2017;14(9):1138-52. doi: 10.1080/15476286.2016.1259781. PubMed PMID: 27911188; PMCID: 5699541.

175. O'Donohue MF, Choesmel V, Faubladier M, Fichant G, Gleizes PE. Functional dichotomy of ribosomal proteins during the synthesis of mammalian 40S ribosomal subunits. J Cell Biol. 2010;190(5):853-66. doi: 10.1083/jcb.201005117. PubMed PMID: 20819938; PMCID: 2935573.

176. Pelletier J, Thomas G, Volarevic S. Ribosome biogenesis in cancer: new players and therapeutic avenues. Nat Rev Cancer. 2018;18(1):51-63. doi: 10.1038/nrc.2017.104. PubMed PMID: 29192214.

177. Bustelo XR, Dosil M. Ribosome biogenesis and cancer: basic and translational challenges. Curr Opin Genet Dev. 2018;48:22-9. doi: 10.1016/j.gde.2017.10.003. PubMed PMID: 29100209.

178. Penzo M, Montanaro L, Trere D, Derenzini M. The ribosome biogenesis-cancer connection. Cells. 2019;8(1). Epub 2019/01/18. doi: 10.3390/cells8010055. PubMed PMID: 30650663; PMCID: PMC6356843.

179. Harold CM, Buhagiar AF, Cheng Y, Baserga SJ. Ribosomal RNA Transcription Regulation in Breast Cancer. Genes (Basel). 2021;12(4). doi: 10.3390/genes12040502. PubMed PMID: 33805424; PMCID: 8066022.

180. Low JY, Sirajuddin P, Moubarek M, Agarwal S, Rege A, Guner G, Liu H, Yang Z, De Marzo AM, Bieberich C, Laiho M. Effective targeting of RNA polymerase I in treatment-resistant prostate cancer. Prostate. 2019;79(16):1837-51. doi: 10.1002/pros.23909. PubMed PMID: 31524299; PMCID: 7025478.

181. Aspesi A, Ellis SR. Rare ribosomopathies: insights into mechanisms of cancer. Nat Rev Cancer. 2019;19(4):228-38. doi: 10.1038/s41568-019-0105-0. PubMed PMID: 30670820.

182. Peltonen K, Colis L, Liu H, Trivedi R, Moubarek MS, Moore HM, Bai B, Rudek MA, Bieberich CJ, Laiho M. A targeting modality for destruction of RNA polymerase I that possesses anticancer activity. Cancer Cell. 2014;25(1):77-90. doi: 10.1016/j.ccr.2013.12.009. PubMed PMID: 24434211; PMCID: 3930145.

183. Drygin D, Lin A, Bliesath J, Ho CB, O'Brien SE, Proffitt C, Omori M, Haddach M, Schwaebe MK, Siddiqui-Jain A, Streiner N, Quin JE, Sanij E, Bywater MJ, Hannan RD, Ryckman D, Anderes K, Rice WG. Targeting RNA polymerase I with an oral small molecule CX-5461 inhibits ribosomal RNA synthesis and solid tumor growth. Cancer Res. 2011;71(4):1418-30. doi: 10.1158/0008-5472.CAN-10-1728. PubMed PMID: 21159662.

184. Scull CE, Zhang Y, Tower N, Rasmussen L, Padmalayam I, Hunter R, Zhai L, Bostwick R, Schneider DA. Discovery of novel inhibitors of ribosome biogenesis by innovative high throughput screening strategies. Biochem J. 2019;476(15):2209-19. doi: 10.1042/BCJ20190207. PubMed PMID: 31341008; PMCID: 7278283.

185. Kirsch VC, Orgler C, Braig S, Jeremias I, Auerbach D, Muller R, Vollmar AM, Sieber SA. The Cytotoxic Natural Product Vioprolide A Targets Nucleolar Protein 14, Which Is Essential for Ribosome Biogenesis. Angew Chem Int Ed Engl. 2020;59(4):1595-600. doi: 10.1002/anie.201911158. PubMed PMID: 31658409; PMCID: 7004033.

186. Ferreira R, Schneekloth JS, Jr., Panov KI, Hannan KM, Hannan RD. Targeting the RNA Polymerase I Transcription for Cancer Therapy Comes of Age. Cells. 2020;9(2). doi: 10.3390/cells9020266. PubMed PMID: 31973211; PMCID: 7072222.

187. Stamatopoulou V, Parisot P, De Vleeschouwer C, Lafontaine DLJ. Use of the iNo score to discriminate normal from altered nucleolar morphology, with applications in basic cell biology and potential in human disease diagnostics. Nat Protoc. 2018;13(10):2387-406. doi: 10.1038/s41596-018-0044-3. PubMed PMID: 30250292.

188. He JS, Soo P, Evers M, Parsons KM, Hein N, Hannan KM, Hannan RD, George AJ. High-Content Imaging Approaches to Quantitate Stress-Induced Changes in Nucleolar Morphology. Assay Drug Dev Technol. 2018;16(6):320-32. doi: 10.1089/adt.2018.861. PubMed PMID: 30148664.

189. Bai B, Moore HM, Laiho M. CRM1 and its ribosome export adaptor NMD3 localize to the nucleolus and affect rRNA synthesis. Nucleus. 2013;4(4):315-25. doi: 10.4161/nucl.25342. PubMed PMID: 23782956; PMCID: 3810339.

190. Lafita-Navarro MC, Blanco R, Mata-Garrido J, Liano-Pons J, Tapia O, Garcia-Gutierrez L, Garcia-Alegria E, Berciano MT, Lafarga M, Leon J. MXD1 localizes in the nucleolus, binds UBF and impairs rRNA synthesis. Oncotarget. 2016;7(43):69536-48. doi: 10.18632/oncotarget.11766. PubMed PMID: 27588501; PMCID: 5342496.

191. Cheng F, Belting M, Fransson LA, Mani K. Nucleolin is a nuclear target of heparan sulfate derived from glypican-1. Exp Cell Res. 2017;354(1):31-9. doi: 10.1016/j.yexcr.2017.03.021. PubMed PMID: 28300561.

192. Hayashi Y, Kato K, Kimura K. The hierarchical structure of the perichromosomal layer comprises Ki67, ribosomal RNAs, and nucleolar proteins. Biochem Biophys Res Commun. 2017;493(2):1043-9. doi: 10.1016/j.bbrc.2017.09.092. PubMed PMID: 28935370.

193. Calo E, Gu B, Bowen ME, Aryan F, Zalc A, Liang J, Flynn RA, Swigut T, Chang HY, Attardi LD, Wysocka J. Tissue-selective effects of nucleolar stress and rDNA damage in developmental disorders. Nature. 2018;554(7690):112-7. doi: 10.1038/nature25449. PubMed PMID: 29364875; PMCID: 5927778.

194. Hayashi Y, Fujimura A, Kato K, Udagawa R, Hirota T, Kimura K. Nucleolar integrity during interphase supports faithful Cdk1 activation and mitotic entry. Sci Adv. 2018;4(6):eaap7777. doi: 10.1126/sciadv.aap7777. PubMed PMID: 29881774; PMCID: 5990311.

195. Rossetti S, Wierzbicki AJ, Sacchi N. Undermining ribosomal RNA transcription in both the nucleolus and mitochondrion: an offbeat approach to target MYC-driven cancer. Oncotarget. 2018;9(4):5016-31. doi: 10.18632/oncotarget.23579. PubMed PMID: 29435159; PMCID: 5797030.

196. Dong C, An L, Yu CH, Huen MSY. A DYRK1B-dependent pathway suppresses rDNA transcription in response to DNA damage. Nucleic Acids Res. 2021;49(3):1485-96. doi: 10.1093/nar/gkaa1290. PubMed PMID: 33469661; PMCID: 7897492.

197. Slomnicki LP, Hallgren J, Vashishta A, Smith SC, Ellis SR, Hetman M. Proapoptotic Requirement of Ribosomal Protein L11 in Ribosomal Stress-Challenged Cortical Neurons. Mol Neurobiol. 2018;55(1):538-53. doi: 10.1007/s12035-016-0336-y. PubMed PMID: 27975169.

198. Lin T, Sun L, Lee JE, Lee JB, Kim SY, Jin DI. Changes of histone H3 lysine 23 acetylation and methylation in porcine somatic cells, oocytes and preimplantation embryos. Theriogenology. 2020;148:162-73. doi: 10.1016/j.theriogenology.2020.03.006. PubMed PMID: 32182524.

199. Mikhaleva EA, Leinsoo TA, Ishizu H, Gvozdev VA, Klenov MS. The nucleolar transcriptome regulates Piwi shuttling between the nucleolus and the nucleoplasm. Chromosome Res. 2019;27(1-2):141-52. doi: 10.1007/s10577-018-9595-y. PubMed PMID: 30539407.

200. Dvořáčková M, Fajkus J. Visualization of the Nucleolus Using Ethynyl Uridine. Front Plant Sci. 2018;9:177. doi: 10.3389/fpls.2018.00177. PubMed PMID: 29503656; PMCID: 5820300.

201. Hayashi K, Matsunaga S. Heat and chilling stress induce nucleolus morphological changes. J Plant Res. 2019;132(3):395-403. doi: 10.1007/s10265-019-01096-9. PubMed PMID: 30847615; PMCID: 7198650.

202. McQuin C, Goodman A, Chernyshev V, Kamentsky L, Cimini BA, Karhohs KW, Doan M, Ding L, Rafelski SM, Thirstrup D, Wiegraebe W, Singh S, Becker T, Caicedo JC, Carpenter AE. CellProfiler 3.0: Next-generation image processing for biology. PLoS

Biol. 2018;16(7):e2005970. doi: 10.1371/journal.pbio.2005970. PubMed PMID: 29969450; PMCID: 6029841.

203. Stoter M, Janosch A, Barsacchi R, Bickle M. CellProfiler and KNIME: Open-Source Tools for High-Content Screening. Methods Mol Biol. 2019;1953:43-60. doi: 10.1007/978-1-4939-9145-7_4. PubMed PMID: 30912015.

204. Dobson ETA, Cimini B, Klemm AH, Wahlby C, Carpenter AE, Eliceiri KW. ImageJ and CellProfiler: Complements in Open-Source Bioimage Analysis. Curr Protoc. 2021;1(5):e89. doi: 10.1002/cpz1.89. PubMed PMID: 34038030.

205. Peltonen K, Colis L, Liu H, Jaamaa S, Zhang Z, Af Hallstrom T, Moore HM, Sirajuddin P, Laiho M. Small molecule BMH-compounds that inhibit RNA polymerase I and cause nucleolar stress. Mol Cancer Ther. 2014;13(11):2537-46. doi: 10.1158/1535-7163.MCT-14-0256. PubMed PMID: 25277384; PMCID: 4221476.

206. Jao CY, Salic A. Exploring RNA transcription and turnover in vivo by using click chemistry. Proc Natl Acad Sci U S A. 2008;105(41):15779-84. doi: 10.1073/pnas.0808480105. PubMed PMID: 18840688; PMCID: 2572917.

207. Lee J, Vogt CE, McBrairty M, Al-Hashimi HM. Influence of dimethylsulfoxide on RNA structure and ligand binding. Anal Chem. 2013;85(20):9692-8. doi: 10.1021/ac402038t. PubMed PMID: 23987474; PMCID: 3855037.

208. Galvao J, Davis B, Tilley M, Normando E, Duchen MR, Cordeiro MF. Unexpected low-dose toxicity of the universal solvent DMSO. Faseb J. 2014;28(3):1317-30. doi: 10.1096/fj.13-235440. PubMed PMID: 24327606.

209. Grandori C, Gomez-Roman N, Felton-Edkins ZA, Ngouenet C, Galloway DA, Eisenman RN, White RJ. c-Myc binds to human ribosomal DNA and stimulates transcription of rRNA genes by RNA polymerase I. Nat Cell Biol. 2005;7(3):311-8. doi: 10.1038/ncb1224. PubMed PMID: 15723054.

210. Turi Z, Senkyrikova M, Mistrik M, Bartek J, Moudry P. Perturbation of RNA Polymerase I transcription machinery by ablation of HEATR1 triggers the RPL5/RPL11-MDM2-p53 ribosome biogenesis stress checkpoint pathway in human cells. Cell Cycle. 2018;17(1):92-101. doi: 10.1080/15384101.2017.1403685. PubMed PMID: 29143558; PMCID: 5815431.

211. Gallagher JE, Dunbar DA, Granneman S, Mitchell BM, Osheim Y, Beyer AL, Baserga SJ. RNA polymerase I transcription and pre-rRNA processing are linked by specific SSU processome components. Genes Dev. 2004;18(20):2506-17. doi: 10.1101/gad.1226604. PubMed PMID: 15489292; PMCID: 529538.

212. Prieto JL, McStay B. Recruitment of factors linking transcription and processing of pre-rRNA to NOR chromatin is UBF-dependent and occurs independent of

transcription in human cells. Genes Dev. 2007;21(16):2041-54. doi: 10.1101/gad.436707. PubMed PMID: 17699751; PMCID: 1948859.

213. Koiwai K, Noma S, Takahashi Y, Hayano T, Maezawa S, Kouda K, Matsumoto T, Suzuki M, Furuichi M, Koiwai O. TdIF2 is a nucleolar protein that promotes rRNA gene promoter activity. Genes Cells. 2011;16(7):748-64. doi: 10.1111/j.1365-2443.2011.01524.x. PubMed PMID: 21668587.

214. Engel KL, French SL, Viktorovskaya OV, Beyer AL, Schneider DA. Spt6 Is Essential for rRNA Synthesis by RNA Polymerase I. Mol Cell Biol. 2015;35(13):2321-31. doi: 10.1128/MCB.01499-14. PubMed PMID: 25918242; PMCID: 4456441.

215. Zhang Y, Forys JT, Miceli AP, Gwinn AS, Weber JD. Identification of DHX33 as a mediator of rRNA synthesis and cell growth. Mol Cell Biol. 2011;31(23):4676-91. doi: 10.1128/MCB.05832-11. PubMed PMID: 21930779; PMCID: 3232920.

216. Miller G, Panov KI, Friedrich JK, Trinkle-Mulcahy L, Lamond AI, Zomerdijk JC. hRRN3 is essential in the SL1-mediated recruitment of RNA Polymerase I to rRNA gene promoters. EMBO J. 2001;20(6):1373-82. doi: 10.1093/emboj/20.6.1373. PubMed PMID: 11250903; PMCID: 145519.

217. Bodem J, Dobreva G, Hoffmann-Rohrer U, Iben S, Zentgraf H, Delius H, Vingron M, Grummt I. TIF-IA, the factor mediating growth-dependent control of ribosomal RNA synthesis, is the mammalian homolog of yeast Rrn3p. EMBO Rep. 2000;1(2):171-5. doi: 10.1093/embo-reports/kvd032. PubMed PMID: 11265758; PMCID: 1084264.

218. Moorefield B, Greene EA, Reeder RH. RNA polymerase I transcription factor Rrn3 is functionally conserved between yeast and human. Proc Natl Acad Sci U S A. 2000;97(9):4724-9. doi: 10.1073/pnas.080063997. PubMed PMID: 10758157; PMCID: 18300.

219. Freed EF, Baserga SJ. The C-terminus of Utp4, mutated in childhood cirrhosis, is essential for ribosome biogenesis. Nucleic Acids Res. 2010;38(14):4798-806. doi: 10.1093/nar/gkq185. PubMed PMID: 20385600; PMCID: 2919705.

220. Gene Ontology Data Archive (Version 2021-07-02) [Internet]2021 [cited 2021-07-12].

221. Raman N, Weir E, Muller S. The AAA ATPase MDN1 Acts as a SUMO-Targeted Regulator in Mammalian Pre-ribosome Remodeling. Mol Cell. 2016;64(3):607-15. doi: 10.1016/j.molcel.2016.09.039. PubMed PMID: 27814492.

222. Chen JY, Tan X, Wang ZH, Liu YZ, Zhou JF, Rong XZ, Lu L, Li Y. The ribosome biogenesis protein Esf1 is essential for pharyngeal cartilage formation in zebrafish. FEBS J. 2018;285(18):3464-84. doi: 10.1111/febs.14622. PubMed PMID: 30073783.

223. Ye C, Liu B, Lu H, Liu J, Rabson AB, Jacinto E, Pestov DG, Shen Z. BCCIP is required for nucleolar recruitment of eIF6 and 12S pre-rRNA production during 60S ribosome biogenesis. Nucleic Acids Res. 2020;48(22):12817-32. doi: 10.1093/nar/gkaa1114. PubMed PMID: 33245766; PMCID: 7736804.

224. Stolc V, Altman S. Rpp1, an essential protein subunit of nuclear RNase P required for processing of precursor tRNA and 35S precursor rRNA in Saccharomyces cerevisiae. Genes Dev. 1997;11(18):2414-25. doi: 10.1101/gad.11.18.2414. PubMed PMID: 9308968; PMCID: 316520.

225. Muller JS, Burns DT, Griffin H, Wells GR, Zendah RA, Munro B, Schneider C, Horvath R. RNA exosome mutations in pontocerebellar hypoplasia alter ribosome biogenesis and p53 levels. Life Sci Alliance. 2020;3(8). doi: 10.26508/lsa.202000678. PubMed PMID: 32527837.

226. Westendorf JM, Konstantinov KN, Wormsley S, Shu MD, Matsumoto-Taniura N, Pirollet F, Klier FG, Gerace L, Baserga SJ. M phase phosphoprotein 10 is a human U3 small nucleolar ribonucleoprotein component. Mol Biol Cell. 1998;9(2):437-49. doi: 10.1091/mbc.9.2.437. PubMed PMID: 9450966; PMCID: 25272.

227. Zorbas C, Nicolas E, Wacheul L, Huvelle E, Heurgue-Hamard V, Lafontaine DL. The human 18S rRNA base methyltransferases DIMT1L and WBSCR22-TRMT112 but not rRNA modification are required for ribosome biogenesis. Mol Biol Cell. 2015;26(11):2080-95. doi: 10.1091/mbc.E15-02-0073. PubMed PMID: 25851604; PMCID: 4472018.

228. Wang Y, Liu J, Zhao H, Lu W, Zhao J, Yang L, Li N, Du X, Ke Y. Human 1A6/DRIM, the homolog of yeast Utp20, functions in the 18S rRNA processing. Biochim Biophys Acta. 2007;1773(6):863-8. doi: 10.1016/j.bbamcr.2007.04.002. PubMed PMID: 17498821.

229. Ghosh T, Peterson B, Tomasevic N, Peculis BA. Xenopus U8 snoRNA binding protein is a conserved nuclear decapping enzyme. Mol Cell. 2004;13(6):817-28. doi: 10.1016/s1097-2765(04)00127-3. PubMed PMID: 15053875.

230. Werner A, Iwasaki S, McGourty CA, Medina-Ruiz S, Teerikorpi N, Fedrigo I, Ingolia NT, Rape M. Cell-fate determination by ubiquitin-dependent regulation of translation. Nature. 2015;525(7570):523-7. doi: 10.1038/nature14978. PubMed PMID: 26399832; PMCID: 4602398.

231. Yang Y, Isaac C, Wang C, Dragon F, Pogacic V, Meier UT. Conserved composition of mammalian box H/ACA and box C/D small nucleolar ribonucleoprotein particles and their interaction with the common factor Nopp140. Mol Biol Cell. 2000;11(2):567-77. doi: 10.1091/mbc.11.2.567. PubMed PMID: 10679015; PMCID: 14794.

232. Poll G, Braun T, Jakovljevic J, Neueder A, Jakob S, Woolford JL, Jr., Tschochner H, Milkereit P. rRNA maturation in yeast cells depleted of large ribosomal subunit proteins. PLoS One. 2009;4(12):e8249. doi: 10.1371/journal.pone.0008249. PubMed PMID: 20011513; PMCID: 2788216.

233. Ferreira-Cerca S, Poll G, Gleizes PE, Tschochner H, Milkereit P. Roles of eukaryotic ribosomal proteins in maturation and transport of pre-18S rRNA and ribosome function. Mol Cell. 2005;20(2):263-75. doi: 10.1016/j.molcel.2005.09.005. PubMed PMID: 16246728.

234. Murayama A, Ohmori K, Fujimura A, Minami H, Yasuzawa-Tanaka K, Kuroda T, Oie S, Daitoku H, Okuwaki M, Nagata K, Fukamizu A, Kimura K, Shimizu T, Yanagisawa J. Epigenetic control of rDNA loci in response to intracellular energy status. Cell. 2008;133(4):627-39. doi: 10.1016/j.cell.2008.03.030. PubMed PMID: 18485871.

235. Bonhoure N, Praz V, Moir RD, Willemin G, Mange F, Moret C, Willis IM, Hernandez N. MAF1 is a chronic repressor of RNA polymerase III transcription in the mouse. Sci Rep. 2020;10(1):11956. doi: 10.1038/s41598-020-68665-0. PubMed PMID: 32686713; PMCID: 7371695.

236. Upadhya R, Lee J, Willis IM. Maf1 is an essential mediator of diverse signals that repress RNA polymerase III transcription. Mol Cell. 2002;10(6):1489-94. doi: 10.1016/s1097-2765(02)00787-6. PubMed PMID: 12504022.

237. Chen H, Shi Z, Guo J, Chang KJ, Chen Q, Yao CH, Haigis MC, Shi Y. The human mitochondrial 12S rRNA m(4)C methyltransferase METTL15 is required for mitochondrial function. J Biol Chem. 2020;295(25):8505-13. doi: 10.1074/jbc.RA119.012127. PubMed PMID: 32371392; PMCID: 7307190.

238. Van Haute L, Hendrick AG, D'Souza AR, Powell CA, Rebelo-Guiomar P, Harbour ME, Ding S, Fearnley IM, Andrews B, Minczuk M. METTL15 introduces N4-methylcytidine into human mitochondrial 12S rRNA and is required for mitoribosome biogenesis. Nucleic Acids Res. 2019;47(19):10267-81. doi: 10.1093/nar/gkz735. PubMed PMID: 31665743; PMCID: 6821322.

239. Dalla Rosa I, Durigon R, Pearce SF, Rorbach J, Hirst EM, Vidoni S, Reyes A, Brea-Calvo G, Minczuk M, Woellhaf MW, Herrmann JM, Huynen MA, Holt IJ, Spinazzola A. MPV17L2 is required for ribosome assembly in mitochondria. Nucleic Acids Res. 2014;42(13):8500-15. doi: 10.1093/nar/gku513. PubMed PMID: 24948607; PMCID: 4117752.

240. Zhu X, Zhang H, Mendell JT. Ribosome Recycling by ABCE1 Links Lysosomal Function and Iron Homeostasis to 3' UTR-Directed Regulation and Nonsense-Mediated Decay. Cell Rep. 2020;32(2):107895. doi: 10.1016/j.celrep.2020.107895. PubMed PMID: 32668236; PMCID: 7433747.

241. Russell J, Zomerdijk JC. The RNA polymerase I transcription machinery. Biochem Soc Symp. 2006(73):203-16. doi: 10.1042/bss0730203. PubMed PMID: 16626300; PMCID: 3858827.

242. Gorski JJ, Pathak S, Panov K, Kasciukovic T, Panova T, Russell J, Zomerdijk JC. A novel TBP-associated factor of SL1 functions in RNA polymerase I transcription. EMBO J. 2007;26(6):1560-8. doi: 10.1038/sj.emboj.7601601. PubMed PMID: 17318177; PMCID: 1829371.

243. Evers R, Grummt I. Molecular coevolution of mammalian ribosomal gene terminator sequences and the transcription termination factor TTF-I. Proc Natl Acad Sci U S A. 1995;92(13):5827-31. doi: 10.1073/pnas.92.13.5827. PubMed PMID: 7597036; PMCID: 41594.

244. Sekiguchi T, Hayano T, Yanagida M, Takahashi N, Nishimoto T. NOP132 is required for proper nucleolus localization of DEAD-box RNA helicase DDX47. Nucleic Acids Res. 2006;34(16):4593-608. doi: 10.1093/nar/gkl603. PubMed PMID: 16963496; PMCID: 1636366.

245. Shao Z, Flynn RA, Crowe JL, Zhu Y, Liang J, Jiang W, Aryan F, Aoude P, Bertozzi CR, Estes VM, Lee BJ, Bhagat G, Zha S, Calo E. DNA-PKcs has KU-dependent function in rRNA processing and haematopoiesis. Nature. 2020;579(7798):291-6. doi: 10.1038/s41586-020-2041-2. PubMed PMID: 32103174.

246. Wallisch M, Kunkel E, Hoehn K, Grummt F. Ku antigen supports termination of mammalian rDNA replication by transcription termination factor TTF-I. Biol Chem. 2002;383(5):765-71. doi: 10.1515/BC.2002.080. PubMed PMID: 12108541.

247. Jackson DA, Pombo A, Iborra F. The balance sheet for transcription: an analysis of nuclear RNA metabolism in mammalian cells. Faseb J. 2000;14(2):242-54. doi: 10.1096/fasebj.14.2.242. PubMed PMID: 10657981.

248. Popov A, Smirnov E, Kovacik L, Raska O, Hagen G, Stixova L, Raska I. Duration of the first steps of the human rRNA processing. Nucleus. 2013;4(2):134-41. doi: 10.4161/nucl.23985. PubMed PMID: 23412654; PMCID: 3621745.

249. Ou L, Duan D, Wu J, Nice E, Huang C. The application of high throughput siRNA screening technology to study host-pathogen interactions. Comb Chem High Throughput Screen. 2012;15(4):299-305. doi: 10.2174/138620712799361834. PubMed PMID: 22221062.

250. Echeverri CJ, Beachy PA, Baum B, Boutros M, Buchholz F, Chanda SK, Downward J, Ellenberg J, Fraser AG, Hacohen N, Hahn WC, Jackson AL, Kiger A, Linsley PS, Lum L, Ma Y, Mathey-Prevot B, Root DE, Sabatini DM, Taipale J, Perrimon N, Bernards R. Minimizing the risk of reporting false positives in large-scale RNAi

screens. Nat Methods. 2006;3(10):777-9. doi: 10.1038/nmeth1006-777. PubMed PMID: 16990807.

251. Reimer G, Pollard KM, Penning CA, Ochs RL, Lischwe MA, Busch H, Tan EM. Monoclonal autoantibody from a (New Zealand black x New Zealand white)F1 mouse and some human scleroderma sera target an Mr 34,000 nucleolar protein of the U3 RNP particle. Arthritis Rheum. 1987;30(7):793-800. doi: 10.1002/art.1780300709. PubMed PMID: 2441711.

252. Schneider CA, Rasband WS, Eliceiri KW. NIH Image to ImageJ: 25 years of image analysis. Nat Methods. 2012;9(7):671-5. doi: 10.1038/nmeth.2089. PubMed PMID: 22930834; PMCID: 5554542.

253. Carpenter AE, Jones TR, Lamprecht MR, Clarke C, Kang IH, Friman O, Guertin DA, Chang JH, Lindquist RA, Moffat J, Golland P, Sabatini DM. CellProfiler: image analysis software for identifying and quantifying cell phenotypes. Genome Biol. 2006;7(10):R100. doi: 10.1186/gb-2006-7-10-r100. PubMed PMID: 17076895; PMCID: 1794559.

254. Zhang XD. Illustration of SSMD, z score, SSMD*, z* score, and t statistic for hit selection in RNAi high-throughput screens. J Biomol Screen. 2011;16(7):775-85. doi: 10.1177/1087057111405851. PubMed PMID: 21515799.

255. Bersaglieri C, Santoro R. Genome organization in and around the nucleolus. Cells. 2019;8(6). doi: 10.3390/cells8060579. PubMed PMID: 31212844.

256. Moss T, Mars JC, Tremblay MG, Sabourin-Felix M. The chromatin landscape of the ribosomal RNA genes in mouse and human. Chromosome Res. 2019. doi: 10.1007/s10577-018-09603-9. PubMed PMID: 30617621.

257. Lafontaine DL. Noncoding RNAs in eukaryotic ribosome biogenesis and function. Nat Struct Mol Biol. 2015;22(1):11-9. doi: 10.1038/nsmb.2939. PubMed PMID: 25565028.

258. Bohnsack KE, Bohnsack MT. Uncovering the assembly pathway of human ribosomes and its emerging links to disease. EMBO J. 2019;38(13):e100278. doi: 10.15252/embj.2018100278. PubMed PMID: 31268599; PMCID: 6600647.

259. Klinge S, Woolford JL, Jr. Ribosome assembly coming into focus. Nat Rev Mol Cell Biol. 2019;20(2):116-31. doi: 10.1038/s41580-018-0078-y. PubMed PMID: 30467428.

260. Nerurkar P, Altvater M, Gerhardy S, Schutz S, Fischer U, Weirich C, Panse VG. Eukaryotic Ribosome Assembly and Nuclear Export. Int Rev Cell Mol Biol. 2015;319:107-40. doi: 10.1016/bs.ircmb.2015.07.002. PubMed PMID: 26404467.

261. Frazier MN, Pillon MC, Kocaman S, Gordon J, Stanley RE. Structural overview of macromolecular machines involved in ribosome biogenesis. Curr Opin Struct Biol. 2021;67:51-60. doi: 10.1016/j.sbi.2020.09.003. PubMed PMID: 33099228; PMCID: 8058114.

262. Hannan KM, Soo P, Wong MS, Lee JK, Hein N, Evers M, Wysoke KD, Williams TD, Montellese C, Smith LK, Al-Obaidi SJ, Núñez-Villacís L, Poh P, Pavy M, He J-S, Parsons KM, Diesch J, Burgio G, Ferreira R, Feng Z-P, Gould CM, Madhamshettiwar PB, Flygare J, Gonda TJ, Simpson KJ, Kutay U, Pearson RB, Engel C, Watkins NJ, Hannan RD, George AJ. Nuclear stabilisation of p53 requires a functional nucleolar surveillance pathway. bioRxiv. 2021:2021.01.21.427535. doi: 10.1101/2021.01.21.427535.

263. Armistead J, Triggs-Raine B. Diverse diseases from a ubiquitous process: the ribosomopathy paradox. Febs Lett. 2014;588(9):1491-500. doi: 10.1016/j.febslet.2014.03.024. PubMed PMID: 24657617.

264. Catez F, Dalla Venezia N, Marcel V, Zorbas C, Lafontaine DLJ, Diaz JJ. Ribosome biogenesis: An emerging druggable pathway for cancer therapeutics. Biochem Pharmacol. 2019;159:74-81. doi: 10.1016/j.bcp.2018.11.014. PubMed PMID: 30468711.

265. Sulima SO, Hofman IJF, De Keersmaecker K, Dinman JD. How Ribosomes Translate Cancer. Cancer Discov. 2017;7(10):1069-87. doi: 10.1158/2159-8290.CD-17-0550. PubMed PMID: 28923911; PMCID: 5630089.

266. Zisi A, Bartek J, Lindstrom MS. Targeting Ribosome Biogenesis in Cancer: Lessons Learned and Way Forward. Cancers (Basel). 2022;14(9). doi: 10.3390/cancers14092126. PubMed PMID: 35565259; PMCID: 9100539.

267. Nakanishi K. Anatomy of four human Argonaute proteins. Nucleic Acids Res. 2022. doi: 10.1093/nar/gkac519. PubMed PMID: 35736234; PMCID: 9262622.

268. Alvarez-Garcia I, Miska EA. MicroRNA functions in animal development and human disease. Development. 2005;132(21):4653-62. doi: 10.1242/dev.02073. PubMed PMID: 16224045.

269. Liang XH, Crooke ST. Depletion of key protein components of the RISC pathway impairs pre-ribosomal RNA processing. Nucleic Acids Res. 2011;39(11):4875-89. doi: 10.1093/nar/gkr076. PubMed PMID: 21321021; PMCID: 3113584.

270. Reza A, Yuan YG. microRNAs Mediated Regulation of the Ribosomal Proteins and its Consequences on the Global Translation of Proteins. Cells. 2021;10(1). doi: 10.3390/cells10010110. PubMed PMID: 33435549; PMCID: 7827472.

271. Bartel DP. MicroRNAs: target recognition and regulatory functions. Cell. 2009;136(2):215-33. doi: 10.1016/j.cell.2009.01.002. PubMed PMID: 19167326; PMCID: 3794896.

272. Peterson SM, Thompson JA, Ufkin ML, Sathyanarayana P, Liaw L, Congdon CB. Common features of microRNA target prediction tools. Front Genet. 2014;5:23. doi: 10.3389/fgene.2014.00023. PubMed PMID: 24600468; PMCID: 3927079.

273. Zeng X, Zhang X, Zou Q. Integrative approaches for predicting microRNA function and prioritizing disease-related microRNA using biological interaction networks. Brief Bioinform. 2016;17(2):193-203. doi: 10.1093/bib/bbv033. PubMed PMID: 26059461.

274. Pinzon N, Li B, Martinez L, Sergeeva A, Presumey J, Apparailly F, Seitz H. microRNA target prediction programs predict many false positives. Genome Res. 2017;27(2):234-45. doi: 10.1101/gr.205146.116. PubMed PMID: 28148562; PMCID: 5287229.

275. Wang Y, Baskerville S, Shenoy A, Babiarz JE, Baehner L, Blelloch R. Embryonic stem cell-specific microRNAs regulate the G1-S transition and promote rapid proliferation. Nat Genet. 2008;40(12):1478-83. doi: 10.1038/ng.250. PubMed PMID: 18978791; PMCID: 2630798.

276. Olarerin-George AO, Anton L, Hwang YC, Elovitz MA, Hogenesch JB. A functional genomics screen for microRNA regulators of NF-kappaB signaling. BMC Biol. 2013;11:19. doi: 10.1186/1741-7007-11-19. PubMed PMID: 23448136; PMCID: 3621838.

277. Eulalio A, Mano M, Dal Ferro M, Zentilin L, Sinagra G, Zacchigna S, Giacca M. Functional screening identifies miRNAs inducing cardiac regeneration. Nature. 2012;492(7429):376-81. doi: 10.1038/nature11739. PubMed PMID: 23222520.

278. Smith JL, Jeng S, McWeeney SK, Hirsch AJ. A MicroRNA Screen Identifies the Wnt Signaling Pathway as a Regulator of the Interferon Response during Flavivirus Infection. J Virol. 2017;91(8). doi: 10.1128/JVI.02388-16. PubMed PMID: 28148804; PMCID: 5375670.

279. Leivonen SK, Sahlberg KK, Makela R, Due EU, Kallioniemi O, Borresen-Dale AL, Perala M. High-throughput screens identify microRNAs essential for HER2 positive breast cancer cell growth. Mol Oncol. 2014;8(1):93-104. doi: 10.1016/j.molonc.2013.10.001. PubMed PMID: 24148764; PMCID: 5528509.

280. Nakano H, Yamada Y, Miyazawa T, Yoshida T. Gain-of-function microRNA screens identify miR-193a regulating proliferation and apoptosis in epithelial ovarian cancer cells. Int J Oncol. 2013;42(6):1875-82. doi: 10.3892/ijo.2013.1896. PubMed PMID: 23588298; PMCID: 3699598.

281. Zhang XD. A new method with flexible and balanced control of false negatives and false positives for hit selection in RNA interference high-throughput screening assays. J Biomol Screen. 2007;12(5):645-55. doi: 10.1177/1087057107300645. PubMed PMID: 17517904.

282. Karagkouni D, Paraskevopoulou MD, Chatzopoulos S, Vlachos IS, Tastsoglou S, Kanellos I, Papadimitriou D, Kavakiotis I, Maniou S, Skoufos G, Vergoulis T, Dalamagas T, Hatzigeorgiou AG. DIANA-TarBase v8: a decade-long collection of experimentally supported miRNA-gene interactions. Nucleic Acids Res. 2018;46(D1):D239-D45. doi: 10.1093/nar/gkx1141. PubMed PMID: 29156006; PMCID: 5753203.

283. Hart T, Komori HK, LaMere S, Podshivalova K, Salomon DR. Finding the active genes in deep RNA-seq gene expression studies. BMC Genomics. 2013;14:778. doi: 10.1186/1471-2164-14-778. PubMed PMID: 24215113; PMCID: 3870982.

284. Ahmad Y, Boisvert FM, Gregor P, Cobley A, Lamond AI. NOPdb: Nucleolar Proteome Database--2008 update. Nucleic Acids Res. 2009;37(Database issue):D181-4. doi: 10.1093/nar/gkn804. PubMed PMID: 18984612; PMCID: 2686505.

285. Jarboui MA, Wynne K, Elia G, Hall WW, Gautier VW. Proteomic profiling of the human T-cell nucleolus. Mol Immunol. 2011;49(3):441-52. doi: 10.1016/j.molimm.2011.09.005. PubMed PMID: 22014684.

286. Thul PJ, Akesson L, Wiking M, Mahdessian D, Geladaki A, Ait Blal H, Alm T, Asplund A, Bjork L, Breckels LM, Backstrom A, Danielsson F, Fagerberg L, Fall J, Gatto L, Gnann C, Hober S, Hjelmare M, Johansson F, Lee S, Lindskog C, Mulder J, Mulvey CM, Nilsson P, Oksvold P, Rockberg J, Schutten R, Schwenk JM, Sivertsson A, Sjostedt E, Skogs M, Stadler C, Sullivan DP, Tegel H, Winsnes C, Zhang C, Zwahlen M, Mardinoglu A, Ponten F, von Feilitzen K, Lilley KS, Uhlen M, Lundberg E. A subcellular map of the human proteome. Science. 2017;356(6340). doi: 10.1126/science.aal3321. PubMed PMID: 28495876.

287. Bryant CJ, McCool MA, Abriola L, Surovtseva YV, Baserga SJ. A high-throughput assay for directly monitoring nucleolar rRNA biogenesis. Open Biol. 2022;12(1):210305. doi: 10.1098/rsob.210305. PubMed PMID: 35078352; PMCID: 8790372.

288. Pfister AS, Kuhl M. Of Wnts and Ribosomes. Prog Mol Biol Transl Sci. 2018;153:131-55. doi: 10.1016/bs.pmbts.2017.11.006. PubMed PMID: 29389514.

289. Xiao X, Gu Y, Wang G, Chen S. c-Myc, RMRP, and miR-34a-5p form a positive-feedback loop to regulate cell proliferation and apoptosis in multiple myeloma. Int J Biol Macromol. 2019;122:526-37. doi: 10.1016/j.ijbiomac.2018.10.207. PubMed PMID: 30389523.

290. Goldfarb KC, Cech TR. Targeted CRISPR disruption reveals a role for RNase MRP RNA in human preribosomal RNA processing. Genes Dev. 2017;31(1):59-71. doi: 10.1101/gad.286963.116. PubMed PMID: 28115465; PMCID: 5287113.

291. Fromm B, Hoye E, Domanska D, Zhong X, Aparicio-Puerta E, Ovchinnikov V, Umu SU, Chabot PJ, Kang W, Aslanzadeh M, Tarbier M, Marmol-Sanchez E, Urgese G, Johansen M, Hovig E, Hackenberg M, Friedlander MR, Peterson KJ. MirGeneDB 2.1: toward a complete sampling of all major animal phyla. Nucleic Acids Res. 2022;50(D1):D204-D10. doi: 10.1093/nar/gkab1101. PubMed PMID: 34850127; PMCID: 8728216.

292. Alles J, Fehlmann T, Fischer U, Backes C, Galata V, Minet M, Hart M, Abu-Halima M, Grasser FA, Lenhof HP, Keller A, Meese E. An estimate of the total number of true human miRNAs. Nucleic Acids Res. 2019;47(7):3353-64. doi: 10.1093/nar/gkz097. PubMed PMID: 30820533; PMCID: 6468295.

293. Fromm B, Zhong X, Tarbier M, Friedlander MR, Hackenberg M. The limits of human microRNA annotation have been met. RNA. 2022;28(6):781-5. doi: 10.1261/rna.079098.122. PubMed PMID: 35236776; PMCID: 9074900.

294. Fromm B, Billipp T, Peck LE, Johansen M, Tarver JE, King BL, Newcomb JM, Sempere LF, Flatmark K, Hovig E, Peterson KJ. A Uniform System for the Annotation of Vertebrate microRNA Genes and the Evolution of the Human microRNAome. Annu Rev Genet. 2015;49:213-42. doi: 10.1146/annurev-genet-120213-092023. PubMed PMID: 26473382; PMCID: 4743252.

295. Fromm B, Domanska D, Hoye E, Ovchinnikov V, Kang W, Aparicio-Puerta E, Johansen M, Flatmark K, Mathelier A, Hovig E, Hackenberg M, Friedlander MR, Peterson KJ. MirGeneDB 2.0: the metazoan microRNA complement. Nucleic Acids Res. 2020;48(D1):D1172. doi: 10.1093/nar/gkz885. PubMed PMID: 31642479.

296. McCool MA, Buhagiar AF, Bryant CJ, Ogawa LM, Abriola L, Surovtseva YV, Baserga SJ. Human pre-60S assembly factors link rRNA transcription to pre-rRNA processing. RNA. 2022. doi: 10.1261/rna.079149.122. PubMed PMID: 36323459.

297. Ghoshal K, Majumder S, Datta J, Motiwala T, Bai S, Sharma SM, Frankel W, Jacob ST. Role of human ribosomal RNA (rRNA) promoter methylation and of methyl-CpG-binding protein MBD2 in the suppression of rRNA gene expression. J Biol Chem. 2004;279(8):6783-93. doi: 10.1074/jbc.M309393200. PubMed PMID: 14610093; PMCID: 2242730.

298. Wang M, Anikin L, Pestov DG. Two orthogonal cleavages separate subunit RNAs in mouse ribosome biogenesis. Nucleic Acids Res. 2014;42(17):11180-91. doi: 10.1093/nar/gku787. PubMed PMID: 25190460; PMCID: 4176171.

299. Schmidt EK, Clavarino G, Ceppi M, Pierre P. SUnSET, a nonradioactive method to monitor protein synthesis. Nat Methods. 2009;6(4):275-7. doi: 10.1038/nmeth.1314. PubMed PMID: 19305406.

300. Rubbi CP, Milner J. Disruption of the nucleolus mediates stabilization of p53 in response to DNA damage and other stresses. EMBO J. 2003;22(22):6068-77. doi: 10.1093/emboj/cdg579. PubMed PMID: 14609953; PMCID: 275437.

301. Kim HK, Fuchs G, Wang S, Wei W, Zhang Y, Park H, Roy-Chaudhuri B, Li P, Xu J, Chu K, Zhang F, Chua MS, So S, Zhang QC, Sarnow P, Kay MA. A transfer-RNA-derived small RNA regulates ribosome biogenesis. Nature. 2017;552(7683):57-62. doi: 10.1038/nature25005. PubMed PMID: 29186115; PMCID: 6066594.

302. Kim JC, Yu JH, Cho YK, Jung CS, Ahn SH, Gong G, Kim YS, Cho DH. Expression of SPRR3 is associated with tumor cell proliferation in less advanced stages of breast cancer. Breast Cancer Res Treat. 2012;133(3):909-16. doi: 10.1007/s10549-011-1868-5. PubMed PMID: 22076481.

303. Yang D, Li R, Xia J, Li W, Ma L, Ye L, Xue H. Long Noncoding RNA PCAT18 Upregulates SPRR3 to Promote Colorectal Cancer Progression by Binding to miR-759. Cancer Manag Res. 2020;12:11445-52. doi: 10.2147/CMAR.S272652. PubMed PMID: 33204157; PMCID: 7667148.

304. Cho DH, Jo YK, Roh SA, Na YS, Kim TW, Jang SJ, Kim YS, Kim JC. Upregulation of SPRR3 promotes colorectal tumorigenesis. Mol Med. 2010;16(7-8):271-7. doi: 10.2119/molmed.2009.00187. PubMed PMID: 20379613; PMCID: 2896463.

305. Wu M, Guo Q, Liu X, Wu L. SPRR3, a novel miR-338-3p target, regulates the malignant progression of clear cell renal cell carcinoma in vitro via the PI3K/Akt signaling pathway. Exp Ther Med. 2022;23(5):317. doi: 10.3892/etm.2022.11246. PubMed PMID: 35350667; PMCID: 8943802.

306. Liu Q, Zhang C, Ma G, Zhang Q. Expression of SPRR3 is associated with tumor cell proliferation and invasion in glioblastoma multiforme. Oncol Lett. 2014;7(2):427-32. doi: 10.3892/ol.2013.1736. PubMed PMID: 24396461; PMCID: 3881942.

307. Li Q, Wang Y, Hu R, Yang G. Dysregulation of SPRR3/miR-876-3p Axis Contributes to Tumorigenesis in Non-Small-Cell Lung Cancer. Onco Targets Ther. 2020;13:2411-9. doi: 10.2147/OTT.S245422. PubMed PMID: 32273714; PMCID: 7106992.

308. Hu X, Peng N, Qi F, Li J, Shi L, Chen R. Cigarette smoke upregulates SPRR3 by favoring c-Jun/Fra1 heterodimerization in human bronchial epithelial cells. Future Oncol. 2018;14(25):2599-613. doi: 10.2217/fon-2018-0043. PubMed PMID: 30073865.

309. Bae JE, Choi H, Shin DW, Na HW, Park NY, Kim JB, Jo DS, Cho MJ, Lyu JH, Chang JH, Lee EH, Lee TR, Kim HJ, Cho DH. Fine particulate matter (PM2.5) inhibits ciliogenesis by increasing SPRR3 expression via c-Jun activation in RPE cells and skin keratinocytes. Sci Rep. 2019;9(1):3994. doi: 10.1038/s41598-019-40670-y. PubMed PMID: 30850686; PMCID: 6408442.

310. Reuter JS, Mathews DH. RNAstructure: software for RNA secondary structure prediction and analysis. BMC Bioinformatics. 2010;11:129. doi: 10.1186/1471-2105-11-129. PubMed PMID: 20230624; PMCID: 2984261.

311. Sheu-Gruttadauria J, Pawlica P, Klum SM, Wang S, Yario TA, Schirle Oakdale NT, Steitz JA, MacRae IJ. Structural Basis for Target-Directed MicroRNA Degradation. Mol Cell. 2019;75(6):1243-55 e7. doi: 10.1016/j.molcel.2019.06.019. PubMed PMID: 31353209; PMCID: 6754277.

312. Jin Y, Chen Z, Liu X, Zhou X. Evaluating the microRNA targeting sites by luciferase reporter gene assay. Methods Mol Biol. 2013;936:117-27. doi: 10.1007/978-1-62703-083-0_10. PubMed PMID: 23007504; PMCID: 3646406.

313. Manakov SA, Shishkin AA, Yee BA, Shen KA, Cox DC, Park SS, Foster HM, Chapman KB, Yeo GW, Van Nostrand EL. Scalable and deep profiling of mRNA targets for individual microRNAs with chimeric eCLIP. bioRxiv. 2022:2022.02.13.480296. doi: 10.1101/2022.02.13.480296.

314. de A Simão T, Souza-Santos PT, de Oliveira DS, Bernardo V, Lima SC, Rapozo DC, Kruel CD, Faria PA, Ribeiro Pinto LF, Albano RM. Quantitative evaluation of SPRR3 expression in esophageal squamous cell carcinoma by qPCR and its potential use as a biomarker. Exp Mol Pathol. 2011;91(2):584-9. doi: 10.1016/j.yexmp.2011.06.006. PubMed PMID: 21777580.

315. Jin HY, Gonzalez-Martin A, Miletic AV, Lai M, Knight S, Sabouri-Ghomi M, Head SR, Macauley MS, Rickert RC, Xiao C. Transfection of microRNA Mimics Should Be Used with Caution. Front Genet. 2015;6:340. doi: 10.3389/fgene.2015.00340. PubMed PMID: 26697058; PMCID: 4667072.

316. Khan AA, Betel D, Miller ML, Sander C, Leslie CS, Marks DS. Transfection of small RNAs globally perturbs gene regulation by endogenous microRNAs. Nat Biotechnol. 2009;27(6):549-55. doi: 10.1038/nbt.1543. PubMed PMID: 19465925; PMCID: 2782465.

317. Sood P, Krek A, Zavolan M, Macino G, Rajewsky N. Cell-type-specific signatures of microRNAs on target mRNA expression. Proc Natl Acad Sci U S A. 2006;103(8):2746-51. doi: 10.1073/pnas.0511045103. PubMed PMID: 16477010; PMCID: 1413820.

318. Engeland K. Cell cycle regulation: p53-p21-RB signaling. Cell Death Differ. 2022;29(5):946-60. doi: 10.1038/s41418-022-00988-z. PubMed PMID: 35361964; PMCID: 9090780.

319. Wu S, Huang S, Ding J, Zhao Y, Liang L, Liu T, Zhan R, He X. Multiple microRNAs modulate p21Cip1/Waf1 expression by directly targeting its 3' untranslated region. Oncogene. 2010;29(15):2302-8. doi: 10.1038/onc.2010.34. PubMed PMID: 20190813.

320. Zhu S, He C, Deng S, Li X, Cui S, Zeng Z, Liu M, Zhao S, Chen J, Jin Y, Chen H, Deng S, Liu Y, Wang C, Zhao G. MiR-548an, Transcriptionally Downregulated by HIF1alpha/HDAC1, Suppresses Tumorigenesis of Pancreatic Cancer by Targeting Vimentin Expression. Mol Cancer Ther. 2016;15(9):2209-19. doi: 10.1158/1535-7163.MCT-15-0877. PubMed PMID: 27353169.

321. Yang W, Ju HY, Tian XF. Hsa-miR-4730 as a new and potential diagnostic and prognostic indicators for pancreatic cancer. Eur Rev Med Pharmacol Sci. 2020;24(17):8801-11. doi: 10.26355/eurrev_202009_22819. PubMed PMID: 32964968.

322. Yata K, Beder LB, Tamagawa S, Hotomi M, Hirohashi Y, Grenman R, Yamanaka N. MicroRNA expression profiles of cancer stem cells in head and neck squamous cell carcinoma. Int J Oncol. 2015;47(4):1249-56. doi: 10.3892/ijo.2015.3145. PubMed PMID: 26323893; PMCID: 4583533.

323. Sanchez-Diaz PC, Hsiao TH, Chang JC, Yue D, Tan MC, Chen HI, Tomlinson GE, Huang Y, Chen Y, Hung JY. De-regulated microRNAs in pediatric cancer stem cells target pathways involved in cell proliferation, cell cycle and development. PLoS One. 2013;8(4):e61622. doi: 10.1371/journal.pone.0061622. PubMed PMID: 23613887; PMCID: 3629228.

324. Liu H, Chen W, Zhi X, Chen EJ, Wei T, Zhang J, Shen J, Hu LQ, Zhao B, Feng XH, Bai XL, Liang TB. Tumor-derived exosomes promote tumor self-seeding in hepatocellular carcinoma by transferring miRNA-25-5p to enhance cell motility. Oncogene. 2018;37(36):4964-78. doi: 10.1038/s41388-018-0309-x. PubMed PMID: 29786077.

325. Cheng L, Wang H, Han S. MiR-3910 Promotes the Growth and Migration of Cancer Cells in the Progression of Hepatocellular Carcinoma. Dig Dis Sci. 2017;62(10):2812-20. doi: 10.1007/s10620-017-4670-3. PubMed PMID: 28823082.

326. Uhlmann S, Mannsperger H, Zhang JD, Horvat EA, Schmidt C, Kublbeck M, Henjes F, Ward A, Tschulena U, Zweig K, Korf U, Wiemann S, Sahin O. Global microRNA level regulation of EGFR-driven cell-cycle protein network in breast cancer.

Mol Syst Biol. 2012;8:570. doi: 10.1038/msb.2011.100. PubMed PMID: 22333974; PMCID: 3293631.

327. Zhang Y, Zhang HE, Liu Z. MicroRNA-147 suppresses proliferation, invasion and migration through the AKT/mTOR signaling pathway in breast cancer. Oncol Lett. 2016;11(1):405-10. doi: 10.3892/ol.2015.3842. PubMed PMID: 26870225; PMCID: 4727187.

328. Lu Y, Luan XR. miR-147a suppresses the metastasis of non-small-cell lung cancer by targeting CCL5. J Int Med Res. 2020;48(4):300060519883098. doi: 10.1177/0300060519883098. PubMed PMID: 31884861; PMCID: 7607764.

329. Raza U, Saatci O, Uhlmann S, Ansari SA, Eyupoglu E, Yurdusev E, Mutlu M, Ersan PG, Altundag MK, Zhang JD, Dogan HT, Guler G, Sahin O. The miR-644a/CTBP1/p53 axis suppresses drug resistance by simultaneous inhibition of cell survival and epithelial-mesenchymal transition in breast cancer. Oncotarget. 2016;7(31):49859-77. doi: 10.18632/oncotarget.10489. PubMed PMID: 27409664; PMCID: 5226553.

330. Li Y, Yan X, Ren L, Li Y. miR-644a Inhibits Cellular Proliferation and Invasion via Suppression of CtBP1 in Gastric Cancer Cells. Oncol Res. 2018;26(1):1-8. doi: 10.3727/096504016X14772410356982. PubMed PMID: 27983935; PMCID: 7844550.

331. Pang J, Li Z, Wang G, Li N, Gao Y, Wang S. miR-214-5p targets KLF5 and suppresses proliferation of human hepatocellular carcinoma cells. J Cell Biochem. 2018. doi: 10.1002/jcb.27498. PubMed PMID: 30206974.

332. Zhang M, Wang D, Zhu T, Yin R. miR-214-5p Targets ROCK1 and Suppresses Proliferation and Invasion of Human Osteosarcoma Cells. Oncol Res. 2017;25(1):75-81. doi: 10.3727/096504016X14719078133401. PubMed PMID: 28081735; PMCID: 7840756.

333. Yamaguchi N, Osaki M, Onuma K, Yumioka T, Iwamoto H, Sejima T, Kugoh H, Takenaka A, Okada F. Identification of MicroRNAs Involved in Resistance to Sunitinib in Renal Cell Carcinoma Cells. Anticancer Res. 2017;37(6):2985-92. doi: 10.21873/anticanres.11652. PubMed PMID: 28551636.

334. Wu X, Cheng YL, Matthen M, Yoon A, Schwartz GK, Bala S, Taylor AM, Momen-Heravi F. Down-regulation of the tumor suppressor miR-34a contributes to head and neck cancer by up-regulating the MET oncogene and modulating tumor immune evasion. J Exp Clin Cancer Res. 2021;40(1):70. doi: 10.1186/s13046-021-01865-2. PubMed PMID: 33596979; PMCID: 7890893.

335. Meng F, Zhang L. miR-183-5p functions as a tumor suppressor in lung cancer through PIK3CA inhibition. Exp Cell Res. 2019;374(2):315-22. doi: 10.1016/j.yexcr.2018.12.003. PubMed PMID: 30528264.

336. Cheng Y, Xiang G, Meng Y, Dong R. MiRNA-183-5p promotes cell proliferation and inhibits apoptosis in human breast cancer by targeting the PDCD4. Reprod Biol. 2016;16(3):225-33. doi: 10.1016/j.repbio.2016.07.002. PubMed PMID: 27476679.

337. Yan H, Sun BM, Zhang YY, Li YJ, Huang CX, Feng FZ, Li C. Upregulation of miR-183-5p is responsible for the promotion of apoptosis and inhibition of the epithelial-mesenchymal transition, proliferation, invasion and migration of human endometrial cancer cells by downregulating Ezrin. Int J Mol Med. 2018;42(5):2469-80. doi: 10.3892/ijmm.2018.3853. PubMed PMID: 30226564; PMCID: 6192766.

338. He RQ, Gao L, Ma J, Li ZY, Hu XH, Chen G. Oncogenic role of miR-183-5p in lung adenocarcinoma: A comprehensive study of qPCR, in vitro experiments and bioinformatic analysis. Oncol Rep. 2018;40(1):83-100. doi: 10.3892/or.2018.6429. PubMed PMID: 29749535; PMCID: 6059757.

339. Liu W, Wang D, Wang X, Liu P, Yan M. hsa_circ_0085539 Promotes Osteosarcoma Progression by Regulating miR-526b-5p and SERP1. Mol Ther Oncolytics. 2020;19:163-77. doi: 10.1016/j.omto.2020.09.009. PubMed PMID: 33209976; PMCID: 7649436.

340. Zhou YX, Wang C, Mao LW, Wang YL, Xia LQ, Zhao W, Shen J, Chen J. Long noncoding RNA HOTAIR mediates the estrogen-induced metastasis of endometrial cancer cells via the miR-646/NPM1 axis. Am J Physiol Cell Physiol. 2018;314(6):C690-C701. doi: 10.1152/ajpcell.00222.2017. PubMed PMID: 29466670.

341. Zhang P, Tang WM, Zhang H, Li YQ, Peng Y, Wang J, Liu GN, Huang XT, Zhao JJ, Li G, Li AM, Bai Y, Chen Y, Ren YX, Li GX, Wang YD, Liu SD, Wang JD. MiR-646 inhibited cell proliferation and EMT-induced metastasis by targeting FOXK1 in gastric cancer. Br J Cancer. 2017;117(4):525-34. doi: 10.1038/bjc.2017.181. PubMed PMID: 28632723; PMCID: 5558677.

342. Zo RB, Long Z. MiR-124-3p suppresses bladder cancer by targeting DNA methyltransferase 3B. J Cell Physiol. 2018;234(1):464-74. doi: 10.1002/jcp.26591. PubMed PMID: 29893409.

343. Wang Y, Chen L, Wu Z, Wang M, Jin F, Wang N, Hu X, Liu Z, Zhang CY, Zen K, Chen J, Liang H, Zhang Y, Chen X. miR-124-3p functions as a tumor suppressor in breast cancer by targeting CBL. BMC Cancer. 2016;16(1):826. doi: 10.1186/s12885-016-2862-4. PubMed PMID: 27842510; PMCID: 5109743.

344. Lwin T, Zhao X, Cheng F, Zhang X, Huang A, Shah B, Zhang Y, Moscinski LC, Choi YS, Kozikowski AP, Bradner JE, Dalton WS, Sotomayor E, Tao J. A microenvironment-mediated c-Myc/miR-548m/HDAC6 amplification loop in non-Hodgkin B cell lymphomas. J Clin Invest. 2013;123(11):4612-26. doi: 10.1172/JCI64210. PubMed PMID: 24216476; PMCID: 3809771.

345. Mansoori B, Mohammadi A, Naghizadeh S, Gjerstorff M, Shanehbandi D, Shirjang S, Najafi S, Holmskov U, Khaze V, Duijf PHG, Baradaran B. miR-330 suppresses EMT and induces apoptosis by downregulating HMGA2 in human colorectal cancer. J Cell Physiol. 2020;235(2):920-31. doi: 10.1002/jcp.29007. PubMed PMID: 31241772.

346. Feng L, Ma J, Ji H, Liu Y, Hu W. miR-330-5p suppresses glioblastoma cell proliferation and invasiveness through targeting ITGA5. Biosci Rep. 2017;37(3). doi: 10.1042/BSR20170019. PubMed PMID: 28336765; PMCID: 5479020.

347. Trehoux S, Lahdaoui F, Delpu Y, Renaud F, Leteurtre E, Torrisani J, Jonckheere N, Van Seuningen I. Micro-RNAs miR-29a and miR-330-5p function as tumor suppressors by targeting the MUC1 mucin in pancreatic cancer cells. Biochim Biophys Acta. 2015;1853(10 Pt A):2392-403. doi: 10.1016/j.bbamcr.2015.05.033. PubMed PMID: 26036346.

348. Chen FF, Sun N, Wang Y, Xi HY, Yang Y, Yu BZ, Li XJ. miR-212-5p exerts tumor promoter function by regulating the Id3/PI3K/Akt axis in lung adenocarcinoma cells. J Cell Physiol. 2020;235(10):7273-82. doi: 10.1002/jcp.29627. PubMed PMID: 32039486.

349. Lin JF, Zeng H, Zhao JQ. MiR-212-5p regulates the proliferation and apoptosis of AML cells through targeting FZD5. Eur Rev Med Pharmacol Sci. 2018;22(23):8415-22. doi: 10.26355/eurrev_201812_16540. PubMed PMID: 30556883.

350. Lv ZD, Yang DX, Liu XP, Jin LY, Wang XG, Yang ZC, Liu D, Zhao JJ, Kong B, Li FN, Wang HB. MiR-212-5p Suppresses the Epithelial-Mesenchymal Transition in Triple-Negative Breast Cancer by Targeting Prrx2. Cell Physiol Biochem. 2017;44(5):1785-95. doi: 10.1159/000485785. PubMed PMID: 29216628.

351. Li X, Li N, Niu Q, Zhu H, Wang Z, Hou Q. Elevated Expression of miR-629 Predicts a Poor Prognosis and Promotes Cell Proliferation, Migration, and Invasion of Osteosarcoma. Onco Targets Ther. 2020;13:1851-7. doi: 10.2147/OTT.S232479. PubMed PMID: 32189967; PMCID: 7065468.

352. Wang J, Guo XJ, Ding YM, Jiang JX. miR-1181 inhibits invasion and proliferation via STAT3 in pancreatic cancer. World J Gastroenterol. 2017;23(9):1594-601. doi: 10.3748/wjg.v23.i9.1594. PubMed PMID: 28321160; PMCID: 5340811.

353. Zhang HY, Li JH, Li G, Wang SR. Activation of ARK5/miR-1181/HOXA10 axis promotes epithelial-mesenchymal transition in ovarian cancer. Oncol Rep. 2015;34(3):1193-202. doi: 10.3892/or.2015.4113. PubMed PMID: 26151663.

354. Monteleone NJ, Lutz CS. miR-708-5p: a microRNA with emerging roles in cancer. Oncotarget. 2017;8(41):71292-316. doi: 10.18632/oncotarget.19772. PubMed PMID: 29050362; PMCID: 5642637.

355. Dong HT, Liu Q, Zhao T, Yao F, Xu Y, Chen B, Wu Y, Zheng X, Jin F, Li J, Xing P. Long Non-coding RNA LOXL1-AS1 Drives Breast Cancer Invasion and Metastasis by Antagonizing miR-708-5p Expression and Activity. Mol Ther Nucleic Acids. 2020;19:696-705. doi: 10.1016/j.omtn.2019.12.016. PubMed PMID: 31945728; PMCID: 6965509.

356. Chen Q, Xu H, Zhu J, Feng K, Hu C. LncRNA MCM3AP-AS1 promotes breast cancer progression via modulating miR-28-5p/CENPF axis. Biomed Pharmacother. 2020;128:110289. doi: 10.1016/j.biopha.2020.110289. PubMed PMID: 32485570.

357. Zhao Z, Qin X. MicroRNA-708 targeting ZNF549 regulates colon adenocarcinoma development through PI3K/AKt pathway. Sci Rep. 2020;10(1):16729. doi: 10.1038/s41598-020-73929-w. PubMed PMID: 33028966; PMCID: 7541523.

358. Yu Y, Chang Z, Han C, Zhuang L, Zhou C, Qi X, Peng Z. Long non-coding RNA MINCR aggravates colon cancer via regulating miR-708-5p-mediated Wnt/beta-catenin pathway. Biomed Pharmacother. 2020;129:110292. doi: 10.1016/j.biopha.2020.110292. PubMed PMID: 32535381.

359. Almeida MI, Nicoloso MS, Zeng L, Ivan C, Spizzo R, Gafa R, Xiao L, Zhang X, Vannini I, Fanini F, Fabbri M, Lanza G, Reis RM, Zweidler-McKay PA, Calin GA. Strand-specific miR-28-5p and miR-28-3p have distinct effects in colorectal cancer cells. Gastroenterology. 2012;142(4):886-96 e9. doi: 10.1053/j.gastro.2011.12.047. PubMed PMID: 22240480; PMCID: 3321100.

360. Luan XF, Wang L, Gai XF. The miR-28-5p-CAMTA2 axis regulates colon cancer progression via Wnt/beta-catenin signaling. J Cell Biochem. 2019. doi: 10.1002/jcb.29536. PubMed PMID: 31709644.

361. Shi X, Teng F. Down-regulated miR-28-5p in human hepatocellular carcinoma correlated with tumor proliferation and migration by targeting insulin-like growth factor-1 (IGF-1). Mol Cell Biochem. 2015;408(1-2):283-93. doi: 10.1007/s11010-015-2506-z. PubMed PMID: 26160280.

362. Huang S, Guo H, Cao Y, Xiong J. MiR-708-5p inhibits the progression of pancreatic ductal adenocarcinoma by targeting Sirt3. Pathol Res Pract.

2019;215(4):794-800. doi: 10.1016/j.prp.2019.01.026. PubMed PMID: 30683474.

363. Fazio S, Berti G, Russo F, Evangelista M, D'Aurizio R, Mercatanti A, Pellegrini M, Rizzo M. The miR-28-5p Targetome Discovery Identified SREBF2 as One of the Mediators of the miR-28-5p Tumor Suppressor Activity in Prostate Cancer Cells. Cells. 2020;9(2). doi: 10.3390/cells9020354. PubMed PMID: 32028704; PMCID: 7072282.

364. Hernandez-Verdun D. Assembly and disassembly of the nucleolus during the cell cycle. Nucleus. 2011;2(3):189-94. doi: 10.4161/nucl.2.3.16246. PubMed PMID: 21818412; PMCID: 3149879.

365. Slack FJ, Chinnaiyan AM. The Role of Non-coding RNAs in Oncology. Cell. 2019;179(5):1033-55. doi: 10.1016/j.cell.2019.10.017. PubMed PMID: 31730848.

366. Samad AFA, Kamaroddin MF. Innovative approaches in transforming microRNAs into therapeutic tools. Wiley Interdiscip Rev RNA. 2023;14(1):e1768. doi: 10.1002/wrna.1768. PubMed PMID: 36437633.

367. Deng Y, Campbell F, Han K, Theodore D, Deeg M, Huang M, Hamatake R, Lahiri S, Chen S, Horvath G, Manolakopoulos S, Dalekos GN, Papatheodoridis G, Goulis I, Banyai T, Jilma B, Leivers M. Randomized clinical trials towards a single-visit cure for chronic hepatitis C: Oral GSK2878175 and injectable RG-101 in chronic hepatitis C patients and long-acting injectable GSK2878175 in healthy participants. J Viral Hepat. 2020;27(7):699-708. doi: 10.1111/jvh.13282. PubMed PMID: 32096313.

368. Ottosen S, Parsley TB, Yang L, Zeh K, van Doorn LJ, van der Veer E, Raney AK, Hodges MR, Patick AK. In vitro antiviral activity and preclinical and clinical resistance profile of miravirsen, a novel anti-hepatitis C virus therapeutic targeting the human factor miR-122. Antimicrob Agents Chemother. 2015;59(1):599-608. doi: 10.1128/AAC.04220-14. PubMed PMID: 25385103; PMCID: 4291405.

369. Enuka Y, Lauriola M, Feldman ME, Sas-Chen A, Ulitsky I, Yarden Y. Circular RNAs are long-lived and display only minimal early alterations in response to a growth factor. Nucleic Acids Res. 2016;44(3):1370-83. doi: 10.1093/nar/gkv1367. PubMed PMID: 26657629; PMCID: 4756822.

370. Tracy KM, Tye CE, Page NA, Fritz AJ, Stein JL, Lian JB, Stein GS. Selective expression of long non-coding RNAs in a breast cancer cell progression model. J Cell Physiol. 2018;233(2):1291-9. doi: 10.1002/jcp.25997. PubMed PMID: 28488769; PMCID: 5673560.

371. Farley-Barnes KI, Deniz E, Overton MM, Khokha MK, Baserga SJ. Paired Box 9 (PAX9), the RNA polymerase II transcription factor, regulates human ribosome

biogenesis and craniofacial development. PLoS Genet. 2020;16(8):e1008967. doi: 10.1371/journal.pgen.1008967. PubMed PMID: 32813698; PMCID: 7437866.

372. Xie Z, Bailey A, Kuleshov MV, Clarke DJB, Evangelista JE, Jenkins SL, Lachmann A, Wojciechowicz ML, Kropiwnicki E, Jagodnik KM, Jeon M, Ma'ayan A. Gene Set Knowledge Discovery with Enrichr. Curr Protoc. 2021;1(3):e90. doi: 10.1002/cpz1.90. PubMed PMID: 33780170; PMCID: 8152575.

373. Kuleshov MV, Jones MR, Rouillard AD, Fernandez NF, Duan Q, Wang Z, Koplev S, Jenkins SL, Jagodnik KM, Lachmann A, McDermott MG, Monteiro CD, Gundersen GW, Ma'ayan A. Enrichr: a comprehensive gene set enrichment analysis web server 2016 update. Nucleic Acids Res. 2016;44(W1):W90-7. doi: 10.1093/nar/gkw377. PubMed PMID: 27141961; PMCID: 4987924.

374. Chen EY, Tan CM, Kou Y, Duan Q, Wang Z, Meirelles GV, Clark NR, Ma'ayan A. Enrichr: interactive and collaborative HTML5 gene list enrichment analysis tool. BMC Bioinformatics. 2013;14:128. doi: 10.1186/1471-2105-14-128. PubMed PMID: 23586463; PMCID: 3637064.

375. Love MI, Huber W, Anders S. Moderated estimation of fold change and dispersion for RNA-seq data with DESeq2. Genome Biol. 2014;15(12):550. doi: 10.1186/s13059-014-0550-8. PubMed PMID: 25516281; PMCID: 4302049.

376. Woolnough JL, Atwood BL, Liu Z, Zhao R, Giles KE. The Regulation of rRNA Gene Transcription during Directed Differentiation of Human Embryonic Stem Cells. PLoS One. 2016;11(6):e0157276. doi: 10.1371/journal.pone.0157276. PubMed PMID: 27299313; PMCID: 4907514.

377. Galiveti CR, Rozhdestvensky TS, Brosius J, Lehrach H, Konthur Z. Application of housekeeping npcRNAs for quantitative expression analysis of human transcriptome by real-time PCR. RNA. 2010;16(2):450-61. Epub 2009/12/31. doi: 10.1261/rna.1755810. PubMed PMID: 20040593; PMCID: PMC2811673.

378. Hanashima Y, Sano E, Sumi K, Ozawa Y, Yagi C, Tatsuoka J, Yoshimura S, Yamamuro S, Ueda T, Nakayama T, Hara H, Yoshino A. Antitumor effect of lenalidomide in malignant glioma cell lines. Oncol Rep. 2020;43(5):1580-90. doi: 10.3892/or.2020.7543. PubMed PMID: 32323826; PMCID: 7108053.

379. Wiza C, Chadt A, Blumensatt M, Kanzleiter T, Herzfeld De Wiza D, Horrighs A, Mueller H, Nascimento EB, Schurmann A, Al-Hasani H, Ouwens DM. Over-expression of PRAS40 enhances insulin sensitivity in skeletal muscle. Arch Physiol Biochem. 2014;120(2):64-72. doi: 10.3109/13813455.2014.894076. PubMed PMID: 24576065.

380. Ladner-Keay CL, Turner RJ, Edwards RA. Fluorescent Protein Visualization Immediately After Gel Electrophoresis Using an In-Gel Trichloroethanol Photoreaction

with Tryptophan. Methods Mol Biol. 2018;1853:179-90. doi: 10.1007/978-1-4939-8745-0_22. PubMed PMID: 30097944.

381. Agarwal V, Bell GW, Nam JW, Bartel DP. Predicting effective microRNA target sites in mammalian mRNAs. Elife. 2015;4. doi: 10.7554/eLife.05005. PubMed PMID: 26267216; PMCID: 4532895.

382. Sticht C, De La Torre C, Parveen A, Gretz N. miRWalk: An online resource for prediction of microRNA binding sites. PLoS One. 2018;13(10):e0206239. doi: 10.1371/journal.pone.0206239. PubMed PMID: 30335862; PMCID: 6193719.

383. Liu H, Naismith JH. An efficient one-step site-directed deletion, insertion, single and multiple-site plasmid mutagenesis protocol. BMC Biotechnol. 2008;8:91. doi: 10.1186/1472-6750-8-91. PubMed PMID: 19055817; PMCID: 2629768.

384. Nazar RN. Ribosomal RNA processing and ribosome biogenesis in eukaryotes. IUBMB Life. 2004;56(8):457-65. doi: 10.1080/15216540400010867. PubMed PMID: 15545225.

385. Wool IG, Chan YL, Gluck A. Structure and evolution of mammalian ribosomal proteins. Biochem Cell Biol. 1995;73(11-12):933-47. doi: 10.1139/o95-101. PubMed PMID: 8722009.

386. Ban N, Beckmann R, Cate JH, Dinman JD, Dragon F, Ellis SR, Lafontaine DL, Lindahl L, Liljas A, Lipton JM, McAlear MA, Moore PB, Noller HF, Ortega J, Panse VG, Ramakrishnan V, Spahn CM, Steitz TA, Tchorzewski M, Tollervey D, Warren AJ, Williamson JR, Wilson D, Yonath A, Yusupov M. A new system for naming ribosomal proteins. Curr Opin Struct Biol. 2014;24:165-9. doi: 10.1016/j.sbi.2014.01.002. PubMed PMID: 24524803; PMCID: 4358319.

387. Schmidt EV. The role of c-myc in cellular growth control. Oncogene. 1999;18(19):2988-96. doi: 10.1038/sj.onc.1202751. PubMed PMID: 10378694.

388. Sondalle SB, Baserga SJ. Human diseases of the SSU processome. Biochim Biophys Acta. 2014;1842(6):758-64. doi: 10.1016/j.bbadis.2013.11.004. PubMed PMID: 24240090; PMCID: 4058823.

389. Ross AP, Zarbalis KS. The emerging roles of ribosome biogenesis in craniofacial development. Front Physiol. 2014;5:26. doi: 10.3389/fphys.2014.00026. PubMed PMID: 24550838; PMCID: 3912750.

390. Da Costa LM, Leblanc TM, Narla M. Diamond-Blackfan Anemia. Blood. 2020. doi: 10.1182/blood.2019000947. PubMed PMID: 32702755.

391. Gazda HT, Sheen MR, Barras N, Shneider H, Sieff CA, Ball SE, Niewiadornska E, Newburger PE, Atsidaftos E, Vlachos A, Lipton JM, Beggs AH. Mutations of the genes

for ribosomal proteins l5 and l11 are a common cause of diamond-blackfan anemia. Blood. 2007;110(11):130a-1a. PubMed PMID: WOS:000251100800422.

392. Boultwood J, Pellagatti A, Wainscoat JS. Haploinsufficiency of ribosomal proteins and p53 activation in anemia: Diamond-Blackfan anemia and the 5q- syndrome. Adv Biol Regul. 2012;52(1):196-203. doi: 10.1016/j.advenzreg.2011.09.008. PubMed PMID: 21930148.

393. Ulirsch JC, Verboon JM, Kazerounian S, Guo MH, Yuan D, Ludwig LS, Handsaker RE, Abdulhay NJ, Fiorini C, Genovese G, Lim ET, Cheng A, Cummings BB, Chao KR, Beggs AH, Genetti CA, Sieff CA, Newburger PE, Niewiadomska E, Matysiak M, Vlachos A, Lipton JM, Atsidaftos E, Glader B, Narla A, Gleizes PE, O'Donohue MF, Montel-Lehry N, Amor DJ, McCarroll SA, O'Donnell-Luria AH, Gupta N, Gabriel SB, MacArthur DG, Lander ES, Lek M, Da Costa L, Nathan DG, Korostelev AA, Do R, Sankaran VG, Gazda HT. The Genetic Landscape of Diamond-Blackfan Anemia. Am J Hum Genet. 2018;103(6):930-47. doi: 10.1016/j.ajhg.2018.10.027. PubMed PMID: 30503522; PMCID: 6288280.

394. Burwick N, Shimamura A, Liu JM. Non-Diamond Blackfan anemia disorders of ribosome function: Shwachman Diamond syndrome and 5q- syndrome. Semin Hematol. 2011;48(2):136-43. doi: 10.1053/j.seminhematol.2011.01.002. PubMed PMID: 21435510; PMCID: 3072806.

395. Warren AJ. Molecular basis of the human ribosomopathy Shwachman-Diamond syndrome. Adv Biol Regul. 2018;67:109-27. doi: 10.1016/j.jbior.2017.09.002. PubMed PMID: 28942353; PMCID: 6710477.

396. Weaver KN, Watt KE, Hufnagel RB, Navajas Acedo J, Linscott LL, Sund KL, Bender PL, Konig R, Lourenco CM, Hehr U, Hopkin RJ, Lohmann DR, Trainor PA, Wieczorek D, Saal HM. Acrofacial Dysostosis, Cincinnati Type, a Mandibulofacial Dysostosis Syndrome with Limb Anomalies, Is Caused by POLR1A Dysfunction. Am J Hum Genet. 2015;96(5):765-74. doi: 10.1016/j.ajhg.2015.03.011. PubMed PMID: 25913037; PMCID: 4570288.

397. Online Mendelian Inheritance in Man, OMIM®. Johns Hopkins University, Baltimore, MD. MIM Number: 612079: 2015-02-06 [Internet]. Available from: https://omim.org/.

398. Bergès T, Petfalski E, Tollervey D, Hurt E. Synthetic lethality with fibrillarin identifies NOP77p, a nucleolar protein required for pre-rRNA processing and modification. EMBO J. 1994;13(13):3136-48.

399. Granneman S, Petfalski E, Tollervey D. A cluster of ribosome synthesis factors regulate pre-rRNA folding and 5.8S rRNA maturation by the Rat1 exonuclease. EMBO J. 2011;30(19):4006-19. doi: 10.1038/emboj.2011.256. PubMed PMID: 21811236; PMCID: 3209772.

400. McCann KL, Charette JM, Vincent NG, Baserga SJ. A protein interaction map of the LSU processome. Genes Dev. 2015;29(8):862-75. doi: 10.1101/gad.256370.114. PubMed PMID: 25877921; PMCID: 4403261.

401. Richards S, Aziz N, Bale S, Bick D, Das S, Gastier-Foster J, Grody WW, Hegde M, Lyon E, Spector E, Voelkerding K, Rehm HL, Committee ALQA. Standards and guidelines for the interpretation of sequence variants: a joint consensus recommendation of the American College of Medical Genetics and Genomics and the Association for Molecular Pathology. Genet Med. 2015;17(5):405-24. doi: 10.1038/gim.2015.30. PubMed PMID: 25741868; PMCID: 4544753.

402. Adzhubei IA, Schmidt S, Peshkin L, Ramensky VE, Gerasimova A, Bork P, Kondrashov AS, Sunyaev SR. A method and server for predicting damaging missense mutations. Nat Methods. 2010;7(4):248-9. doi: 10.1038/nmeth0410-248. PubMed PMID: 20354512; PMCID: 2855889.

403. Vaser R, Adusumalli S, Leng SN, Sikic M, Ng PC. SIFT missense predictions for genomes. Nat Protoc. 2016;11(1):1-9. doi: 10.1038/nprot.2015.123. PubMed PMID: 26633127.

404. Jaganathan K, Kyriazopoulou Panagiotopoulou S, McRae JF, Darbandi SF, Knowles D, Li YI, Kosmicki JA, Arbelaez J, Cui W, Schwartz GB, Chow ED, Kanterakis E, Gao H, Kia A, Batzoglou S, Sanders SJ, Farh KK-H. Predicting Splicing from Primary Sequence with Deep Learning. Cell. 2019. doi: 10.1016/j.cell.2018.12.015.

405. Karczewski KJ, Francioli LC, Tiao G, Cummings BB, Alfoldi J, Wang Q, Collins RL, Laricchia KM, Ganna A, Birnbaum DP, Gauthier LD, Brand H, Solomonson M, Watts NA, Rhodes D, Singer-Berk M, England EM, Seaby EG, Kosmicki JA, Walters RK, Tashman K, Farjoun Y, Banks E, Poterba T, Wang A, Seed C, Whiffin N, Chong JX, Samocha KE, Pierce-Hoffman E, Zappala Z, O'Donnell-Luria AH, Minikel EV, Weisburd B, Lek M, Ware JS, Vittal C, Armean IM, Bergelson L, Cibulskis K, Connolly KM, Covarrubias M, Donnelly S, Ferriera S, Gabriel S, Gentry J, Gupta N, Jeandet T, Kaplan D, Llanwarne C, Munshi R, Novod S, Petrillo N, Roazen D, Ruano-Rubio V, Saltzman A, Schleicher M, Soto J, Tibbetts K, Tolonen C, Wade G, Talkowski ME, Genome Aggregation Database C, Neale BM, Daly MJ, MacArthur DG. The mutational constraint spectrum quantified from variation in 141,456 humans. Nature. 2020;581(7809):434-43. doi: 10.1038/s41586-020-2308-7. PubMed PMID: 32461654; PMCID: 7334197.

406. Shapiro MB, Senapathy P. RNA splice junctions of different classes of eukaryotes: sequence statistics and functional implications in gene expression. Nucleic Acids Res. 1987;15(17):7155-74. PubMed PMID: 3658675; PMCID: 306199.

407. Desmet FO, Hamroun D, Lalande M, Collod-Beroud G, Claustres M, Beroud C. Human Splicing Finder: an online bioinformatics tool to predict splicing signals. Nucleic

Acids Res. 2009;37(9):e67. doi: 10.1093/nar/gkp215. PubMed PMID: 19339519; PMCID: 2685110.

408. Carmel I, Tal S, Vig I, Ast G. Comparative analysis detects dependencies among the 5' splice-site positions. RNA. 2004;10(5):828-40. PubMed PMID: 15100438; PMCID: 1370573.

409. Reese MG, Eeckman FH, Kulp D, Haussler D. Improved splice site detection in Genie. J Comput Biol. 1997;4(3):311-23. doi: 10.1089/cmb.1997.4.311. PubMed PMID: 9278062.

410. Bretschneider H, Gandhi S, Deshwar AG, Zuberi K, Frey BJ. COSSMO: predicting competitive alternative splice site selection using deep learning. Bioinformatics. 2018;34(13):i429-i37. doi: 10.1093/bioinformatics/bty244. PubMed PMID: 29949959; PMCID: 6022534.

411. Wang T, Birsoy K, Hughes NW, Krupczak KM, Post Y, Wei JJ, Lander ES, Sabatini DM. Identification and characterization of essential genes in the human genome. Science. 2015;350(6264):1096-101. doi: 10.1126/science.aac7041. PubMed PMID: 26472758; PMCID: 4662922.

412. Meyers RM, Bryan JG, McFarland JM, Weir BA, Sizemore AE, Xu H, Dharia NV, Montgomery PG, Cowley GS, Pantel S, Goodale A, Lee Y, Ali LD, Jiang G, Lubonja R, Harrington WF, Strickland M, Wu T, Hawes DC, Zhivich VA, Wyatt MR, Kalani Z, Chang JJ, Okamoto M, Stegmaier K, Golub TR, Boehm JS, Vazquez F, Root DE, Hahn WC, Tsherniak A. Computational correction of copy number effect improves specificity of CRISPR-Cas9 essentiality screens in cancer cells. Nat Genet. 2017;49(12):1779-84. doi: 10.1038/ng.3984. PubMed PMID: 29083409; PMCID: 5709193.

413. Broad. DepMap 20Q2 Public. Figshare2020.

414. Fernandez AG, Gunsalus KC, Huang J, Chuang LS, Ying N, Liang HL, Tang C, Schetter AJ, Zegar C, Rual JF, Hill DE, Reinke V, Vidal M, Piano F. New genes with roles in the C. elegans embryo revealed using RNAi of ovary-enriched ORFeome clones. Genome Res. 2005;15(2):250-9. doi: 10.1101/gr.3194805. PubMed PMID: 15687288; PMCID: 546526.

415. Guthrie C, Nashimoto H, Nomura M. Structure and function of E. coli ribosomes. 8. Cold-sensitive mutants defective in ribosome assembly. Proc Natl Acad Sci U S A. 1969;63(2):384-91. PubMed PMID: 4895536; PMCID: 223576.

416. Qiu H, Eifert J, Wacheul L, Thiry M, Berger AC, Jakovljevic J, Woolford JL, Jr., Corbett AH, Lafontaine DL, Terns RM, Terns MP. Identification of genes that function in the biogenesis and localization of small nucleolar RNAs in Saccharomyces cerevisiae. Mol Cell Biol. 2008;28(11):3686-99. doi: 10.1128/MCB.01115-07. PubMed PMID: 18378690; PMCID: 2423305.

417. Warda AS, Freytag B, Haag S, Sloan KE, Gorlich D, Bohnsack MT. Effects of the Bowen-Conradi syndrome mutation in EMG1 on its nuclear import, stability and nucleolar recruitment. Hum Mol Genet. 2016;25(24):5353-64. doi: 10.1093/hmg/ddw351. PubMed PMID: 27798105; PMCID: 5418833.

418. Adamus K, Le SN, Elmlund H, Boudes M, Elmlund D. AgarFix: Simple and accessible stabilization of challenging single-particle cryo-EM specimens through crosslinking in a matrix of agar. J Struct Biol. 2019;207(3):327-31. doi: 10.1016/j.jsb.2019.07.004. PubMed PMID: 31323306.

419. Stark H. GraFix: Stabilization of Fragile Macromolecular Complexes for Single Particle Cryo-EM. Cryo-EM Part A Sample Preparation and Data Collection2010. p. 109-26.

420. Fischer N, Neumann P, Bock LV, Maracci C, Wang Z, Paleskava A, Konevega AL, Schroder GF, Grubmuller H, Ficner R, Rodnina MV, Stark H. The pathway to GTPase activation of elongation factor SelB on the ribosome. Nature. 2016;540(7631):80-5. doi: 10.1038/nature20560. PubMed PMID: 27842381.

421. Loveland AB, Demo G, Grigorieff N, Korostelev AA. Ensemble cryo-EM elucidates the mechanism of translation fidelity. Nature. 2017;546(7656):113-7. doi: 10.1038/nature22397. PubMed PMID: 28538735; PMCID: 5657493.

422. Gietz RD. Yeast transformation by the LiAc/SS carrier DNA/PEG method. Methods Mol Biol. 2014;1205:1-12. doi: 10.1007/978-1-4939-1363-3_1. PubMed PMID: 25213235.

423. Zhang T, Lei J, Yang H, Xu K, Wang R, Zhang Z. An improved method for whole protein extraction from yeast Saccharomyces cerevisiae. Yeast. 2011;28(11):795-8. doi: 10.1002/yea.1905. PubMed PMID: 21972073.

424. Shedlovskiy D, Shcherbik N, Pestov DG. One-step hot formamide extraction of RNA from Saccharomyces cerevisiae. RNA Biol. 2017;14(12):1722-6. doi: 10.1080/15476286.2017.1345417. PubMed PMID: 28692404; PMCID: 5731811.

425. Barlow JL, Drynan LF, Hewett DR, Holmes LR, Lorenzo-Abalde S, Lane AL, Jolin HE, Pannell R, Middleton AJ, Wong SH, Warren AJ, Wainscoat JS, Boultwood J, McKenzie AN. A p53-dependent mechanism underlies macrocytic anemia in a mouse model of human 5q- syndrome. Nat Med. 2010;16(1):59-66. doi: 10.1038/nm.2063. PubMed PMID: 19966810; PMCID: 2803774.

426. Tiu GC, Kerr CH, Forester CM, Krishnarao PS, Rosenblatt HD, Raj N, Lantz TC, Zhulyn O, Bowen ME, Shokat L, Attardi LD, Ruggero D, Barna M. A p53-dependent translational program directs tissue-selective phenotypes in a model of ribosomopathies. Dev Cell. 2021;56(14):2089-102 e11. doi: 10.1016/j.devcel.2021.06.013. PubMed PMID: 34242585; PMCID: 8319123.

427. Chakraborty A, Uechi T, Nakajima Y, Gazda HT, O'Donohue MF, Gleizes PE, Kenmochi N. Cross talk between TP53 and c-Myc in the pathophysiology of Diamond-Blackfan anemia: Evidence from RPL11-deficient in vivo and in vitro models. Biochem Biophys Res Commun. 2018;495(2):1839-45. doi: 10.1016/j.bbrc.2017.12.019. PubMed PMID: 29225165.

428. Watt KEN, Neben CL, Hall S, Merrill AE, Trainor PA. tp53-dependent and independent signaling underlies the pathogenesis and possible prevention of Acrofacial Dysostosis-Cincinnati type. Hum Mol Genet. 2018;27(15):2628-43. doi: 10.1093/hmg/ddy172. PubMed PMID: 29750247; PMCID: 6927876.

429. Lodish HF. Model for the regulation of mRNA translation applied to haemoglobin synthesis. Nature. 1974;251(5474):385-8. doi: 10.1038/251385a0. PubMed PMID: 4421673.

430. Khajuria RK, Munschauer M, Ulirsch JC, Fiorini C, Ludwig LS, McFarland SK, Abdulhay NJ, Specht H, Keshishian H, Mani DR, Jovanovic M, Ellis SR, Fulco CP, Engreitz JM, Schutz S, Lian J, Gripp KW, Weinberg OK, Pinkus GS, Gehrke L, Regev A, Lander ES, Gazda HT, Lee WY, Panse VG, Carr SA, Sankaran VG. Ribosome Levels Selectively Regulate Translation and Lineage Commitment in Human Hematopoiesis. Cell. 2018;173(1):90-103 e19. doi: 10.1016/j.cell.2018.02.036. PubMed PMID: 29551269; PMCID: 5866246.

431. Ludwig LS, Gazda HT, Eng JC, Eichhorn SW, Thiru P, Ghazvinian R, George TI, Gotlib JR, Beggs AH, Sieff CA, Lodish HF, Lander ES, Sankaran VG. Altered translation of GATA1 in Diamond-Blackfan anemia. Nat Med. 2014;20(7):748-53. doi: 10.1038/nm.3557. PubMed PMID: 24952648; PMCID: 4087046.

432. Norris K, Hopes T, Aspden JL. Ribosome heterogeneity and specialization in development. Wiley Interdiscip Rev RNA. 2021;12(4):e1644. doi: 10.1002/wrna.1644. PubMed PMID: 33565275; PMCID: 8647923.

433. Lord J, Baralle D. Splicing in the Diagnosis of Rare Disease: Advances and Challenges. Front Genet. 2021;12:689892. doi: 10.3389/fgene.2021.689892. PubMed PMID: 34276790; PMCID: 8280750.

434. Lord J, Gallone G, Short PJ, McRae JF, Ironfield H, Wynn EH, Gerety SS, He L, Kerr B, Johnson DS, McCann E, Kinning E, Flinter F, Temple IK, Clayton-Smith J, McEntagart M, Lynch SA, Joss S, Douzgou S, Dabir T, Clowes V, McConnell VPM, Lam W, Wright CF, FitzPatrick DR, Firth HV, Barrett JC, Hurles ME, Deciphering Developmental Disorders s. Pathogenicity and selective constraint on variation near splice sites. Genome Res. 2019;29(2):159-70. doi: 10.1101/gr.238444.118. PubMed PMID: 30587507; PMCID: 6360807.

435. Zhang S, Samocha KE, Rivas MA, Karczewski KJ, Daly E, Schmandt B, Neale BM, MacArthur DG, Daly MJ. Base-specific mutational intolerance near splice sites

clarifies the role of nonessential splice nucleotides. Genome Res. 2018;28(7):968-74. doi: 10.1101/gr.231902.117. PubMed PMID: 29858273; PMCID: 6028136.

436. Krawczak M, Thomas NS, Hundrieser B, Mort M, Wittig M, Hampe J, Cooper DN. Single base-pair substitutions in exon-intron junctions of human genes: nature, distribution, and consequences for mRNA splicing. Hum Mutat. 2007;28(2):150-8. doi: 10.1002/humu.20400. PubMed PMID: 17001642.

437. Jung H, Lee KS, Choi JK. Comprehensive characterisation of intronic mis-splicing mutations in human cancers. Oncogene. 2021;40(7):1347-61. doi: 10.1038/s41388-020-01614-3. PubMed PMID: 33420369; PMCID: 7892346.

438. Belkadi A, Bolze A, Itan Y, Cobat A, Vincent QB, Antipenko A, Shang L, Boisson B, Casanova JL, Abel L. Whole-genome sequencing is more powerful than whole-exome sequencing for detecting exome variants. Proc Natl Acad Sci U S A. 2015;112(17):5473-8. doi: 10.1073/pnas.1418631112. PubMed PMID: 25827230; PMCID: 4418901.

439. Meienberg J, Bruggmann R, Oexle K, Matyas G. Clinical sequencing: is WGS the better WES? Hum Genet. 2016;135(3):359-62. doi: 10.1007/s00439-015-1631-9. PubMed PMID: 26742503; PMCID: 4757617.

440. Lavelle TA, Feng X, Keisler M, Cohen JT, Neumann PJ, Prichard D, Schroeder BE, Salyakina D, Espinal PS, Weidner SB, Maron JL. Cost-effectiveness of exome and genome sequencing for children with rare and undiagnosed conditions. Genet Med. 2022;24(6):1349-61. doi: 10.1016/j.gim.2022.03.005. PubMed PMID: 35396982.

441. de Sainte Agathe JM, Filser M, Isidor B, Besnard T, Gueguen P, Perrin A, Van Goethem C, Verebi C, Masingue M, Rendu J, Cossee M, Bergougnoux A, Frobert L, Buratti J, Lejeune E, Le Guern E, Pasquier F, Clot F, Kalatzis V, Roux AF, Cogne B, Baux D. SpliceAI-visual: a free online tool to improve SpliceAI splicing variant interpretation. Hum Genomics. 2023;17(1):7. doi: 10.1186/s40246-023-00451-1. PubMed PMID: 36765386; PMCID: 9912651.

442. Leman R, Parfait B, Vidaud D, Girodon E, Pacot L, Le Gac G, Ka C, Ferec C, Fichou Y, Quesnelle C, Aucouturier C, Muller E, Vaur D, Castera L, Boulouard F, Ricou A, Tubeuf H, Soukarieh O, Gaildrat P, Riant F, Guillaud-Bataille M, Caputo SM, Caux-Moncoutier V, Boutry-Kryza N, Bonnet-Dorion F, Schultz I, Rossing M, Quenez O, Goldenberg L, Harter V, Parsons MT, Spurdle AB, Frebourg T, Martins A, Houdayer C, Krieger S. SPiP: Splicing Prediction Pipeline, a machine learning tool for massive detection of exonic and intronic variant effects on mRNA splicing. Hum Mutat. 2022;43(12):2308-23. doi: 10.1002/humu.24491. PubMed PMID: 36273432.

443. Mangan H, McStay B. Human nucleoli comprise multiple constrained territories, tethered to individual chromosomes. Genes Dev. 2021;35(7-8):483-8. doi: 10.1101/gad.348234.121. PubMed PMID: 33664058; PMCID: 8015717.

444. van Sluis M, McStay B. A localized nucleolar DNA damage response facilitates recruitment of the homology-directed repair machinery independent of cell cycle stage. Genes Dev. 2015;29(11):1151-63. doi: 10.1101/gad.260703.115. PubMed PMID: 26019174; PMCID: 4470283.

445. Berus T, Markiewicz A, Biecek P, Orlowska-Heitzman J, Halon A, Romanowska-Dixon B, Donizy P. Clinical Significance of Nucleoli Cytomorphology Assessment in Patients With Uveal Melanoma. Anticancer Res. 2020;40(6):3505-12. doi: 10.21873/anticanres.14338. PubMed PMID: 32487651.

446. Donizy P, Biecek P, Halon A, Maciejczyk A, Matkowski R. Nucleoli cytomorphology in cutaneous melanoma cells - a new prognostic approach to an old concept. Diagn Pathol. 2017;12(1):88. doi: 10.1186/s13000-017-0675-7. PubMed PMID: 29284501; PMCID: 5747151.

447. Kardos GR, Robertson GP. Therapeutic interventions to disrupt the protein synthetic machinery in melanoma. Pigment Cell Melanoma Res. 2015;28(5):501-19. doi: 10.1111/pcmr.12391. PubMed PMID: 26139519; PMCID: 4716672.

448. Vincent KM, Postovit LM. Investigating the utility of human melanoma cell lines as tumour models. Oncotarget. 2017;8(6):10498-509. doi: 10.18632/oncotarget.14443. PubMed PMID: 28060736; PMCID: 5354675.

449. Jiang X, Prabhakar A, Van der Voorn SM, Ghatpande P, Celona B, Venkataramanan S, Calviello L, Lin C, Wang W, Black BL, Floor SN, Lagna G, Hata A. Control of ribosomal protein synthesis by the Microprocessor complex. Sci Signal. 2021;14(671). doi: 10.1126/scisignal.abd2639. PubMed PMID: 33622983; PMCID: 8012103.

450. Meyuhas O, Kahan T. The race to decipher the top secrets of TOP mRNAs. Biochim Biophys Acta. 2015;1849(7):801-11. doi: 10.1016/j.bbagrm.2014.08.015. PubMed PMID: 25234618.

451. Patil AH, Baran A, Brehm ZP, McCall MN, Halushka MK. A curated human cellular microRNAome based on 196 primary cell types. Gigascience. 2022;11. doi: 10.1093/gigascience/giac083. PubMed PMID: 36007182; PMCID: 9404528.

452. Yan Q, Zhu C, Guang S, Feng X. The Functions of Non-coding RNAs in rRNA Regulation. Front Genet. 2019;10:290. doi: 10.3389/fgene.2019.00290. PubMed PMID: 31024617; PMCID: 6463246.

453. Li D, Zhang J, Wang M, Li X, Gong H, Tang H, Chen L, Wan L, Liu Q. Activity dependent LoNA regulates translation by coordinating rRNA transcription and methylation. Nat Commun. 2018;9(1):1726. Epub 2018/05/02. doi: 10.1038/s41467-018-04072-4. PubMed PMID: 29712923; PMCID: PMC5928123.

454. Bierhoff H, Schmitz K, Maass F, Ye J, Grummt I. Noncoding transcripts in sense and antisense orientation regulate the epigenetic state of ribosomal RNA genes. Cold Spring Harb Symp Quant Biol. 2010;75:357-64. Epub 2011/04/20. doi: 10.1101/sqb.2010.75.060. PubMed PMID: 21502405.

455. Zhao Z, Senturk N, Song C, Grummt I. lncRNA PAPAS tethered to the rDNA enhancer recruits hypophosphorylated CHD4/NuRD to repress rRNA synthesis at elevated temperatures. Genes Dev. 2018;32(11-12):836-48. Epub 2018/06/17. doi: 10.1101/gad.311688.118. PubMed PMID: 29907651; PMCID: PMC6049515.

456. Liao M, Liao W, Xu N, Li B, Liu F, Zhang S, Wang Y, Wang S, Zhu Y, Chen D, Xie W, Jiang Y, Cao L, Yang BB, Zhang Y. LncRNA EPB41L4A-AS1 regulates glycolysis and glutaminolysis by mediating nucleolar translocation of HDAC2. EBioMedicine. 2019;41:200-13. Epub 2019/02/19. doi: 10.1016/j.ebiom.2019.01.035. PubMed PMID: 30796006; PMCID: PMC6444057.

457. Prats AC, David F, Diallo LH, Roussel E, Tatin F, Garmy-Susini B, Lacazette E. Circular RNA, the Key for Translation. Int J Mol Sci. 2020;21(22). doi: 10.3390/ijms21228591. PubMed PMID: 33202605; PMCID: 7697609.

458. Hahne JC, Lampis A, Valeri N. Vault RNAs: hidden gems in RNA and protein regulation. Cell Mol Life Sci. 2021;78(4):1487-99. doi: 10.1007/s00018-020-03675-9. PubMed PMID: 33063126; PMCID: 7904556.

459. Nakanishi K. Are Argonaute-Associated Tiny RNAs Junk, Inferior miRNAs, or a New Type of Functional RNAs? Front Mol Biosci. 2021;8:795356. doi: 10.3389/fmolb.2021.795356. PubMed PMID: 34926585; PMCID: 8678501.

460. McGeary SE, Lin KS, Shi CY, Pham TM, Bisaria N, Kelley GM, Bartel DP. The biochemical basis of microRNA targeting efficacy. Science. 2019;366(6472). doi: 10.1126/science.aav1741. PubMed PMID: 31806698; PMCID: 7051167.

461. Jacquet K, Vidal-Cruchez O, Rezzonico R, Nicolini VJ, Mograbi B, Hofman P, Vassaux G, Mari B, Brest P. New technologies for improved relevance in miRNA research. Trends Genet. 2021;37(12):1060-3. doi: 10.1016/j.tig.2021.08.006. PubMed PMID: 34474931.

462. Kampmann M. CRISPRi and CRISPRa Screens in Mammalian Cells for Precision Biology and Medicine. ACS Chem Biol. 2018;13(2):406-16. doi: 10.1021/acschembio.7b00657. PubMed PMID: 29035510; PMCID: 5886776.

463. Bock C, Datlinger P, Chardon F, Coelho MA, Dong MB, Lawson KA, Lu T, Maroc L, Norman TM, Song B. High-content CRISPR screening. Nature Reviews Methods Primers. 2022;2(1):8. doi: 10.1038/s43586-021-00093-4.

464. Jost M, Santos DA, Saunders RA, Horlbeck MA, Hawkins JS, Scaria SM, Norman TM, Hussmann JA, Liem CR, Gross CA, Weissman JS. Titrating gene expression using libraries of systematically attenuated CRISPR guide RNAs. Nat Biotechnol. 2020;38(3):355-64. doi: 10.1038/s41587-019-0387-5. PubMed PMID: 31932729; PMCID: 7065968.

465. Mathis AD, Otto RM, Reynolds KA. A simplified strategy for titrating gene expression reveals new relationships between genotype, environment, and bacterial growth. Nucleic Acids Res. 2021;49(1):e6. doi: 10.1093/nar/gkaa1073. PubMed PMID: 33221881; PMCID: 7797047.

466. Bowman EK, Deaner M, Cheng JF, Evans R, Oberortner E, Yoshikuni Y, Alper HS. Bidirectional titration of yeast gene expression using a pooled CRISPR guide RNA approach. Proc Natl Acad Sci U S A. 2020;117(31):18424-30. doi: 10.1073/pnas.2007413117. PubMed PMID: 32690674; PMCID: 7414176.

467. Krystosek A. Repositioning of human interphase chromosomes by nucleolar dynamics in the reverse transformation of HT1080 fibrosarcoma cells. Exp Cell Res. 1998;241(1):202-9. doi: 10.1006/excr.1998.4046. PubMed PMID: 9633529.

468. Potapova TA, Unruh JR, Yu Z, Rancati G, Li H, Stampfer MR, Gerton JL. Superresolution microscopy reveals linkages between ribosomal DNA on heterologous chromosomes. J Cell Biol. 2019;218(8):2492-513. doi: 10.1083/jcb.201810166. PubMed PMID: 31270138; PMCID: 6683752.

469. McLean LO. Discovering Novel Regulators of Nucleolar Form and Function [Ph.D.]. United States -- Connecticut: Yale University; 2021.

470. Singh S, Banerjee A, Vanden Broeck A, Klinge S. Rapid clonal identification of biallelic CRISPR/Cas9 knock-ins using SNEAK PEEC. Sci Rep. 2023;13(1):1719. doi: 10.1038/s41598-023-28732-8. PubMed PMID: 36720908; PMCID: 9889345 and S.K are inventors. All other authors have no competing interests.

471. Singh S, Vanden Broeck A, Miller L, Chaker-Margot M, Klinge S. Nucleolar maturation of the human small subunit processome. Science. 2021;373(6560):eabj5338. doi: 10.1126/science.abj5338. PubMed PMID: 34516797; PMCID: 8744464.

472. Damianov A, Kann M, Lane WS, Bindereif A. Human RBM28 protein is a specific nucleolar component of the spliceosomal snRNPs. Biol Chem. 2006;387(10-11):1455-60. doi: 10.1515/BC.2006.182. PubMed PMID: 17081119.

473. Lin X, Zhou L, Zhong J, Zhong L, Zhang R, Kang T, Wu Y. RNA-binding protein RBM28 can translocate from the nucleolus to the nucleoplasm to inhibit the transcriptional activity of p53. J Biol Chem. 2022;298(2):101524. doi: 10.1016/j.jbc.2021.101524. PubMed PMID: 34953860; PMCID: 8789582.